Studying and Modelling the Complete Gravitational-Wave Signal from Precessing Black Hole Binaries

by

Patricia Schmidt

A thesis submitted for the degree of

Doctor of Philosophy (Ph.D.)

School of Physics and Astronomy
Cardiff University
Wales, United Kingdom

August 2014

Supervisor: Dr Mark Hannam

External examiner: Prof Bernd Brügmann
Internal examiner: Prof Bangalore Sathyaprakash
Chair: Dr Patrick Sutton
Date of submission: 14.5.2014
Date of viva: 19.6.2014
Final version: 31.8.2014

Declaration of authorship

- **Declaration:**
  This work has not been submitted in substance for any other degree or award at this or any other university of place of learning, nor is being submitted concurrently in candidature for any degree or other award.

  Signed: .... (candidate) Date: ....

- **Statement 1:**
  This thesis is being submitted in partial fulfillment of the requirements for the degree of Doctor of Philosophy (PhD).

  Signed: .... (candidate) Date: ....

- **Statement 2:**
  This thesis is the result of my own independent work/investigation, except where otherwise stated. Other sources are acknowledged by explicit references. The views expressed are my own.

  Signed: .... (candidate) Date: ....

- **Statement 3:**
  I hereby give consent for my thesis, if accepted, to be available for photocopying and for inter-library loan, and for the title and summary to be made available to outside organisations.

  Signed: .... (candidate) Date: ....

- **Statement 4: PREVIOUSLY APPROVED BAR ON ACCESS**
  I hereby give consent for my thesis, if accepted, to be available for photocopying and for inter-library loans **after expiry of a bar on access previously approved by the Academic Standards & Quality Committee.**

  Signed: .... (candidate) Date: ....

Summary of thesis

The coalescence of two stellar mass black holes is regarded as one of the most promising sources for the first gravitational-wave (GW) detection with ground-based detectors. The current detection strategies, however, rely on theoretical knowledge of the gravitational waveforms. It is therefore crucial to obtain an accurate and complete description of the GW signal.

This thesis concerns the description of precessing black holes. Misalignment between the orbital angular momentum and the spin angular momenta of the two black holes induces precession, leading to complex dynamics that leaves a direct imprint on the GW. Additionally, the evolution of the binary depends on the mass ratio and both spins spanning a seven-dimensional intrinsic parameter space. This makes it difficult to obtain a simple, closed-form description of the waveform through inspiral, merger and ringdown. We are therefore interested in 1) developing a conceptually intuitive framework to systematically model precessing waveforms and 2) exploring the possibility of representing the seven-dimensional parameter space by a lower-dimensional subset.

First, we introduce an accelerated frame of reference, which allows us to track the precession of the orbital plane. We then analyse the waveforms in this co-precessing frame resulting in an approximate decoupling between the inspiral and precession dynamics. This leads to the important identification of the inspiral rate of a precessing binary with the inspiral rate of an aligned-spin binary. Based on this decoupling, we develop a general framework to construct precessing waveforms by "twisting up" an aligned-spin waveform with a model for the precession dynamics.

In general, precession depends on all seven intrinsic physical parameters, which complicates modelling efforts. However, we find a parameter-reduced representation of the dynamics, which allows us to produce a first closed-form description of the complete waveforms of precessing black-hole binaries within this general and easy-to-grasp framework.

Co-authored papers

Sections of this thesis include collaborative work that has either been published/submitted for publication or is in preparation. The author is either lead author or has contributed significantly to the work presented.

- Chapter 3 has partially been published in "Towards models of gravitational waveforms from generic binaries: A simple approximate mapping between precessing and non-precessing inspiral signals" [197]. P. Schmidt is lead author.
- Chapter 4 has been published in "Tracking the precession of compact binaries from their gravitational-wave signal" [196]. P. Schmidt is lead author.
- Chapter 5 has largely been published in "Towards models of gravitational waveforms from generic binaries: A simple approximate mapping between precessing and non-precessing inspiral signals" [197]. P. Schmidt is lead author.
- An adaptation of Chapter 6 with the title "Towards models of gravitational waveforms from generic binaries II: Modelling precession effects with a single effective precession parameter" [198] has recently been submitted to the preprint server arXiv and the journal Phys. Rev. D for publication. P. Schmidt is lead author.
- Chapter 7 is an expansion of the first version of "Twist and shout: A simple model of complete precessing black-hole-binary gravitational waveforms" [117], which has been submitted for publication. P. Schmidt has contributed to the results presented therein.

Für Mamsch

"Es ist nicht das Ziel der Wissenschaft,
der unendlichen Weisheit eine Tür zu öffnen,
sondern eine Grenze zu setzen dem unendlichen Irrtum."

Bertolt Brecht aus "Das Leben des Galilei"

Acknowledgements

First and foremost, I would like to thank the Austrian Academy of Sciences (Österreichische Akademie der Wissenschaften, ÖAW) for enabling this research by sponsoring my postgraduate studies with a DOC-fFORTE fellowship from January 2011 until December 2013.

The research presented in this thesis is the result of numerous discussions with many colleagues and friends, which I am very grateful for. Thank you!

I would like to thank my supervisor Mark Hannam for giving me opportunity to work on such a fantastic topic and his positive thinking throughout the years. Many thanks go to Prof. Sathyaprakash, who has been a fantastic mentor, to Stephen Fairhurst for sharing his incredible knowledge and to Patrick Sutton for his advice and pints of delicious cider. I would also like thank my external collaborators Sascha Husa and P. Ajith for their discussions and support.

I am particularly grateful to Frank Ohme, who is a valued colleague and good friend. Many insights in this thesis stem from fantastic discussions with Frank. My various office mates over the years have contributed to a really nice working environment – a big thanks to all of them, especially to Laura Nuttall, Tom Adams, Duncan Macleod and Ian Harry for welcoming me to the UK and helping me settling in. Girly drinks with Laura Nuttall, Georgina Klemencic and Erin Macdonald were always a great pleasure and a perfect opportunity to release tension and to relax – I am missing them already. Many thanks to the entire Cardiff crew (fellow students, postdocs and staff) for making it such a nice time here!

Ich möchte mich an dieser Stelle auch ganz herzlich bei meinen langjährigen Freunden zu Hause für ihre Unterstützung und Freundschaft trotz der Distanz danken. Es ist zwar nicht immer ganz leicht, den Kontakt zu halten, aber daran erkennt man auch wahre Freunde. Vielen lieben Dank Miriam Kollmann, Magdalena Hydzik & Florian Hammer, Florian Aigner, Teresa Torzicky, Michael Bartel, Nicolai Friis und Cornelia Deiss.

I would also like to express my thankfulness to the entire Pratten family, who has welcomed me with open arms and has been nothing short of wonderful.

Ganz besonderer Dank gilt natürlich meiner Familie, v.a. meiner Mama & Gerhard, meinem Papa & Uschi, sowie meiner Omi. Ihr habt mich auf diesem beschwerlichen Weg uneingeschränkt unterstützt, wart immer für mich da, auch wenn es oft nicht einfach für euch war – das werde ich euch nie vergessen. Vielen, vielen Dank für eure Liebe und Unterstützung!

Lastly, I would like to thank my beloved partner. Geraint, your love and support have been a great source of inspiration and energy. You have brought such happiness into my life, showing me that the home is where the heart is. You have always been there for me on sunny as well as on rainy days. No words could ever express how grateful I am that our worldlines have crossed. Thank you so, so much for everything!

Contents

List of Figures

List of Tables

CHAPTER 1

Introduction

Gravity is the weakest of the four fundamental forces, but it is responsible for shaping our Universe. Our current understanding is based on Einstein's theory of *General Relativity* (GR), which describes the interaction between masses, or more general energy, with space and time. It agrees with Newtonian gravity where applicable, but also predicts phenomena that go well beyond the Newtonian picture. One such phenomenon is the occurrence of gravitational radiation, called *gravitational waves* (GWs). These waves are perturbations of spacetime itself, produced by accelerated masses, which distort the fabric of spacetime in their vicinity. These distortions propagate away from the source at the speed of light. Analogously to electromagnetic radiation, GWs carry physical information and can therefore be regarded as "fingerprints" of the generating source revealing its true nature, which opens a new window to the Universe.

Gravitational radiation is, however, very weak far from the source. In order to directly observe GWs in a controlled experiment on Earth, extremely violent events such as the merger of two black holes or a supernova explosion need to take place in the nearby Universe. Until today, no such observation has been confirmed, but the existence of GWs as predicted by GR has been confirmed by other means: in 1974, Russel A. Hulse and Joseph H. Taylor discovered a binary system consisting of one neutron star and a pulsar (i.e., a magnetised and therefore radiating neutron star) [125]. The regular detection of the emitted radio pulses allowed them to identify a systematic variation in the arrival time of the pulses on Earth. They realised that this behaviour is predicted by Einstein's GR for a pulsar in orbit with another compact star. According to GR, such compact binary systems lose gravitational binding energy in the form of GWs, causing the orbital separation to shrink with time. This orbital decay causes a shift in the periastron which, in turn changes the arrival time of the radio pulses. This shift is observed and compared to the predictions of General Relativity. The observations show remarkable agreement with the theoretical predictions as illustrated in Fig. 1.1, strongly supporting the assumption that the orbital decay is indeed driven by the emission of gravitational waves.

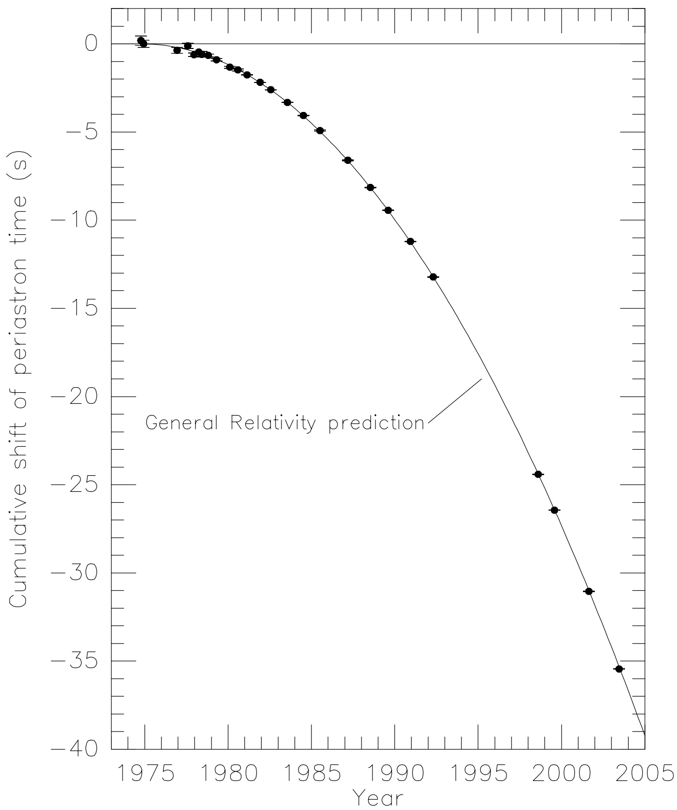

Figure 1.1: The orbital decay of the Hulse-Taylor binary pulsar PSR B1913+16. The data points indicate the observed shift in the periastron. The solid line shows the theoretical predictions from GR for a binary system emitting gravitational waves; figure taken from [224].

Most recently, evidence for the existence of another type of GWs, *primordial gravitational waves* has been presented by the BICEP-2 collaboration [7]. These GWs are predicted to be generated in the very early Universe immediately after the Big Bang [103, 105, 106, 143, 206, 207]. Such gravitational perturbations in the early Universe leave a measurable imprint in the B-mode polarisation of the photons of the cosmic microwave background [131, 201]. A signal consistent with primordial GWs has been reported in [7].

In order to directly observe gravitational waves by their effects on spacetime itself, ground-based Michelson laser interferometers are considered to be the most promising laboratory experiment. A worldwide network of such GW detectors has been operating for more than a decade and is currently undergoing an upgrade to reach a design sensitivity, which will allow for the detection of several GW signals per year [5].

The signals these detectors are predominantly "listening" for are generated by coalescing compact binaries, in particular two black holes. Inspiraling and merging black holes are among the most violent, gravitationally-driven events in the Universe. Unless they are surrounded by matter, black holes binaries shine only gravitationally. The observation of their GWs would open an entirely new window to the Universe, allowing us to probe some of the most exotic phenomena in GR, and to complement what we can infer today from electromagnetic and other observations to obtain a more complete understanding of the Universe.

Although black hole binaries are gravitationally luminous, a binary formed of two Schwarzschild black holes of the same mass emits $10^{23}L_\odot$ when they merge, the effective cross section of the radiation is so small that the signal recorded by the detector is extremely weak. This poses a theoretical and computational challenge for analysing the noise-dominated data and identifying a GW buried therein. One of the most successful strategies employed in GW searches is based on theoretical knowledge of the gravitational waveform emitted by a compact binary system. These theoretical waveform templates are compared against the noisy data and a statistical significance is assigned to whether or not a true GW is contained in the data stream.

Modelling the gravitational waves from black hole binaries, however, is a challenging task. Exact solutions to the binary-black-hole problem can only be obtained by solving the Einstein equations numerically, which is only possible since 2005 [24, 68, 183]. On the other hand, analytic approximation methods, such as post-Newtonian theory, are available and allow for an approximate description of the GW signal when the two black holes are far apart. Ideally, waveform templates should contain all information available, and therefore complete waveform models, which combine the analytic with the numerical information, are desired. The construction of such a waveform model for the most general class of black hole binaries, precessing binaries, is the focus of this thesis. The overall contribution of this thesis is the development of a simple framework based on a method to untangle the complex dynamics and the waveform mode structure of precessing binaries, the identification of the key parameters of generic binaries, and the construction of a prototype generic-binary waveform model to aid future modelling and source parameter estimation efforts as well as the development of GW searches.

This thesis is organised as follows: in Chapter 2 we give brief summaries of the topics relevant to this thesis, before moving on to the discussion of the phenomenology of precessing black hole binaries in Chapter 3. In this chapter, we focus on the qualitative description of the binary motion and how precession affects the gravitational waveforms. In Chapter 4 we introduce a co-precessing frame, the quadrupole-aligned frame, by identifying the direction of maximal emission using only information from the GW signal. The algorithm, which determines this axis, is presented in detail. The introduction of this non-inertial frame and the analysis of waveforms as viewed therein then allows us to identify the secular phasing of a precessing binary as the same as for a corresponding spinning, non-precessing binary. This identification is presented in detail in Chapter 5. In doing so, we show that the secular inspiral and the precession dynamics approximately decouple and that this decoupling even holds through the late stages of the binary evolution, meaning that the secular phase is well approximated by the phase of an aligned-spin binary. This decoupling is one of the key insights of this thesis, which has subsequently allowed for the systematic construction of a series of precessing waveform models [117, 148, 174].

Based on the approximate decoupling, in Chapter 6 we present an effective precession spin, which allows for a simplified description of the precession dynamics. The precessional motion is predominantly encoded in the evolution of the orbital plane given by the time evolution of the inclination angle $\iota(t)$ and the precession angle $\alpha(t)$. We show that the precession dynamics a generic system undergoes can be well represented by a reduced set of spin parameters. This effective parameterisation significantly simplifies the challenging task of modelling the precession dynamics as a function of physical parameters.

In Chapter 7 we present the first inspiral-merger-ringdown model for precessing black hole binaries in the frequency domain based on the individual ingredients presented in the Chapters 4-6. We conclude with a brief discussion of our results in Chapter 8.

CHAPTER 2

Preliminaries and framework

2.1 Convention and notation

In the following, the signature of the metric of a Lorentzian manifold (M, g) is chosen to be $sign(g) = (-, +, +, +)$. Spacetime indices are denoted by Greek letters and run from 0 to 3, whereas spatial indices are represented by Latin letters running from 1 to 3. Repeated co- and a contravariant indices denote the *Einstein summation convention*

$$\Lambda^{\mu}{}_{\mu} \equiv \sum_{\mu=0}^{3} \Lambda^{\mu}{}_{\mu} = \Lambda^{0}{}_{0} + \Lambda^{1}{}_{1} + \Lambda^{2}{}_{2} + \Lambda^{3}{}_{3}. \tag{2.1}$$

We adopt *geometrical units*, where the speed of light c and the gravitational constant G are set to unity $(G = c \equiv 1)$ unless the constants are explicitly inserted for reasons of clarity.

2.2 General Relativity in a nutshell

The following section is intended to refresh readers' knowledge of some fundamental concepts and aspects of General Relativity that are relevant for this thesis. For a comprehensive description of the subject we refer the reader to the textbooks by [120, 151, 199] and for a more mathematical treatment of the subject to [123, 167, 218].

Gravity is one of the four fundamental forces in physics. It is responsible for the apple falling to the ground, for the planets going around the sun, for the stars moving around the centre of our Galaxy. Due to its long reach, it is the shaping force on the large scales of the universe. The first theory of gravity was Isaac Newton's, which explains the gravitational attraction of the Earth and the motion of the planets around the sun, but it fails to explains observable effects like the perihelion precession of Mercury. In 1915 Albert Einstein published a new theory of gravity: the theory of a *General Relativity* (GR) [92]. In this geometric theory of gravity, space and time are unified to build a four dimensional continuum, *spacetime*, and gravity manifests itself as a geometric property of this manifold: *curvature*. Any form of matter, or in general energy content, deforms the fabric of spacetime causing it to curve and bend. This warping of spacetime affects the path of light rays travelling from a distant source and it also explains the deviation of Mercury's trajectory from a Keplerian orbit – effects measurable in our solar system allowing for experimental tests of GR [74, 91].

General relativity also predicts the existence of one of the most fascinating class of objects in the universe: *black holes*. These are thought to be causally disconnected regions of spacetime, with a gravitational field so strong that nothing, not even light, can escape. Black holes are not just a singular point in spacetime but cover an extended region which is bounded by the *event horizon*. Inside this horizon, the spacetime singularity is hidden and as of today the laws that describe the physics beyond the singularity are yet unknown.

General Relativity is a geometric theory that relies on the concept of spacetime. Mathematically, spacetime is a four-dimensional differentiable semi-Riemannian manifold M together with a non-degenerate symmetric bilinear form, the *Lorentzian metric* g. A Lorentzian metric need not be positive definite, which induces the causal structure, allowing for vectors to be null, timelike or spacelike. The metric is used to measure the (Lorentz-invariant) distance between two points $p_1, p_2 \in M$. This distance, or *line element*, is given by

$$ds^2 = g_{\mu\nu} dx^\mu dx^\nu, \tag{2.2}$$

where dx^μ denotes infinitesimal coordinate differences.

The presence of gravitational fields is entirely encoded in the metric tensor. If there are no gravitational fields, the metric corresponds to $\eta_{\mu\nu}$,

$$\eta_{\mu\nu} = \mathrm{diag}(-1, 1, 1, 1), \tag{2.3}$$

and we recover flat *Minkowski space*, the spacetime of Special Relativity. The geometric measure for the presence of gravitational fields is the curvature. One natural way to define curvature is in terms of the *parallel transport*. In flat space, a vector transported along a closed curve does not change its direction. In curved space though, this is not necessarily true anymore. In order to define parallel transport, the notion of a derivative operator is needed. Generally, no global coordinate system exists on a Lorentzian manifold and therefore the coordinate systems, i.e., the basis vectors, at two points in the manifold will differ form each other. A derivative operator needs to take this change of basis vectors into account. Let $\mathcal{C}$ be a smooth curve, e.g., the worldline $x^\mu(\lambda)$ of an observer, in M with a tangent vector $t^\mu = dx^\mu/d\lambda$, where $\lambda \in \mathbb{R}$ is an *affine* parameter. A vector v^ν is parallel transported along the curve if and only if

$$t^\mu \nabla_\mu v^\nu = 0, \tag{2.4}$$

where ∇_μ denotes the *covariant derivative*, a derivative operator with the desired property. The covariant derivative of a vector is given by

$$\nabla_\mu v^\nu = \partial_\mu v^\nu + v^\sigma \Gamma^\nu_{\mu\sigma}, \tag{2.5}$$

where ∂_μ is the partial derivative and $\Gamma^\nu_{\mu\sigma}$ are the *connection coefficients*. There is no unique choice of a derivative operator on a manifold, but once a metric tensor is provided, a unique operator can be defined. We can now impose an extra requirement on the derivative operator, namely that the scalar product between two vectors is preserved under parallel transport. This condition can be fulfilled if and only if

$$\nabla_\sigma g_{\mu\nu} = 0. \tag{2.6}$$

This defines the unique derivative operator ∇_μ induced by the metric $g_{\mu\nu}$. This condition then implies that the connection coefficients must take the following form:

$$\Gamma^\sigma_{\mu\nu} = \frac{1}{2} g^{\sigma\lambda} \left\{ \partial_\mu g_{\nu\lambda} + \partial_\nu g_{\mu\lambda} - \partial_\lambda g_{\mu\nu} \right\}. \tag{2.7}$$

These specific connection coefficients are commonly referred to as *Christoffel symbols*.
A vector's directional change after having been parallel transported along a closed curve is encoded in the *Riemann curvature tensor* given by

$$R^\lambda_{\mu\nu\sigma} v_\lambda = \nabla_\mu \nabla_\nu v_\sigma - \nabla_\nu \nabla_\mu v_\sigma. \tag{2.8}$$

This identity is also called the *Ricci identity*; its right hand-side can be interpreted as the commutation of the covariant derivative. We can also express Eq.(2.8) in terms of partial derivatives and Christoffel symbols, yielding

$$R^\lambda_{\mu\nu\sigma} = \partial_\nu \Gamma^\lambda_{\mu\sigma} - \partial_\sigma \Gamma^\lambda_{\mu\nu} + \Gamma^\lambda_{\nu\rho} \Gamma^\rho_{\mu\sigma} - \Gamma^\lambda_{\sigma\rho} \Gamma^\rho_{\mu\nu}. \tag{2.9}$$

The $(1,3)$-contraction of the Riemann tensor with the metric yields the *Ricci curvature tensor*

$$R_{\mu\nu} := R^\lambda_{\mu\lambda\nu}. \tag{2.10}$$

Yet another contraction defines the *Ricci scalar* or scalar curvature

$$R := R^\mu{}_\mu. \tag{2.11}$$

In General Relativity, massive particles move along timelike worldlines and if they are freely falling, they satisfy the *geodesic equation of motion*:

$$u^\mu \nabla_\mu u^\nu = 0, \tag{2.12}$$

where u^μ is the 4-velocity of a particle. A geodesic is the generalisation of a straight line in a curved manifold. In the presence of tidal forces, freely falling particles do not move along geodesics. The acting of tidal forces on a set of freely falling observers is measured by the relative acceleration of two freely falling bodies given by $-R_{\mu\nu\sigma}{}^\lambda u^\mu \xi^\nu u^\sigma$, where ξ^λ is the deviation vector, i.e., the vector that connects the two test particles. It follows that the geodesic deviation is directly encoded in the Riemann curvature tensor. Therefore, if $R_{\mu\nu\sigma}{}^\lambda$ vanishes, the two worldlines stay parallel – the spacetime is flat and no coordinate transformation can be found such that the second derivatives of the metric vanish. If the components of the Riemann tensor do not vanish, two initially parallel worldlines will either converge or diverge due to the presence of gravitational forces. But how do these geometric quantities describe gravity?

Let us first recall the field equation in Newtonian gravity, the Poisson equation, which connects the gravitational potential Φ_N with the mass density ρ of an object

$$\triangle \Phi_N = 4\pi\rho, \tag{2.13}$$

where $\triangle$ is the Laplace operator. The covariant generalisation of the right hand-side of the Poisson equation needs to be compatible with the special relativistic limit $g_{\mu\nu} \equiv \eta_{\mu\nu}$. In Special Relativity, continuous matter distributions are described by the *stress-energy-momentum tensor* $T_{\mu\nu}$. In order to recover the correct limit, the energy properties of matter in GR also have to be described by a stress energy tensor. The generalisation of the left side of Eq.(2.13) is the *Einstein tensor*

$$G_{\mu\nu} := R_{\mu\nu} - \frac{1}{2} g_{\mu\nu} R. \tag{2.14}$$

Finally, the desired field equations describing the metric of spacetime and hence the gravitational fields, the *Einstein field equations*, are given by

$$G_{\mu\nu} \equiv R_{\mu\nu} - \frac{1}{2} g_{\mu\nu} R = 8\pi T_{\mu\nu}. \tag{2.15}$$

In a nutshell, general relativity can be summarised as follows: spacetime is a four-dimensional manifold M with a Lorentzian metric $g_{\mu\nu}$. Gravity is in encoded in the metric as the curvature of spacetime and the curvature is related to the mass distribution in spacetime by the Einstein equations.

One should not be fooled by the apparent elegance of these equations. If a coordinate basis is chosen, the true nature of the field equations is revealed: they are a highly non-linear system of ten coupled second-order partial differential equations. In order to solve these equations, one must simultaneously solve for the metric and the matter distribution as the stress-energy tensor depends explicitly on the metric. This particular feature makes it very difficult to solve the field equations in the presence of sources.

By taking the trace of Eq.(2.15), the field equations can be cast in an equivalent form

$$R_{\mu\nu} = 8\pi \left(T_{\mu\nu} - \frac{1}{2} g_{\mu\nu} T \right). \tag{2.16}$$

If no sources are present, then $T_{\mu\nu} = 0$ and the trace $T^{\mu}{}_{\mu} = 0$, yielding the Einstein equations in vacuum:

$$R_{\mu\nu} = 0. \tag{2.17}$$

Due to the mathematically complex structure of the field equations, only a handful of exact analytic solutions are known. Undoubtedly one of the most important exact solution is that for a static, spherically symmetric vacuum spacetime: the *Schwarzschild solution.* Its metric in Schwarzschild coordinates is given by

$$ds^2 = -\left(1 - \frac{2M}{r}\right) dt^2 + \left(1 - \frac{2M}{r}\right)^{-1} dr^2 + r^2 d\Omega^2, \tag{2.18}$$

where $d\Omega^2 = d\theta^2 + sin^2\theta d\phi^2$, the line element on the unit sphere with (θ, ϕ) the polar and azimuth angle. The function r can be interpreted as a "radial coordinate" given by

$$r = \sqrt{A/4\pi}, \tag{2.19}$$

where A is the total area of S^2; the value $r_S = 2M$ is the *Schwarzschild radius.*

The Schwarzschild solution was derived by Karl Schwarzschild [200] only a few months after the publication of Einstein's theory of General Relativity and is a one-parameter family of solutions, which describes the gravitational field outside some spherically symmetric mass distribution of total mass M. The derivation exploits the assumption of a particular symmetry, in this case spatial spherical symmetry, a strategy very commonly used to derive exact solutions. The difficulty of finding exact solutions is illustrated by the fact that it took almost 50 years to find the solution for an axisymmetric vacuum spacetime, the Kerr solution [132], describing the gravitational field outside a rotating mass distribution like a neutron star. Further generalisations are the Reissner-Nordström [161, 187] and the Kerr-Newman [158, 160] solutions. Other exact solutions are known in the context of cosmology, most notably the Friedmann-Lemaître-Robertson-Walker solution [98, 99, 138, 139, 189, 190, 220], which is the standard model used to describe the large-scale universe and is derived under the assumption of spatial homogeneity and isotropy.

The Schwarzschild solution, which describes the exact exterior field of a spherical body like our sun, predicts small deviations from Newtonian gravity, which can be measured in our solar system and used to test GR. Various predictions have been successfully confirmed by precise measurements in our solar system. However, the Schwarzschild solution also allows us to understand much more about the strong-field regime of gravity. Massive stars which have reached the end of their life cycle will run out of fuel generating the radiation pressure to support themselves and will start to undergo gravitational collapse. If the initial mass of the star was large enough, the end product of this collapse contains a spacetime singularity hidden within an event horizon and is also described by the vacuum Schwarzschild solution. The event horizon is a boundary in spacetime which represents a point of no return. Once the event horizon is crossed, nothing, not even light, can escape. At $r = 0$, the metric and the Ricci scalar diverge, forming a true spacetime singularity which cannot be avoided by a change of coordinates. The entire region inside the event horizon is commonly referred to as a black hole (see Chapter 6 in [218] or Chapters 5 and 6 in [73]).

In this thesis, we are particularly interested in spacetimes containing two spinning black holes (Kerr black holes). Such general spacetimes do not possess symmetries which could be exploited to find analytical solutions and therefore no such exact solutions for general binary spacetimes exist. The Einstein equations can be solved only approximately through analytical approximations or numerical techniques, which will be discussed in Sec. 2.5.1 and Sec. 2.5.2.

The existence of black holes is an integral part of our understanding of the universe and is strongly supported by observational evidence like the peculiar motion of stars in the centre of our Galaxy or active galactic nuclei (AGNs). However, any such observation infers the presence of a central black hole from the measured effects on surrounding matter. Can we detect black holes directly via their effect on spacetime itself? One way to directly detect black holes is the main motivation for this work: the observation of gravitational waves emitted by a black hole binary.

2.3 Gravitational waves

Einstein's theory of General Relativity makes another fascinating prediction: *gravitational waves* (GWs) [93]. These are small perturbations of spacetime itself caused by accelerating masses, which propagate away from their source at the speed of light. The most straightforward way to derive the existence and the main properties of GWs is in the context of linearised gravity. We shall briefly summarise the derivation and the main properties of GWs here, as they are the main focus of this thesis, but direct the interested reader to [120, 149, 199] for a more comprehensive treatment of the subject.

2.3.1 Linearised gravity

In this section, we derive the solution of the vacuum field equation under the assumption that gravity is "weak". In GR this means that the spacetime metric is nearly flat $g_{\mu\nu} \simeq \eta_{\mu\nu}$. In practice this is an excellent approximation for many situations in nature except for highly relativistic phenomena such as gravitational collapse or to describe the vicinity of black holes.

Let us start by assuming that the spacetime metric is close to Minkowski apart from small gravitational perturbations, yielding

$$g_{\mu\nu} = \eta_{\mu\nu} + h_{\mu\nu}, \tag{2.20}$$

where $h_{\mu\nu}$ is a small metric perturbation in the sense that $||h_{\mu\nu}|| \ll 1$. Linearised gravity is the approximation to GR obtained by substituting this perturbed Minkowski metric into the Einstein equations Eq.(2.15) and only retaining terms linear in $h_{\mu\nu}$. From this it follows immediately that the inverse metric is given by

$$g^{\mu\nu} = \eta^{\mu\nu} - h^{\mu\nu}, \tag{2.21}$$

where $h^{\mu\nu} = \eta^{\mu\lambda}\eta^{\nu\sigma}h_{\lambda\sigma}$. We see that indices are raised and lowered with the flat metric $\eta_{\mu\nu}$, since the corrections would be of higher order in $h_{\mu\nu}$. We can view the linearised version of GR as the theory describing the propagation of the symmetric tensor field $h_{\mu\nu}$ on a flat background spacetime. This theory is Lorentz invariant in the sense of Special Relativity.
By inserting Eq.(2.20) into Eq.(2.7), we find the linearised Christoffel to be given by

$$^{(1)}\Gamma^{\sigma}{}_{\mu\nu} = \frac{1}{2}\eta^{\sigma\lambda}\left(\partial_\mu h_{\nu\lambda} + \partial_\nu h_{\mu\lambda} - \partial_\lambda h_{\mu\nu}\right), \tag{2.22}$$

where $^{(1)}$ indicates the linearised quantity to distinguish from the fully covariant expression. By inserting Eq.(2.20) into the expression for the Riemann tensor Eq.(2.9), we obtain the Riemann tensor in linearised gravity:

$$^{(1)}R_{\mu\nu\sigma\lambda} = \frac{1}{2}\left(\partial_\nu\partial_\sigma h_{\mu\lambda} + \partial_\mu\partial_\lambda h_{\nu\sigma} - \partial_\nu\partial_\lambda h_{\mu\sigma} - \partial_\mu\partial_\sigma h_{\nu\lambda}\right). \tag{2.23}$$

The linearised Ricci tensor then becomes

$$^{(1)}R_{\mu\nu} = \partial_\sigma {}^{(1)}\Gamma^{\sigma}{}_{\mu\nu} - \partial_\mu {}^{(1)}\Gamma^{\sigma}{}_{\sigma\nu}, \tag{2.24}$$

where we have used the definition of the Riemann tensor in a coordinate basis and the fact that the partial coordinate derivative ∂_σ of the flat metric vanishes, i.e., $\partial_\sigma\eta_{\mu\nu} = 0$. We can now evaluate the expressions on the left side of the above equation, which yields

$$\partial_\sigma {}^{(1)}\Gamma^\sigma{}_{\mu\nu} = \frac{1}{2}\partial^\sigma \left(\partial_\mu h_{\nu\sigma} + \partial_\nu h_{\mu\sigma} - \partial_\sigma h_{\mu\nu}\right) \tag{2.25}$$

$$\partial_\mu {}^{(1)}\Gamma^\sigma{}_{\sigma\nu} = \frac{1}{2}\partial_\mu\partial_\nu h, \tag{2.26}$$

where $h = \eta^{\mu\nu}h_{\mu\nu} = h^\mu{}_\mu$ is the trace of the metric perturbation. The linearised Ricci tensor then reduces to

$$^{(1)}R_{\mu\nu} = \frac{1}{2}\partial^\lambda \left(\partial_\mu h_{\nu\lambda} + \partial_\mu h_{\nu\lambda} - \partial_\lambda h_{\mu\nu}\right) - \frac{1}{2}\partial_\mu\partial_\nu h. \tag{2.27}$$

By contracting the above equation with the flat metric, we obtain the linearised Ricci scalar:

$$^{(1)}R = \partial^\mu\partial^\nu h_{\mu\nu} - \partial^\mu\partial_\mu h. \tag{2.28}$$

We have now all ingredients to derive the linearised field equations. By inserting the linearised expressions for the Ricci tensor and scalar into the field equations Eq.(2.15), we obtain

$$\begin{aligned} ^{(1)}G_{\mu\nu} &\equiv {}^{(1)}R_{\mu\nu} - \frac{1}{2}\eta_{\mu\nu}{}^{(1)}R \\ &= \frac{1}{2}\left(\partial^\lambda\partial_\mu h_{\nu\lambda} + \partial^\lambda\partial_\nu h_{\mu\lambda} - \partial^\lambda\partial_\lambda h_{\mu\nu} - \partial_\mu\partial_\nu h - \eta_{\mu\nu}\partial^\lambda\partial^\sigma h_{\lambda\sigma} + \eta_{\mu\nu}\partial^\lambda\partial_\lambda h\right) \end{aligned} \tag{2.29}$$

This is a rather cumbersome expression but it can be significantly simplified by a change of variable. Instead of using the metric perturbation itself, we can use the trace-reversed metric perturbation $\bar{h}$, where

$$\bar{h}_{\mu\nu} := h_{\mu\nu} - \frac{1}{2}\eta^{\mu\nu}h. \tag{2.30}$$

If we now express $h_{\mu\nu}$ in terms of $\bar{h}_{\mu\nu}$ and substitute it into Eq.(2.29), all terms containing the trace h vanish resulting in

$$^{(1)}G_{\mu\nu} = \frac{1}{2}\left(\partial^\lambda\partial_\mu \bar{h}_{\nu\lambda} + \partial^\lambda\partial_\nu \bar{h}_{\mu\lambda} - \partial^\lambda\partial_\lambda \bar{h}_{\mu\nu} - \eta_{\mu\nu}\partial^\lambda\partial^\sigma h_{\lambda\sigma}\right) = 8\pi T_{\mu\nu}. \tag{2.31}$$

These are the *linearised Einstein field equations*, but we have not yet exploited the *gauge freedom* of General Relativity. The gauge freedom in GR corresponds to the invariance under coordinate transformations. Applied to the linear approximation it implies that two perturbations $h_{\mu\nu}$ and $h'_{\mu\nu}$ represent the same physical perturbation if they do not differ under an infinitesimal coordinate transformation

$$x^\mu \to x'^\mu = x^\mu + \xi^\mu, \tag{2.32}$$

where ξ^μ is the generator of the gauge transformation.

Applying the general transformation law for tensors under coordinate changes to the metric perturbation yields

$$h_{\mu\nu} \to h'_{\mu\nu} = h_{\mu\nu} - \partial_\mu \xi_\nu - \partial_\nu \xi_\mu. \tag{2.33}$$

We may now use this freedom to further simplify the linearised field equations. By applying the gauge transformation to the trace-reversed metric Eq.(2.30), we find that it transforms as

$$\bar{h}_{\mu\nu} \to \bar{h}'_{\mu\nu} = \bar{h}_{\mu\nu} - \partial_\nu \xi_\mu - \partial_\mu \xi_\nu + \eta_{\mu\nu}\partial^\lambda \xi_\lambda. \tag{2.34}$$

We can now choose a gauge parameter ξ_μ such that it satisfies

$$\partial^\nu \partial_\nu \xi_\mu = -\partial_\nu \bar{h}^\nu{}_\mu. \tag{2.35}$$

Differentiating Eq.(2.34) with respect to ∂^μ and making use of Eq.(2.35) yields the *Lorenz gauge condition*

$$\partial^\nu \bar{h}_{\mu\nu} = 0. \tag{2.36}$$

In this particular gauge, the linearised Einstein equations Eq.(2.31) take the following form:

$$\Box \bar{h}_{\mu\nu} = -16\pi T_{\mu\nu}, \tag{2.37}$$

where $\Box = \partial^\mu \partial_\mu$ is the flat-space d'Alambertian. We find that in the Lorenz gauge, the linearised field equations have reduced to simple wave equations for each component of the trace-reversed metric perturbation. This is the crucial result for the generation of gravitational waves within the linearised theory of gravity. The general solutions to these simplified field equations in the weak-field limit can be found via the standard method of Green functions.

In order to study the propagation of gravitational waves and their interaction with test masses, we are interested in the governing equations outside the source, i.e., $T_{\mu\nu} = 0$:

$$\Box \bar{h}_{\mu\nu} = 0. \tag{2.38}$$

In the vacuum case, the Lorenz gauge condition alone is not enough to fix the gauge freedom. Further inspection shows that the Lorenz gauge condition is not violated by imposing $\bar{h} = 0$, then $\bar{h}_{\mu\nu} \equiv h_{\mu\nu}$, and $h^{0i} = 0$. The Lorenz condition then becomes

$$\partial^0 h_{00} = 0, \tag{2.39}$$

$$\partial^i h_{ij} = 0. \tag{2.40}$$

This means that h_{00} corresponds to the static (time-independent) part of the gravitational field; the time-varying gravitational degrees of freedom, the GW itself, is contained in the time-dependent components h_{ij}. In summary, via exploiting the gauge degrees of freedom we have set

$$h^{0\mu} = 0, \tag{2.41}$$

$$h^i{}_i = 0, \tag{2.42}$$

$$\partial^i h_{ij} = 0. \tag{2.43}$$

This set of conditions defines the *transverse-traceless gauge* (TT gauge), the most convenient gauge to express gravitational waves outside the source. The general complex solutions of Eq.(2.38) are plane-wave solutions

$$h_{\mu\nu} = A_{\mu\nu} e^{ik_\sigma x^\sigma}, \tag{2.44}$$

with $k^\mu = (\omega, k^i)$ the wave vector. In the TT-gauge this general expression can be rewritten as

$$h_{ij}^{\mathrm{TT}} = e_{ij} e^{ik_\mu x^\mu}, \tag{2.45}$$

where e_{ij} is the *polarisation tensor*. If we now choose the direction of the wave propagation, e.g., the z-axis, then we are left with only two independent components, which represent the two gravitational degrees of freedom:

$$h_{\mu\nu}^{\mathrm{TT}} = \begin{pmatrix} 0 & 0 & 0 & 0 \\ 0 & h_+ & h_\times & 0 \\ 0 & h_\times & -h_+ & 0 \\ 0 & 0 & 0 & 0 \end{pmatrix},$$

where h_+ and $h_\times$ are two independent gravitational-wave polarisations. With this set of gauge conditions, we have fully exploited the gauge freedom and hence the two polarisations are the true gravitational degrees of freedom.

2.3.2 Interaction of GWs with test masses

In the previous section we have seen how the existence of gravitational waves arises in the linearised version of General Relativity. We now briefly discuss their interaction with test masses closely following [73, 199].

In the absence of external gravitational forces, test masses move along the straightest possible lines in a curved background, geodesics as described by Eq.(2.12). In order to quantify how an external time-varying field, like a gravitational-wave, affects the motion of freely-falling test masses in a Minkowski background, we need to consider at least two nearby geodesics, $x^\mu(\lambda)$ and $x^\mu(\lambda)+\xi^\mu(\lambda)$ separated by a vector ξ^μ and parameterised by some affine parameter $\lambda \in \mathbb{R}$. If the separation of the two geodesics is much smaller than the typical scale of variation of the gravitational field, we can take the difference between the two geodesics and expand it to leading order in ξ in the local inertial frame (LIS) of one test particle. By doing so, we find [199]

$$\frac{D^2\xi^\mu}{D\lambda^2} = -{}^{(1)}R^\mu{}_{\nu\rho\sigma}\xi^\rho \frac{dx^\nu}{d\lambda}\frac{dx^\sigma}{d\lambda}, \tag{2.46}$$

where $D := \xi^\alpha \nabla_\alpha$. This equation shows that two nearby freely-falling test masses experience a tidal accerleration encoded in the linearised Riemann tensor and therefore deviate from a geodesic motion. According to the Stewart-Walker lemma [208], the inearised Riemann tensor is gauge-invariant, therefore the components of the separation vector ξ^μ can be identified as its proper length. By inserting Eq.(2.23) into the above equation, we can express the relative acceleration in terms of the gravitational perturbation, yielding

$$\frac{d^2\xi^\mu}{d\lambda^2} = \frac{1}{2}\xi^\nu \frac{d^2 h^{\mathrm{TT}}_{\mu\nu}}{d\lambda^2}. \tag{2.47}$$

We see immediately that a passing GW acts like a force on one of the freely falling particles if we are in the LIS of the other particle. To lowest order for slowly-moving particles $\lambda = x^0 = t$, the geodesic deviation equation in the LIS reduces to

$$\frac{\partial^2}{\partial t^2}\xi^\mu = \frac{1}{2}\xi^\nu \ddot{h}^\mu{}_\nu. \tag{2.48}$$

The leading-order solution to the above equation is

$$\xi^\mu(t) = \left(\delta^\mu{}_\nu + \frac{1}{2}h_{\mu\nu}(t)\right)\xi^\nu(0), \tag{2.49}$$

where $\delta^\mu{}_\nu$ is the Kronecker delta and $\xi^\mu(0)$ is the initial separation of the two geodesics. The above equation allows us to deduce a clear picture of how gravitational waves affect a ring of freely-falling test particles: let us assume a gravitational wave travels along the z-direction and the ring of particles is contained in the xy-plane. Now consider a GW such that h_{xx} does not vanish but $h_{xy} = 0$. As the wave passes through the ring of particles, it stretches and squeezes the proper distance between the particles as depicted in the left panel of Fig. 2.1. If we now set $h_{xx} = -h_{yy} = 0$ but allow for $h_{xy} \neq 0$, we find a similar effect on the ring of particles but rotated by 45° as shown the right panel of Fig. 2.1. This periodic squeezing and stretching of the proper distance between test masses is the basic principle used in interferometric GW observatories. The notion of cross and plus polarisation as introduced earlier should be clear from the illustrations.

2.3.3 The generation of gravitational waves

So far, we have introduced gravitational waves as perturbations of the flat Minkowski metric. Here, we briefly outline the basics of how gravitational waves are generated. In this section

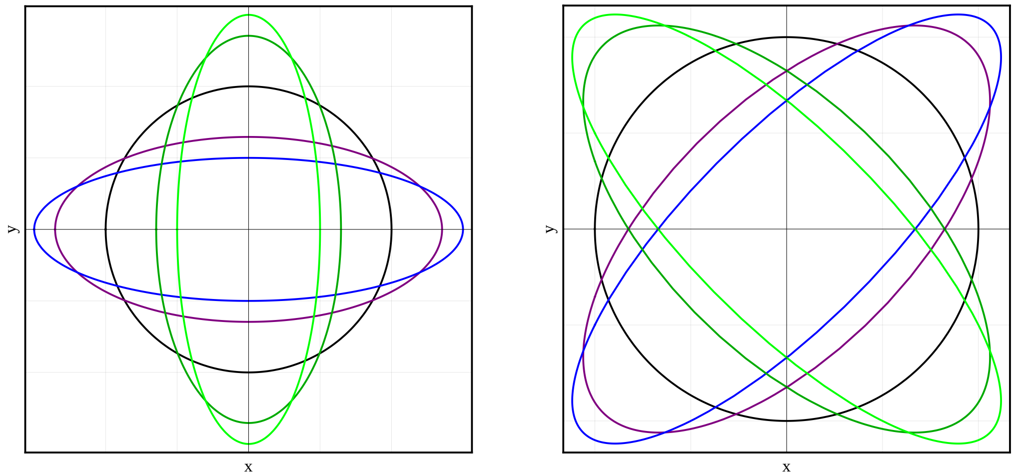

Figure 2.1: The effect of gravitational-waves travelling in the z-direction on a ring of freely-falling particles in the xy-plane. The left panel assumes a GW with plus polarisation only, the right panel a GW with cross polarisation. The ring of test masses is initially at rest (black) and is periodically distorted due to the passing GW.

we follow the explanations of [73, 97, 120, 149].

The general solution of Eq.(2.37) is given by the retarded integral

$$\bar{h}_{\mu\nu}(x) = -16\pi \int d^4x' G(x-x') T_{\mu\nu}(x'). \tag{2.50}$$

Analogously to electromagnetism, the appropriate solution is governed by the retarded Green's function

$$G(x-x') = -\frac{1}{4\pi |x^i - x'^i|} \delta(t_{\text{ret}} - t'), \tag{2.51}$$

where the retarded time is given by $t_{\text{ret}} = t - |x - x'|$. If we substitute the Green's function into Eq.(2.50) we find the general solution to the inhomogeneous linearised field equations to be

$$\bar{h}_{\mu\nu}(t, x^i) = 4 \int d^3x' \frac{T_{\mu\nu}(t - |x^i - x'^i|), x'^i}{|x^i - x'^i|}, \tag{2.52}$$

where the integration is performed over the past light cone of the event (t, x^i).

Let us now assume that the GWs are generated by a weak source and observed at large distance from the source, i.e., $r \gg R$, where R is the characteristic size of the source. In this case, one can perform the standard multipole expansion of the denominator analogous to the expansion of the electromagnetic field at large distance from the source:

$$\frac{1}{|x^i - x'^i|} \simeq \frac{1}{r} + \frac{x^i x'^i}{r^3} + \ldots \tag{2.53}$$

In the limit $r \to \infty$ the asymptotic solution of the linearised field equations therefore is

$$\bar{h}_{\mu\nu} \to \frac{4}{r} \int d^3x' T_{\mu\nu}(t-r, x'^i). \tag{2.54}$$

We note that in linearised theory $T_{\mu\nu}$ fulfills the flat-space conservation law, i.e., $\partial^\mu T_{\mu\nu} = 0$ and sources therefore move on geodesics in flat Minkowski space. Applying the conservation law, we find that

$$\int d^3x T_{ij} = \frac{1}{2} \frac{d^2}{dt^2} \int d^3x x^i x^j T_{00}. \tag{2.55}$$

Assuming a standard stress-energy tensor, the tt-component denotes the rest-mass energy density of the source $\mu(x)$. We can now define the *second moment of mass* or *moment of inertia tensor*

$$I_{ij} := \int d^3x \mu(t, x^i) x_i x_j. \tag{2.56}$$

Hence, the asymptotic solution describing GWs generated by weak sources is found to be

$$\bar{h}_{ij} \underset{r\to\infty}{=} \frac{2}{r} \frac{d^2}{dt^2} I_{ij}(t-r). \tag{2.57}$$

The above result is rather instructive: 1) it shows that GWs are generated by accelerated sources similar to electromagnetism where accelerated charges generate EM radiation, 2) the radiation obeys a $\frac{1}{r}$-fall-off, which implies that GWs generated by astrophysical sources are indeed weak when they reach ground-based detectors (far from the source), and 3) gravitational radiation is of *quadrupolar* nature as the conservation laws do not permit monopole and dipole gravitational radiation (for more details see for example [97]).

The focus of this thesis lies on *compact binary systems* and they gravitational radiation they generate. We are therefore interested in how well this approximation works for such self-gravitating systems. We immediately observe that this derivation is not consistent with a dynamical system dominated by gravitational forces since the background metric cannot be assumed to be flat in such cases due to the back-reaction of the motion of the binary onto the background spacetime. Nevertheless, it turns out that this approximation is still valid for widely-separated binary systems, i.e., binaries far from coalescence. To lowest-order, this approximation then describes a point-like binary system undergoing Newtonian dynamics in a flat Minkowski background. Let us therefore use such a binary system in a circular orbit to illustrate the explicit solution of Eq.(2.57). Let us assume that the binary moves on a circular orbit in the xy-plane of the source frame as illustrated in Fig. 2.2. The trajectory of the binary is then given by

$$\vec{x}(t) = \begin{pmatrix} R\cos(\omega_{\text{orb}} t) \\ R\sin(\omega_{\text{orb}} t) \\ 0 \end{pmatrix}, \tag{2.58}$$

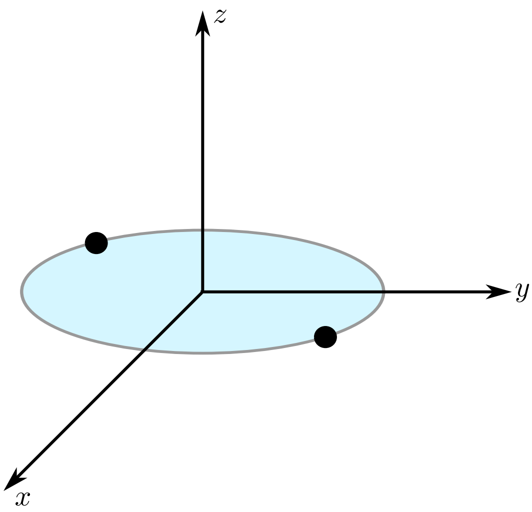

Figure 2.2: A nonspinning binary system in a circular orbit. In the Cartesian source frame attached to the binary, the two compact objects are in a circular orbit in the xy-plane.

where R is the orbital separation of the binary and $\omega_{\rm orb}$ the orbital frequency of the binary motion. We can now compute the components of I_{ij} in the centre-of-mass frame to obtain

$$h_{ij}^{TT} = \frac{4M\eta R^2\omega_{\rm orb}^2}{r}\begin{pmatrix} -\cos(2\omega_{\rm orb}(t-r)) & -\sin(2\omega_{\rm orb}(t-r)) & 0 \\ -\sin(2\omega_{\rm orb}(t-r)) & \cos(2\omega_{\rm orb}(t-r)) & 0 \\ 0 & 0 & 0 \end{pmatrix}, \tag{2.59}$$

where $M = m_1 + m_2$ denotes the *total mass* of the system and η is the *symmetric mass ratio*,

$$\eta = \frac{m_1 m_2}{M^2} \in (0, 0.25]. \tag{2.60}$$

Instead of η, commonly also the mass ratio $q \geq 1$ is used. In this thesis, we use both expression with the convention

$$q = \frac{m_2}{m_1} \geq 1. \tag{2.61}$$

We note that the frequency of the emitted gravitational radiation at quadrupole order is twice the frequency of the orbital motion. Although we have not solved for the dynamics of the binary but assumed a prescribed Keplerian orbit, this is a very useful starting point for a more concise treatment of the two-body problem in General Relativity. In this approximation, we have completely neglected the energy carried away by GWs as well as the effect of the motion of the source onto the background spacetime. In order to compute the evolution of the binary system, the emitted gravitational energy needs to be consistently taken into account, which is the goal of the post-Newtonian approximation summarised in Sec. 2.5.1.

2.3.4 Gravitational-wave sources

In this section we briefly summarise the most important gravitational-wave sources. Although the main focus of this thesis lies on compact binaries, we give a short overview of the prime sources for reasons of completeness. A full treatment is presented in [195].

Compact binary coalescences (CBC): These are believed to be among the most promising gravitational-wave sources for interferometric GW detectors based on Earth. These binary systems comprise of two compact objects such as black holes, neutron stars or white dwarfs in various combinations. The two compact objects form a binary system, which is dominated by their gravitational interaction. The accelerated masses lose gravitational binding energy via the emission of gravitational-waves, which leads to the decay of their orbits until they plunge together and merge to one single object. This can either be the direct merger into a black hole, or they could form a hypermassive neutron star first which then collapses into a black hole, or it could form a stable neutron star if the individual masses were not too large initially ($M_* < 10M_\odot$). The emitted gravitational-wave signal is a *chirp signal*, which increases its frequency during the inspiral phase up to the merger before it decays exponentially during the ringdown phase, as predicted by perturbation theory (see for example [135] for more details). The largest amount of energy, however, is emitted during the violent merger. This crucial phase cannot be modelled by analytic approximations, instead the full nonlinear Einstein field equations have to be solved numerically as we will elucidate in Sec. 2.5.2.

Gravitational collapse: Massive stars ($M_* \geq 10M_\odot$) at the end of their lifetime cannot support their inner core via radiation pressure anymore. This leads to a core collapse, where the infalling matter is compressed and sent radially outwards in the form of a supernova explosion after it is abruptly decelerated when it hits the core. It is widely believed that the collapse is non-spherical, potentially due to differential rotation or magnetic fields, and therefore a burst of gravitational radiation is emitted. Such burst waveforms are most conveniently modelled by sine Gaussians.

Quasi-normal modes of black holes: An individual black hole does not emit gravitational waves due to the symmetry of the system. However, if a stationary black hole is perturbed it oscillates with a very particular mode spectrum known as quasi-normal modes (QNMs) (see [135] for a complete treatment). QNMs are excited during the merger of two black holes, but other mechanism, such as infalling particles, the scattering of GWs, EM and scalar fields as well as stellar collapse or tidal disruptions can excite QNMs. The emitted gravitational waves only depend on the mass and spin angular momentum of the black hole and can therefore be considered as the "fingerprints" of black holes. This is in accordance with the no-hair theorem and therefore the detection of such quasi-normal modes from perturbed black holes via gravitational-wave observations can be used to test the theorem as well as strong-field predictions of GR.

Continuous waves: Isolated, asymmetric spinning neutron stars, known as pulsars, continuously emit gravitational waves of approximately constant frequency. The asymmetry or bump is needed to induce the time-varying quadrupole moment and stimulate the emission of gravitational waves. The loss of energy causes the pulsar to lose angular momentum and spin down. Depending on the size of asymmetry, the emitted gravitational radiation is strong enough to be detected by ground-based GW observatories. To date, no gravitational waves from known pulsars have been detected, which allows us to put upper limits on the asymmetry in the mass distribution (see for example [4, 6]).

Stochastic background: In addition to individual gravitational-wave events, we expect the universe to also contain a gravitational-wave background made of GWs not only from discrete sources, but also from fundamental processes like the expansion of the universe and the Big Bang (see for example Les Houches lectures by Allen [15]).

2.4 Detecting gravitational waves

We have seen in Sec. 2.3.2 that a gravitational wave passing a ring of freely-falling test masses changes the proper distance between them, squeezing and stretching their relative separations whilst the coordinate distances are kept constant. Due to the change of proper distances though, it is indeed possible to experimentally detect gravitational waves in a thoroughly designed experiment, which is sensitive to the extremely small changes in proper length induced by an incident gravitational wave. Generally, two classes of GW detectors are currently used: bar detectors and beam detectors.

The first attempt to design a ground-based experiment to detect gravitational waves was undertaken in the 1960s by Joseph Weber [221]. In his pioneering work Weber suggested the use of a resonant bar detector to detect a passing gravitational wave. It would excite the bar's resonant frequency if it was a) strong enough and b) indeed of the resonant frequency. Despite claims made in 1969 [222], no significant signals were conclusively detected. Until today, no gravitational-wave signals have been detected by those means, mainly due to their weakness with an expected GW amplitude (strain) of $h \sim 10^{-21}$. Resonant bar detectors have been improved since to increase their sensitivity, and are still used in experiments like AURIGA [231] to detect GWs.

However, the most promising effort today is the use of laser interferometers. As of today, a world-wide large-scale network of such beam detectors is operating. The current network is comprised of detectors in the US, the Laser Interferometer Gravitational Wave Observatory (LIGO) [119, 219], the German-UK detector GEO600 in Germany [104], the French-Italian detector VIRGO near Pisa, Italy [1] and the Japanese detector KAGRA [205]. The basic

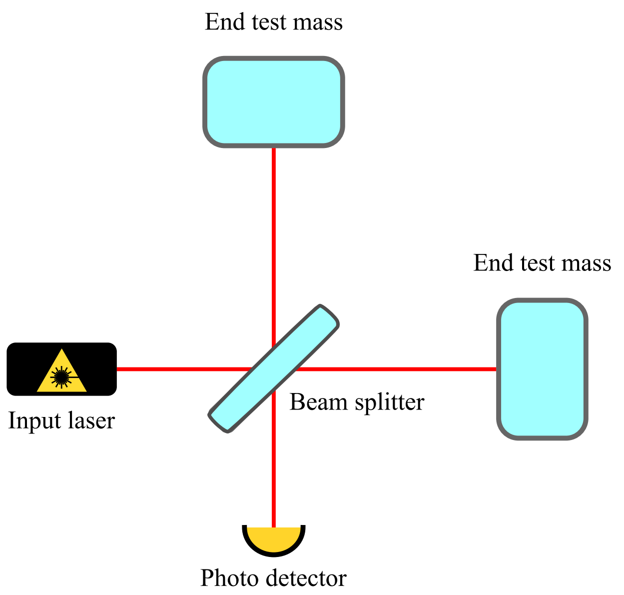

Figure 2.3: The layout of a basic Michelson interferometer. The laser beam is split into two paths via the beam splitter. The end test masses are mirrors, which allow for the reflection of the laser beams. After the recombination of the split beams, the phase difference is measured at the output port (photo detector).

principle of the interferometric detection of GWs can be summarised as follows:

When a gravitational wave passes, it changes the proper distance between two defined points like the sender and receiver of a laser beam. Since interferometers are used to register extremely small changes in length, they are a very natural instrument to measure GWs. Analogously to the Michelson-Morley experiment with the aim to detect the ether [150], the two (nearly) perpendicular arms can be used to measure the affect of a passing GW on the time interval it takes the beam to travel from its source to its receiver.

Ground-based detectors like LIGO consist of a very stable and powerful laser source, which generates the electromagnetic beam. This beam is sent down a vacuum tube to a beam splitter, which transmits around 50% of the laser power and reflects the other 50% at an angle close to 90° to travel into the perpendicular vacuum tube. The end of each tube contains a test mass which reflects the incoming laser beam. After a round-trip the beams recombine and the detected phase difference in the recombined beam is used to measure the presence of GWs. We note two things: firstly, only for very special geometries an interferometer is not able to measure an incident wave because both arms are affected equally and secondly, that a passing GW does not change the position of the test masses (end mirrors) in the laboratory reference frame but alters the travel time of the laser light hence the appearance of phase differences. This basics layout of an interferometric GW detector is depicted in Fig. 2.4. In practice, interferometric GW detectors are much more refined and employ sophisticated modern technologies (see for example [119] for the detailed layout of aLIGO).

If a gravitational wave now passes a Michelson-type laser interferometer, it stretches and squeezes the proper distances between the beam splitter and the end test masses. Depending on the direction of the GW, the laser beams in each arm are affected differently, introducing a phase difference when the laser beams are recombined and measured at the output port.

To illustrate this effect, let us assume a GW detector with one arm parallel to the x-axis of the detector frame and the other one to the y-axis. Due to its transverse nature, a GW only acts in the plane transverse to its direction of propagation. Let us denote the direction of propagation by $\hat{k}$ and use it to set up a radiation basis in the transverse plane $\{\hat{e}_x^R, \hat{e}_y^R, \hat{k}\}$, such that $\hat{e}_x^R$ is parallel to the detector arm along the x-axis. In this *radiation frame*, the gravitational wave tensor can be expressed as

$$\mathbf{h}(t) = h_+(t)\mathbf{e}_+ + h_\times(t)\mathbf{e}_\times, \tag{2.62}$$

where $\mathbf{e}_{+,\times}$ are the polarisation tensors expressed in this particular radiation frame basis. In the TT-gauge, the proper distance L between the beam splitter and the end test mass is given by

$$L(t) \equiv L_c + \Delta L = \int_0^{L_c} dx\sqrt{g_{xx}} = \int_0^{L_c} dx\sqrt{1 + h_{xx}(t,0)} \simeq L_c\left(1 + \frac{1}{2}h_{xx}(t,0)\right), \tag{2.63}$$

where L_c is the coordinate location of the test mass in the x-arm of the interferometer. It follows from the above equation that the relative change of arm length, known as the *fractional strain* produced by the gravitational wave is

$$\frac{\Delta L}{L_c} = \frac{1}{2}h_{xx}(t,0). \tag{2.64}$$

We can now perform an analogous calculation for the y-arm to find that generally

$$\Delta L = \frac{1}{2}d^{ij}h_{ij}, \tag{2.65}$$

where $\mathbf{d}$ denotes the detector tensor, which describes the geometry of the detector, given by

$$\mathbf{d} = L_c(\hat{e}_x \otimes \hat{e}_x - \hat{e}_y \otimes \hat{e}_y). \tag{2.66}$$

In general, the basis vectors in the radiation frame i.e., the polarisation tensors, are not aligned with the arms of the detector but are related by a rotation angle ψ. The *detector response* can then be expressed in terms of the angles (θ, ϕ, ψ), which completely specify the location of the source with respect to the detector frame

$$h_{resp}(t) = F_+(\theta,\phi,\psi)h_+(t) + F_\times(\theta,\phi,\psi)h_\times(t), \tag{2.67}$$

where $F_{+,\times}(\theta,\phi,\psi)$ are the antenna pattern functions, geometrical functions, which determine how well the detector responds to an incident GW depending on the location of the source in the sky and its relative orientation in the plane in the sky (see Sec. 4.2 in [195] for a detailed description).

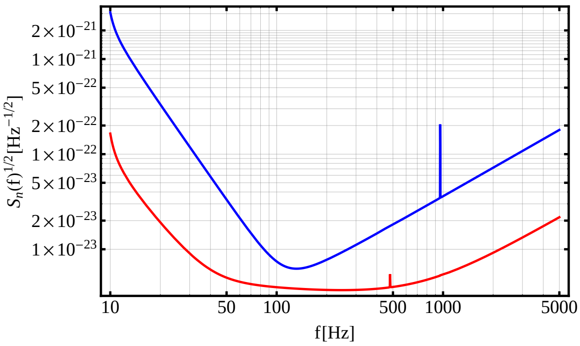

Figure 2.4: Two noise curves for Advanced LIGO. The blue curve depicts the sensitivity for the early operation stage of the advanced detector, the red one shows the anticipated design sensitivity commonly referred to as zero detuned high-power. The sharp features are violin modes of the mirror suspension due to Brownian motion.

2.4.1 Sensitivity

Ground-based interferometric GW observatories measure the presence of a GW via extremely small phase differences of two interfering laser beams with a fractional change of the order of $h \sim 10^{-21}$. In order to be able to measure these small changes, the effective optical path needs to be increased. This is commonly done by adding additional input test masses to build a Fabry-Pérot cavity. Secondly, all other noise sources which cause phase differences need to be well understood in order not to confuse their contributions with a real gravitational wave. The main noise sources for ground-based detectors are seismic noise, thermal noise, shot noise, radiation pressure noise and gravity gradient noise. There are many more noise sources and some of them are poorly understood. The sum of all noise contributions defines the sensitivity of the detector, which is characterised by the *noise power spectral density* (PSD). Despite its dimension being time, more commonly the units Hz^{-1} are used. The square root of the PSD is referred to as the noise amplitude with dimension $\mathrm{Hz}^{-1/2}$. Some of the anticipated sensitivities for Advanced LIGO [204] are summarised in Fig. 2.4. The anticipated design sensitivity curve is known as "zero-detuned high-power", which is expected to be reached by 2018. In the subsequent chapters, the design PSD (zdetHP) as well as an anticipated early Advanced LIGO PSD are used [204].

2.4.2 Searching for GWs: matched filtering

We have seen that on average the gravitational strain amplitude detected in a ground-based interferometer is of the order $h \sim 10^{-21}$ and we have also seen that the detector sensitivity is just below this threshold. Given this, one might ask how to measure the presence of a true gravitational-wave signal in noisy data. One of the most efficient data analysis techniques applied to the search of GWs from coalescing binaries is *matched filtering* [215]. In order to pursue this strategy, theoretical knowledge of the shape of the waveform is crucial.

Let us assume that the detector output data stream is given as a real time series $s(t)$, which is composed of the noise contribution $n(t)$ and some GW-signal $h_{\mathrm{GW}}(t;\vec{\lambda})$. The GW signal observed in a detector is, in general, a function of a set of physical parameters $\vec{\lambda}$ of the

GW source. Schematically, the data stream is then given by

$$s(t) = n(t) + h_{\mathrm{GW}}(t), \tag{2.68}$$

where we have suppressed the dependence on $\vec{\lambda}$. The matched-filtering approach is based on correlating the detector output $s(t)$ with a *template waveform* or filter $h_T(t)$, and the task is to find the filter which maximises the correlation. In other words, one estimates the likelihood of the presence of a signal in the data stream. If this correlation is above a certain threshold, one is confident that a true signal is indeed hidden in the noisy detector output.

The analysis is most conveniently performed in the Fourier domain, where the Fourier transform $\mathcal{F}$ of some arbitrary function (time series) $x(t)$ is given by

$$\mathcal{F}(x(t)) \equiv \tilde{x}(f) := \int_{-\infty}^{\infty} x(t) e^{2\pi i f t} dt. \tag{2.69}$$

Under the assumption of stationary Gaussian noise, the noise auto-correlation is directly related to the (one-sided) *power spectral density* $S_n(f)$ by

$$\overline{\tilde{n}(f)\tilde{n}^*(f')} = \frac{1}{2} S_n(|f|)\delta(f - f'), \tag{2.70}$$

where the bar denotes the average over an ensemble of noise realisations, δ the delta-distribution and * the complex conjugate. The correlation between the detector output and a template waveform $h_T(t)$ is given by

$$c(t) = \int_{-\infty}^{\infty} \tilde{s}(f)\tilde{h}_T^*(f) e^{-2\pi i f t} df. \tag{2.71}$$

If the noise realisation is Gaussian with a zero mean, then the mean value of the correlation corresponds to the correlation of the true signal $h(t; \vec{\lambda})$ with the template $h_T(t)$. This now allows us to define the *optimal filter* (template) as the inner product between the data stream $s(t)$ and the filter $h_T(t)$

$$\langle s, h_T \rangle = 4\mathrm{Re} \int_0^{\infty} \frac{\tilde{s}(f)\tilde{h}_T^*(f)}{S_n(f)} df. \tag{2.72}$$

The *signal-to-noise ratio* (SNR) ρ is given by the square root of Eq.(2.72). It is necessarily maximised when the h_T indeed corresponds to the true GW signal, i.e.,

$$\rho_{opt} := \sqrt{\langle h_{\mathrm{GW}}(\vec{\lambda}), h_{\mathrm{GW}}(\vec{\lambda}) \rangle} \equiv ||h_{\mathrm{GW}}(\vec{\lambda})||. \tag{2.73}$$

Since a true gravitational-wave signal depends on a set of physical parameters $\vec{\lambda}$, it is highly unlikely an exact template is present in the set of all templates used to perform the matched filtering analysis, as the filter, in general, depends on a different set of parameters $\vec{\mu}$. However, the agreement between the signal h_{GW} and the template h_T can be quantified by defining a normalised inner product between two waveforms, the *overlap*,

$$\mathcal{O}(h_{\rm GW}(\vec{\lambda}), h_T(\vec{\mu})) := \frac{\langle h_{\rm GW}, h_T \rangle}{||h_{\rm GW}||||h_T||}. \tag{2.74}$$

Apart from the physical parameters, the waveform also depends on the (unknown) time of arrival t_0 of the signal at the detector as well as the corresponding phase Φ_0. Eq.(2.72) normalised and optimised only over a time and phase shift is the *match* [27, 90, 171, 193, 194]

$$\mathscr{M}(h_{\rm GW}, h_T) := \max_{\Delta t, \Delta\Phi} \frac{\langle h_{\rm GW}, h_T \rangle}{||h_{\rm GW}||||h_T||}. \tag{2.75}$$

The match is a particularly useful measure in the context of waveform modelling and will play a crucial role in the subsequent analysis presented in this thesis. One consequence of the above expression is that no matter how small the agreement between the signal and the template is, as long as a signal is present in the data, i.e., $h_{\rm GW} \neq 0$, it will always be extracted from the data stream if the SNR is high enough. However, loud events are expected to occur very rarely and therefore accurate template waveforms are needed to also extract very quiet signals.

In the context of gravitational-wave searches, one also seeks the optimisation over the physical parameters $\vec{\mu}$ of the template, in order to define the fraction of the optimal SNR recovered by the suboptimal set of all templates used in the search. This quantity is referred to as the *fitting factor*,

$$\mathrm{FF} = \max_{\Delta t, \Delta\Phi, \vec{\mu}} \frac{\langle h_{\rm GW}, h_T(\vec{\mu}) \rangle}{||h_{\rm GW}||||h_T(\vec{\mu})||}. \tag{2.76}$$

In gravitational-wave searches, if the set of all templates, i.e., the template family, has FF $\geq$ 0.965, it is considered to be *effectual* for signal detection, while templates with high matches, i.e., $\mathscr{M} \geq 0.965$, are considered to be both effectual in detection and *faithful* in estimating the physical parameters of the GW source [81]. The threshold of 0.965 corresponds to a loss of no more than 10% of all signals. In the following chapters, we will predominantly use the match to quantify the agreement between waveforms as we are mainly interested in faithful representations.

2.5 Modelling gravitational waves from coalescing compact binaries

Coalescing compact binaries, in particular binary-black-holes, are the main focus of this thesis. In order to facilitate the matched-filtering detection strategy exploited by ground-based detectors such as LIGO, it is crucial to understand these systems and to accurately model the gravitational waveforms they emit. In this section, we shall briefly outline to most commonly used strategies to develop such waveform models. However, the two-body problem in full

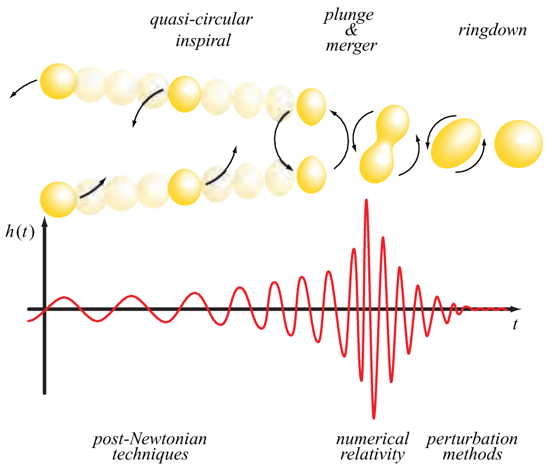

Figure 2.5: The panel schematically depicts the three distinct stages of the binary evolution and the corresponding gravitational waveform during each stage. Graphics taken from Fig. 12.1, p. 396 from [33].

General Relativity is nontrivial due to the nonlinear nature of the theory. The two main approaches to determine the evolution of a coalescing binary and the emitted gravitational-wave signal of particular interest to this thesis are: 1) post-Newtonian theory (PN) and 2) Numerical Relativity (NR). We shall briefly summarise both methods in the subsequent sections, closely following [14, 36].

In general, the evolution of a compact binary system is composed of three significantly different stages: when the two gravitationally bound companions are far apart, i.e., their separation R is much larger than the characteristic intrinsic scale of the binary set by the total mass, they undergo a quasi-spherical inspiral motion, with a slowly decaying orbital separation due to the emission of GWs. In this regime, the nonlinear field equations need not be solved exactly but can be approximately solved utlising an expansion in $\frac{v}{c}$ known as the *post-Newtonian approximation*. Here, v is the characteristic velocity of the binary. During the later stages of the inspiral, the nonlinear contributions cannot be neglected anymore and the solution can only be obtained by solving the full nonlinear Einstein field equations Eq.(2.15). Since there exist no analytical solutions for binary spacetimes, the field equations have to be solved numerically. Once the two companions have plunged together and merged into a single remnant black hole, it sheds itself of the remaining gravitational perturbations during the ringdown phase, before settling down to the stationary Kerr solution.

During the inspiral, the frequency of the gravitational waveform increases slowly before peaking when the two black holes plunge together. This type of signal is commonly referred to as *chirp signal*. The gravitational waveform decays exponentially during the ringdown, which can either be approximately described by black-hole perturbation theory or one may use the results of numerical simulations. This three-stage evolution and the gravitational-wave signal are schematically depicted in Fig. 2.5.

The following two sections briefly summarise the basics of post-Newtonian theory and Numerical Relativity before we introduce the concept of complete waveform models, which are synthesised models that describe the complete GW signal from the inspiral, through the merger to the ringdown.

2.5.1 Post-Newtonian theory

In linearised gravity, the GW sources move in the flat background spacetime without affecting the spacetime in return. This means, the dynamics of GW the source is described using Newtonian gravity rather then General Relativity. This approximation is valid for systems which are either non-relativistic or whose motion is not dominated by the acting gravitational fields such as charged particles accelerated by an acting electric field. However, compact binary systems are self-gravitating, relativistic systems whose dynamics contributes to the curvature of the background spacetime and hence the motion and the background spacetime cannot be treated independently. The deviation from Minkowski space near the source needs to be consistently taken into account. One method to do so is known as the post-Newtonian (PN) formalism, which is of particular importance for the theoretical computation of GWs from inspiralling binaries.

The PN formalism is based on the expansion of the Einstein field equations in terms of $\frac{v}{c}$, where v is the characteristic velocity of the source, for example the relative velocity in a compact binary system. This allows us to derive the equations of motion of the source as an order-by-order series corresponding to the relativistic corrections to the Newtonian equations of motion (see for example [223]). We note that this is only valid in the regime where the binary's separation is large, i.e., when $\frac{v^2}{c^2} \sim \frac{R_S}{R}$, where R_S is the Schwarzschild radius of the binary and R the orbital separation. As the source becomes highly relativistic, the PN formalism becomes less accurate and methods applicable to the strong-field regime need to be used to compute the motion of the source and the gravitational waveforms. In order to produce a gravitational waveform in the PN formalism, the PN equations of motion have to be solved first. The solution is then used to evaluate the PN equations, which describe the generation of the waves (the source multipoles).

Making use of the gauge freedom in GR, the PN calculations are performed most conveniently in the harmonic gauge, i.e.,

$$\partial_\mu \left(\sqrt{-g} g^{\mu\nu}\right) = 0. \tag{2.77}$$

Further, at lowest PN order extended bodies can be treated as point-like masses, as tidal effects due to the bodies' volume occur at higher PN order. Schematically, the equations of motion at 2.5 PN-order can be written as [133]

$$\frac{d^2x^i}{dt^2} = -\frac{Mx^i}{r^3}\left[1 + O(v^2) + O(v^3) + O(v^4) + O(v^5) + ...\right], \tag{2.78}$$

where the leading-order term (0PN) is the standard Newtonian expression. For a Newtonian binary we have seen in Eq.(2.59) that the GW-signal takes the form

$$h(t) = \frac{4M\eta v^2}{r} e^{-i(2\omega_{\rm orb}t+\Phi_0)}. \tag{2.79}$$

It becomes clear from the above equation that the evolution of the binary and hence the GWs are governed by the evolution of the orbital phase, since

$$\omega_{\rm orb} = \frac{d\Phi_{\rm orb}}{dt} \equiv \dot{\Phi}_{\rm orb}. \tag{2.80}$$

It is therefore crucial to also accurately predict the time evolution of the orbital phase of the binary as a perturbative series in v. Under the assumption that the orbital decay is entirely due to the emission of GWs, the gravitational binding energy E and the GW flux $\mathcal{F}$ are related by the "energy balance" equation

$$\mathcal{F}(v) = -\frac{dE(v)}{dt}. \tag{2.81}$$

Further, it is commonly assumed that the binary undergoes *adiabatic inspiral*, where adiabacity means that the fractional change of the orbital frequency over one orbital period is small, i.e., $\dot{\omega}_{\rm orb}/\omega_{\rm orb}^2 \ll 1$. In this approximation, the phasing can be specified by two ordinary differential equations

$$\begin{aligned} \frac{\Phi(t)}{dt} &\equiv \dot{\Phi}_{\rm orb}(t) = \frac{v}{M^3}, \\ \frac{dv(t)}{dt} &\equiv \dot{v} = -\frac{\mathcal{F}(v)}{E'(v)}, \end{aligned} \tag{2.82}$$

where $E'(v)$ denotes the derivative of the energy with respect to v. Inspiralling binaries of relevance to ground-based detectors undergo a quasi-circular inspiral as eccentricity is removed earlier from the system via GW radiation [177, 178]. The decay of the orbital separation can then be described as a series of quasi-circular orbits with decreasing radius. Under the assumption of circular orbits, the invariant velocity becomes $v = (M\omega_{\rm orb})^{1/3}$, Kepler's familiar law. For a Newtonian binary, the energy of a circular orbit is

$$E = -\frac{\eta M^2}{2R}, \tag{2.83}$$

and the gravitational-wave flux is

$$\mathcal{F} = \frac{32\eta^2 M^5}{5R^5}, \tag{2.84}$$

which is the famous *quadrupole formula*.

The PN approximation provides an elaborate scheme to extend the Newtonian expressions for the E and $\mathcal{F}$ to higher PN orders. In order to define the GW energy and the GW flux, a stress-energy tensor associated with the GWs themselves has to be introduced. It is shown for example in [97] how such a pseudo-tensor can be constructed from second-order terms in $h_{\mu\nu}$ when the GWs are assumed to be perturbations of Minkowski space.

In Eq.(2.57) we have seen that, at leading order, GWs are generated by a time-varying mass quadrupole moment. The PN formalism now provides a systematic description of the waveform in terms of higher order *radiative multipoles*, which are in turn coupled to the energy and flux [36, 134, 214]. Once all ingredients are computed, the waveform polarisations $h_{+,\times}$ can schematically be written as [36]

$$h^{(p)}_{+,\times} = \frac{2M\eta}{r} v^2 \sum_{p=0}^{\infty} v^p H^{(p/2)}_{+,\times}, \tag{2.85}$$

where (p) denotes the PN-order and the functions $H_{+,\times}$ for nonspinning systems for example are provided in [36]. It is straightforward to show that for $p = 0$ we obtain the Newtonian result Eq.(2.57).

However, with the connection to Numerical Relativity in mind, it is convenient to not only consider the waveform polarisations h_+ and $h_\times$, but also the complex GW strain

$$h = h_+ - ih_\times \tag{2.86}$$

and its decomposition into GW modes h_{lm} in terms of *spin-weighted spherical harmonics* with spin weight $s = -2$, which encode the directional dependence of the gravitational radiation field. To do so, we introduce basis functions on the unit sphere $Y^{-s}_{lm}(\theta, \varphi)$ defined by [101]

$$Y^{-s}_{lm}(\theta, \varphi) = (-1)^s \sqrt{\frac{2l+1}{4\pi}} d^l_{ms}(\theta) e^{im\varphi}, \tag{2.87}$$

where d^l_{ms} denotes the small-d Wigner matrices [191] and (θ, φ) are the polar and azimuth angle on the sphere. The GW strain expanded in terms of these basis functions reads as

$$h(t; \theta, \varphi) = \sum_{l=2}^{\infty} \sum_{m=-l}^{l} h_{lm}(t) Y^{-2}_{lm}(\theta, \varphi). \tag{2.88}$$

The GW modes h_{lm} are extracted by means of the surface integral.

$$h_{lm} = \int d\Omega h(\theta, \varphi) Y_{lm}^{-s*}(\theta, \varphi), \tag{2.89}$$

where $d\Omega = \sin\theta d\theta d\varphi$ and * denotes complex conjugation. The $(l = 2, |m| = 2)$-modes are the *quadrupole modes*, also known as the dominant harmonics. The decomposition now allows us to rewrite the PN polarisations as GW modes given by

$$h_{lm}(t) = A_{lm} e^{-im\Phi_{\text{orb}}}. \tag{2.90}$$

The explicit expressions for the mode amplitudes A_{lm} up to 3PN order for nonspinning binaries are given in [43]; spin contributions up to 2PN order can be found in [23].

2.5.2 Numerical Relativity

In this section, we will briefly summarise the foundations of Numerical Relativity, since results from this branch of GR are an integral part of this thesis. We refer the interested reader to the textbooks by Alcubierre [14] and Baumgarte and Shapiro [33] for comprehensive treatments of the subject.

The goal of Numerical Relativity is to obtain general solutions of the Einstein field equations for complex spacetimes that do not allow for simple, analytical solutions. One example of a nontrivial spacetime is the treatment of the classic two-body problem in General Relativity. In general, it is not possible to analytically solve the field equations for spacetimes that involve strong gravitational fields or comprise of little or no exact symmetries, which is the case for astrophysically relevant situations. This has given the rise to the need to solve Einstein's equations numerically using sophisticated computational codes and advanced numerical techniques. But in order to be able to construct a numerical solution, first of all the tensorial field equations need to be recast in a form suitable for numerical integration. If one is interested in the time-evolution of a dynamical system, in this case spacetime itself, a natural approach is to reformulate Einstein's four-dimensional equations as an *initial value problem*. It is a priori not clear that such a formulation indeed exists. However, the fundamental works by Lichnerowicz [142] and Choquet-Bruhat [56] have proven the wellposedness of the Cauchy problem in General Relativity and the existence of solutions, which marks the starting point for a formulation suitable for numerical evolution. The next step is to separate the four-dimensional fabric of spacetime accordingly to allow for the dynamical evolution of the gravitational fields in time. There are various approaches to split spacetime and here we focus on what is known as the "3 + 1 formulation", which splits spacetime into three-dimensional spacelike hypersurfaces, which evolve in time. This is one of the most commonly used splittings in numerical relativity and of particular interest in the numerical code used to

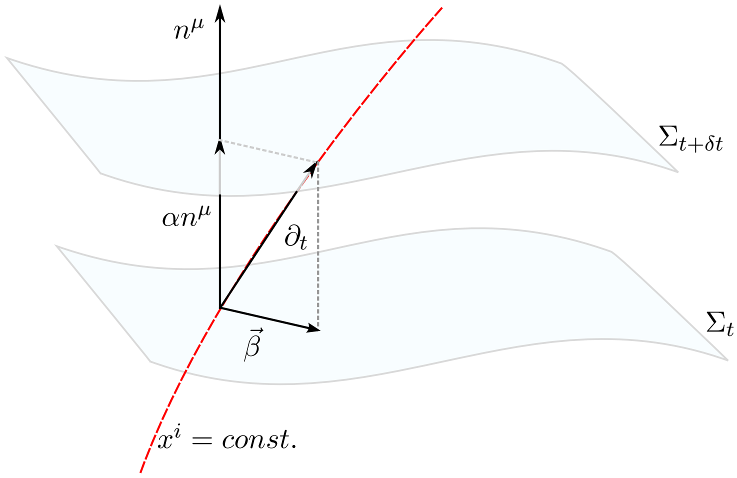

Figure 2.6: Spacetime slicing in the $3+1$ formulation of GR. Depicted are two adjacent spacelike hypersurfes, the definition of the shift vector β^i and the lapse α.

obtain results presented in this thesis.

Let us consider a *globally hyperbolic* spacetime $(M, g_{\mu\nu})$. Any such manifold can be foliated into three-dimensional spacelike hypersurfaces Σ_t such that the disjoint union of all slices covers the complete manifold, i.e.,

$$M = \bigcup_{t\in\mathbb{R}} \Sigma_t. \tag{2.91}$$

Each hypersurface can be identified as a level surface of a regular scalar field t, which is considered to be a universal time function. The intrinsic geometry of each spacelike hypersurface is encoded in the induced 3-metric γ_{ij}. Let us now consider two adjacent hypersurfaces Σ_t and $\Sigma_{t+\delta t}$. Between these two points in the evolution, a coordinate time of δt has elapsed. The proper time between those two surfaces as measured by an observer moving along the direction orthogonal to both hypersurfaces n^μ is given by

$$d\tau = \alpha(t, x^i)dt, \tag{2.92}$$

where α denotes the *lapse*. The relative velocity of two such observers with respect to the lines of constant spatial coordinates is given by the *shift* vector β^i. This is illustrated in Fig. 2.6. Neither the choice of foliation nor the propagation of the spatial coordinates from one hypersurface to the next are unique, the four freely specifiable functions (α, β^i) are gauge functions. With the above ingredients, we can rewrite the complete spacetime metric in terms of $(\alpha, \beta^i, \gamma_{ij})$ to obtain the following line element

$$ds^2 = (-\alpha^2 + \beta_i\beta^i)dt^2 + 2\beta_i dt dx^i + \gamma_{ij} dx^i dx^j. \tag{2.93}$$

The $3+1$-splitting allows for the separation of the fully covariant Einstein equations into six evolution and four constraint equations, in the literature commonly referred to as *ADM equations* named after Arnowitt, Deser and Misner [21][1], who first derived these equations with the aim to quantise gravity. The *evolution equations* for vacuum spacetimes are given by

$$\partial_t \gamma_{ij} = -2\alpha K_{ij} + D_i\beta_j + D_j\beta_i, \tag{2.94}$$

$$\partial_t K_{ij} = \beta^k \partial_k K_{ij} + K_{ki}\partial_j \beta^k + K_{kj}\partial_i\beta^k - D_i D_j \alpha + \alpha(R_{ij} + KK_{ij} - 2K_{ik}K^k{}_j), \tag{2.95}$$

where D_i is the induced covariant derivative on a hypersurface Σ and K_{ij} is the *extrinsic curvature*, which encodes how a hypersurface is embedded in the higher dimensional spacetime manifold and corresponds to the second fundamental form in differential geometry. The Einstein equations are a set of ten coupled partial differential equations, hence to close the system four more equations are needed, the *constraint equations*. In vacuum these are

$$R + K^2 + K_{ij}K^{ij} = 0, \tag{2.96}$$

$$D_j(K^{ij} - \gamma^{ij}K) = 0, \tag{2.97}$$

where R is the Ricci curvature of the hypersurface, i.e., the Riemann tensor projected onto the hypersurface and contracted twice, and K is the trace of K_{ij}. Eq.(2.96) is commonly referred to as Hamiltonian constraint, Eq.(2.97) as momentum constraints.

By applying this particular splitting, the fully covariant field equations have been recast as a constrained initial value problem. Mathematically, the Bianchi identities[2] guarantee that the constraints are satisfied during the evolution if they are satisfied initially. However, this is an exact statement which is no longer true in a numerical evolution. It is therefore important to monitor the constraint violation, which then in return allows us to assess the accuracy of the numerical evolution.

The $3+1$ equations are not unique. One can always add a multiple of the constraint equations to obtain a new set of evolution equations, which are equally as valid as Eq.(2.94)-Eq.(2.95). Additionally, this particular formulation is not numerically well posed. One of the most commonly used reformulations, which is numerically particularly robust, is known as the *Baumgarte-Shapiro-Shibata-Nakamura* (BSSN) formulation [32, 202]. In this formulation similar quantities are evolved, but they are conformally rescaled such that

$$\tilde{\gamma}_{ij} := \psi^{-4}\gamma_{ij}, \tag{2.98}$$

where ψ is the conformal factor. Additionally, three connection functions $\tilde{\Gamma}^i$ are introduced, reducing the evolution equations Eq.(2.94)-Eq.(2.95) to wave equations for the conformal

[1] Note, however, that ADM derived these expressions in terms of the conjugate momenta π_{ij}. The form used here is after York.

[2] i.e., $\nabla_{[\lambda}R_{\rho\sigma]\mu\nu} = 0$.

metric, which are coupled to the evolution equations for the connection functions.

However, the system of equations is not yet complete, because the gauge variables α and β^i have not yet been specified by a set of gauge conditions. The question of how to choose an appropriate gauge is rather difficult with no exact answer other than that the choice should be motivated by the problem one wishes to solve. Ideally, the gauge conditions should enforce symmetries if present, or avoid the formation of coordinate singularities in the numerical domain. In the case of black-hole spacetimes, gauge conditions may also be chosen such that they avoid the physical singularity.

Since numerical evolutions are performed on a finite computational domain, one must additionally impose artificial boundary conditions at some finite spatial distance. The numerical code used to obtain the numerical results presented in this thesis uses a radiative boundary condition, which assumes that far away from the source, i.e., the binary, all fields behave like outgoing spherical waves.

Since this thesis is concerned with black-hole spacetimes, let us briefly mention their numerical representation. These spacetimes are simple, in the sense that no matter or complicated microphysics needs to be taken into account. However, the numerical representation and evolution of singularities poses complex and unique computational challenges.

Historically, the numerical study of such spacetimes goes back to the 1960s with the pioneering work by Hahn and Linquist [107]. However, the first successful numerical simulation of a black-hole-binary merger and the extraction of the gravitational-wave signal was only conducted in 2005 by Frans Pretorius [183]. His approach did not use the BSSN-formulation of the field equations, but what is known as the *generalised harmonic* decomposition. It is obtain by imposing the generalised harmonic coordinate condition, i.e., $\Box x^\mu = H^\mu$, where H^μ are source functions [182]. The black hole singularity is not avoided but instead completely removed from the numerical domain via black hole excision [213]. Although no physical information is lost by the removal of this causally disconnected area, additional boundary conditions at the excision surface have to be introduced.

Another very successful approach of evolving black-hole spacetimes is known as the moving puncture approach [24, 68]. Therein, black holes are initially represented by a wormhole topology connecting two asymptotically flat ends, where the ends are compactified and then identified with points in $\mathbb{R}^3$ referred to as "punctures". In order for the punctures to indeed move on the grid, the (singular) conformal factor ψ needs to be evolved and singularity-avoiding gauge conditions have to be imposed. This method, in particular the choice of initial data, is based on the assumption of spatial conformal flatness. However, binary black hole spacetimes are not conformally flat and therefore, a short burst of additional radiation, commonly referred to as junk radiation, is introduced but quickly leaves the system.

Independently of the formulation of the ADM equations and the representation of the black holes in the numerical domain, before the relevant fields can be evolved, *initial data* have to be constructed, i.e., the gravitational fields (γ_{ij}, K_{ij}) have to be specified on the initial slice Σ_0, which can then be evolved in time. To do so, the constraint equations Eq.(2.96)-Eq.(2.97) have to be solved, but we see immediately that only four out of the twelve components of the gravitational fields can be determined. Four of the remaining eight undetermined functions can be specified by imposing a gauge, the other four represent the two dynamical degrees of freedom of the gravitational field. Two of these four variables are freely specifiable and one can introduce a decomposition of γ_{ij} and K_{ij}, which allows for a convenient split of the constrained from freely specifiable variables. Such a split is obtained by conformally decomposing the constraint equations [166, 227, 228]. The two most commonly used conformal decompositions are the conformal transverse-traceless method and the conformal thin sandwich method. For more details on the subject, we refer the reader to [75] for a comprehensive treatment.

Since the remarkable breakthroughs in 2005 the simulation of the late stages of binary black holes have become a standard tool to calculate the gravitational-wave signal. However, long numerical evolutions of binaries with large mass ratios are still time-consuming and exceptionally challenging. As of today, only small parts the complete binary-black-hole parameter space have been covered by NR simulations. Most of the investigated configurations are between mass ratio 1 and 10 (comparable mass ratio regime), and are either nonspinning or have spins (anti-)aligned with the orbital angular momentum. The Kerr parameters in these simulations range between -0.95 to +0.97 for equal mass [147], but have lower values for unequal-mass binaries. Recently, a number of simulations of binaries with arbitrarily oriented spins have been carried out [72, 155, 170, 196], but the coverage of the full binary parameter space is yet far from complete. Nevertheless, the availability of numerical solutions to a wide range of binary configurations allows us to establish a more complete picture of the evolution of coalescing black hole binaries and to understand the dynamics as well as the emitted GWs.

However, so far we have not mentioned how gravitational radiation is extracted from a numerical evolution. We have seen earlier that far from the source, the gravitational radiation is weak and can be described by the means of linearised gravity and PN theory. Numerical Relativity simulations, however, focus on the strong-field regime close to the relativistic source and compute the evolution of spacetime, i.e., the metric, itself. The explicit functional form of the metric depends on the coordinate choice and it is therefore nontrivial to extract the GW polarisations h_+ and $h_\times$ in a gauge-invariant way. Most commonly, two different approaches are used to extract the GW signal, which we will briefly summarise below:

One approach is based on the early work on linear perturbations of a Schwarzschild black hole [186] by Zerilli [232] and Moncrief [152] known as the Zerilli-Moncrief formalism. In this formalism, the spacetime metric is perturbatively decomposed and the perturbations are split into even- and odd-parity parts, which are then decomposed into modes by projecting them onto the spin-weighted spherical harmonic basis functions. For each mode, a gauge-invariant Moncrief function can be obtained. The GW polarisations are determined from these functions (see for example Chapter 9 of [33] or [156] for more details).

In recent years, an alternative approach known as the *Newman-Penrose formalism* [157], has become a standard tool to extract gravitational radiation. Therein, the outgoing transverse gravitational radiation is given by the Weyl scalar Ψ_4, which is a component of the Weyl tensor in a particular complex tetrad. In this formalism, the Weyl scalar is related to the GW polarisations by

$$\Psi_4 \equiv \partial_t^2 h = \partial_t^2 (h_+ - i h_\times). \tag{2.99}$$

2.5.2.1 BAM

In this section, we will briefly summarise the binary-black-hole code, BAM, used in this thesis to obtain numerical results. More details can be found in [53, 55].

The BAM code evolves black-hole spacetimes following the moving puncture approach. Therein, the black holes are modelled by adopting the wormhole topology. The asymptotically flat ends are compactified and identified with points in $\mathbb{R}^3$. The resulting coordinate singularities are referred to as "punctures".

The initial data are constructed following the conformal transverse-traceless decomposition method. Initially, the conformal background metric is chosen to be flat, i.e., $\tilde{\gamma}_{ij} = \delta_{ij}$, and the initial slice is maximal ($K = 0$). With this choice, the Hamiltonian and momentum constraints decouple and admit Bowen-York solutions [48, 51]. These are generated using a pseudo-spectral elliptic solver [17].

To complete the set of initial data, the initial values for the gauge quantities, the lapse and the shift, need to be specified, which are chosen to be

$$\alpha = 1 \quad \text{or} \quad \alpha = \psi_0^{-2}, \tag{2.100}$$

$$\beta^i = 0, \tag{2.101}$$

where ψ_0 denotes the initial conformal factor. The numerical simulations carried out for the work presented here use $\alpha = \psi_0^{-2}$.

The initial data are then evolved with the χ-variant of the moving-puncture [24, 68, 110] version of the BSSN [32, 202] formulation of the 3+1 Einstein evolution equations. The numerical method uses sixth-order finite differencing in space [126] and explicit fourth-order Runge-Kutta time stepping with mesh refinement following Berger and Oliger [34]. The numerical domain is represented by a hierarchy of nested Cartesian grids to obtain enough numerical resolution on different scales: we wish to resolve the black holes and their vicinity well, at the same time enough resolution in the GW extraction zone is also required. The various boxes have different grid spacings to allow for the desired resolution. The GWs emitted

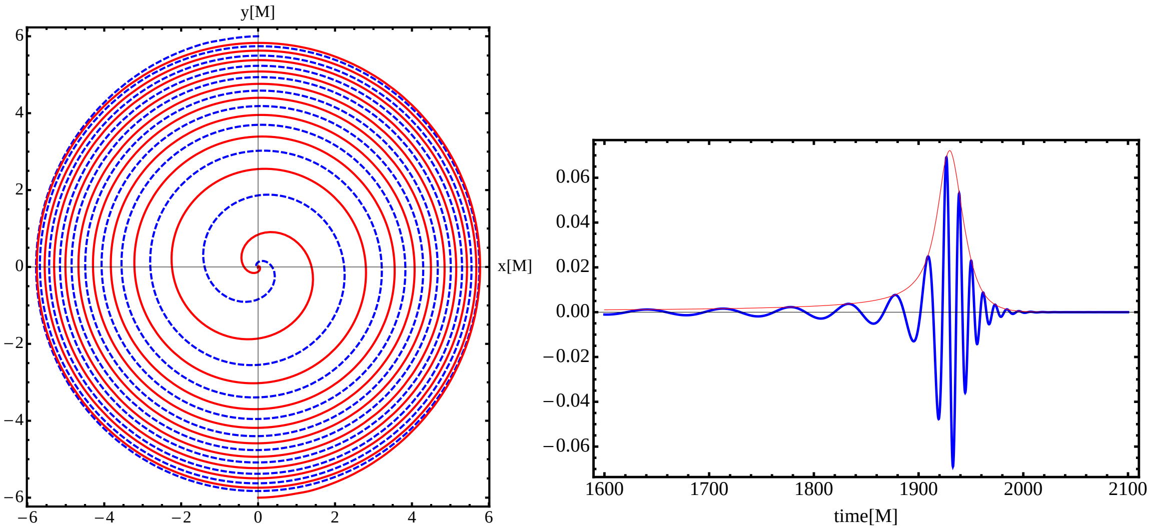

Figure 2.7: The left panel shows the trajectories traced out by the moving punctures until merger in an equal-mass nonspinning numerical simulation with the BAM code. Initially, the two punctures are separated by $\sim 12M$.The right panel shows the real part (blue) and the magnitude (red envelope) of the $\Psi_{4,22}$-mode extracted from the simulation.

by the binary are calculated from the Weyl scalar Ψ_4. The details of the implementation of this procedure are given in [55].

In each numerical simulation, the black-hole punctures are initially separated by a coordinate distance D and are placed on the y-axis at $y_1 = -qD/(1+q)$ and $y_2 = D/(1+q)$, where $q = M_2/M_1$ is the ratio of the black hole masses in the binary, with the convention $M_1 < M_2$. The masses M_i are estimated from the Arnowitt-Deser-Misner (ADM) mass at each puncture, according to the method described in [51]; see also the Appendix of [116] and the discussion in [114]. The Bowen-York punctures are given linear momenta $p_x = \mp p_t$ tangential to their separation vector and $p_y = \pm p_r$ towards each other. The latter momentum component accounts for the (initially small) radial motion of the black holes as they spiral together. Initial parameters for low-eccentricity inspiral are produced using integrations of the PN equations of motion, as described in [116, 127].

The eccentricity is measured with respect to the frequency of the orbital motion $\omega_{\rm orb}$ as discussed in [102, 111, 116, 127] as well as in [66, 154] and references therein. The eccentricity is estimated as the extrema of

$$e_\omega(t) = \frac{\omega(t) - \omega_{QC}(t)}{2\omega_{QC}(t)}, \tag{2.102}$$

where ω is the frequency of the $(l = 2, m = 2)$-mode of the waveform, and $\omega_{QC}(t)$ is an estimate of the frequency evolution for a non-eccentric, quasi-circular binary, calculated by a smooth curve fit through the numerical data. The base configuration to set up the numerical grid is of the following form:

$$\chi_{M\eta=2}[l_1 \times N : l_2 \times 2N : \mathrm{buf}][h_{\mathrm{min}}^{-1} : h_{\mathrm{max}}], \tag{2.103}$$

which indicates that the following: the simulation used is the χ-variant of the moving-puncture method, l_1 is the number of moving nested mesh-refinement boxes with a base value of N^3 points surrounding each black hole, l_2 is the number of fixed nested boxes with $(2N)^3$ points around the entire system and buf is the number of mesh-refinement buffer points. The η-parameter in the BSSN system is $M\eta = 2$; h_{min} denotes the resolution of the finest level and h_{max} the one of the coarsest, outmost refinement level.

The resolution around the puncture is denoted by M_1/h_{min}, which is the resolution with respect to the *smaller black hole* M_1. The puncture of the second black hole will have the same numerical resolution, but if the black hole is bigger, $M_2 > M_1$, then it will effectively be better resolved, which is not necessary. Therefore, some of the finer levels are not used for the larger black hole. Far from the sources, the meaningful length scale is the total mass of the binary, $M = M_1 + M_2$, and so the resolution on the coarsest level is given by h_{max}/M.

The puncture motion and the $(2, 2)$-mode of the gravitational-wave signal from an equal-mass nonspinning NR simulation performed using the BAM code are illustrated in Fig. 2.7.

2.5.3 Complete waveform models

So far we have seen how pure inspiral waveforms can be constructed via the post-Newtonian formalism and also how GWs emitted during the merger and ringdown can be extracted from Numerical Relativity simulations. However, depending on the total mass of the binary, the amount of time a binary signal can be observed with a ground-based GW detector varies. The higher the mass, the shorter the time a signal spends in the sensitivity band of the detector at a given luminosity distance D_L. A binary comprised of two neutron stars cannot exceed a total mass of $\sim 6M_\odot$ [137]. For such a low-mass binary system, only the inspiral part of the binary evolution lies within the sensitivity band of the advanced ground-based detectors and hence PN template waveforms are thought to be efficient to detect them. If we, on the other hand, consider a binary with a black hole of $10M_\odot$ and a neutron star with $1.4M_\odot$, the late inspiral and the merger will also be observable by the detector. This shift to the later stages of the binary evolution becomes more and more pronounced the heavier the binary system, which is illustrated in Fig. 2.8. Ideally, we wish to have waveform templates h_T that describe the complete evolution of the binary system including inspiral, merger and ringdown.

There exist different approaches in obtaining such complete inspiral-merger-ringdown (IMR) waveforms. One approach, which is adopted later in this thesis, is a *phenomenological* approach [10]. Its goal is to find a simple, analytical closed-form expression, which,

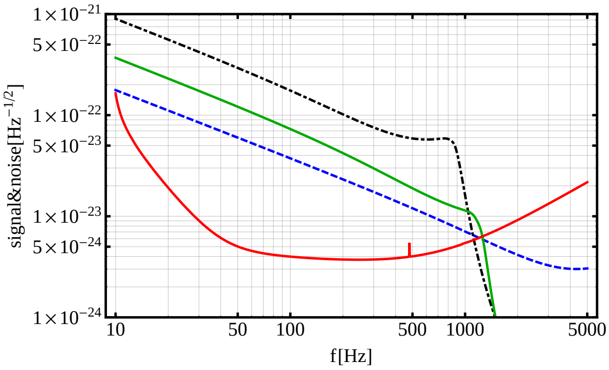

Figure 2.8: GW signals from various binary systems at a distance of 100Mpc. The dashed blue curve is the GW signal from a neutron star binary $1.4M_\odot + 1.4M_\odot$. The solid green curve shows the signal of a neutron star-black hole binary with masses $1.4M_\odot + 10M_\odot$. Finally, the dot-dashed black curve is the signal of a black-hole-binary with $10M_\odot + 10M_\odot$. The red curve shows the design sensitivity of Advanced LIGO.

when evaluated for a set of physical binary parameters, gives the corresponding gravitational waveform. The phenomenological approach has been applied to the modelling problem before in the context of efficiently generating inspiral waveforms without performing the time consuming evolution of the equations of motion [59]. We shall briefly summarise the main ingredients of the phenomenological approach.

Let us consider the simplest class of black-hole-binaries: two Schwarzschild black holes. Such a nonspinning binary configuration is intrinsically defined by the two component masses m_1 and m_2 respectively the symmetric mass ratio η. Even for such "simple" systems, the numerical evolution is rather expensive and it is therefore not feasible to produce accurate numerical waveforms of several hundred orbits for every such configuration. However, GW searches are significantly improved by including the numerical information. Moreover, waveforms which include the merger and ringdown part of the evolution also allow for deeper surveys and for the search of high-mass systems ($M \geq 12M_\odot$) [64]. It is therefore important to have an efficient representation of the complete evolution of the binary from the early inspiral to the ringdown. One way to address this problem is to combine the knowledge from PN theory with the numerical information in an appropriate way. Thus, the first step is to construct *hybrid waveforms*. Such complete waveforms are built by smoothly attaching a PN inspiral waveform to a numerical waveform. Most commonly in this approach, only the dominant harmonics (quadrupole modes) are matched. The hybridisation is done by matching the two waveforms in an overlapping time interval $t_1 < t < t_2$ (or frequency interval; see [192]).

In the simplest case, the waveform is a function of a small number of parameter: $h(t;\vec{\lambda})$, where $\vec{\lambda} = \{M, \eta, t_0, \Phi_0\}$ with t_0 being the starting time of the waveform and Φ_0 the initial phase. After the construction of a set of hybrid waveforms, the next step is to produce an ansatz for the GW phase as well as an ansatz for the GW amplitude. This is most conveniently done in the Fourier domain and can schematically be written as [10]

$$\tilde{h}^{phen}(f;\vec{\alpha},\vec{\beta}) := A(f;\vec{\alpha})e^{i\Psi(f;\vec{\beta})}, \tag{2.104}$$

where $\vec{\alpha}$ are phenomenological amplitude parameters and $\vec{\beta}$ are phenomenological phase parameters. Once this ansatz is in place, the hybrid waveforms are used to tabulate the values of the coefficients $(\vec{\alpha}, \vec{\beta})$.

Since we are interested in describing the complete GW signal as a function of physical parameters rather than phenomenological parameters, a mapping between these two sets of parameters needs to be established. The best match amplitude and phase parameters for every waveforms is used to allow for the identification

$$(\vec{\alpha}, \vec{\beta}) \mapsto (M, \eta). \tag{2.105}$$

These are the basic ingredients to produce a phenomenological waveform family parameterised by the physical parameters of the binary system. The more complex the binary system, the more difficult the construction of such a family. As of today, there exist complete phenomenological waveform families for nonspinning binaries [10, 11] and for binaries where the individual spin angular momenta are aligned with the orbital angular momentum (spin-aligned binaries) [12, 192]. Also available is a phenomenological model for the most general class of binary systems, precessing binaries, in the time-domain [209]. And most recently, a phenomenological waveform family for precessing black-hole-binaries in the Fourier domain has become available [117]. This particular model will be described in detail in Chapter 7.

The phenomenological approach is not the only formalism to construct waveform families for arbitrary binary configurations. Another successful strategy is to map the two-body problem in General Relativity onto an effective-one-body problem (EOB) [57, 58] to describe the inspiral part of the waveform. This description is then extended to the merger and ringdown using information from Numerical Relativity. By doing so, a set of differential equations provides the inspiral-merger signal, which is then completed by attaching an analytical ringdown waveform [65, 172, 174, 210].

CHAPTER 3

The phenomenology of black hole binaries

In this Chapter we aim to familiarise the reader with the qualitative behaviour of compact binary coalescences, their evolution and their waveform characteristics within the post-Newtonian framework. The subsequent sections explore the phenomenology of the three main types of black-hole-binaries: 1) nonspinning binaries, 2) aligned-spin binaries and 3) precessing binaries. All three types undergo inspiral, merger and ringdown, but the dynamics of the system as well as the waveforms are qualitatively different. The investigation of those differences is the subject of the following sections. Parts of this analysis have already been published in [197].

3.1 Nonspinning and aligned-spin binaries

The simplest class of binary black holes is formed by *nonspinning* binaries. In such binaries, the two companions are Schwarzschild black holes characterised only by their mass parameters m_1 and m_2. The set of all nonspinning binaries forms a two dimensional manifold which represents their *intrinsic parameter space*. Similar to the Newtonian two-body problem, the two compact objects trace out a trajectory in a fixed two dimensional plane, whose spatial orientation does not change with time. Due to the emission of gravitational waves, the orbital separation of the binary decays continuously until they merge. A few orbits of the PN insprial motion in the fixed orbital plane are shown in Fig. 3.1a. Moreover, the emission of gravitational radiation tends to circularise the orbit on the orbital time scale, removing eccentricity from the motion long before the binary enters the sensitivity band of ground-based GW detectors [177, 178]. At the same time, the decay of the orbit, i.e., the inspiral, occurs on the (long) radiation-reaction time scale, the time needed to radiate orbital angular momentum away in order to drive the decay [177, 178]. It is therefore valid to assume that the inspiral can be described as a series of quasi-circular orbits. This assumes that the fractional change of the orbital velocity is small compared to the orbital velocity, meaning that the orbit evolves slowly. This is commonly referred to as *adiabatic inspiral*, which we will consider henceforth.

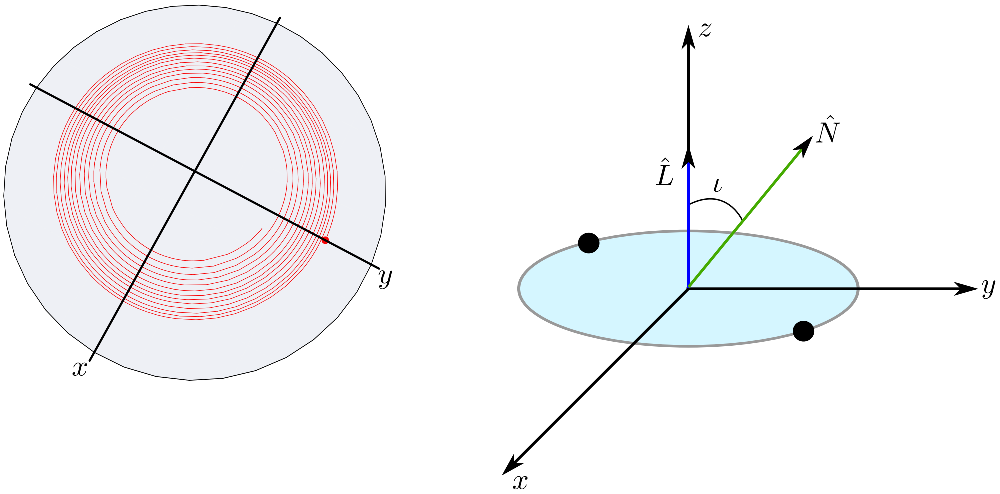

(a) Inspiral motion of a nonspinning equal-mass binary.

(b) Cartesian source frame of a nonspinning binary.

Figure 3.1: The left panel shows the inspiral motion of a nonspinning equal-mass binary. The starting point of the evolution is on the y-axis and is marked by the red dot. The orbital decay as well as the fixed two dimensional plane of motion, here the xy-plane, are clearly visible. The right panel depicts the source frame $\{x, y, z\}$ of a nonspinning binary with the orbital plane in the xy-plane. The line-of-sight of some static observer is indicated by $\hat{N}$. The inclination of the orbital plane as seen by the observer is given by ι.

In order to describe the geometry of any binary system, it is useful to attach a coordinate system to the binary. We will refer to this coordinate system as the *source frame* of the binary and denote it by the Cartesian coordinates $\{x, y, z\}$. The geometry of nonspinning binaries is depicted in Fig. 3.1b. Without loss of generality we can choose the xy-plane of the source frame to be the plane of the orbital motion. In the Newtonian limit, the orthonormal direction of the orbital plane is the direction of the orbital angular momentum $\hat{L}$. Since the orientation of the orbital plane is fixed, so is $\hat{L}$ and it is therefore the defining direction in the geometry of the binary configuration. Apart from having a well-defined geometrical meaning, gravitational radiation is predominantly emitted along this direction $\hat{L}$, making this frame a natural basis for the spin-weighted spherical harmonics.

Let $\hat{N}$ be the direction to some static observer. In general, we denote this direction with respect to the source frame by the polar angle θ. If we choose a source frame such that $\hat{L} \equiv \hat{z}$, then θ corresponds to the inclination of the orbital plane relative to the observer,i.e., $\theta = \iota$, as illustrated in Fig. 3.1b.

The GW strain measured by a static observer whose line-of-sight is parallel to $\hat{L}$, will predominantly contain GW energy from the dominant harmonic, i.e., $h(t; 0, \phi) \simeq h_{22}(t) Y_{22}^{-2}(\theta = 0, \phi)$. This is commonly referred to as an *optimally oriented binary*, i.e., $\hat{L}||\hat{N}$ with $\theta = \iota \equiv 0$.

Let us now assume the binary is arbitrarily oriented with respect to the static observer

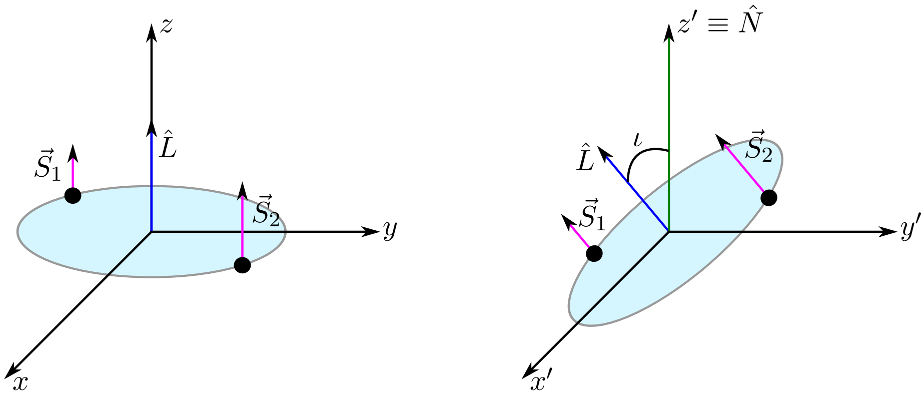

Figure 3.2: The left panel shows the source frame of a spin-aligned binary. The right panel illustrates the relative inclination of a spin-aligned binary with respect to the reference frame $\{x', y', z'\}$ of a static observer.

and indicate the misalignment between the line-of-sight and the orbital angular momentum by the inclination angle ι. The inspiral motion of the binary is still confined to a spatially fixed two-dimensional plane, but the observer does not receive the full power contained in the dominant harmonic. Only a fraction of this energy is seen, but some higher modes, which are subdominant for an optimally oriented binary, appear stronger relative to the quadrupole mode. The observed strain is then inaccurately approximated by the (22)-mode as the energy is spread across various modes and therefore signal power is lost, since these modes are in general substantially weaker. For a fixed sky location, optimally-oriented binaries can thus be observed to a much larger distance than arbitrarily oriented binaries [94, 215].

The qualitative behaviour of the binary evolution changes minimally if we now include spin angular momenta $\vec{S}_i$ aligned with each other and with the orbital angular momentum. Such binaries are referred to as *aligned-spin* binaries and a typical setup is illustrated in Fig. 3.2. We note here that the dimensionless spin parameters χ_i are commonly used:

$$\chi_i = \frac{S_i}{m_i^2}, \tag{3.1}$$

where $i = 1, 2$ indicates the black hole and $S_i := ||\vec{S}_i||$. This notation is common in PN theory, whereas in Numerical Relativity often the Kerr parameter a_i is used instead. We will use both notations interchangeably.

The main effect of the presence of aligned-spin angular momenta on the motion of the binary is that it either slows down or speeds up the inspiral rate, in other words the phase evolution of the binary is affected. To illustrate this, let us briefly recall the PN description of the motion of the binary: the PN approximation computes the evolution of the orbital phase $\Phi_{\rm orb}(t)$ as an expansion series in the invariant velocity parameter. In the adiabatic approximation, the orbital phase is computed by solving the system of coupled ordinary differential equations given in Eq.(2.82). The main ingredients are the binding energy E and the GW flux $\mathcal{F}$. Currently, the energy function $E(v)$ for a nonspinning binary in circular orbit has been calculated to 4PN order (v^8) [37, 39, 40, 42, 84, 89, 129, 130, 133, 179, 226], the spin-orbit contributions to 3.5PN [46, 121] and the spin-spin terms to 3PN and some at 4PN [122, 141]; the nonspinning GW flux function $\mathcal{F}(v)$ is known to 3.5PN order (v^7) [41, 42, 185], but the spin effects have only been computed to 2PN order (spin spin) [100] and 3.5PN order (spin-orbit) [45, 46, 181] respectively.

There exist different ways of solving this system of equations, giving rise to a variety of *PN approximants*. To illustrate the effect of aligned spins on the GW phase, we give the explicit expression $\Phi_{\rm orb}(t)$ for one particular approximant, "TaylorT5" [9]:

$$\begin{aligned}
\Phi_{\rm orb}(v) = \Phi_0 - \frac{1}{32v^5\eta}\Bigg\{ & 1 + v^2\left[\frac{55\eta}{12}+\frac{3715}{1008}\right] + v^3\left[\frac{565}{24}\left(\left(1-\frac{76\eta}{113}\right)\vec{\chi}_s\cdot\hat{L}+\delta\vec{\chi}_a\cdot\hat{L}\right)-10\pi\right] \\
& + v^4\Bigg[(\vec{\chi}_a\cdot\hat{L})^2\left(150\eta-\frac{3595}{96}\right)-\frac{3595\delta(\vec{\chi}_a\cdot\hat{L})(\vec{\chi}_s\cdot\hat{L})}{48}+(\vec{\chi}_a)^2\left(\frac{1165}{96}-50\eta\right) \\
& + \frac{1165\delta(\vec{\chi}_a\cdot\hat{L})(\vec{\chi}_s\cdot\hat{L})}{48}+(\vec{\chi}_s\cdot\hat{L})^2\left(-\frac{5\eta}{24}-\frac{3595}{96}\right)+(\vec{\chi}_s)^2\left(\frac{35\eta}{24}+\frac{1165}{96}\right) \\
& + \frac{3085\eta^2}{144}+\frac{27145\eta}{1008}+\frac{15293365}{1016064}\Bigg] \\
& + v^5\Bigg[\Bigg((\vec{\chi}_a\cdot\hat{L})\left(-\frac{35\delta\eta}{2}-\frac{732985\delta}{2016}\right)+(\vec{\chi}_s\cdot\hat{L})\left(\frac{85\eta^2}{2}+\frac{6065\eta}{18}-\frac{732985}{2016}\right) \\
& - \frac{65\pi\eta}{8}+\frac{38645\pi}{672}\Bigg)\ln(v)\Bigg] \\
& + v^6\Bigg[-\frac{127825\eta^3}{5184}+\frac{76055\eta^2}{6912}+\frac{2255\pi^2\eta}{48}-\frac{15737765635\eta}{12192768}-\frac{1712\gamma_E}{21} \\
& - \frac{160\pi^2}{3}+\frac{12348611926451}{18776862720}-\frac{1712\ln(4v)}{21}\Bigg] \\
& + v^7\left[-\frac{74045\pi\eta^2}{6048}+\frac{378515\pi\eta}{12096}+\frac{77096675\pi}{2032128}\right]\Bigg\},
\end{aligned} \tag{3.2}$$

where $\eta = m_1 m_2/m^2$ is the symmetric mass ratio, Φ_0 is a certain reference phase, γ_E is Euler's constant, $\delta = m_1 - m_2$ and $\vec{\chi}_{s,a}$ the symmetric and antisymmetric dimensionless spin combinations

$$\vec{\chi}_s = \frac{1}{2}\left(\vec{\chi}_1+\vec{\chi}_2\right), \tag{3.3}$$

$$\vec{\chi}_a = \frac{1}{2}\left(\vec{\chi}_1-\vec{\chi}_2\right). \tag{3.4}$$

We see immediately from the above expression that the leading order spin contribution occurs at 1.5PN order (v^3) and is a weighted combination of $\vec{\chi}_1$ and $\vec{\chi}_2$ projected onto the orbital angular momentum $\hat{L}$, which can be rewritten in terms of a only one spin parameter by defining an *effective total spin* $\chi_{\rm eff}$

$$\chi_{\rm eff} := \left(1 - \frac{76\eta}{113}\right) \vec{\chi}_s \cdot \hat{L} + \delta\vec{\chi}_a \cdot \hat{L}. \tag{3.5}$$

With this definition, at leading spin-orbit order, the inspiral phase of an aligned-spin binary is then given by

$$\Phi_{\rm orb}(v) = \Phi_0 - \frac{1}{32v^5\eta}\left\{1 + v^2\left[\frac{55\eta}{12} + \frac{3715}{1008}\right] + v^3\left[\frac{565}{24}\chi_{\rm eff} - 10\pi\right]\right\}. \tag{3.6}$$

Therefore, rather than describing the binary in terms of the two individual spin magnitudes, the mass-weighted combination $\chi_{\rm eff}$ can be used instead, allowing for a simplified description of the parameter dependencies. We note that a range of physical spin parameters map to the same effective spin, revealing spin degeneracies and highlighting the difficulty in measuring the individual spins from GW observations.

It can be shown that if the total spin

$$\vec{S} = \vec{S}_1 + \vec{S}_2 \tag{3.7}$$

is parallel to the orbital angular momentum, the inspiral is slowed down and the binary produces more orbits before it can finally merge. This effect is known as the *orbital hang up* [69]. If, on the other hand, the total spin is antiparallel to $\hat{L}$, the evolution occurs more rapidly and less time is spent in orbit before the final plunge. We shall emphasise here that the direction of the orbital angular momentum as well as the orientation of the spins relative to it are constant in space and time. During the evolution also the magnitudes of the two spin momenta are approximately constant. Therefore, the intrinsic parameter space of spin-aligned binaries has dimension three: the mass ratio and the two spin magnitudes $\{\eta, \chi_1, \chi_2\}$. This completely defines the binary configuration. The spin directions can be neglected as this information is already incorporated in the notion of aligned spins.

3.2 Precessing black hole binaries

In this section we summarise the main features of precessing-binary systems, introduce their geometry and illustrate the effects of precession on the gravitational-wave signal within the post-Newtonian framework. In this context, we will use the terms "precessing" and "generic" synonymously. For a comprehensive discussion of precessing-binary systems we refer the reader to Refs. [20, 133], which remain the standard references in the field.

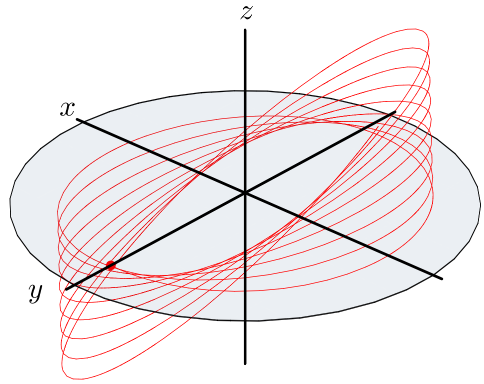

Figure 3.3: Illustration of the complex inspiral motion of a precessing binary. The starting point of the evolution is on the y-axis and is marked by the red dot. It is clearly visible how the orbital motion starts off in the xy-plane but then continuously moves out of it.

3.2.1 The precessing geometry

The most general class of black-hole-binaries is formed by including arbitrarily oriented spin angular momenta. As soon as the spins are misaligned with the orbital angular momentum $\hat{L}$, *precession* is induced due to spin-orbit and spin-spin coupling effects. The spin-orbit couplings cause the orbital plane (i.e., the direction of the orbital angular momentum) to evolve not only in time but also in space. The binary's motion is no longer confined to a two-dimensional plane but traces out a trajectory in the full three dimensional space continuously changing its orientation. The trajectory of the relative motion for an equal-mass precessing black-hole-binary with spins $\vec{\chi}_1 = (0, 0, 0)$ and $\vec{\chi}_2 = (0.75, 0, 0)$ is illustrated in Fig. 3.3. We see the binary initially moves in the xy-plane of the source frame, but evolves out of this plane with time, clearly showing the precession of the orbital plane.

On top of the orbital precession, spin-spin couplings, which enter at 2PN order, act like torques on the spin angular momenta introducing *nutation*. We note that the nutation of L is not observed in single-spin precessing binaries. In conclusion, the orientation of the spin angular momenta is crucial for the occurrence of precession in a binary system and therefore needs be taken into account to intrinsically define a binary configuration. In general, this yields a seven-dimensional parameter space spanned by the mass ratio and the two spin vectors $\{\eta, \vec{\chi}_1, \vec{\chi}_2\}$.

Geometrically, the defining difference between a precessing and an aligned-spin system is the evolution of the direction of the orbital angular momentum $\hat{L}$. Whereas only its magnitude changed in the nonspinning and aligned-spin case due to the emission of gravitational waves, now also its direction evolves in time and space. $\hat{L}(t)$ traces out an evolving *precession cone* centered around some direction. Therefore, due to its time-dependency, $\hat{L}$ does not constitute a useful direction to characterise the dynamics of a generic binary. This goes hand in hand with reconsidering the definition of the orientation of a binary system with respect to some observer. In order to do so, a geometrically meaningful direction in the binary system needs to be identified, and indeed one such direction also exists in precessing configurations: the direction of the *total angular momentum* $\hat{J}$, where

$$\vec{J}(t) = \vec{L}(t) + \vec{S}(t). \tag{3.8}$$

The direction $\hat{J}$ is not exactly constant in time, but it remains very close to its initial direction when the binary has infinite separation, i.e., $t \to -\infty$. We denote this the "asymptotic total angular momentum direction" $\hat{J}_{-\infty} \equiv \hat{J}(t \to -\infty)$. This is the approximately fixed direction the precession cone of $\hat{L}$ is centred around.

In Newtonian solid-body mechanics the total angular momentum is a natural fixed direction, around which the rotation occurs. This picture is still true for Newtonian and first-order post-Newtonian binary systems. However, when spin effects are included, starting at 1.5PN order (spin-orbit), the post-Newtonian approximation of the Einstein field equations reveals that this natural direction of rotation still exists, but it is no longer exactly fixed: the direction of the total angular momentum is now also time-dependent. It evolves as well, but in cases with small precession, and for large separations, it describes a precession cone that is rather small, in particular compared to the precession cone traced out by $\hat{L}$. Therefore, it is almost natural to consider $\hat{J}_{-\infty}$ to be the geometrically defining direction in a generic binary system. To recaptitulate, the orientation of the orbital angular momentum $\hat{L}$ is no longer fixed but instead evolves, tracing out a precession cone around the approximately fixed direction of the total angular momentum $\hat{J}$. The spin angular momenta also precess, but their precessing motion is centred around $\hat{L}$. This type of precessing motion is known as *simple precession*. An example of the precession cone traced out by $\hat{L}$ for a binary with mass ratio $q = 3$ and initial spins $\vec{\chi}_1 = (0, 0, 0)$ and $\vec{\chi}_2 = (0.75, 0, 0)$ with an initial separation of $D_i = 40M$ is shown in in the left panel of Fig. 3.4; see Sec. V in [20] for more examples of simple precession.

Simple precession is the most common type of precession, but not the only one: in a few special cases, namely where the orbital and spin angular momenta are nearly equal and opposite and the total angular momentum passes through zero during the inspiral, the direction of the total angular momentum changes significantly during the binary's evolution; this is called *transitional precession* and is illustrated in the right panel of Fig. 3.4. However, for transitional precession to occur within the sensitivity band of the Advanced ground-based GW detectors, only a very narrow range of physical parameters is allowed in order to fulfill the conditions mentioned above. In order to produce the transitional phase shown in the right panel of Fig. 3.4, a large initial separation of $D_i = 53M$ for the mass ratio $q = 10$ and the

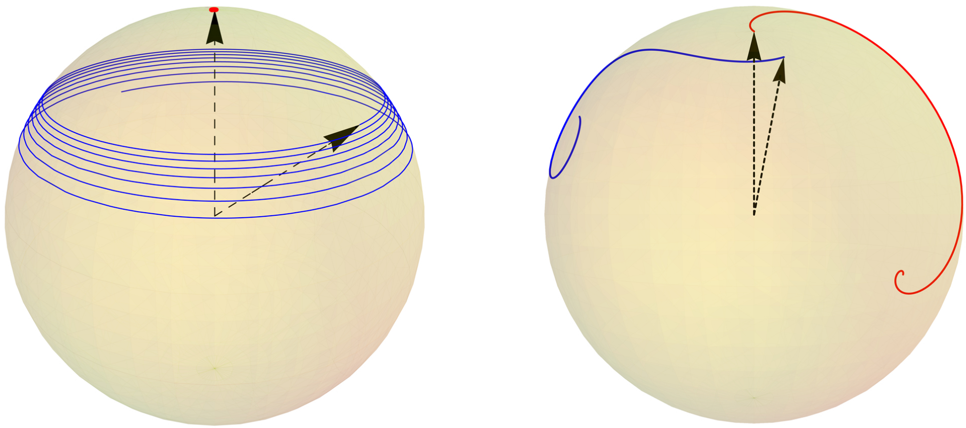

Figure 3.4: Evolution of $\hat{J}$ (red) and $\hat{L}$ (blue)plotted on the unit sphere, where $\hat{J}_0$ is initially aligned with the z-axis of the source frame. The left panel shows the evolution of these two directions for a case of simple precession. The precession cone described by $\hat{J}$ is very small in comparison to the one described by $\hat{L}$, and appears on the figure as only a red dot at the end of the vertical arrow. The right panel shows the same characteristic directions for a case of transitional precession. In this case $\hat{J}$ clearly moves along the unit sphere away from its initial direction (to the right side of the sphere) and separates from $\hat{L}$, which moves to the left side of the sphere in the figure.

following initial spins $\vec{\chi}_1 = (0,0,0)$ and $\vec{\chi}_2 = 0.65(0, -\sin(3°), -\cos(3°))$ were chosen. The transitional phase lasts for about $500,000M$, a fourth of the entire evolution from $D_i = 53M$ to $D_\mathrm{f} = 6M$.

Since $\hat{J}$ is the only approximately constant direction in a precessing binary, it proves useful to adapt a source frame, i.e., a Cartesian coordinate frame attached to the binary, such that the initial total angular momentum is parallel to the z-direction at some initial time t_0 at which we define the binary configuration. In practice, this corresponds to some finite time or GW frequency. We refer to the direction of J at the moment of definition as $\hat{J}_0 \equiv \hat{z}$. Henceforth, we will refer to this frame as the "J_0-aligned frame". In this particular frame, let the direction of $\hat{L}$ be defined on the unit sphere by the two polar angles $(\iota(t), \alpha(t))$. The intrinsic geometry of a precessing configuration is depicted in Fig. 3.5. These two angles encode the complete information about the orientation of the binary with respect to the J_0-aligned source frame. The inclination angle $\iota(t)$ is defined as

$$\iota(t) := \arccos\left(\hat{L}(t) \cdot \hat{J}(t)\right), \tag{3.9}$$

and the azimuth angle $\alpha(t)$ is given by

$$\alpha(t) := \arctan\left(\frac{L_y}{L_x}\right), \tag{3.10}$$

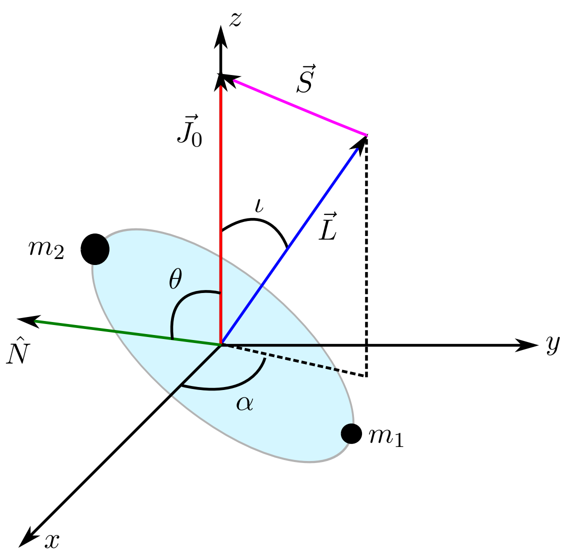

Figure 3.5: The panel depicts the geometry of a precessing binary in the $\hat{J}_0$-aligned source frame.

with the standard convention of being measured counterclockwise from the x-axis of the source frame (mathematically positive) in the interval $[0, 2\pi]$. In the case of simple precession, $\iota(t)$ represents the (time-evolving) opening angle of the precession cone. The azimuth angle $\alpha(t)$ describes how $\hat{L}$ moves around $\hat{J}_0$ and is therefore directly related to the *precession frequency*, i.e., the rate of change of the orbital angular momentum:

$$\omega_p(t) = \frac{d\alpha(t)}{dt}. \tag{3.11}$$

Let us emphasise at this point that the inclination ι of an aligned-spin binary refers to the relative orientation of $\hat{L} = \text{const.}$ to the line-of-sight. In the general case of a precessing binary, $\iota(t)$ is the intrinsic angle between J and L; the orientation of the binary with respect to some static observer is encoded in the angle θ, which, in this case, generalises to the angle between $\hat{J}$ and $\hat{N}$.

Although it is convenient to work in the $\hat{J}_0$-aligned source frame for simplicity, we will see later that it is very useful to still define the intrinsic geometry of the binary, and in particular the spin angular momenta, with respect to the orbital angular momentum in the following way. Any vector $\vec{v} \in \mathbb{R}^3$ can be decomposed into its vector components parallel $\vec{v}_{||}$ and orthogonal $\vec{v}_{\perp}$ relative to some other vector. We therefore define

$$\vec{S}_{i||} := \left(\vec{S}_i \cdot \hat{L}\right) \hat{L}, \tag{3.12}$$

$$\vec{S}_{i\perp} := \hat{L} \times \left(\vec{S}_i \times \hat{L}\right). \tag{3.13}$$

The magnitudes of the parallel and orthogonal spin components are denoted by $S_{i||}$ and $S_{i\perp}$ respectively. For certain applications it might be more intuitive to directly introduce the angle between $\hat{L}$ and the spin angular momenta,

$$\cos\kappa_i = \hat{S}_i \cdot \hat{L}. \tag{3.14}$$

With this decomposition we can now rewrite the precession cone opening angle Eq.(3.9) in terms of the decomposed spin angular momenta to obtain

$$\iota(t) \equiv \arccos\left(\frac{L(t) + S_{||}(t)}{\sqrt{(L(t) + S_{||}(t))^2 + S_{\perp}^2(t)}}\right), \tag{3.15}$$

where $S_{||}$ and $S_{\perp}$ are the magnitudes of the projections of the total spin as given in Eq.(3.7) onto $\hat{L}$. In general, in order to compute these functions the time evolutions for $L(t)$ and $S(t)$ need to be known. However, under the approximation that $S_{||}$ and $S_{\perp}$ are constant, only the time evolution of L is needed.

3.2.2 The PN precession equations

We have seen that in order to qualitatively understand precession in binary systems, it is useful to investigate the effects within the post-Newtonian framework. As mentioned before, in the PN approximation the leading-order precession effect occurs due to the spin-orbit coupling and already appears at 1.5PN order. This term induces the precession of the orbital plane, an effect also known as Lense-Thirring precession [140] or "frame-dragging", a purely relativistic effect, which does not occur in Newtonian physics. The next-to-leading order spin term occurs at 2PN order and encapsulates the dominant spin-spin coupling.

Precession does not only alter the otherwise simple motion of the binary, but also affects the emitted gravitational waves as will be illustrated later. An advantage of the PN framework is that it allows one to derive the governing equations of motions for $\vec{L}$ and $\vec{S}_i$. These equations fully describe the precession dynamics up to a given PN order. The precession equations accurate through 2PN order obtained after averaging over one circular orbit[1] read as [20]:

$$\begin{aligned}\dot{\vec{L}} = {} & \frac{L}{r^3}\left[\left(2 + \frac{3m_2}{2m_1}\right)\vec{S}_1 + \left(2 + \frac{3m_1}{2m_2}\right)\vec{S}_2\right] \times \hat{L} - \frac{3}{2r^3}[(\vec{S}_2 \cdot \hat{L})\vec{S}_1 + (\vec{S}_1 \cdot \hat{L})\vec{S}_1] \times \hat{L} \\ & - \frac{32\mu^2}{5r}\left(\frac{M}{r}\right)^{5/2}\hat{L},\end{aligned} \tag{3.16}$$

$$\dot{\vec{S}}_1 = \frac{1}{r^3}\left[\left(2 + \frac{3m_2}{2m_1}\right)(\mu\sqrt{Mr})\hat{L}\right] \times \vec{S}_1 + \frac{1}{r^3}\left[\frac{1}{2}\vec{S}_2 - \frac{3}{2}(\vec{S}_2 \cdot \hat{L})\hat{L}\right] \times \vec{S}_1, \tag{3.17}$$

$$\dot{\vec{S}}_2 = \frac{1}{r^3}\left[\left(2 + \frac{3m_1}{2m_2}\right)(\mu\sqrt{Mr})\hat{L}\right] \times \vec{S}_2 + \frac{1}{r^3}\left[\frac{1}{2}\vec{S}_1 - \frac{3}{2}(\vec{S}_1 \cdot \hat{L})\hat{L}\right] \times \vec{S}_2. \tag{3.18}$$

[1] In the adiabatic approximation one expects the bulk GW flux to result from the average change of the orbital velocity over one orbit.

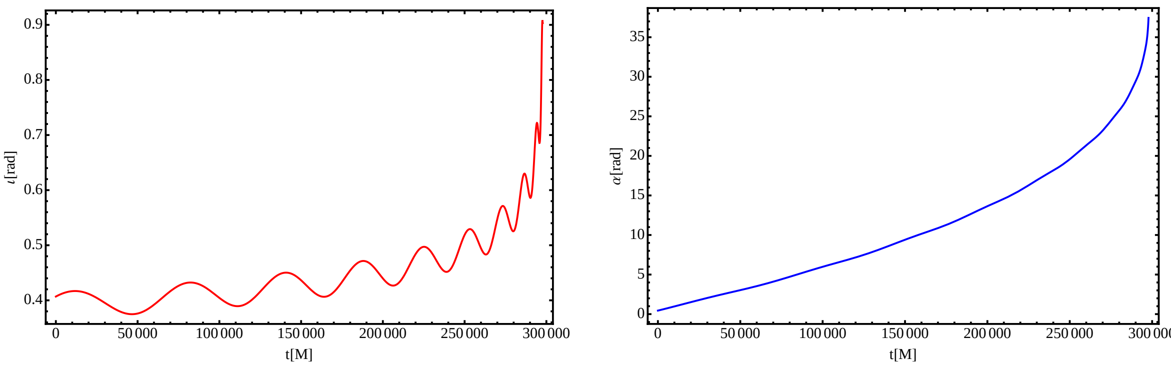

Figure 3.6: The left panel shows the time evolution of the opening angle $\iota(t)$; the right panel shows the evolution of the precession angle $\alpha(t)$ from a PN evolution of the generic binary configuration with initial spins $\vec{\chi}_1 = (0.4, -0.2, 0.3)$ and $\vec{\chi}_2 = (0.75, 0.4, -0.1)$ and mass ratio $q = 3$, where the components of $\vec{\chi}_i$ are defined with respect to $\hat{L}$ at the initial time $t_0 = 0$ corresponding to an initial separation of $D_i = 40M$.

Here, the overdot denotes the time derivative, $\mu := (m_1 m_2)/m$ is the reduced mass, L the magnitude of the orbital angular momentum and $r(t)$ the binary's separation. The first term in Eq.(3.16) is the spin-orbit contribution, the second one denotes the spin-spin term and the third is due to radiation-reaction, which drives the decrease of the orbital separation. These equations allow us to fully investigate the evolution of the orbital plane (characterised by $\dot{\hat{L}}(t)$, which yields $\iota(t)$ and $\alpha(t)$) during the inspiral regime for any precessing configuration.[2] A typical time evolution of the two defining precession angles $(\iota(t), \alpha(t))$ for a simply precessing generic binary obtained by solving the above system of ordinary differential equations (ODEs) is shown in Fig. 3.6.

Further, we note that the spin components driving the precession of the orbital plane are the ones contained within the instantaneous orbital plane, i.e., $\vec{S}_{i\perp}$, as can directly be seen from the leading-order term in Eq.(3.16). In contrast to this, in Eq.(3.2) we have seen that the spin components parallel to $\hat{L}$, i.e., $\chi_{i||}$, influence the evolution of the orbital phase of the binary. In this sense, the phase and the precession are influenced by the complementary components of the spins. Once we have solved for the dynamics of the precessing binary, we are now able to investigate how the complex motion affects the emitted gravitational-wave signal.

3.2.3 Precessing waveforms

The complex motion of the orbital plane in space is directly reflected in the emitted gravitational waveforms. Precession predominantly introduces phase and amplitude modulations in the GW signal [20] and additionally contributes to the GW phase as we will see in the following. However, the strength of the observed modulations depends highly on the orientation of

[2] We have done so to investigate the phenomenology presented in Sec. 3.2.1

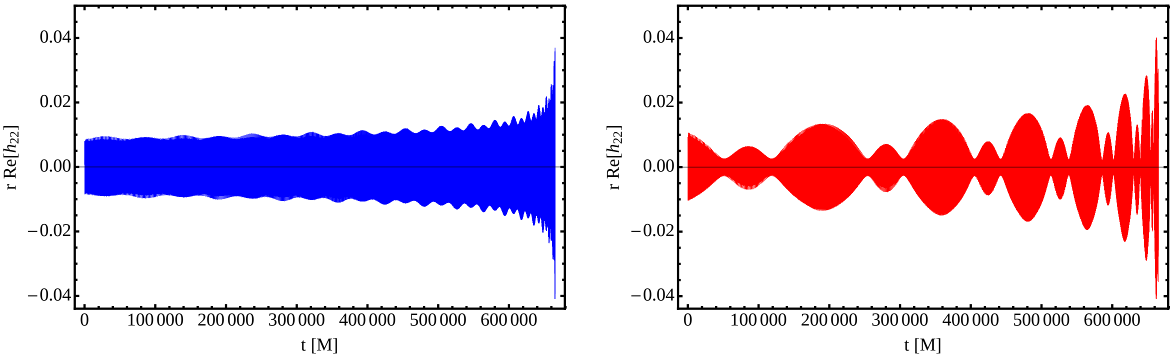

Figure 3.7: Waveforms viewed at different binary orientations. The first panel shows the real part of the ($l = 2, m = 2$)-mode with $\hat{J}_0$ initially aligned with $\hat{N}$ ($\theta = 0$), for a precessing configuration with mass ratio of mass ratio $q = 10$. The second panel shows the same quantity, but now with $\hat{L}$ initially aligned with $\hat{N}$. Since $\hat{L}$ continuously changes its relative orientation to $\hat{N}$, the observed modulations are much more pronounced compared to the optimally oriented precessing binary on the left.

the binary, i.e, $\hat{J}_0$, with respect to the line-of-sight $\hat{N}$, henceforth denoted by θ:

$$\theta := \angle\left(\hat{J}_0, \hat{N}\right). \tag{3.19}$$

We emphasise once more that it is necessary in precessing binaries to distinguish between the intrinsic inclination of the binary $\iota(t)$ and the relative orientation of the binary with respect to some static observer denoted by θ. Note that for nonspinning and aligned-spin binaries such a distinction is not needed as $\hat{L} \equiv \hat{J}$. Thus, an optimally oriented precessing binary is now defined by $\theta = 0$, i.e., the line-of-sight is parallel to the total angular momentum. For aligned-spin binaries the orientation $\iota = \theta = 0$ is commonly referred to as "face-on", whereas $\iota = \theta = \pi/2$ is known as "edge-on" – we will use these standard terms also for precessing binaries, but emphasise that they do not actually refer to the orbital plane in this context.

If a precessing binary now happens to be optimally-oriented towards some static observer, the observed amplitude modulations in the gravitational waveform will be smaller than for any other orientation, since the relative orientation between the observer and the least-precessing axis of the binary does not change much during the evolution of the binary. Nonetheless, since the GW signal is to first approximation produced by the acceleration of the two bodies in orbit, the bulk of the GW energy is emitted along the direction of the orbital angular momentum $\hat{L}$. On average, however, i.e., over one precession cycle, we expect the strongest and simplest GW emission for simple precession along the direction of $\hat{J}_0$ as discussed in [169]. On the other hand, if the observer's orientation does not coincide with $\hat{J}_0$, strong modulations will be observed in the GW signal, which peak whenever $\hat{L}$ crosses the line-of-sight. This orientation dependence is depicted in Fig. 3.7.

Modulations in the phase and the amplitude are not the only complications induced by precession. In the case of nonspinning or aligned-spin binaries, the misalignment between the line-of-sight and the orbital angular momentum ($\theta \neq 0$) yields a different power distribution among the emitted GW modes. This can be understood in the following way: the maximal GW power is emitted along the direction of L, governed by the dominant harmonic. The total gravitational radiation field, however, has directional dependence. In a source frame such that $\hat{L} \equiv \hat{z}$, which is also the frame where the mode decomposition is performed, the maximal emission will be in the direction $\theta = 0$. For any other orientation, the radiation field at this point contains significantly large contributions from higher modes, such as h_{21}, and less observable power in the dominant harmonic. Current gravitational searches predominantly use search templates which model only the dominant harmonic. In practice, this means that a binary oriented face-on is observable to much higher distances, whereas an edge-on binary, where the contribution of the dominant harmonic to the total signal power is much weaker, can only be detected if it is relatively close-by. For precessing binaries, the situation is much more complicated as the signal power is spread over a large number of modes due to the precession of L, which breaks the nice mode structure observed in aligned-spin binaries. Similar to a non-optimally oriented spin-aligned binary, subdominant harmonics are excited and the hierarchical mode structure is broken as will be discussed in detail in Chapter 4.

The generation of precessing waveform modes in PN theory is a rather complicated task. The lengthy, explicit expressions for the precessing waveform polarisations for arbitrary orientations have first been calculated by *Arun et al.* [23] with precession through 1.5PN order. Currently, the amplitude functions are only known for precession effects through 2PN order [67]. Schematically, the precessing waveform modes can be written as

$$h_{lm} = A_{lm} e^{-im(\Phi+\alpha)}, \tag{3.20}$$

where we explicitly see the contribution of the precession to the gravitational-wave phase. Φ here denotes *total phase* of the binary $\Phi(t)$, a particularly important difference to non-precessing systems. Let us recall that $h_{lm} \sim e^{-im\Phi_{\rm orb}}$ for nonprecessing binaries. Therein, the orbital phase is related to the orbital frequency by Eq.(2.80), which simply describes the motion of the relative separation vector within the orbital plane. However, for precessing binaries the orbital phase is replaced by the total phase Φ, which consists of two parts: firstly, the projection of the orbital motion in the xy-plane of the source frame, which is the standard integral of the orbital frequency. Secondly, the motion of the orbital plane within the source frame due to precession. The total phase of the binary is then given by [133]

$$\Phi(t) = \int_0^t \left(\omega_{\rm orb}(t') - \frac{d\alpha(t')}{dt'} \cos\iota(t') \right) dt'. \tag{3.21}$$

The total phase can be constructed by solving the set of ODEs given by Eq.(3.16)-Eq.(3.18) as well as the additional evolution equation for the separation $r(t)$ (Eq.(4.12) in [133])

$$\dot{r}(t) = -\frac{64\eta}{5}\left(\frac{m}{r}\right)^3\left[1 - \frac{1}{336}(1751 + 588\eta) - \left\{\frac{7}{12}\sum_{i=1,2}\left[\chi_i(\hat{L}\cdot\hat{S}_i)\left(19\frac{m_i^2}{m^2} + 15\eta\right)\right]\right.\right.$$
$$\left.\left. -4\pi\right\}\left(\frac{m}{r}\right)^{3/2} - \frac{5}{48}\eta\chi_1\chi_2\left[59(\hat{S}_1\cdot\hat{S}_2) - 173(\hat{L}\cdot\hat{S}_1)(\hat{L}\cdot\hat{S}_2)\right]\left(\frac{m}{r}\right)^2\right], \tag{3.22}$$

and evaluating the equation for the orbital frequency $\omega_{\rm orb}(t)$ (Eq.(4.5) in [133])

$$\omega_{\rm orb}^2 = \left(\frac{m}{r^3}\right)\left\{1 - (3-\eta)\left(\frac{m}{r}\right) - \sum_{i=1}^{2}\left[\chi_i(\hat{L}\cdot\hat{S}_i)\left(2\frac{m_i^2}{m^2} + 3\eta\right)\right]\left(\frac{m}{r}\right)^{3/2} + \left[\left(6 + \frac{41}{4}\eta + \eta^2\right)\right.\right.$$
$$\left.\left. -\frac{3}{2}\eta\chi_1\chi_2\left[(\hat{S}_1\cdot\hat{S}_2) - 3(\hat{L}\cdot\hat{S}_1)(\hat{L}\cdot\hat{S}_2)\right]\right]\left(\frac{m}{r}\right)^2\right\}, \tag{3.23}$$

as well as the expressions for the precession angles Eq.(3.10) and Eq.(3.9). Alternatively, one may wish to directly integrate $\dot{\omega}_{\rm orb}(t)$ (Eq.(4.14) in [133]). Once these quantities have been determined, the expressions for the polarisations respectively the h_{lm}-modes given in [23] can be evaluated yielding precessing inspiral waveforms.

Solving the explicit PN evolution equations is one way to compute the precessing motion. Alternatively, one may use the Hamiltonian formulation provided by the effective-one-body framework to solve for the dynamics of the binary [57, 78].

CHAPTER 4

Tracking the precession of the orbital plane

In the previous chapter we have explored the phenomenology of precessing black-hole-binaries during the inspiral regime in the context of PN theory. So far, we have entirely neglected the analysis of precession during the late inspiral, merger and ringdown, which needs to be explored with Numerical Relativity (NR). The understanding of the late precession dynamics is particularly important, as we aim to systematically explore precession during all three binary evolution stages to ultimately facilitate the construction of a complete inspiral-merger-ringdown (IMR) waveform model for precessing binary black holes. We therefore also need to investigate precession in NR simulations and isolate interesting features like the precession of the orbital plane, which is the main goal of this chapter. To do so, we present a simple method to track the precession of a black-hole-binary system during the late inspiral and merger, using only information from the gravitational-wave signal extracted from NR simulations. The method consists of locating the frame of reference from which the magnitudes of the dominant harmonics, the $(l = 2, |m| = 2)$-modes, are maximised, which we henceforth refer to as the *"quadrupole-aligned" frame*. The analysis and results were published in:
[196] Schmidt et al., "Tracking the precession of compact binaries from their gravitational-wave signal", Phys.Rev., D84:024046, 2011.

4.1 Introduction

Numerical Relativity simulations produce waveforms for only discrete points in the parameter space of binary configurations, but significant progress has been made in synthesising information from post-Newtonian (PN) and effective-one-body (EOB) methods, numerical relativity and perturbation theory, to produce analytic models of the complete IMR signal over some regions of the parameter space. At the time this work was completed (Dec 2010), the majority of then available complete waveform models treated nonspinning binaries [8, 10, 11, 26, 62, 65, 79, 80, 87, 88, 153], or spin-aligned binaries [12, 172, 192, 210].

Precession adds a number of complications, as was illustrated in Chapter 3. Therein we have seen that when the spins $\vec{S}_i$ are not parallel to the orbital angular momentum $\hat{L}$ their orientation varies with time, as does the orbital angular momentum itself, meaning that he orbital plane also precesses. Both the precession of the spins and of the orbital plane introduce modulations into the GW amplitude, oscillations into the GW frequency and phase, and variations in the distribution of signal power across different harmonics of the waveform. All of these features complicate efforts to produce an analytic model of precessing-binary waveforms. In addition, they make it difficult to uniquely characterise the GW signal. For example, the total phase Eq.(3.21) of the dominant mode of the signal depends on the initial orientation, i.e., (ι_0, α_0), of the orbital plane. This makes it difficult to determine whether two waveforms were produced by the same binary configuration, or to compare independent numerical simulations, a task that is relatively simple for non-precessing binaries [25, 118, 175] in quasi-circular orbits.

In the following, we introduce a method to put a precessing-binary waveform into a particularly simple form by identifying a preferred time dependent coordinate system, which tracks the precession of the orbital plane during the late inspiral and merger.

Gravitational-wave signals are most conveniently expressed in terms of spherical harmonics $Y^s_{lm}(\theta, \varphi)$ of spin-weight $s = -2$, where (θ, φ) are the standard polar coordinates on the unit sphere (see Sec. 2.5.1 for details). The mode decomposition is performed in the time-independent Cartesian coordinate system of the numerical simulation, henceforth referred to as the *simulation frame*. It is chosen such that the black holes are initially placed on the y-axis. The dominant modes are the *quadrupole modes*, where $(l = 2, m = \pm 2)$. If we now choose a different coordinate system to perform the mode decomposition, for example by rotating the system, the modes of a particular l mix among each other according to the transformation law described in Appendix A.

In linearised gravity it can be shown that a binary system emits GWs predominantly in the direction *orthogonal* to the orbital plane. In a purely Newtonian picture, we associate this direction with the Newtonian orbital angular momentum L_N. Correspondingly, if the binary system is oriented such that this dominant-emission direction is parallel the z-axis of the mode-decomposition frame (i.e., $\theta = 0$), then we expect that the dominant signal is given by the $(l = 2, |m| = 2)$ spherical harmonics of the wave. In general, the $|m| = 1$-modes vanish when the two black holes can be exchanged by symmetry; the $m = 0$-mode is a non-oscillating mode related to memory effects, see e.g., [95, 180]. If we now choose different (rotated) coordinates (θ', φ') to define a new mode-decomposition basis $Y^s_{lm}(\theta', \varphi')$, then mode-mixing will complicate the spherical harmonic description of the signal, and for example even an equal-mass nonspinning binary will exhibit nonvanishing $|m| = 1$ modes. This coordinate change $(\theta, \varphi) \mapsto (\theta', \varphi')$ is equivalent to decomposing the GW signal in the source frame $\{x', y', z'\}$ of some static observer (see for example Fig. 3.2). We illustrate this effect in more detail in Sec. 4.4.1.

Therefore, we can determine a preferred direction *from the gauge-invariant wave signal alone* by finding the orientation that maximises the $(l = 2, |m| = 2)$-modes. This is the method that we will discuss in this chapter. Henceforth, we will refer to waveforms that are given in terms of a spherical harmonics basis that is aligned with this direction of maximal emission as "quadrupole-aligned" waveforms.

In a precessing system there are two contributions to the frequency of the binary motion: the frequency of the motion about the orbital-plane axis, $\omega_{\rm orb}$, which increases during a non-eccentric inspiral as a monotonic function, and the frequency due to the precessional motion, which oscillates as a function of time (see Eq.(3.21)). The total frequency of the motion of the binary in the simulation frame is $\omega = \omega_{\rm orb} - \dot{\varphi}\cos\theta$, where θ is the inclination of the normal to the orbital plane from the z-axis, and φ is the rotation of the normal about the z-axis in the xy-plane of the simulation frame[1]; this corresponds to the result in Eq.(3.10) in [23]. In a kinematical description of the binary, these two frequencies together prescribe the bodies' acceleration, which is the dominant source of gravitational radiation. One of the properties we expect from our quadrupole-aligned waveform is that during the inspiral the frequency of the $(l = 2, |m| = 2)$-modes will to a good approximation satisfy the relation

$$\omega_{22} = 2(\omega_{\rm orb} - \dot{\varphi}\cos\theta). \tag{4.1}$$

Our main results are that 1) we can determine the quadrupole-aligned direction from the GW signal to high accuracy (within a fraction of a degree during most of the inspiral), and 2) the GW signal is indeed much simplified, see in particular Fig. 4.11 of the GW frequency before and after our (2,2)-maximisation procedure, where the final frequency does approximately satisfy Eq.(4.1). In addition, we show that the GW signal is emitted in the direction of the orbital angular momentum of the binary, which is *not* in general perpendicular to the orbital plane. This is counterintuitive to the Newtonian picture, but we illustrate this effect with an example from PN theory, where it can be seen explicitly that the effective orbital angular momentum is not parallel to the naive Newtonian angular momentum.

In Sec. 4.2 we describe our numerical methods and numerical simulations and in Sec. 4.3 we provide details of our algorithm to find the dominant-emission direction from the GW signal, which will subsequently be identified as the direction of the orbital angular momentum. The results of our method are presented in Sec. 4.4, where we verify our method using a simple test case of an equal-mass nonspinning binary and then apply the method to an unequal-mass spinning binary that undergoes significant precession. We discuss these results in Sec. 4.5.

[1] We note that we use the general polar coordinates (θ, φ) in this chapter to denote the direction of $\hat{L}$ in the simulation frame.

4.2 Numerical methods and simulations

We performed numerical simulations with the moving-puncture code BAM [55, 126] as described in detail in Sec. 2.5.2.1. The numerical grid setup is similar to that used in [55], although in the precessing-binary simulation the number of grid points on each refinement level is varied to achieve greater wave extraction accuracy.

In this analysis we consider two configurations: the first is an *equal-mass nonspinning binary*, using the same setup as first described in [113]. The initial separation is $D = 12M$ and the binary completes on the order of nine orbits before merger. To test our orbital-plane tracking algorithm (which we will discuss in Sec. 4.3), we performed a new simulation of this case in which the (Newtonian) orbital angular momentum was first rotated by 10° about the y-axis (tilt), and then around the z-axis by 25° (twist). For this simulation the grid configuration was the same as the $N = 64$ simulation in [113] (although of course with a full grid and no symmetries applied). For reference, this grid was characterised by $N = 64$, $l_1 = l_2 = 5$, $M_1/h_{\rm min} = 21.3$, $h_{\rm max} = 12M$, and the extent of the grid was $x_{i,\rm max} = 774M$; the resolution on the wave-extraction level was $h_{ex} = 1.5M$.

The second configuration in this study is a *precessing binary* with mass ratio $q = 3$, where the larger black hole has spin $\chi_2 = 0.75$. In the calculation of the initial parameters, the spin is directed perpendicular to the Newtonian orbital angular momentum, i.e., $\cos\kappa_2 = 0$, when the binary is at a separation of $D = 30M$. The configuration is evolved using the PN equations of motion until about $D = 10M$ and the linear momenta are read off from the PN evolution at a point where the point particles pass through the xy-plane. A low-resolution simulation is performed with these initial parameters, and then an additional iteration is performed to further reduce the eccentricity; more details of a refined version of this procedure can be found in [184]. This leads to the parameters given in Tab. 4.1. The number of grid point for this simulation is $N = 112$. The number of moving levels is $l_1 = 4$ around the large black hole, and $l_1 = 5$ around the small black hole. The number of fixed levels is $l_2 = 8$, but the fixed boxes are of varying sizes, with 448^3 points on the wave-extraction level and with $h_{ex} = 0.46M$. The resolution at the puncture is $M_1/h_{\rm min} = 35.7$ and the maximal resolution is $h_{\rm max} = 29.26M$ on the coarsest level that extends to $x_{i,\rm max} = 1653M$. This ensures that the outer boundary is causally disconnected from the source over the course of the simulation.

Some key physical properties of the simulations are given in the last three rows of Tab. 4.1: the estimate of the eccentricity of the binary, the time when the GW signal reaches its peak amplitude and the number of GW cycles up until that time (excluding the initial pulse of junk radiation).

	nonspinning	precessing
q	1	3
M_i	$\{0.488278, 0.488278\}$	$\{0.47790, 1.02343\}$
$\vec{S}_1$	$\{0, 0, 0\}$	$\{0, 0, 0\}$
$\vec{S}_2$	$\{0, 0, 0\}$	$\{-1.048, 1.197, 0.560\}$
$\vec{x}_1$	$\{0, 6, 0\}$	$\{0, 15.0478, 0\}$
$\vec{x}_2$	$\{0, -6, 0\}$	$\{0, -5.0159, 0\}$
D/M	12.00	10.03
p_x	∓ 0.085035	∓ 0.126292
p_y	± 0.000537	∓ 0.00139578
p_z	0	± 0.0696932
e	0.0016	0.0015
t_{peak}/M	1940	1271
N_{cycles}	19	14

Table 4.1: Parameters for the two configurations that we consider in this paper: the equal-mass nonspinning case and the $q = 3$ precessing-spin case. (For the rotated equal-mass nonspinning case, the momenta are $\vec{p}_i = \mp\{0.07567, 0.03588, 0.01477\}$.) The lower rows indicate some physical properties of the configuration: the initial eccentricity e, the time until the peak amplitude of the $(l = 2, m = 2)$-mode and the number of GW cycles up to that time.

4.3 Maximisation procedure algorithm

The Weyl scalar Ψ_4 as calculated from the numerical code is decomposed into standard spin-weighted spherical harmonics (see [55] for our implementation). We expect that if the orbital angular momentum $\vec{L}$ of the binary is parallel to the z-axis of the numerical simulation frame, then the GW signal will be dominated by the $(l = 2, |m| = 2)$-modes. We also expect that the coefficients of the $(l = 2, |m| = 2)$-modes will be maximal in this case; for any other orientation of the orbital angular momentum, the $(l = 2, |m| = 2)$-modes will be weaker and higher harmonics will be excited.

Given the $l = 2$ modes $\Psi'_{4,2m}$ from the numerical code, we can rotate the mode-decomposition frame (i.e., the numerical simulation frame) to any other orientation using the general transformation described in Appendix A, to produce the corresponding $\Psi_{4,2m}$ in the new frame of reference. We locate the direction of maximal emission by searching over a range of the Euler angles (β, γ) to find a global maximum in $\Psi_{4,22}$ at each time step. The two frames and the orientation of the maximal emission direction are schematically depicted in Fig. 4.1.

The procedure in practice is as follows: we start our analysis after the passage of the pulse of junk radiation. Since we extract the GW signal at either $R_{ex} = 90M$ or $R_{ex} = 94M$, we take the start time to be at about $t = 150M$ respectively $t = 200M$. We produce a first (Newtonian) guess of the direction of $\hat{L}$ from the locations and velocities of the black-hole punctures at that time. This provides a guess (β_0, γ_0) of the Euler angles by which to rotate the system. Given this initial guess, we then search over a range of $(\beta, \gamma) = (\beta_0 \pm 10°, \gamma_0 \pm 10°)$ with

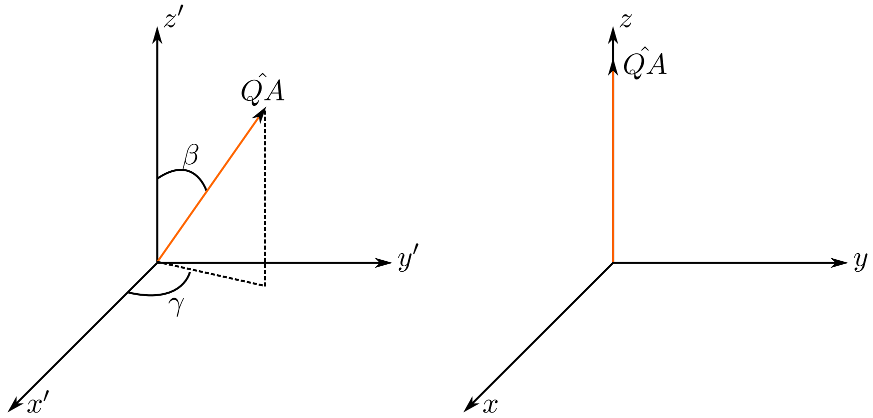

Figure 4.1: The left panel shows the simulation frame $\{x', y', z'\}$ of a generic binary at a time t_1. The maximal emission direction points along some arbitrary direction (β, γ) and is denoted by $\hat{\mathrm{Q}}\mathrm{A}$. The right panel illustrates the effect of quadrupole-alignment: the emission direction is identified and re-aligned with the z-axis of the mode-decomposition frame $\{x, y, z\}$.

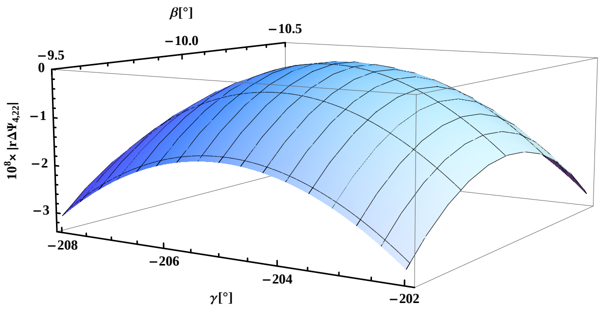

Figure 4.2: Profile of the magnitude of $\Psi_{4,22}$ as the system is rotated by the Euler angles β and γ, shown relative to the maximum value. The example is taken from one time step ($t = 562M$) of the rotated equal-mass nonspinning case discussed in Sec. 4.4.1. Note that the maximum is clearly defined, which in this case is at $(\beta, \gamma) = (-10°, -205°)$.

an angular resolution of $0.1°$ and find the angles for which the function $\sqrt{|\Psi_{4,22}|^2 + |\Psi_{4,2-2}|^2}$ has a maximum. In our test cases, where the orientation is constant, this procedure is trivial, but in general this first guess may not be very accurate. In particular, it does not take into account the time lag from the source to the GW extraction sphere. However, we do not expect the system to precess by as much as $10°$ over $\sim 100M$ of evolution. We also know that the Newtonian orbital angular momentum $\vec{L}_N$ calculated from the puncture motion is not in general parallel to the direction that maximises the $(l = 2, m = 2)$-mode, but we do not expect the deviation to be larger than a few degrees.

For subsequent times, we use the angles from the previous time step as the first guess and then search over the smaller range of $\pm 3°$ in each angle. We locate the maximum in $\sqrt{|\Psi_{4,22}|^2 + |\Psi_{4,2-2}|^2}$ with a quadratic curve fit through the data from the search.

At all times we find a clear maximum in the amplitude of $\Psi_{4,22}$ as a function of the rotation angles β and γ. An example is given in Fig. 4.2, based on one time step of the rotated equal-mass nonspinning case presented in Sec. 4.4.1.

4.4 Numerical results

4.4.1 Test case: equal-mass nonspinning binary

In order to test our maximisation procedure, we consider two simulations of an equal-mass nonspinning binary. In one, a *reference case*, the orbital angular momentum is oriented parallel to the z-axis of the source frame. Since the orientation of the orbital plane is time-independent in this case and since $\hat{L} = \hat{L}_N$ for vanishing spins, the waveforms are already decomposed in the quadrupole-aligned frame. The simulation starts at a separation $D = 12M$ and covers about nine orbits before merger.

For the second nonspinning simulation we change the orientation of the orbital plane. It is first rotated about the y-axis by $10°$ and then around the z-axis by $25°$. The motion of the punctures in both the reference (red) and rotated (blue) case is shown in Fig. 4.3. In the reference case (denoted by $\tilde{\Psi}_{4,lm}$), the $(l = 2, m = 1)$-mode is zero by symmetry and the $(l = 2, m = 0)$-mode is dominated by numerical noise. The dominating mode is the $(l = 2, m = 2)$-mode. This can be seen in the left panel of Fig. 4.4. In the rotated case, however, both originally sub-dominant modes have become significant. Note that oscillations are visible in the $(l = 2, m = 0)$-mode amplitude because it is a purely real function. In this case, the modes of $\Psi_{4,2m}$ are now mixed and the power in the $\Psi_{4,22}$ mode is distributed amongst the other $(l = 2)$-modes. Nevertheless, the modes show a hierarchical structure. This is illustrated in the right panel of Fig. 4.4.

We now want to see if our maximisation procedure, when applied to the waveforms from the rotated configuration, recovers the waveforms from the reference configuration. In our procedure we search for a rotation of the system by the Euler angles (β, γ) such that the coefficients of the $(l = 2, |m| = 2)$-modes are maximised. If the method works, we will recover the reverse angles $(-10°, -205°)$[2].

Fig. 4.5 shows the error in the determination of the Euler angles. The maximisation procedure was applied from $t = 150M$, after the burst of junk radiation has passed, through to $t = 2000M$, which is late in the ringdown phase. Up until about $t = 500M$ the waveform is rather noisy, and so the error in β can be as large as $1°$ and in γ the error is up to $4°$. During most of the inspiral, however, when the wave signal is clean, the error in β is below $0.05°$, and the error in γ is below $0.2°$ and even during the ringdown (when the waveform amplitude is falling exponentially), the angles are determined to within $\pm(0.5°, 2.0°)$.

Note that during the merger and ringdown we do not expect the method to necessarily work. The dominance of the $(l = 2, |m| = 2)$-modes, which we expect during inspiral, may not hold through merger. In addition, the signal during ringdown is no longer a superposition of spin-weighted spherical harmonics, but of spin-weighted *spheroidal* harmonics [211]. In this

[2] The Euler angle to reverse the twist is $-205°$ due to the freedom in performing the rotation about the z-axis clockwise or counterclockwise.

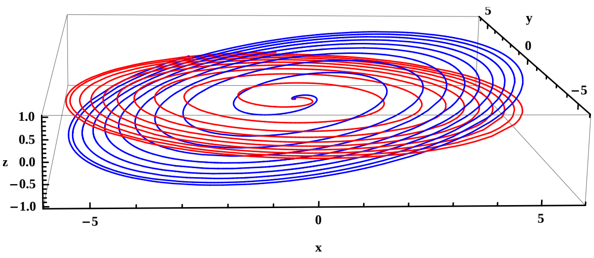

Figure 4.3: Motion of one black-hole puncture for the reference (red) and rotated (blue) equal-mass nonspinning cases. The orbital planes are related by a rotation about the y-axis of $10°$, and about the z-axis of $25°$.

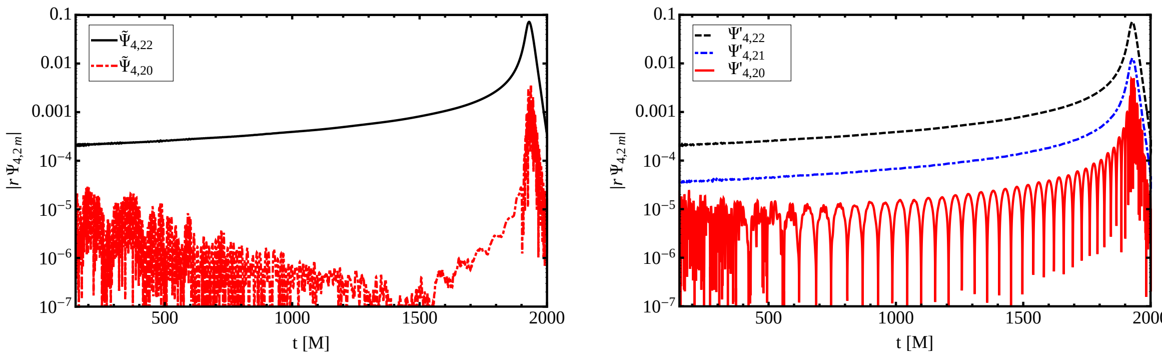

Figure 4.4: The left panel shows the amplitude of the $\tilde{\Psi}_{4,2m}$-modes for the reference case. The $(l = 2, m = 1)$-mode is zero by symmetry, and we see that the $(l = 2, m = 0)$-mode is much smaller than the dominant mode and is essentially noise during most of the inspiral. The right panel shows the corresponding amplitudes for the rotated case. We now see that both sub-dominant modes have become significant. The amplitude of the $(l = 2, m = 0)$-mode is oscillatory because it is a purely real function.

test case we also find that our method continues to work well through merger and ringdown.

The magnitudes of the $(l = 2)$-modes in the quadrupole-aligned frame agree well with those in the reference case. The $(l = 2, |m| = 2)$-modes agreed within numerical error in the raw data, and the $(l = 2, |m| = 1)$-modes, which should be zero by symmetry, were reduced by three orders of magnitude, to a level that would generally be regarded as noise. During the inspiral, for example, $|\Psi_{4,21}|$ was reduced from $\sim 10^{-4}$ to $\sim 10^{-7}$.

These results demonstrate that our method works and give us an indication of the error bounds. We expect that in general the errors will depend on the orientation angles of the binary and will be worse when the angles are small. In these cases the sub-dominant modes will be smallest and therefore will be resolved with less accuracy in the numerical code and will then contribute more noise to the waveform in the rotated frame. However, we will take the errors from this example as the basis for our error bounds in other applications of our method.

We also note that we could directly replace the set of Euler angles (β, γ) with the direction of the orbital angular momentum denoted by (ι, α) in PN theory, but since this not true in general, we will distinguish between the angles determined by the maximisation routine and the polar coordinates of $\hat{L}$ in PN.

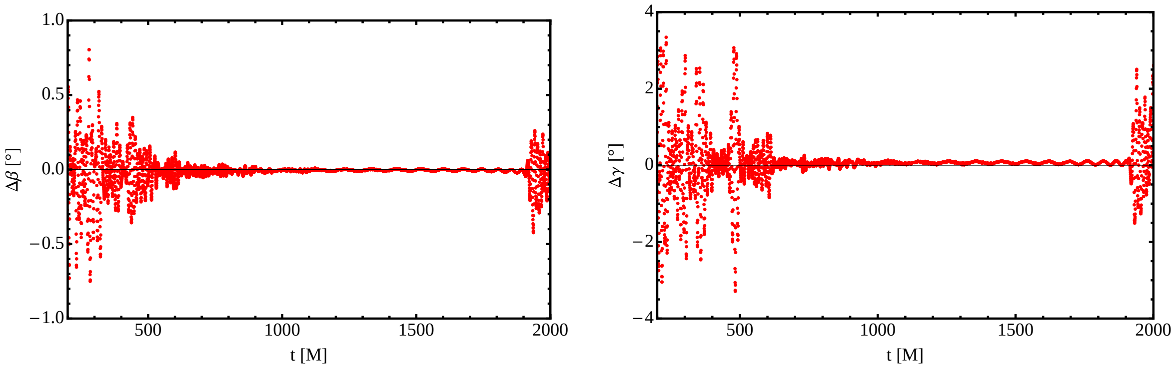

Figure 4.5: Error in the angles for the tilt (β) and twist (γ) of the orbital plane, as determined by the maximisation procedure.

4.4.2 Precessing binary

Having shown that the maximisation procedure works for the equal-mass nonspinning test case, where the orientation of the orbital plane is known and time-independent, we now apply the method to a generic precessing binary. The configuration we have chosen has a mass ratio of $q = 3$, the larger black hole has a spin of $\chi_2 = 0.75$ and the spin lies initially in the orbital plane, i.e., perpendicular to the Newtonian orbital angular momentum. The small black hole is not spinning, i.e. $\chi_1 = 0$.

By inspection of Eq.(3.16), we expect this configuration to exhibit significant precession. Alternatively, the 2PN-order equations of motion can also be derived from a generalised Lagrangian. The spin-orbit interaction can be characterised by the Hamiltonian [133] (see also, for example, Ref. [61])

$$H_{\rm SO}(t) = 2\frac{\vec{S}_{\rm eff}\cdot\vec{L}}{r^3}, \tag{4.2}$$

where r is the coordinate separation of the black holes and the effective spin $\vec{S}_{\rm eff}$ is defined as

$$\vec{S}_{\rm eff} = \left(1+\frac{3}{4}\frac{M_2}{M_1}\right)\vec{S}_1 + \left(1+\frac{3}{4}\frac{M_1}{M_2}\right)\vec{S}_2, \tag{4.3}$$

where in our case one of the spins would be zero. From the spin-orbit interaction one can derive a post-Newtonian evolution equation for the total black-hole spin [133],

$$\dot{\vec{S}} = -\frac{2}{r^3}\vec{S}_{\rm eff}\times\vec{L}. \tag{4.4}$$

This indicates that the maximum amount of spin precession will be achieved when the spin is perpendicular to the orbital angular momentum. If one of the black holes has a Kerr parameter S_i/M_i^2, then S will be largest if the larger black hole is spinning. This is also convenient from a numerical point of view, because the resolution requirements increase both as the mass is decreased, and spin is added; it is computationally cheaper to put the spin on

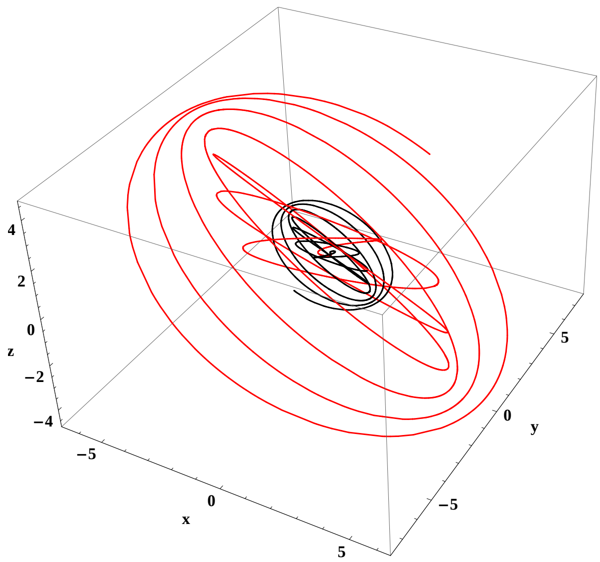

Figure 4.6: Motion of the black-hole punctures for the $q = 3$ precession simulation. The motion of the small black hole is shown in red, and the large black hole is shown in black. The precession of the orbital plane is clearly visible through the late inspiral until the merger.

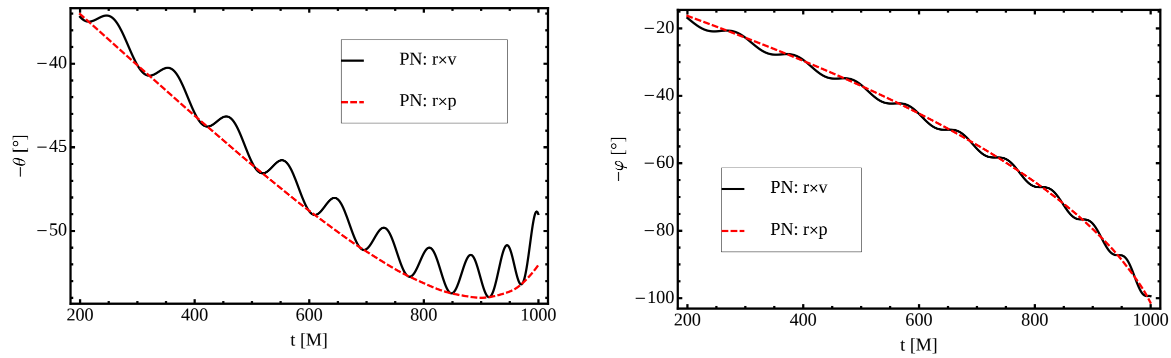

Figure 4.7: Comparison of the polar angles θ and φ for the unit directions of $\vec{r} \times \vec{v}$ (normal to the orbital plane) and $\vec{r} \times \vec{p}$ (orbital angular momentum) in a PN calculation. The comparison shows that the direction of $\vec{r} \times \vec{v}$ exhibits extra oscillations.

the larger black hole.

We also know from PN theory that $\dot{\vec{S}} = -\dot{\vec{L}}$ due to the conservation of the total angular momentum $\vec{J}$ in the absence of gravitational radiation. If we increase the mass ratio, then the orbital angular momentum L at a given separation will decrease, but the magnitude of the spin will stay the same. Therefore the relative change in $\vec{L}$ due to the precession of the spins will increase. This means that we will get greater spin precession for higher mass ratios. We have chosen $q = 3$ because this is reasonably large compared to typical simulations we have performed in the past, but low enough that we still expect to be able to achieve high accuracy.

Fig. 4.6 shows the orbital motion of the two punctures in the numerical simulation. The precession of the orbital plane is clearly visible in the figure.

Considering the leading order spin-orbit interaction Eq.(4.2) also exhibits another subtle feature of spinning binaries. The time evolution of the momentum vector $\vec{p}$ is given by the

Hamiltonian evolution equation

$$\frac{d\vec{p}}{dt} = -\frac{\partial H}{\partial \vec{r}}. \tag{4.5}$$

If the Hamiltonian H depends on the spins, then consequently the momentum also picks up a contribution from the spins and the relative velocity vector $\dot{\vec{r}}$ is in general *not* parallel to the momentum $\vec{p}$. Consequently, the directions of the orbital frequency vector $\vec{\omega}_{\rm orb}$,

$$\vec{\omega}_{\rm orb} = \frac{\vec{r}\times\vec{v}}{r^2} \tag{4.6}$$

is in general *not* aligned with the angular momentum $\vec{L} = \vec{r}\times\vec{p}$. For the spin-orbit interaction defined by the Hamiltonian in Eq.(4.2), this contribution to the angular momentum can be computed as [133]

$$\begin{aligned}\vec{L}_{\rm SO} = \frac{\mu}{M}\Bigg[&\frac{M}{r}\hat{n}\times\left(\hat{n}\times\left(3\vec{S}+\frac{\delta m}{M}\Delta\right)\right)\\ &-\frac{1}{2}\vec{v}\times\left(\vec{v}\times\left(\vec{S}+\frac{\delta m}{M}\Delta\right)\right)\Bigg],\end{aligned} \tag{4.7}$$

where

$$\Delta = M\left(\frac{\vec{S}_1}{M_2}-\frac{\vec{S}_2}{M_1}\right), \tag{4.8}$$

and $\vec{v} = \dot{\vec{r}}$ and $\vec{n}$ is the unit vector in the direction of $\vec{r}$. The total orbital angular momentum at next-to-next-to leading order is then $\vec{L} = \vec{L}_{\rm NS} + \vec{L}_{\rm SO}$, where $L_{\rm NS}$ is the nonspinning contribution to the angular momentum (which is parallel to the vector $\vec{r}\times\vec{v}$).

Note that the effect of the non-alignment of $\vec{\omega}_{\rm orb}$ and $\vec{L}$ is maximal when the total spin $\vec{S}$ is in the orbital plane. This is indeed the case for our initial conditions. We also find that during the numerical evolution the spin component out of the orbital plane is significantly smaller than the components in the orbital plane. Note also that since the spin typically varies on a timescale larger than the orbital time scale, Eq.(4.7) will lead to oscillations in the angle between $\vec{\omega}_{\rm orb}$ and $\vec{L}$ with roughly the orbital period.

Such oscillations are not present in the direction of $\hat{L}$, as illustrated in Fig. 4.7. We will see later that the quadrupole-aligned frame moves consistently with $\hat{L}$ (i.e., as a smooth function), suggesting that our maximisation procedure indeed tracks the direction of the orbital angular momentum.

The left panel of Fig. 4.8 shows the amplitude of the $(l=2, m=2)$- and $(l=2, m=1)$-modes during the late inspiral. We clearly see that the "sub-dominant" $(2,1)$-mode is of comparable magnitude to the $(2,2)$-mode and shows significant modulation. (It is also instructive to compare with the results in [72], where a precessing binary is also considered from a fixed frame of reference and all of the $(l=2)$-modes are of significant amplitude.) The

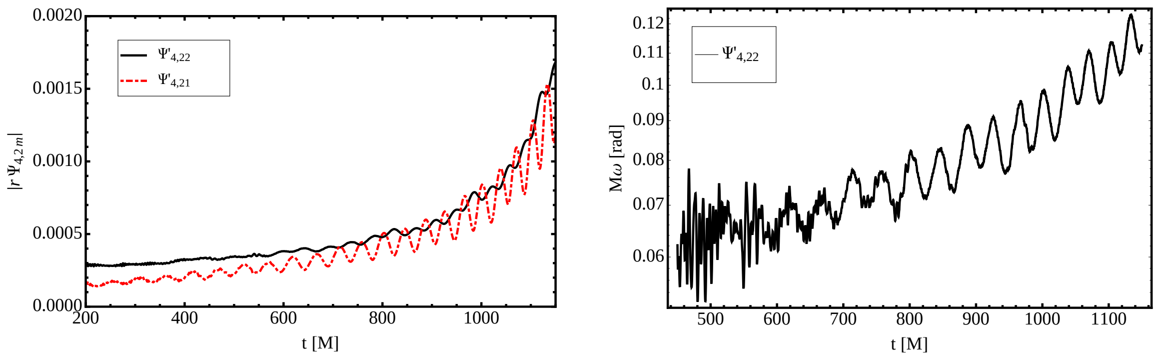

Figure 4.8: Amplitude of raw numerical data for inspiral (left), for the "dominant" mode $\Psi'_{4,22}$ and the "sub-dominant" mode $\Psi'_{4,21}$. The right panel shows the frequency of the $(l = 2, m = 2)$-mode, which exhibits significant oscillations. (The data are also noisy at early times, but this is typical for such data.)

right panel of Fig. 4.8 shows the frequency of the $(2, 2)$-mode, $\omega_{22} = \dot{\Phi}_{22}$, over the same time interval. The frequency clearly exhibits large oscillations. Based on the discussion around Eq.(4.1) we expect oscillations in ω_{22} of purely physical origin, but we also assume that the physical oscillations will be exaggerated and their frequency modified in the fixed frame of an inertial observer, e.g., the simulation frame.

We now apply the maximisation procedure to the waveform signal from $t = 200M$, when the junk radiation has passed, through merger and ringdown (up to $t = 1350M$). At each time step the system is rotated such that the $(l = 2, |m| = 2)$-mode amplitudes are maximised.

Having applied our maximisation procedure to track the precession, we first address the question of whether the GW signal is emitted normal to the orbital plane, or parallel to the orbital angular momentum. Although we cannot unambiguously define the direction of orbital angular momentum in General Relativity, we can certainly determine whether the GW signal is emitted normal to the orbital plane.

Fig. 4.9 shows the Euler angles $(\beta(t), \gamma(t))$ that were found in the maximisation procedure, time shifted by $103M$ to approximately compensate for the time lag to the GW extraction spheres. It also shows the angles $(\theta(t), \varphi(t))$ of the direction orthogonal to the orbital plane as computed from the NR simulation and for the orbital angular momentum $\vec{L}$ as computed from a PN simulation (as in Fig. 4.7). The PN angles are approximately aligned with (β, γ) at early times. If the GW signal were emitted normal to the orbital plane, we would expect to be able to align β with $-\theta$ from the numerical relativity simulation and likewise for γ and $-\varphi$. However, it is clear from Fig. 4.9 that the orbital-plane angles contain extra oscillations. Based on the illustration in Fig. 4.7, this suggests that the GW signal is emitted in the direction of the orbital angular momentum. In particular, we plot in Fig. 4.9 the direction of the orbital angular momentum as predicted in PN theory, which shows good agreement with the angles that define the quadrupole-aligned frame. We conclude that the maximisation tracks the true orbital angular momentum, which is roughly approximated by the Newtonian

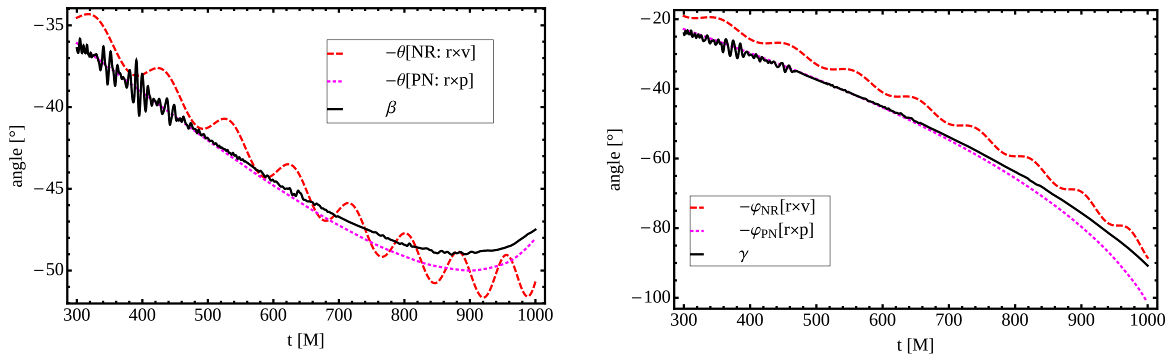

Figure 4.9: The Euler angles (β, γ) found when the maximisation procedure was applied to the $q = 3$ precessing-binary waveform. For comparison we show the corresponding angles $(-\theta, -\varphi)$ of the normal to the orbital plane as computed from the NR simulation and for the angular momentum $\vec{L}$ from a PN simulation (as in Fig. 4.7). We approximately align the PN angles with β and γ at early times. We clearly see that the orbital-plane angles show additional oscillations that are not present in the $(2, 2)$-maximisation angles.

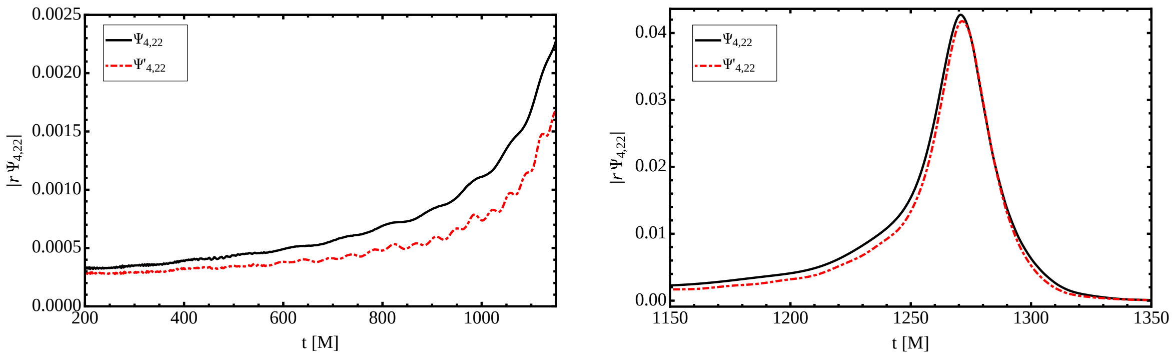

Figure 4.10: Amplitude of the $(l = 2, m = 2)$-mode, before $(\Psi'_{4,22})$ and after $(\Psi_{4,22})$ the maximisation procedure.

orbital angular momentum.

Fig. 4.10 shows the amplitude of the original $\Psi'_{4,22}$ and the quadrupole-aligned signal that results from the maximisation procedure, $\Psi_{4,22}$. We see that the maximisation procedure has indeed increased the amplitude of the dominant harmonics at all times. Additionally, it also seems to have removed some oscillations.

The frequency of the $(l = 2, m = 2)$-mode before and after the maximisation procedure is shown in Fig. 4.11. This figure illustrates one of the key results of this work: the high-frequency oscillations in the GW frequency have been removed by the maximisation procedure, leaving it in a far simpler functional form, almost as simple as for aligned-spin binaries. We note, however, that the oscillations in the frequency have not been completely removed. This is to be expected from Eq.(4.1). In the absence of precession, during the inspiral the gravitational wave frequency of a spherical harmonic mode (l, m) is with a high degree of accuracy proportional to the orbital frequency, $\omega_{lm} = m\omega_{\mathrm{orb}}$. In the presence of precession,

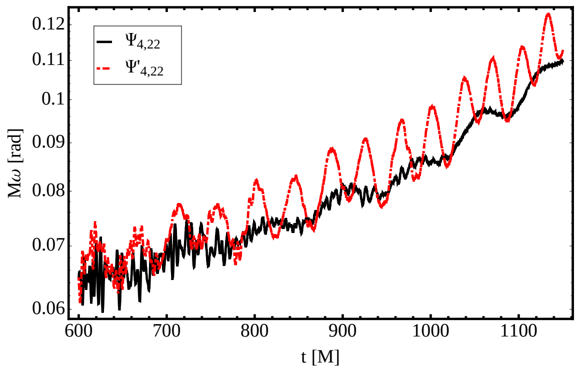

Figure 4.11: Frequency of the $(l = 2, m = 2)$-mode before $(\Psi'_{4,22})$ and after $(\Psi_{4,22})$ the maximisation procedure. We see that the high-frequency oscillations have been removed. The remaining oscillations are of a lower frequency and much lower amplitude; see text and Fig. 4.12.

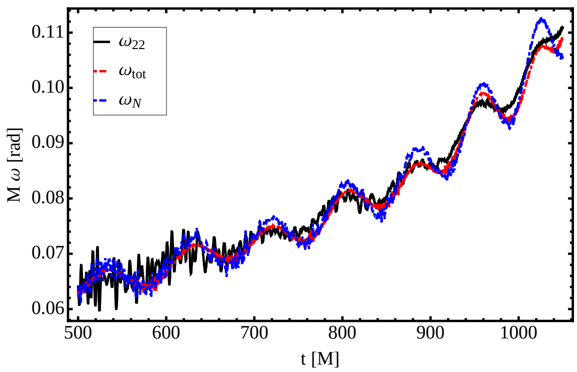

Figure 4.12: Frequency of the $(l = 2, m = 2)$-mode after the maximisation procedure compared with the "total frequency" ω_{tot}, which is the orbital frequency with a precession term added according to Eq.(4.1). We also show the frequency that results from rotating the system according to the direction of the Newtonian orbital angular momentum, ω_N, i.e., the normal to the orbital plane. The frequencies, in order of increasing magnitude of oscillation, are ω_{22}, $\omega_{\rm tot}$ and ω_N.

this is however replaced by Eq.(4.1), which adds an extra term depending on the precessing motion of the orbital plane. In Fig. 4.12 we compare the frequency of the $(l = 2, m = 2)$-mode after the maximisation procedure with the orbital frequency with the precession term added according to Eq.(4.1). We find reasonable agreement. We also show the frequency ω_N that results from rotating the system according to the direction perpendicular to the orbital plane, which is also the direction of the naive Newtonian orbital angular momentum. It is clear from Fig. 4.12 that the oscillations due to the orbital-plane rotations are much larger, and this further suggests that the quadrupole-aligned frame is optimal. We have also verified that the remaining oscillations are *not* due to residual eccentricity in the system, by repeating our analysis on a simulation with roughly twice the eccentricity as well as by studying PN examples.

It is clear that the maximisation procedure produces $(l = 2, |m| = 2)$-modes that are of a simpler form than in the original NR data. However, this is not a guarantee that we have correctly tracked the direction of the GW emission; we have not necessarily put the waveform into a physically meaningful frame of reference. One test of our method is to calculate the effect on the sub-dominant modes. We expect that in the quadrupole-aligned frame the amplitude of the GW signal will agree to a good approximation with that from a $q = 3$ nonspinning binary for the following reason: the spin effect on the rate of inspiral is dominated by $\vec{S} \cdot \vec{L}$, and this is close to zero throughout our simulation, so we expect the secular inspiral to be similar to that for a nonspinning binary with the same mass ratio.

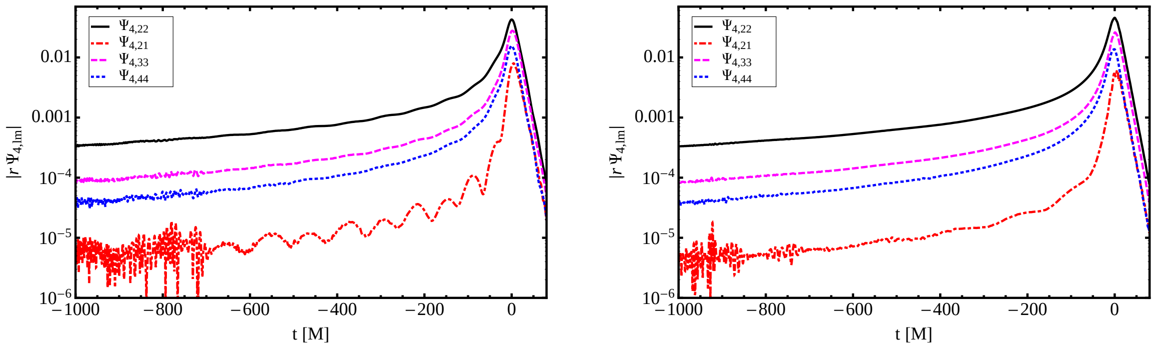

Figure 4.13: Left: selected modes of the precessing-binary waveform after being transformed into the co-precessing frame, i.e., after the system has been rotated by the angles that were found from the $(2,2)$-maximisation procedure. The right-hand plot shows the same modes for a nonspinning (and therefore non-precessing) $q = 3$ waveform. The agreement is remarkable. Note in particular the qualitative agreement of the $(l = 2, m = 1)$-mode, which is of comparable magnitude to the $(l = 2, m = 2)$ mode in the raw data (see Fig. 4.8).

Fig. 4.13 shows a selection of modes for the quadrupole-aligned waveform. The left panel shows the transformed modes for the precessing binary and the right frame shows the same modes for the nonspinning $q = 3$ waveform presented in [116]. Two things are remarkable about this figure. The first is that the amplitudes of the modes show extremely good agreement. The other is that we have found that the magnitude of the $(l = 2, m = 1)$-mode is extremely sensitive to the angle by which the system is rotated. If, for example, we were to modify β or γ by a fraction of a degree, $\Psi_{4,21}$ could change by orders of magnitude. With this fact borne in mind, the oscillations in $|\Psi_{4,21}|$ are not very large at all. This figure suggests that we have indeed located an optimal frame from which to study the GW signal of precessing binaries.

Finally, we will discuss the application of our procedure to the merger and ringdown. We can calculate the final black hole's spin magnitude and direction using information from the apparent horizon [70]. Ideally our method would locate the same spin direction. However, as pointed out in Sec. 4.4.1, the ringdown signal is a superposition of spheroidal (rather than spherical) harmonics [52, 211], and so we do not expect a maximisation of the $l = 2, |m| = 2$ coefficients of a spherical-harmonic decomposition of the waveform to necessarily produce accurate results. Moreover, the identification of the final spin direction is yet another example, which highlights the importance of geometrically meaningful frame choices. Originally, we believed that the maximisation method does not identify the correct final-spin direction. This is, however, not true: we expect the direction of the final spin to be close to the direction of J_0 in the case of simple precession. The quadrupole-alignment is performed with respect to the rather arbitrary simulation frame. If the analysis was performed in the J_0-aligned frame, though, the correct final spin direction would be identified, as the actual vector components are, of course, coordinate-dependent.

4.5 Discussion

In summary, we have presented a simple method to track the precession of the orbital plane of a binary system, using only information from the GW signal. Our procedure is to rotate the system such that the magnitudes of the $(l = 2, |m| = 2)$-modes are maximised, based on the physical assumption that this is the direction of dominant GW emission. This frame represents a frame which is to a first approximation co-precessing with the instantaneous orbital plane, i.e., $(\beta, \gamma) \approx (-\iota, -\alpha)$. We refer to the waveforms in this frame as "quadrupole-aligned" waveforms. Based on evidence from PN theory, we have shown evidence that this direction corresponds to that of the orbital angular momentum, which is in general *not* perpendicular to the orbital plane. Further, we have also seen that our method produces higher-mode amplitudes consistent with what we know from comparable aligned-spin binaries.

The result of our procedure is that the waveforms are represented in a more simple form than the ones produced directly from the numerical code. This is particularly true for the subdominant modes; compare Figs. 4.8 and 4.13. We will see in the subsequent chapters that this insight will significantly simplify the task of producing analytic inspiral-merger-ringdown models, which is the main motivation for this work. This method also provides a *normal form* for the waveforms, which is useful for comparisons between numerical and analytic results.

In our analysis, we have neglected an important subtlety: in general, any such co-rotating frame is defined by three Euler angles. We have only made use of the two geometrically obvious angles, the two polar coordinates which define the maximal emission direction on the unit sphere. However, it was subsequently pointed out by Boyle et al. [50] that the third Euler angle is rather important to completely fix the frame, leaving it invariant under BMS transformations (see Appendix A). This third angle corresponds to an additional rotation about the z-axis and is commonly referred to as *minimal rotation*. Therefore, the invariant co-precessing radiation frame is the quadrupole-aligned frame completed with the third Euler angle.

One could propose alternative procedures to track the orbital precession of the system and we will now discuss some of them as well as their difficulties.

In General Relativity, only the total angular momentum of the spacetime is unambiguously defined. The form of Bowen-York puncture initial data is such that we can analytically calculate the angular momentum ([55, 166, 229, 230]) of the initial slice from the initial-data parameters; it is simply given by $\vec{L} = \vec{x}_1 \times \vec{p}_1 + \vec{x}_2 \times \vec{p}_2$, where $\vec{x}_i$ are the coordinate locations of the punctures and $\vec{p}_i$ are the momenta that are input into the Bowen-York extrinsic curvature. We can calculate the angular momentum radiated through the spheres on which we measure the GW signal and can then determine the total angular momentum of the system as a function of time. However, we want the *orbital* angular momentum, $\vec{L} = \vec{J} - \vec{S}$. To calculate this we need to know the black-hole spins as a function of time (which can be estimated with reasonable accuracy from the black holes' apparent horizons [70]), but these quantities are calculated at the black holes, not at the GW extraction sphere and cannot easily be translated. Instead, one could attempt to calculate the orbital angular momentum entirely at the sources, but this also presents difficulties. The proper distance between the black-hole horizons and their momenta could be calculated by some quasi-local procedure (for example [136]) and hence the orbital angular momentum could be determined. But it will be difficult to assess the gauge errors in any such method. Alternatively, one could calculate the angular momentum using the puncture locations and PN theory, but this will only be an approximation to the true general relativistic angular momentum. One direction we can easily determine from the puncture motion is the normal to the orbital plane of the binary, but we have seen in Sec. 4.4 that this is not the direction in which the dominant GW signal is emitted, and nor does it define a reference frame from which the GW signal appears simpler than what can be achieved by the maximisation procedure that we have used.

One may also question whether this method will work beyond the single-spin precessing case that we have considered, which involved only one spinning black hole and the spin direction was explicitly chosen such that $\vec{S} \cdot \vec{L} = 0$. However, we have made additional studies with a number of other precessing-binary configurations, and find results consistent with those presented here. A PN study will be presented in the next chapter.

CHAPTER 5

Towards generic waveform models I

An approximate mapping between precessing and non-precessing waveforms

In the previous chapter we have introduced a co-precessing frame of reference, which allows us to put the rather complex gravitational waveforms emitted by precessing binaries in a very simple form. In this chapter, we will make use of this convenient waveform description, to analyse the secular component of the waveform and introduce an approximation that significantly simplifies the problem of modelling precessing waveforms. We show that generic precessing-binary inspiral waveforms can be mapped to a two-dimensional space of non-precessing binaries, characterised by the mass ratio and a single effective total spin. The mapping consists of a time-dependent rotation of the waveforms into the quadrupole-aligned frame (see Chapter 4) and is extremely accurate (matches > 0.99 with parameter biases in the total spin of $\Delta\chi \leq 0.04$), even in the exotic case of transitional precession. In addition, we demonstrate a simple method to construct hybrid post-Newtonian–Numerical-Relativity precessing-binary waveforms in the quadrupole-aligned frame and provide evidence that our approximate mapping can be used all the way to the merger. Finally, based on these results, we outline a general strategy for the construction of generic waveform models, which will be used in Chapter 7 to produce a precessing IMR waveform model. The analysis and results presented in this chapter have been previously published in:
[197] Schmidt et al., Towards models of gravitational waveforms from generic binaries: A simple approximate mapping between precessing and non-precessing inspiral signals. Phys.Rev., D86:104063, 2012.

5.1 Introduction

The detection and subsequent analysis of gravitational waves relies strongly on the accuracy and completeness of theoretical waveform models. For black-hole binaries, this includes the inspiral, merger and ringdown of the final black hole. Such waveform models combine information from analytic approximation methods and numerical-relativity (NR) simulations [165]. At the time this work was carried out, a number of theoretical inspiral-merger-ringdown (IMR) waveform models existed for non-spinning binaries and configurations where the spin angular momentum is either aligned or anti-aligned with the orbital angular momentum (a summary of these models is given in Ref. [165]). But most astrophysical binary systems are expected to have arbitrary spin configurations, which lead to complicated precession effects (see Chapter 3 for a detailed analysis of the phenomenology). Although there did exist one preliminary precessing-binary IMR model [209] at the time, the systematic modelling of generic binaries remained a serious challenge.

The complicated structure of precessing-binary waveforms suggests that in order to construct accurate IMR waveform models, we may need to produce numerical simulations that densely sample a seven-dimensional parameter space. At first glance, this does not seem feasible on the timescale of second-generation GW detectors (i.e., within the next ten years), although valiant efforts are underway [124, 155, 162].

In this chapter we introduce an approximation that has proven to dramatically simplify the modelling of precessing-binary waveforms. Motivated by the results presented in Chapter 4, we show that the seven-dimensional space of intrinsic physical parameters of generic precessing-binary waveforms can be mapped to a *two-dimensional* space of non-precessing waveforms, parametrised by the mass ratio q and one effective total spin parameter χ_{eff}. The mapping consists of transforming the precessing-binary waveforms into a "co-precessing" frame of reference, described by three Euler rotation angles $(\gamma(t), \beta(t), \epsilon(t))$, which is closely related to the "quadrupole-aligned" (QA) frame described in Chapter 4. In this geometric framework, the waveform modelling problem then factorises into two much smaller tasks:

1. the construction of a non-precessing waveform model (and candidates for such a model already exist [12, 173, 192]) and

2. the construction of a model for the rotation angle functions $(\gamma(t), \beta(t), \epsilon(t))$ with respect to the binary's seven physical parameters.

In this chapter we do not address the task of producing a model for the rotation angles as well as the behavior of the signal during the ringdown, which is subject to Chapter 6 and Chapter 7. Here, we restrict ourselves to the approximate mapping between precessing-binary and non-precessing-binary waveforms and test its validity on a series of inspiral waveforms generated by post-Newtonian (PN) theory.

Generic binary systems undergoing quasi-circular inspiral are characterised by a set of intrinsic physical parameters: the binary's total mass $M = m_1 + m_2$, the mass ratio $q = m_2/m_1$ (we adopt the convention that $m_1 < m_2$), and the six spin components $\vec{S}_1$ and $\vec{S}_2$. We note that the total mass of the system sets the overall scale in General Relativity and can therefore be factored out in for modelling purposes. The individual masses m_1 and m_2 are uniquely determined given M and q.

We have seen in the previous chapter that precessing-binary waveforms take a far simpler form when transformed into the quadrupole aligned (QA) frame [196]. In a nutshell, the QA frame approximately follows the instantaneous orbital plane of the binary. In this frame the binary is essentially viewed "face-on", .i.e., $\hat{L}||\hat{N}$, throughout the course of its evolution. Note that this frame corresponds to a co-rotating, accelerated frame of reference. In this "co-precessing" frame the amplitudes of the waveform modes as well as their frequency evolution are significantly simplified and most of the energy is emitted in the $(l = 2, |m| = 2)$-modes, just as in a non-precessing binary. In fact, in this accelerated frame the mode structure of a non-precessing binary appears to be restored (see Fig. 4.13). Based on this observation we postulate that QA- and non-precessing-binary waveforms may agree well in both amplitude *and* phase. Note that a related frame, defined by the direction of the Newtonian orbital angular momentum, was introduced in Ref. [59], along with the observation that the precession-induced phase oscillations can be removed in this "precessing frame". The key new result, beyond the use of the QA frame (which can be determined from the GW signal alone), is the simple identification between QA waveforms and non-precessing-binary waveforms utilising the co-precessing frame.

In the context of gravitational-wave searches and parameter estimation, waveforms from different binary configurations are most strongly characterised by their phase evolution, i.e., their rate of inspiral. When the black holes are widely separated their motion can be described well by PN methods as summarised in Sec. 2.5.1. In Chapter 3 we have seen that the leading-order influence of the spin on the inspiral rate and therefore the phase evolution is the spin-orbit coupling, which is due to a sum of the components of the black-hole spins parallel to the orbital angular momentum [133]. If the binary precesses, the precession introduces both secular and oscillatory changes in the phase, but in the QA frame, where the precession has been removed to some extent, we expect to recover the underlying orbital phase evolution, which will be similar to that of a non-precessing binary. Since the leading-order spin effects on the phase arise from the total black-hole spin, it is additionally possible to make an approximate parametrisation of non-precessing binaries by a single effective total spin parameter, χ_{eff}, and this idea has been used in both inspiral [9] and IMR [192] models. In this chapter we focus on inspiral PN models and so we will use the same effective spin parameter as in [9]; see Eq.(5.10). For complete IMR waveforms other parameterisations have been found to work better [12, 192], but here we restrict ourselves to PN inspiral waveforms.

The fundamental hypothesis investigated in this chapter is twofold:

1. precessing-binary waveforms can be approximately mapped to non-precessing-binary waveforms and

2. the equivalent non-precessing-binary signal is parameterised only by the mass ratio q and χ_{eff}.

It is the goal of the subsequent sections to quantify the accuracy of that approximation. Our approach is to consider a selection of PN inspiral precessing-binary waveforms and to match them against a family of non-precessing-binary signals to determine the best-match value of χ_{eff}. We can then see how well these values agree with our expectation and the level of agreement with the best-match waveform. We use PN waveforms because they allow us to study the long inspiral regime with many precession cycles and they are far more computationally convenient to produce than numerical simulations of only the last ~ 10 orbits before merger.

5.2 Precessing-binary inspiral waveforms

5.2.1 Post-Newtonian waveforms

In order to produce the precessing post-Newtonian inspiral waveforms used in this analysis, we evolved the full PN equations of motion formulated as the *Hamiltonian equations of motion* in the standard Taylor-expanded form [116, 127], which were integrated using a Mathematica package. More specifically, we use the non-spinning 3PN accurate Hamiltonian [82, 84, 128] (see also [37, 38, 89]) and the 3.5PN accurate radiation flux [35, 40, 41]. We add both leading-order [29–31, 77, 133, 179] and next-to-leading order [42, 86, 96] contributions to the spin-orbit and spin-spin Hamiltonians, and the spin-induced radiation flux terms as described in [61](see also [133, 179]). In addition we include the flux contribution due to the energy flowing into the black holes, which appears at the relative 2.5PN order, as derived in [16].

The precessing PN waveforms were then generated making use of the explicit formulae for the waveform modes h_{lm} as given by Eqn. (B1) and (B2) in [23]. The expression for the $(2,0)$-mode was provided by G. Faye and the $(2,-m)$-modes were constructed according to Eq. (4.15) in [23]. The positions, momenta and spins of the masses were read off the full PN solution and used to generate the parameters for the construction of the precessing waveform modes h_{2m}. The amplitudes contain only the leading-order spin contributions but higher-order corrections are contained in the dynamics, since the Hamiltonian is known to higher order (see above). Therefore, even if the h_{lm} expressions were evaluated only at quadrupole-order, the waveforms would still show many features of precession, since the dominant contribution to the waveforms is from the motion itself. We note that the dynamical calculations are performed in the ADMTT gauge, while the mode expressions are written in the harmonic gauge. This inconsistency will introduce errors into the waveforms, but we do not expect these to be larger than those due to the neglect of higher-order PN contributions.

We have chosen the source frame to be the J_0-aligned frame, where $\hat{J}_0 = (0, 0, 1)$ at the initial separation D_i. To achieve this, the PN initial data in the centre-of-mass frame $\{\vec{x}, \vec{p}, \vec{S}_1, \vec{S}_2\}$ were rotated by applying a standard rotation about the y- and z-axes in the Cartesian source frame. This is purely a convention as all of the physics is invariant with respect to rotations. The system was evolved for 15M to reduce eccentricity (as done previously in numerical applications [116, 127]), and then evolved from an initial separation of $D_i = 40$M down to a final separation of $D_\mathrm{f} = 6$M, which corresponds to the innermost stable circular orbit (ISCO) of a test particle around a Schwarzschild black hole.

The orbital frequency of the quasi-spherical motion is given by the general expression Eq.(4.6). The Newtonian orbital angular momentum in relative coordinates, where $\vec{r}$ is the separation vector, is given by

$$\vec{L}_N = \mu(\vec{r} \times \dot{\vec{r}}), \tag{5.1}$$

where μ denotes the reduced mass $\mu = (m_1 + m_2)/M$. The general PN orbital angular momentum vector $\vec{L}$ is given by

$$\vec{L} = \vec{r} \times \vec{p}. \tag{5.2}$$

Note that $\vec{L}_N$ and $\vec{L}$ differ significantly in the case of precession since $\dot{\vec{r}}$ and $\vec{p}$ are no longer strictly parallel to each other, as explained in [133] and in Chapter 4 unless the two masses m_1 and m_2 are far apart.

The Newtonian orbital angular momentum $\vec{L}_N$ is defined by the polar coordinates $(\iota(t), \alpha(t))$ as introduced in Chapter 3. We have already seen that the evolution of these two angles describes the dynamics of the instantaneous orbital plane. The total phase of the binary is then constructed from Eq.(3.21). Let us briefly recap the physical interpretation of the integral: the phase seen by an observer on the z-axis (which is the axis that defines our mode decomposition of the GW signal) is a combination of the actual motion of the orbital plane in the source frame and its projection onto the xy-plane.

The symmetric and anti-symmetric spin combinations as given in Eq.(3.3) are constructed directly from the data of the PN solution. Once all time-dependent dynamical parameters are constructed, the waveform modes, h_{lm}, are evaluated. We remind the reader that for a non-precessing binary this means that if the source frame was chosen such that $\hat{L}_N$ is parallel to $\hat{z}$, the quadrupole contributions are h_{22} and $h_{2,-2}$. For precessing binaries, $\hat{L}_N$ is not in general parallel to $\hat{z}$, and hence modes with $m \neq |2|$ appear *even at quadrupole order*. They only vanish when $\iota = 0$ and $\alpha = \pi$.

Schematically, the precessing h_{lm} modes can be written as a function with the following explicit dependencies:

$$h_{lm}(t) = f(M, D_L, q, \omega_{orb}, \iota, \alpha, \Phi, \vec{\chi}_s, \vec{\chi}_a). \tag{5.3}$$

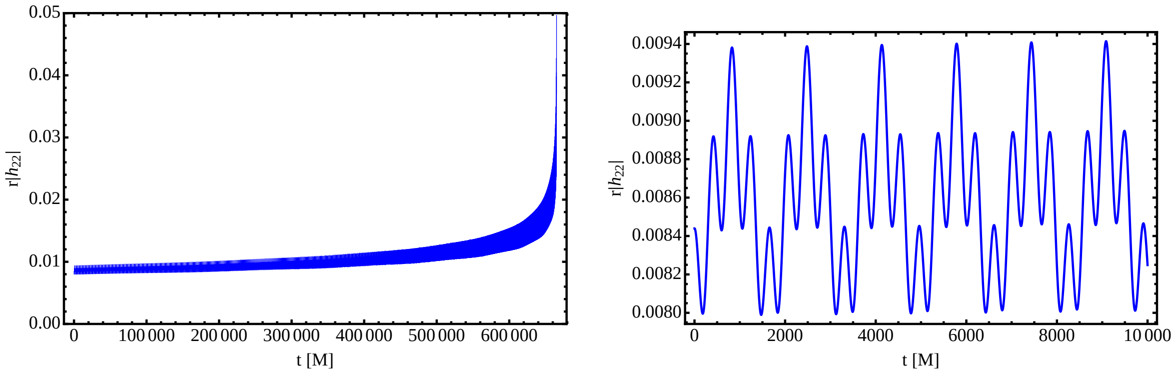

Figure 5.1: The top panel shows the magnitude of the $(2, 2)$-mode for a strongly precessing case over the whole length of the evolution, and over a length of the first $10000M$ in the lower panel. The source frame was chosen such that $\hat{J}_0 \simeq (0, 0, 1)$, and $\vec{L}$ and $\vec{\chi}_2$ are initially orthogonal to each other with $\|\vec{\chi}_2\| = 0.75$; the smaller black hole is not spinning. The close-up of the waveform magnitude over a shorter timescale reveals strong amplitude modulations.

The expressions are evaluated for a constant luminosity distance D_L, which is scaled out of our results. Fig. 5.1 shows the magnitude of the $(2, 2)$-mode for a precessing case with parameters $\{\vec{\chi}_1 = (0, 0, 0), \vec{\chi}_2 = (0.75, 0, 0), q = 10\}$. Despite this being a strongly precessing case $\left(\vec{S} \cdot \vec{L} = 0\right)$, long-timescale modulations are hardly noticeable. This is because a preferred frame was already chosen for the evolution, as described previously. Only an observer whose line-of-sight coincides with $\hat{J}_0$ will see a signal of this form. The appearance and strength of amplitude modulations strongly depends on the relative viewing angle as illustrated in Fig. 3.7.

5.2.2 Quadrupole-Alignment of PN waveforms

Let us briefly recapitulate the main idea behind quadrupole-alignment (see Chapter 4 for details). The idea is to track the direction of the dominant radiation emission. This means that, at *leading order*, it follows the precessing motion of the instantaneous orbital plane characterised by $\hat{L}_N$. This allows us to significantly simplify the gravitational-wave signature by artificially removing the precession of the instantaneous orbital plane and describing the signal in a co-precessing frame. Previously, we have seen that the quadrupole-aligned direction actually tracks the full PN angular momentum direction $\hat{L}$, which differs slightly from the normal to the orbital plane.

We have specified an explicit algorithm to determine the two time-dependent general Euler angles $(\beta(t), \gamma(t))$ that specify the direction which maximises the amplitude of the $(l = 2, |m| = 2)$-modes. A third angle, $\epsilon(t)$, which adjusts the phase, was ignored in the previous prescription, but its importance was pointed out in [50], particularly in whenever β is close to zero and γ changes rapidly.

The alignment itself is based on the general transformation behavior of spin-weighted spherical harmonics under coordinate transformations as given in Appendix A. This allows us to find the instantaneous, average direction of maximal emission by transforming the $(l = 2, |m| = 2)$-modes and averaging over the dominant harmonics. This direction is uniquely defined by two angles, β and γ, which are determined by the maximisation algorithm presented earlier:

$$(\beta_{\max}, \gamma_{\max}) = \max_{\beta,\gamma} \sqrt{\|\tilde{h}_{22}(\beta,\gamma)\|^2 + \|\tilde{h}_{2,-2}(\beta,\gamma)\|^2}, \tag{5.4}$$

where $\tilde{h}_{22}$ and $\tilde{h}_{2,-2}$ are explicitly given by

$$\tilde{h}_{22}(\beta,\gamma) = \sum_{m'=-2}^{2} e^{-im'\gamma(t)} d^2_{m'2}(-\beta(t)) h_{2m'}(t), \tag{5.5}$$

$$\tilde{h}_{2,-2}(\beta,\gamma) = \sum_{m'=-2}^{2} e^{-im'\gamma(t)} d^2_{m',-2}(-\beta(t)) h_{2m'}(t), \tag{5.6}$$

where $d^2_{m'm}$ denote the Wigner d-matrices [101, 225]. The maximisation determines the two Euler angles $\beta_{\max}$ and $\gamma_{\max}$. In general, the transformation of spin-weighted spherical harmonics involves three degrees of freedom and, as noted in [50], the third angle can be provided by the analog of Eq.(3.21), given the other two angles:

$$\epsilon(t) = -\int \dot{\gamma}_{\max}(t') \cdot \cos\beta_{\max}(t') dt'. \tag{5.7}$$

We may set $\epsilon(0) = 0$ without loss of generality.

Once all three time-dependent angles $(\beta_{\max}, \gamma_{\max}, \epsilon)$ have been determined, the dominant quadrupole-aligned mode can then explicitly be written as

$$h^{QA}_{22}(t) = e^{-2i\epsilon(t)} \sum_{m'=-2}^{2} e^{-im'\gamma_{\max}(t)} d^2_{m'2}(-\beta_{\max}(t)) h_{2m'}(t). \tag{5.8}$$

All other QA modes can be constructed as well, as long as the h_{lm}-modes for a given l are known. One may see that this transformation differs slightly from the one presented in Chapter 4. This is because the numerical-relativity waveforms presented there are related to the PN waveforms in this work by an overall complex conjugation.

The three angles $(\gamma, \beta, \epsilon)$ define a standard Euler rotation of the reference frame: a rotation by γ about the z-axis, followed by a rotation by β about the y-axis, followed by another rotation by ϵ about the (new) z-axis. This is important to bear in mind if we consider the reverse procedure to "wrap up" a QA waveform back into its original precessing-binary waveform. In that case, the inverse procedure consists of applying the rotations in the opposite

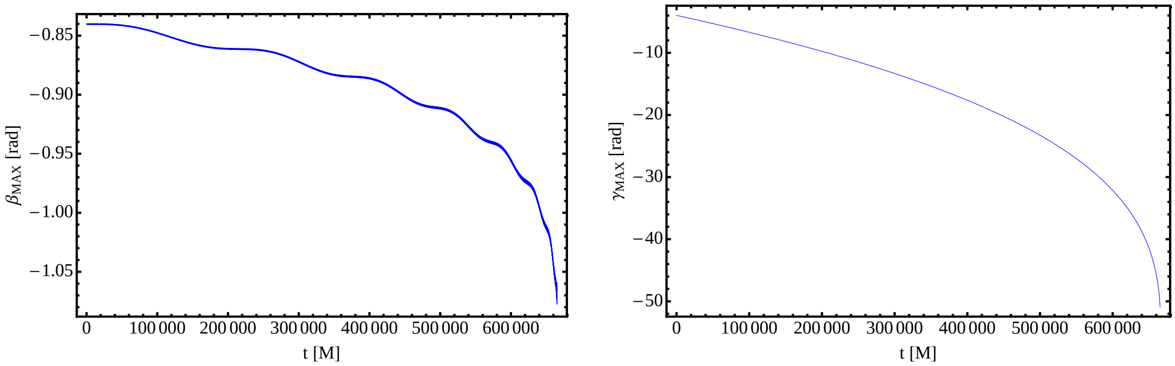

Figure 5.2: The two panels show the angles found in an example of the maximisation routine. The first panel shows the inclination angle $\beta_{\max}$ vs. time, the second panel shows the azimuth $\gamma_{\max}$ vs. time over the full length of the PN inspiral.

order, i.e., the same procedure but with

$$QA^{-1} : \{\gamma, \beta, \epsilon\} \to \{-\epsilon, -\beta, -\gamma\}. \tag{5.9}$$

Although we expect QA waveforms to be useful tools in standardising the representation of precessing waveforms for comparison purposes (as in, for example, Ref. [118] for equal-mass nonspinning waveforms) and in waveform modelling, we emphasise that they do not correspond to a signal seen by a gravitational-wave detector. The QA waveforms are the waves as seen in a very specific accelerated "co-precessing" frame. One of the consequences of this frame choice is that the usual relationship $\Psi_4 = -\ddot{h}$ no longer holds, as can be seen by inspection of Eq.(5.8). Hence, in order to obtain quadrupole-aligned Weyl scalar modes, one has to construct the precessing modes first and then transform them into the quadrupole-aligned counterparts. Note also that the QA angles will differ slightly when calculated from either h or Ψ_4 (this point is also made in [163]; the Ψ_4 angles tend to be smoother than the h angles).

To leading PN order, the recovered angles naturally correspond to the inverse Newtonian angles $(\iota(t), \alpha(t))$, but higher order contributions in the wave amplitudes lead to a deviation from those angles, which is consistent with the results from the pure numerical analysis presented in the previous chapter. Therein we have seen that the identified angles correspond to the smooth evolution of $\hat{L}$ in the limit of a complete description. The angles found by the maximisation routine when applied to precessing PN waveforms are shown in Fig. 5.2. They deviate slightly from the inverse Newtonian ones $(-\iota, -\alpha)$ due to higher-order PN contributions to the mode amplitudes but this difference is not visible over the scale of the plots. If we were to use only the quadrupole contribution of the h_{lm} expressions, then we would indeed recover the direction of $\hat{L}_N$ as given by $\iota(t)$ and $\alpha(t)$.

Once the three Euler angles are determined, those are then used to reconstruct the QA

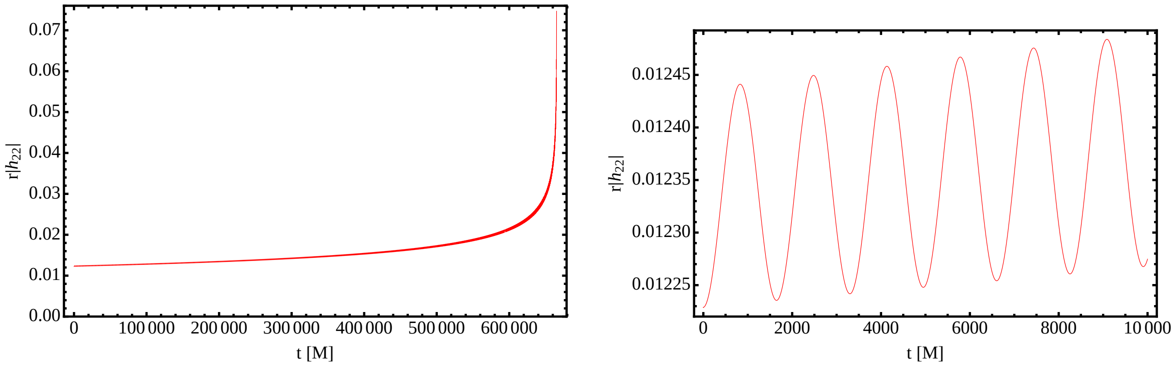

Figure 5.3: QA magnitude for the $q = 10$ configuration considered in Fig. 5.1. The left panel shows the complete waveform, while the right panel zooms in on the first $10000\,M$. We see that the oscillations in the amplitude have been reduced and simplified from those in Fig. 5.1.

modes. Fig. 5.3 shows the quadrupole-aligned $(2, 2)$-mode for the configuration shown in Fig. 5.1.

In the next section we will present a detailed study of how these simplified QA waveforms compare against corresponding non-precessing cases.

5.3 Results

The aim of this section is to test and quantify the accuracy of our hypothesis that generic inspiral signals can be mapped onto non-precessing counterparts (see Sec. 5.1). Numerical-Relativity waveforms are too short for a real inspiral comparison and, moreover, it is computationally very expensive to produce a large number of accurate numerical precessing waveforms. Instead, we have restricted this analysis to PN waveforms to allow a more detailed study for a larger subset of the precessing parameter space.

First, we will take a look at simple precession (see Sec. 3.2.1 for more details about simple precession) and consider a range of spin configurations for two mass ratios. The first is mass ratio $q = 3$ and includes the configuration of the numerical precessing case that we studied in Chapter 4. The second is mass ratio $q = 10$, motivated by the observation that precession effects become more significant for higher mass ratios; see, for example, Eq.(2.11) in [133], and the results presented in [9]. We will show that the mapping works extremely well; the non-precessing waveforms that agree best with each QA-transformed precessing configuration follow closely the $\chi_{\rm eff}$-parameter that we discussed in Sec. 5.1 and Sec. 3.1 (and will elucidate further below). Finally, as the most challenging test of our hypothesis, we look at a case of transitional precession.

This study covers only a small range of the full precessing-binary parameter space, but the configurations were carefully chosen to test the hypothesis for varying spin magnitudes and for two mass ratios within the range that is likely to be treated in IMR models in the near future, i.e., cases which can also be realised in current numerical simulations to high accuracy.

From the PN expressions for the phase evolution of the binary [133], we see that the dominant spin contribution is proportional to the projection of each spin vector onto the orbital angular momentum, $(\vec{S}_i \cdot \hat{L})$. We characterise the degree of spin-orbit-alignment with κ_i as given in Eq.(3.14). When the spin interaction is restricted to the leading order spin-orbit coupling and radiation reaction is switched off, each κ_i is conserved and is a constant of the motion [133]. When radiation reaction is included and, to a lesser degree, when higher order spin interactions are included, κ_i has been observed to show only small variation in time.

The agreement or disagreement between two waveforms is mainly due to their phasing. If the inspiral rate is significantly different, two waveforms are not expected to agree very well. For the QA waveforms, the precession of the orbital plane has been factored out, but the physical spins are, of course, present and contribute to the phase evolution. Thus, in general, we expect the best comparison waveform to be in general from an aligned-spin black-hole binary. At leading PN spin-order, where only the leading order spin-orbit terms contribute, each spin contribution is proportional to $\cos\kappa_i$, and thus by looking at the leading-order terms, we expect that all waveforms with $\cos\kappa_i = 0$ (aligned spins) map onto nonspinning counterparts, while all waveforms with $\cos\kappa_i \neq 0$ map onto aligned-spin waveforms, which can be parameterised by an effective total-spin parameter. This 2-part leading-order spin term can be represented by a *single* reduced spin parameter [9]:

$$\chi_{\text{eff}} = \chi_{sz} + \frac{(m_1 - m_2)}{m}\chi_{az} - \frac{76\eta}{113}\chi_{sz}, \tag{5.10}$$

where we have assumed $\hat{L} \equiv \hat{z}$; η denotes the symmetric mass ratio. Note that this parameter is not the same effective spin parameter as introduced in Ref. [77]. In this work the effective total spin used *is* indeed the reduced spin parameter as defined by Eq.(5.10) due to its PN nature.

In our study the non-precessing-binary comparison modes were parameterised by $\vec{\chi}_1 = \vec{\chi}_2 = (0, 0, \chi)$. For each of these cases we have $\chi_{\text{eff}} = \chi(1 - 76\eta/113)$.

The first set of configurations was chosen such that $\kappa_i = 0$ for the spinning hole, yielding an effective spin of zero. The second set was chosen such that all configurations have the same theoretical effective spin of $\chi_{\text{eff}} = 0.5$, but with varying $\kappa_1 = \kappa_2$. The details are listed in Tab. 5.1 and Tab. 5.2. The PN comparison family with (anti-)aligned spins was generated by the same method as the precessing ones, solving the full PN equations of motion and using the same h_{lm} expressions [23], where $\alpha = \pi$ and $\iota = 0$. This ensures that the results are not contaminated by differences due to the choice of the PN approximant.

The agreement between two waveforms can be quantified by a single number, the *match* $\mathscr{M}$, which corresponds to a noise-weighted inner product (overlap) between them [76] (see

Sec. 2.4.2 for details). Since QA waveforms are not in an inertial (detector) frame and we are interested in quantifying the difference between two waveforms independently of a detector, we primarily use the white-noise spectrum $S_n(f) = 1$. Match calculations are performed in the frequency domain and hence the Fourier transforms (FFTs) of the time-domain waveform modes are computed first. In our examples the PN waveforms are defined in the frequency range Mf $\in [0.0018, 0.01]$. The upper frequency corresponds to $M\omega \approx 0.06$, which is typical of the frequency at which we would start using NR results in full IMR hybrids; in this study we are not interested in the performance of the PN waveforms beyond that frequency. Since the matches are calculated with a flat noise spectrum, they are independent of the binary's mass.

Although the QA waveforms are not in a detector's frame of reference, it is also instructive to calculate matches with respect to realistic detector noise curves. In this case different choices of binary mass correspond to giving extra weight to different frequency ranges in the waveforms and provide a more stringent test on the robustness of our results. We repeated the match calculation for every configuration with the early Advanced LIGO [203] and the zero-detuned high-power [212] noise curves. The matches were calculated for masses between $20\,M_\odot$ and $50\,M_\odot$ in the frequency range between 20 Hz and 8 kHz.

The idea of the comparison is to find the non-precessing waveform as a function of χ that gives the best match with each QA waveform of our study. If the second part of our hypothesis holds, then the best-match spin, $\chi_{\rm BM}$, will be close to the effective spin $\chi_{\rm eff}$.

5.3.1 Simple precession

The first two sets of PN configurations are cases of simple precession. For most arbitrary binary configurations, simple precession will occur and only a small set of configurations will undergo "transitional precession", as it requires fine-tuned physical parameters (see [20] and Sec. 5.3.2 below). In the case of simple precession, the total spin angular momentum $\vec{S}$ precesses around the orbital angular momentum vector $\vec{L}$ and both of these vectors precess around the centre of the rather small precession cone described by $\hat{J}_0$ as illustrated in the left panel of Fig. 3.4.

Each precessing time-domain waveform was generated in the $\hat{J}_0$-aligned source frame. The quadrupole-alignment algorithm was then applied to determine the time series of the two Euler rotation angles $(\beta_{\rm max}(t), \gamma_{\rm max}(t))$. Given those, the third angle, $\epsilon(t)$, was determined and Eq.(5.7) applied to reconstruct the time-domain quadrupole-aligned $(2, 2)$-mode. [1]

The first set of configurations tests the mapping hypothesis for a vanishing proposed theoretical effective spin $\chi_{\rm eff} = 0$, for various spin configurations for the two mass ratios $q = 3$ and $q = 10$. The results in Tab. 5.1 suggest that the hypothesis works very well for single-spin

[1] Higher modes can be reconstructed as well but here we consider only the dominant harmonic in the match calculations.

systems with only the smaller black hole spinning. In these cases, we obtain best matches $\geqslant 0.99$ for the theoretical χ_{eff}-value for both mass ratios. In the reversed cases, i.e., now the larger black hole is spinning, the maximal matches are still $\geqslant 0.99$ but we see a small parameter bias of $\Delta\chi = 0.02$. If both black holes are spinning with the same spin magnitude and the spins initially parallel to each other ($\kappa_1 = \kappa_2$), the parameter bias increases slightly to $\Delta\chi = 0.03$. Note that in all of these cases the match has a sharp peak at its maximum, but the match at the theoretical χ_{eff} value is well above 0.97 in many cases.

The results do not change appreciably when the calculations are repeated with the Advanced LIGO noise curves. The matches improve slightly as the mass is increased, but so does the bias in χ_{eff}. However, the bias never increases by more than $\Delta\chi = 0.01$. The results for the $20M_\odot$ bin are displayed in the last two columns of Tab. 5.1 and 5.2. We would like to emphasise again that QA waveforms are *not* in a detector frame: the matches using the detector noise curves are only to rule out the possibility of spurious results with the white-noise curve.

The second set was chosen such that all configurations have the same theoretical χ_{eff}-value, but that the amount of precession changes due to a varying $\kappa_1 = \kappa_2 \equiv \kappa$ angle. All configurations in this set are equal-spinning, i.e., the spins are initially equal in magnitude and parallel to each other. The results are given in Tab. 5.2. We see for both mass ratios $q = 3$ and $q = 10$ that the best-match χ agrees with χ_{eff} for small κ. A bias appears as κ increases beyond $30°$, but is again never more than $\Delta\chi = 0.02$.

It is important to note that the parameter that describes the rate of inspiral, i.e., the phasing of the binary, is given by Eq.(5.10) and that the geometric quantity that defines the amount of precession is quantitatively described by the spin components perpendicular to $\vec{L}$, $\chi_{1||}$ and $\chi_{2||}$, which are proportional to $\sin\kappa_i$ (see Sec. 3.1 for more details). We have looked at various other cases with varying relative azimuth angle between the spin vectors as well as varying relative inclination between $\vec{S}_1$ and $\vec{S}_2$, i.e. $\kappa_1 \neq \kappa_2$. For equal spin magnitudes we find that the azimuth has no effect on the best-match χ_{eff}. For unequal κ_i but equal spin magnitude we find that the best-match bias increases with increasing κ_i but that the relative inclination angle between the two spin vectors does not have a significant influence on the results.

The approximation that χ_{eff} is constant becomes less accurate as the binary approaches merger. Remarkably, the effective spin value associated with the initial χ_{eff} value seems to characterise the best-match non-precessing-binary system in all cases. Even when using detector noise curves and choosing masses such that the late inspiral (when χ_{eff} changes fastest) is in the most sensitive part of the detector band, the best-match χ_{eff} varies by only $\Delta\chi \leq 0.04$ from the value predicted by our hypothesis. However, it is likely that when we move to full IMR configurations, some other appropriate effective total spin will be more appropriate, as was found for the full IMR waveforms in [12].

q	$\vec{\chi}_1$	$\vec{\chi}_2$	$\chi_{\rm BM}$	$\mathscr{M}_0$	$(\chi_{\rm BM})_{early}$	$(\chi_{\rm BM})_{zdethp}$
3	$(0,0,0)$	$(0.75,0,0)$	0.02	0.9815	0.02	0.02
3	$(0.75,0,0)$	$(0,0,0)$	0.00	0.9997	0.00	0.00
3	$(0.75,0,0)$	$(0.75,0,0)$	0.03	0.9576	0.04	0.03
10	$(0,0,0)$	$(0.75,0,0)$	0.03	0.8209	0.03	0.03
10	$(0.75,0,0)$	$(0,0,0)$	0.00	0.9999	0.00	0.00
10	$(0.75,0,0)$	$(0.75,0,0)$	0.03	0.8075	0.03	0.03

Table 5.1: PN configurations with constant $\kappa_i = 90°$ for the spinning hole and varying spins. The best matches, not necessarily for the predicted $\chi_{\rm eff} = 0$ but for the values displayed in column 4, are all well above 0.999 for $q = 3$ and above 0.995 for $q = 10$. $\mathscr{M}_0$ denotes the match with the counterpart waveform that has $\chi_{\rm eff} = 0$. The last two columns show the best match for two potential Advanced LIGO noise curves, evaluated for a $20M_\odot$ binary. For all cases the best match is above 0.999 for both detector noise curves.

When interpreting these results, one should bear in mind that the phasing of a PN waveform can change significantly with respect to the choice of PN approximant. The matches that we calculated between QA and non-precessing waveforms are in general far better than those between, for example, the same non-precessing configuration produced with TaylorT1 and TaylorT4; see Fig. 6 in [13]. In this sense, our approximation can be considered to hold, well within the level of accuracy of our PN waveforms.

We also emphasise once again that the QA waveforms do not correspond to the waveforms as seen by a detector, since the QA frame is accelerating, and would not be directly employed in a GW search; the matches as shown therefore do not constitute a study of the efficacy of these waveforms for either searches or parameter estimation. What they do tell us, however, is the following:

> If we were to take the non-precessing waveforms used in this study and to apply the reverse QA procedure to them, i.e., "wrap them up" into mock precessing waveforms using the inverse QA angles calculated for each of these configurations, then we expect them to agree well with the original precessing-binary waveforms.

Schematically, the above proposition can be expressed in the following way:

$$h^{\rm Prec}(t;\eta,\vec{\chi}_1,\vec{\chi}_2) \approx \mathbf{R}(-\epsilon,-\beta,-\gamma)h^{\rm Spin}(t;\eta,\chi_{\rm eff}). \tag{5.11}$$

Alternatively, if one does not want to combine the two parallel spin components into the effective total spin, these can be used instead:

$$h^{\rm Prec}(t;\eta,\vec{\chi}_1,\vec{\chi}_2) \approx \mathbf{R}(-\epsilon,-\beta,-\gamma)h^{\rm Spin}(t;\eta,\chi_{1||},\chi_{2||}). \tag{5.12}$$

Further, this study also suggests that if we were to construct a waveform model from "wrapped

q	$\vec{\chi}_1 = \vec{\chi}_2$	$\kappa_1 = \kappa_2$	$\chi_{\rm BM}$	$\mathscr{M}_{0.5}$	$(\chi_{\rm BM})_{early}$	$(\chi_{\rm BM})_{zdethp}$
3	$(0.050, 0, 0.572)$	5°	0.50	0.9998	0.50	0.50
3	$(0.101, 0, 0.572)$	10°	0.50	0.9998	0.50	0.50
3	$(0.208, 0, 0.572)$	20°	0.50	0.9992	0.51	0.50
3	$(0.330, 0, 0.572)$	30°	0.51	0.9975	0.51	0.51
3	$(0.480, 0, 0.572)$	40°	0.52	0.9917	0.52	0.52
3	$(0.682, 0, 0.572)$	50°	0.52	0.9719	0.52	0.52
10	$(0.093, 0, 0.529)$	10°	0.50	0.9986	0.50	0.50
10	$(0.193, 0, 0.529)$	20°	0.50	0.9996	0.50	0.50
10	$(0.306, 0, 0.529)$	30°	0.50	0.9965	0.51	0.50
10	$(0.444, 0, 0.529)$	40°	0.51	0.9771	0.51	0.51
10	$(0.631, 0, 0.529)$	50°	0.52	0.8925	0.53	0.52

Table 5.2: PN configurations with the same effective spin value $\chi_{\rm eff} = 0.5$ but varying $\kappa_1 = \kappa_2$ for the two mass ratios $1:3$ and $1:10$. $\chi_{\rm BM}$ denotes the effective $\chi_{\rm eff}$-value yielding the best match. In all cases the best matches are above 0.999 for $q = 3$ and above 0.997 for $q = 10$. $\mathscr{M}_{0.5}$ denotes the match with the counterpart waveform that has $\chi_{\rm eff} = 0.5$. Column 5 lists the match for the predicted $\chi_{\rm eff}$-value. The last two columns show the best match for two potential Advanced LIGO noise curves, evaluated for a $20M_\odot$ binary.

up" non-precessing waveforms, then it is possible that this model could be used to measure the effective total spin $\chi_{\rm eff}$ with only a small bias. However, the true behavior of such a model in a parameter estimation exercise requires an exhaustive study that is beyond the scope of this thesis.

To back up this claim, we performed the following exercise: from the first case in Tab. 5.1 we took the corresponding $\chi_{\rm eff}$-waveform, which is a nonspinning $q = 3$ waveform, and wrapped it up with the inverse QA angles that we calculated for the $\{q = 3, \chi_1 = 0, \chi_{2x} = 0.75\}$ configuration. The resulting waveform is shown in Fig. 5.4; we have plotted the amplitude of the GW strain, constructed from all $(l = 2)$-modes, at an arbitrarily chosen inclination of $\theta = 2.8$rad from the initial direction of the total angular momentum. Also shown is the same quantity for the "true" precessing-binary waveform and for comparison we also show the original non-precessing-binary waveform, constructed from only the $(l = 2, |m| = 2)$-modes. We see that the twisted-up non-precessing-binary waveform (red) captures the main features of the amplitude of the true precessing-binary waveform (black) extremely well; how well the phases agree can be judged by calculating the match between the two waveforms. This we did, once again over the frequency range of Mf $\in [0.0018, 0.01]$. Note that now we *are* considering waveforms as they would be observed in a detector.

We find that the match between the true precessing-binary waveform and the mock-precession waveform have a match greater than 0.97 for all masses and binary orientations. By contrast, the match between the unmodified non-precessing $q = 3$ waveform and the true precessing waveform is below 0.97 even for the best-performing orientation. These results provide an important cross-check that we can indeed mimic the original PN precessing-binary

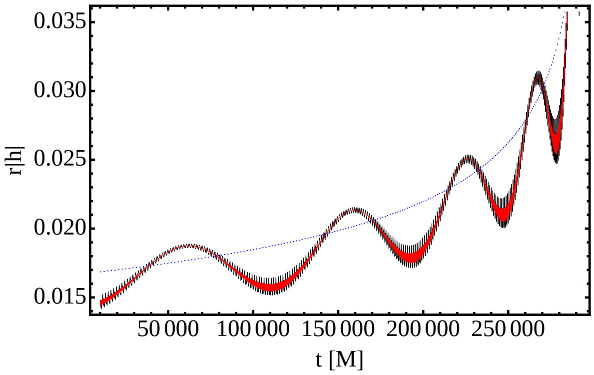

Figure 5.4: The absolute value of the GW strain for a precessing binary, as viewed at an arbitrary inclination of 2.8 rad from $\hat{J}_0$. The signal includes all ($l = 2$)-modes. The true precessing signal (black) has the finer structure; the other signal with the lower-amplitude high-frequency oscillations (red) was generated by twisting a non-spinning $q = 3$ waveform with the inverse QA angles. The dotted line (blue) shows the amplitude of the original nonspinning waveform.

signal by suitably transforming the signal from a non-precessing binary.

As an aside, note that there is one mode of the precessing-binary signal that we cannot fully model in this way, the $(l = 2, m = 0)$-mode. In the non-precessing waveforms, the $(2, 2)$- and $(2, -2)$-modes are complex conjugates of each other. When this is true, the transformed $(2, 0)$-mode will always be real. This can be seen from inspection of Eq.(5.8). But in the true precessing-binary waveform the $(2, 0)$-mode has real and imaginary parts; it is straightforward to produce an example to illustrate this from Sec. IV of Ref. [23]. In order to capture these effects, we would need to break the symmetry between the non-precessing h_{lm}-modes, which would require that the corresponding aligned-spin includes unequal spins — this is therefore one limitation of a single-effective-spin model. In practice, however, the relative signal power in the *imaginary part* of the $(2, 0)$-mode (that part that our model cannot reproduce) will always be small, and we expect the other errors in this approximate waveform, for example in the phasing, will be more significant.

5.3.2 Transitional precession

In the previous section we have seen that our mapping works extremely well in cases of simple precession; in fact it can be considered to be an exact mapping within the error bars of the PN phasing. In this section, we demonstrate that it also works in the more extreme case of transitional precession [20]. This second type of precession occurs when $\vec{L}$ and $\vec{S}$ are almost opposite and equal in magnitude and so J is small. During the inspiral, the magnitude of $\vec{S}$ hardly changes but since orbital angular momentum is radiated away, the magnitude of $\vec{L}$ decreases with time. With the appropriate choice of parameters, the total angular momentum $\vec{J}$ is initially small and positive, but due to the loss of orbital angular momentum, decreases until it crosses the xy-plane of the Cartesian source frame, where it changes sign. See [20] for an extensive discussion of transitional precession.

As opposed to simple precession, where $\hat{J}_0$ represents the least evolving axis in the binary's geometry, this direction changes significantly during the transitional phase, as illustrated in the right panel of Fig. 3.4. In order to test the validity of our precessing $\mapsto$ non-precessing

Figure 5.5: The panel shows the magnitudes of the (2, 2)-modes for the transitional precession case before (red; lower curve) and after (blue; upper curve) the quadrupole alignment was applied. The change of the direction of $\hat{J}$ at $t = 1.587 \cdot 10^6 M$ is indicated by the vertical line. A strong modulation is introduced into the original waveform at that time, which is completely removed after quadrupole alignment.

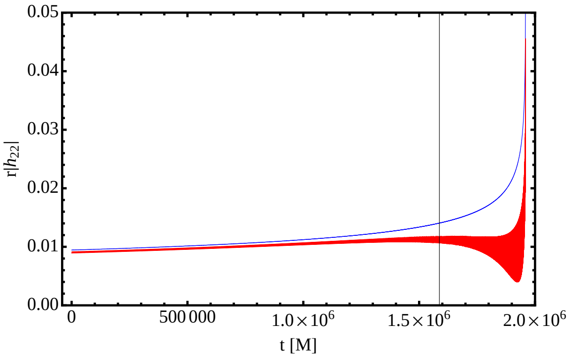

mapping for a transitional-precession case, we have chosen one specific configuration with PN parameters $q = 10$, initial separation $D_i = 53$M and initial spins $\vec{\chi}_1 = (0, 0, 0)$ and $\vec{\chi}_2 = 0.65 \cdot (0, -\sin(3°), -\cos(3°))$. This is a single-spin configuration, where the initial spin is 3° from complete anti-alignment and the generated inspiral waveform is about $2 \cdot 10^6 M$ long, terminating at a final separation of $D_\mathrm{f} = 6M$.

It is worth mentioning that in order to produce a transitional phase, the parameters have to be fine-tuned such that $\vec{J}$ changes sign. If $\vec{S}$ and $\vec{L}$ were completely anti-aligned, no precession would occur at all. The transitional phase is not brief: it takes up most of the duration of the inspiral that we have calculated and, as noted in [20], cases where a binary undergoes transitional precession within the sensitivity band of ground-based detectors are expected to be rare.

The dramatic change of the direction of $\hat{J}$ is reflected in the GW signal and the transitional waveforms in the standard source frame look particularly distorted when the total angular momentum crosses the xy-plane, as is shown in Fig. 5.5.

We do not expect any of these features to be present in the quadrupole-aligned waveform, since we now track the direction of dominant emission and this is completely independent from any asymptotic direction of $\hat{J}$. We see in Fig. 5.5 that this is indeed the case. The angles found by the maximisation routine are shown in Fig. 5.6. The zero-crossing of the total angular momentum occurs at $t = 1.587 \cdot 10^6 M$, which is indicated in the figures with a vertical line.

If our hypothesis is correct, then the QA waveform should be very close to a non-precessing waveform with $\chi_\mathrm{eff} = -0.572$, from Eq.(5.10). As before, we compared the QA mode with a series of spin-aligned waveforms with varying spin parameter to locate the non-precessing configuration that agrees best with the QA waveform. We find the best match to be 0.998 for a spin anti-aligned waveform with effective spin parameter $\chi_\mathrm{eff} = -0.576$. This is remarkably close to the theoretically expected value, with a bias of only $\Delta\chi = 0.004$!

On the other hand, naively using the non-aligned transitional-precession waveform and calculating the matches with the same comparison waveforms gives the same effective spin value, since the phase is dominated by the inspiral rate, but yields a best match of only 0.940.

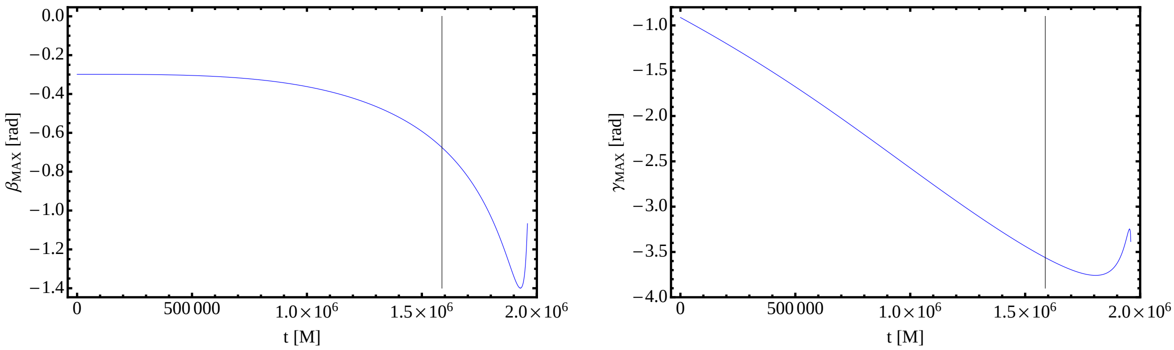

Figure 5.6: The two panels show the two Euler angles β and γ determined by the quadrupole-alignment procedure for the transitional case. The time when the z-component of $\vec{J}$ changes sign is indicated by the vertical line.

Note also that this is for the $(2,2)$-mode as seen from only one orientation; for many other orientations that matches are likely to be far worse.

This example demonstrates that even in the case of transitional precession, our method proves to be accurate (expected χ_{eff}-value) and robust ($\mathscr{M} > 0.99$) for mapping precessing waveforms onto single-spin-parameterised non-precessing-binary waveforms.

5.4 PN-NR hybrid waveforms

So far we have only discussed PN inspiral waveforms. To produce complete waveforms that include the late inspiral, merger and ringdown, we need to include results from NR simulations. In this section we will show how the quadrupole-alignment procedure simplifies the production of hybrid PN-NR waveforms.

A variety of methods have been introduced to construct hybrid waveforms for non-precessing configurations [10, 11, 49, 115, 175, 192], and see [13] for a unified summary of the methods in use. In all methods the PN and NR waveforms are aligned at some time, or over a time or frequency window, and then blended together. Such waveforms have been used to produce phenomenological waveform models [8, 10–12, 192], and are now also being used to test GW search and parameter estimation tools [13].

The construction of hybrids for precessing-binary configurations is more complex: not only do the time and phase of the PN and NR waveforms have to be aligned, but to some extent the orientations of the spins and orbital plane must agree as well. For the precessing-binary hybrids that were used in [12], the hybrid waveforms were constructed by matching the NR waveforms with PN waveforms computed from the same PN evolution that was employed to construct the initial data for the NR simulations. This technique ignores mismatches in the binary orientation and physical parameters due to the emission of junk radiation [109, 146] and gauge changes [110, 112] in the early stages of an NR simulation, although these effects are expected to be small; see [192] for a detailed discussion of this point in the context of non-precessing-binary hybrids.

These complications can be avoided through the use of QA waveforms. The PN and NR waveforms, both converted to the QA frame, can now be aligned exactly as in the non-precessing cases. In order to reverse the QA process, it is also necessary to align the QA angles $(\beta, \gamma, \epsilon)$, but this is straightforward, as we show below.

In the next section we will outline how we produce a QA hybrid for the precessing-binary waveform that we used in Chapter 4. This also corresponds to the first configuration discussed in Tab. 5.1: $\{q = 3, \chi_1 = 0, \chi_2 = 0.75\}$ and $\vec{S} \cdot \hat{L} = 0$. Having produced the QA hybrid, we will examine where our non-precessing-binary mapping hypothesis breaks down as we approach merger. That the hypothesis must break down is clear, because the spin of the final merged black hole will be influenced by the black-hole spins in a way that the orbital phase evolution is not, and the mass and spin of the final black hole will *not* be the same as that for the corresponding non-precessing inspiral configuration.

5.4.1 Construction of QA hybrids

A QA hybrid can be produced by making use of the same procedure as for a non-precessing-binary hybrid. We will briefly summarise the method that we used.

We start with a PN and an NR waveform, each for the same physical configuration. The last requirement is achieved to good approximation by using results from the PN evolution to produce the initial parameters for the NR evolution. The PN and NR waveforms are then put into the QA frame by the procedure described in Sec. 5.2.2. We will produce a hybrid of Ψ_4, and note that, since the QA frame is non-inertial, we cannot produce Ψ_4^{QA} by taking two time derivatives of h^{QA}. We must first produce the $\Psi_{4,2m}$ modes from the original precessing-binary GW-strain modes, h_{2m}, and apply the QA algorithm to $\Psi_{4,2m}$.

We then choose a matching frequency $M\omega_m$ and locate the times t_{PN} and t_{NR} when each waveform passes through that frequency. For our $q = 3$ configuration, $M\omega_m = 0.07$. We align the PN and NR frequencies around that time such that

$$\phi_{\mathrm{PN}}(t_{\mathrm{PN}}) = \phi_{\mathrm{NR}}(t_{\mathrm{NR}}), \tag{5.13}$$

$$\omega_{\mathrm{PN}}(t_{\mathrm{PN}}) = \omega_{\mathrm{NR}}(t_{\mathrm{NR}}) = \omega_m. \tag{5.14}$$

The hybrid waveform is then produced by blending together $\Psi_{4,\mathrm{PN}}^{\mathrm{QA}}$ and $\Psi_{4,\mathrm{NR}}^{\mathrm{QA}}$ with a linear transition function of width $\Delta t = 200\,M$ around the matching frequency. The final waveform is then

$$\Psi_{4,\mathrm{hyb}}^{\mathrm{QA}}(t) = a_- \Psi_{4,\mathrm{PN}}^{\mathrm{QA}}(t - t_{\mathrm{PN}}) + a_+ \Psi_{4,\mathrm{NR}}^{\mathrm{QA}}(t - t_{\mathrm{NR}}), \tag{5.15}$$

where $a_\pm = (\Delta t/2 \pm t)/\Delta t$ when $t \in [-\Delta t, \Delta t]$ and zero or one otherwise, and the time has been shifted such that $t = 0$ coincides with the point at which $\omega = \omega_m$. This constitutes

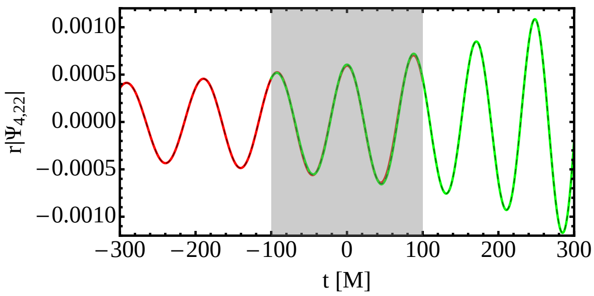

Figure 5.7: The PN (red, from $t = -300M$ to $t = 100M$), NR (green, from $-100M$ to $300M$) and hybrid (dashed black) waveforms near the matching time ($t = 0$). The PN and NR waveforms are blended together in the window $\Delta t = [-100, 100]$, indicated by the shaded region.

the QA hybrid. Fig. 5.7 shows the real part of Ψ_4 around the time where the matching was performed, which is at $t = 0$. The figure shows the PN and NR waveforms, as well as the final hybrid, and we see that the matching between the PN and NR waveforms is smooth.

To convert this QA-hybrid into a physical precessing-binary hybrid, we also require hybrids of the QA angles $(\beta(t), \gamma(t), \epsilon(t))$. These are produced as follows. The two polar angles $(\beta(t), \gamma(t))$ define a vector $\hat{n}(t) = (\sin(-\beta(t))\cos(-\gamma(t)), \sin(-\beta(t))\sin(-\gamma(t)), \cos(-\beta(t)))$ on the unit sphere. The QA angles for the PN waveform define $\hat{n}_{\rm PN}(t)$, while those for the NR waveform define $\hat{n}_{\rm NR}(t)$. We perform a fixed rotation $\mathbf{R}_{\rm PN}$ to $\hat{n}_{\rm PN}(t)$ (and another $\mathbf{R}_{\rm NR}$ to $\hat{n}_{\rm NR}(t)$), such that both vectors are equal at the matching frequency, $\hat{n}_{\rm PN}(t_{\rm PN}) = \hat{n}_{\rm NR}(t_{\rm NR})$. Since the angle γ is ill-defined when $\hat{n} = \{0, 0, 1\}$, we do not choose that as our (arbitrary) matching direction, but rather the vector such that $\beta(t_{\rm PN}) = 0.1\,\mathrm{rad}$. Specification of a third Euler angle allows us to require that the vectors not only meet at the matching time, but that the curves they trace out are parallel at that time. To do this we simply measure the angle between the two curves at the matching time, and then rotate $\hat{n}_{\rm NR}(t)$ around the axis defined by the matching direction, $\hat{n}_{\rm NR}(t_{NR})$. Fig. 5.8 shows the first two angles at the times close to the matching frequency and the final aligned PN and NR curves are shown in the lower panel of Fig. 5.8. The hybrid angles are constructed by smoothly blending between the PN and NR angles, in the same way as for the QA waveform with a linear transition function. The precessing-binary hybrid can then be constructing by simply performing the reverse QA procedure with $(\gamma, \beta, \epsilon) \to (-\epsilon, -\beta, -\gamma)$.

5.4.2 Breakdown of the non-precessing-binary equivalence

We expect the simple mapping between QA- and non-precessing-binary waveforms to break down near merger. As we have seen, the effect of the spins on the inspiral rate, i.e., the secular phasing, comes predominantly from the spin components parallel to the orbital angular momentum; this is why our mapping works. At merger, however, the spin of the final black hole is, to first approximation, $\vec{J}_{\rm fin} = \vec{L} + \vec{S}_1 + \vec{S}_2$, where the orbital and spin angular momentum vectors are those at the point of merger. (A far more sophisticated treatment of the final spin ingredients is given in [63], and a number of estimates of the final spin as a function of the initial configuration exist in the literature [145, 188, 216].) All components of

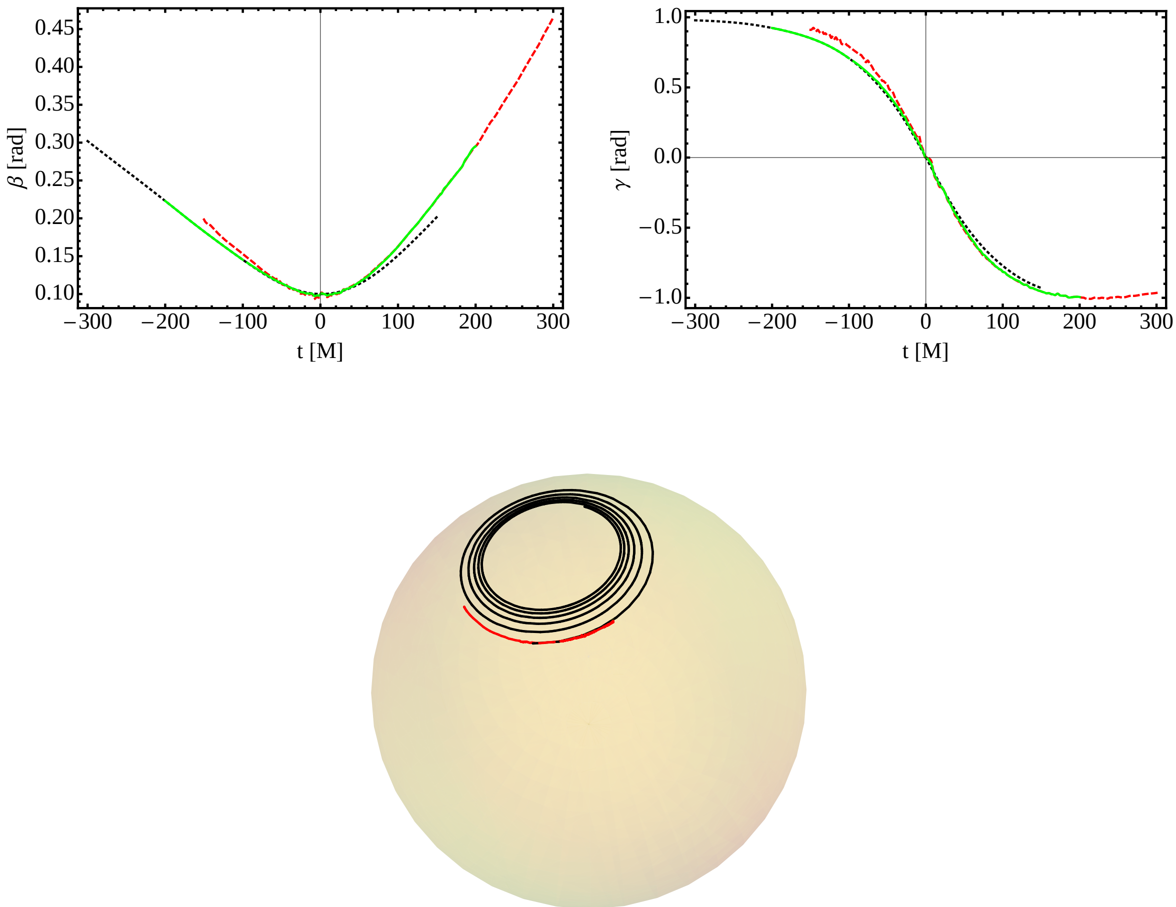

Figure 5.8: Hybridisation of the QA angles $\beta(t)$ and $\gamma(t)$. Upper panels: The black (dotted) lines indicate the inspiral PN values, the red (dashed) lines indicate the later NR values and the green (solid) lines indicate the hybrids. The lower panel shows the evolution of the aligned QA directions, where here the black line indicates long PN inspiral of duration $2.9 \times 10^5\, M$, and the red line indicates the NR results up to merger.

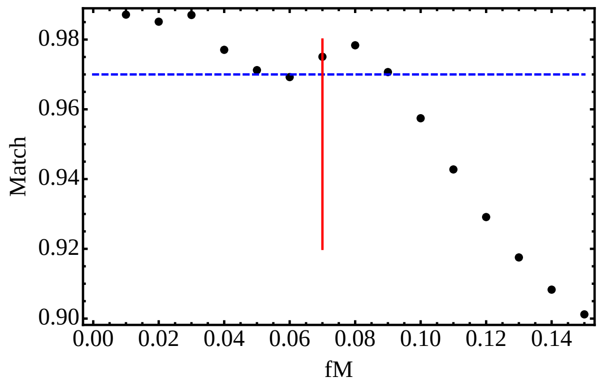

Figure 5.9: Matches between QA and non-precessing hybrids for our standard $q = 3$ configuration.The horizontal axis represents the frequency at which both waveforms are cut off in the match calculation and indicates that the two hybrids agree well (match > 0.97) right up to the merger, indicated by the vertical line.

the spin now become important and the appropriate parameterisation may no longer be the effective total spin χ_{eff}.

It is instructive to investigate where the mapping breaks down, and we can use the hybrid waveform constructed in the previous section to do this. Fig. 5.9 shows the match between the QA hybrid constructed above, and a non-spinning $q = 3$ hybrid (which would be the corresponding non-precessing configuration during the inspiral). The match is calculated for a range of termination frequencies of the two waveforms. For reference, the frequency Mf $= 0.016$ corresponds roughly to $M\omega = 0.1$, and is close to the point where PN waveforms are typically terminated in inspiral searches. Below this frequency the white-noise match is consistent with the results in Sec. 5.3.1. The peak of the waveform occurs at Mf $= 0.07$, which is indicated by the red vertical line. The fiducial acceptable match of 0.97 is indicated by a horizontal line. We see that the match is at or above 0.97 through the merger, and only degrades significantly during the ringdown.

Once again we emphasise that these matches were computed using a white-noise power spectrum. Nonetheless, these provide evidence that the QA procedure is valid very close to the merger, and perhaps even up to ringdown. We will discuss the implications of this result for waveform modelling in the final section.

5.5 Discussion: a route to generic-binary waveform models

We have extended the work in Chapter 4 on the quadrupole-alignment (QA) procedure to show that it can be used not only to cast precessing-binary waveforms in a simple form, but to map these waveforms onto a sub-family of non-precessing spin-aligned waveforms. Additionally, we have verified that this sub-family can be parametrised by only mass ratio and an effective total spin parameter and that the non-precessing waveform that best matches each QA waveform (with white-noise matches of at least 0.995), corresponds to our predicted χ_{eff} value to within $\Delta\chi \leq 0.04$. The mapping was tested on a range of inspiral PN waveforms with mass ratios $q = 3$ and $q = 10$ and even on an example of transitional precession; in all cases the approximations holds well within the level of accuracy of the PN phasing.

As a final test, we used the inverse QA procedure to "wrap up" a non-precessing-binary waveform to produce a mock precessing signal and found that it matched the corresponding true precessing waveform with a match of > 0.97 for all binary orientations. We also showed that this procedure can simplify the construction of hybrid PN-NR waveforms and that the approximate mapping seems to hold all the way through to merger.

Our results suggest that generic precessing-binary waveforms can be generated with good accuracy by applying the reverse of the quadrupole-alignment transformation to a small class of non-precessing-binary waveforms. These waveforms appear to faithfully represent the "true" precessing-binary waveforms up to the point of merger, and perhaps even up to the ringdown. The complex problem of constructing a generic waveform model can then be factorised into two smaller tasks, namely in developing a model for the secular phase (and such models already exist) and in modelling the rotation operator, which encodes all information regarding the precession. We emphasise that this simple structure is only possible due to the correct identification of the secular phase. Otherwise, the simple rotation operator becomes a more complex modulation operator with a less geometric meaning as it also needs to compensate for the incorrect inspiral rate.

More concretely, we propose the following strategy, which will be used in Chapter 7: once the evolution of the Euler angles $\beta(t)$ and $\gamma(t)$ has been determined for a large sample of the configuration space, these can be modelled as functions that depend on some set of physical parameters $\vec{\lambda}$

$$\beta = \beta(\vec{\lambda}(t)), \tag{5.16}$$

$$\gamma = \gamma(\vec{\lambda}(t)). \tag{5.17}$$

We emphasise that the $\vec{\lambda}$ should be *physical* parameters, or a combination of physical parameters. The third angle $\epsilon(t)$ is automatically determined given the two others. The rotation angles are unique up to an overall rotation of the frame of reference; we expect that they will assume the simplest form if in the limit of infinite binary separation $\hat{J}_{-\infty} = (0, 0, 1)$.

We have seen that precessing inspiral-merger (IM) waveforms can be mapped onto non-precessing ones via quadrupole alignment using the angles $(\gamma(t), \beta(t), \epsilon(t))$. This suggests that a phenomenological IM model with (anti-)aligned spins as a base model to describe the secular phase evolution can be used and "twisted up" with the inverse angles $(-\epsilon(t), -\beta(t), -\gamma(t))$. This will give us a precessing phenomenological IM model,

$$h_{lm}^{\mathrm{PrecIM}}(t) = \mathbf{R}(-\epsilon, -\beta, -\gamma)\, h_{lm}^{\mathrm{IM}}(\eta, \chi_{\mathrm{eff}}; t). \tag{5.18}$$

Needless to say, an *inspiral* model is not urgently needed: we can already produce generic waveforms by integrating the PN equations of motion, as we have for the PN analysis.

Given in addition a phenomenological model for the ringdown, $h_{lm}^{R}(\vec{\lambda}_R; t)$, which is parameterised by some yet-to-be determined subset $\vec{\lambda}_R$ of the full binary parameters $\vec{\lambda}$, we expect that we can produce a combined IMR model, which can be schematically written as

$$h_{lm}^{\mathrm{PrecIMR}}(t) = \mathbf{R}(-\epsilon, -\beta, -\gamma)\, h_{lm}^{\mathrm{IM}}(t; \eta, \chi_{\mathrm{eff}}) \times h_{\ell m}^{R}(\vec{\lambda}_R; t). \tag{5.19}$$

For ease of use in GW searches, ideally such a model should be cast in closed-form expressions in the frequency domain.

There is still one problem remaining: the modelling of a seven-dimensional parameter space, but we now have to model only two functions, and, as we can see from Fig. 5.2 (and even Fig. 5.6 for transitional precession), they are smooth, simple functions, that may be far easier to model than the complicated amplitude and phase modulations that are standard features of the physical waveforms. We will see in the subsequent chapters that many of the features of the full seven-dimensional parameter space can be captured by a model that considers only a subset of the physical parameters. It is also quite possible that we will need to employ a non-precessing model that treats both black-hole spins, and/or the effective spin that proves most useful will differ from that presented here.

CHAPTER 6

Towards generic waveform models II

Modelling precession with a single effective precession parameter

6.1 Introduction

In Chapter 3 we have explored the complex phenomenology of precessing binaries, before we have seen in Chapters 4 and 5 that the inspiral dynamics and the precession dynamics approximately decouple. This decoupling was identified by introducing a co-precessing frame, the QA frame, which allows us to partially remove the precession of the orbital. In this frame, we can more directly measure the secular phasing of a precessing binary and we have subsequently shown that the secular phase evolution of a precessing binary can be accurately mapped onto the phase of an aligned-spin binary. This then allowed us to rewrite precessing waveforms in a simple way, which is the basis of a general framework to produce precessing binary waveforms, namely by applying a rotation operator, which encodes the precession dynamics, to an aligned-spin waveform (see Eq.(5.11) and Eq.(5.12)). However, we are still left with the problem of modelling the precession dynamics, which, in general, depends on all six spin components as well as the mass ratio of the binary. In this chapter, we explore the possibility of reducing the number of *physical parameters* to accurately describe the precession dynamics of generic systems.

Precession leaves a direct, nontrivial imprint on the precessing-binary waveforms, which suggests that one may need to produce a large number of numerical simulations to fully explore the rich phenomenology in order to construct an accurate complete IMR waveform model for such systems. We are interested in reducing the number of model parameters for two main reasons: first, to provide a simple ansatz for the description of the waveform that is associated with a small number of degrees of freedom, and secondly to increase computational efficiency of the waveform model. Models with many parameters are in general more costly to use in gravitational-wave data analysis and parameter estimation. Also, from a Numerical Relativity point of view, if one wants to accurately span the seven-dimensional precessing parameter space, assuming that a sampling with four configurations in each parameter direction as indicated by [12, 192] is sufficient, one would need on the order of $4^7 \approx 16,000$ numerical simulations. Currently, it is not feasible to produce such a large number of Numerical Relativity waveforms. However, the identification of a reduced set of physical parameters may allow us to feasibly model generic-binary waveforms as it facilitates the identification of the important directions in the precessing-binary parameter space. Additionally, parameter reductions and combinations also indicate approximate parameter degeneracies and the measurability of certain binary parameters from a GW detection.

The investigation presented here is entirely based on the study of post-Newtonian inspiral waveforms. In principle, no parameter reductions are needed as one can simply solve the full system of PN evolution equations and then use the explicit waveform mode expressions available in the literature to compute the gravitational waveforms. However, we expect PN theory to give us the dominant phenomenology of the inspiral and therefore the parameter dependencies. In the past, the leading-order spin-orbit expression in the PN phase evolution for aligned-spin binaries was the starting point to introduce one effective inspiral spin rather than the two individual spin magnitudes. Even though the first insight came from PN, it was later used as the spin parameter in the complete phenomenological waveform models PhenomB and PhenomC. Similarly, we take the viewpoint that PN provides us with useful insight into the construction of effective parameters governing the leading-order precession effects, in particular, we will motivate and identify only one *effective precession spin*, which allows us to capture the dominant precession effects of a generic binary configuration and therefore significantly simplifies the task of modelling the precession dynamics. An adaptation of the work presented in this chapter has recently been submitted to the preprint server arXiv:
[198] Patricia Schmidt, Frank Ohme and Mark Hannam "Towards models of gravitational waveforms from generic binaries II: Modelling precession effects with a single effective precession parameter"

6.2 Modelling simple precession

In Chapter 3 we have explored the phenomenology of precessing binaries without looking at waveform modelling efforts. In this chapter, however, we are interested in modelling precessing waveforms by capturing the main effects described in the aforementioned chapter. We therefore give a brief summary of the routes to modelling precessing binaries taken in the past to highlight the differences in the various approaches. For a more concise current status update we refer the reader to [108].

6.2.1 Summary and recent progress

First attempts to construct search templates for precessing signals [18, 19] followed soon after the careful analysis of the phenomenology of precessing binaries within the post-Newtonian framework in the pioneering work by Apostolatos et al. [20] and Kidder [133]. Apostolatos was the first to observe the potential of modulating the *secular phase*, which he referred to as the "carrier phase", to describe the phase of the precessing system. Schematically, the precessing strain is then given as

$$h(t) \propto \Lambda(t) h_C(t), \tag{6.1}$$

where $h_C(t)$ is the unmodulated carrier signal and $\Lambda(t)$ is the modulation factor, which contains all information regarding the precession-induced modulations of the amplitude and the phase. For more details see Eq.(6)-Eq.(17) in [18]. However, this ansatz modulates the phase of a *nonspinning binary* to mimick the secular phase evolution. The agreement between the artifically modulated waveforms and true precessing waveforms is quantified in the form of the fitting factor (FF) as defined in Sec. 2.4.2. Apostolatos found that a template family built from this ansatz is able to capture systems with mild precession, but even moderate precession leads to unacceptably low FFs [18].

Several years later, Buonanno, Chen and Vallisneri [59] (BCV) improved the modulation factor in Apostolatos' general ansatz to produce precessing waveforms. However, they also used the nonspinning phase to describe the secular phase evolution. The new improved modulation factor captures the precession-induced modulations better, but in order to do so, up to six free non-physical parameters have to be introduced, which has subsequently been shown to prove problematic for use in GW searches [217].

Additionally, BCV introduced the *precession convention*, which defines a rigid-body system attached to the binary and allows for a much simpler computation of the GW strain. This convention is closely related to the QA-frame from Chapter 4.

Sturani et al. [209] later provided a phenomenological description of the complete inspiral-merger-ringdown signal in the time domain by calibrating a power-law ansatz for amplitude and phase to a small set of short precessing numerical relativity simulations. This was the first precessing IMR waveform model. Large-scale studies regarding the faithfulness and/or effectualness of this model have not yet been performed.

In order to model the waveforms from precessing binaries in a more systematic way, we took the following approach: first, we introduced a co-precessing frame, the quadrupole-aligned frame, which used an analytic maximisation procedure to determine the direction of maximal GW emission (see Chapter 4 for details). Comparison with PN results suggested that the QA-axis corresponds to the orientation of the orbital angular momentum $\hat{L}$, which, at leading order, is given by the polar angles (ι, α) as defined in Sec. 3.2.1. Henceforth, we will approximate the general Euler angles (β, γ) by the polar angles (ι, α).

Importantly, we realised that the GW modes as viewed in this co-precessing frame resemble the modes of aligned-spin systems. Later on, O'Shaughnessy et al. [168] described a similar co-precessing frame making use of an algebraic method, which was shown to be the same as the quadrupole-aligned frame if only the ($l = 2$)-modes are taken into account. In general, any such co-precessing frame is determined by three Euler angles analogous to the mechanics of a rigid body. It was a priori not clear how to fix one of these angles and was thus omitted. However, Boyle et al. [50] identified this third angle as an overall rotation around the z-axis given by

$$\epsilon(t) = -\int \dot{\alpha}(t') \cos\iota(t') dt'. \tag{6.2}$$

One might wonder what the purpose of viewing GWs in a co-precessing, unobservable frame is, but by doing so we were able to directly observe the secular phasing due to the partial removal of the precession effects. In other words, it allowed us to observe the *correct carrier phase*. In subsequent work and as opposed to the earlier attempts summarised above, we identified the corresponding secular phase of a given precessing binary as the inspiral rate of a very particular *aligned-spin* binary (see Chapter 5 for details). This is a key insight which allows for the direct identification of the secular phase evolution between precessing and non-precessing binaries – no ansatz for the carrier phase is needed as the phase of aligned-spin binaries is known to high PN order. Moreover, this geometric approach allowed us to make a more systematic ansatz than the power-law ansatz for the phase modulation factor in earlier work – with this correspondence the modulation factor is identified as a simple rotation operator with a concrete physical meaning, i.e.,

$$h_C^{\text{nonspinning}}(t) \rightarrow h^{\text{spinning}}(t), \tag{6.3}$$

$$\Lambda(t) \rightarrow \mathbf{R}(\iota, \alpha, \dot{\alpha}\cos\iota). \tag{6.4}$$

The transformation into the co-precessing frame is based on the transformation behaviour of the spin-weighted spherical harmonics. In practice, this reduces to applying three simple time-dependent rotation operators, which encode the evolution of the orbital plane. In order to accurately model the precession of the orbital plane on top of the inspiral rate of an aligned-spin binary, the inverse rotation operators need to be applied. We demonstrated the efficacy and accuracy of this systematic approach on pure PN, pure NR as well as on a PN-NR hybrid waveform. We are now left with the task of analytically modelling the two precession angles functions (ι, α), which encode the evolution of the orbital plane as a function of physical parameters as discussed in detail in Chapter 3.

The opening angle of the precession cone, $\iota(t)$, is well defined by Eq.(3.9) and can be computed in a straightforward way assuming that $S(t)$ and $L(t)$ are known, but the precession angle, $\alpha(t)$, is directly related to the precession frequency given by Eq.(3.11). Analytic solutions for $\alpha(t)$ are only known for two special cases: equal-mass or single-spin binaries [20].

No analytic solution for general double-spin binaries in the comparable mass regime is known. Further, the precession angle is particularly important for the modulation of the phase and hence it is crucial to obtain an accurate description of $\alpha(t)$ as a function of the physical parameters of the binary system. The influence of $\iota(t)$ on the phase is less strong and therefore we do not expect its accuracy to be as important. Nonetheless, the angles depend in general on all six spin components, which complicates the modelling efforts. Therefore, in order to establish a sufficient model for the two angle functions all the way up to merger by incorporating information from Numerical Relativity, it is advantageous to reduce the number of dependent parameters.

6.2.2 Parameter reductions

As elaborated in Chapter 3, generic binary systems are intrinsically characterised by a large number of *physical parameters*. For precessing black-hole binaries, a total of seven physical parameters need to be taken into account. These are the mass ratio q and the six spin components of the two spin angular momentum vectors; the total mass M of the system is irrelevant in the context of source modelling as it only sets the scale in General Relativity. This is already one important reduction of the parameter space spanned by binary configurations, which has already been used in the past to develop complete waveform models for coalescing binaries.

Another important parameter reduction concerns aligned-spin binaries. In general, such binaries are intrinsically characterised by the mass ratio and their two spin magnitudes χ_1 and χ_2. However, these two magnitudes can be combined into one effective spin parameter, χ_{eff} as introduced in [9] and given in Eq.(5.10) and discussed subsequently, which captures the inspiral dynamics to a very high degree.

The introduction of the effective total spin was a first important step towards a reduced parameterisation for a complete IMR model and was indeed used in existing models for the waveform from aligned-spin binaries. Moreover, in Chapter 5 we have seen that this effective total spin parameter is also useful to describe the phasing, i.e., the inspiral rate, of precessing binaries in the co-precessing QA-frame. In the general case, the effective spin combines the spin components parallel to the orbital angular momentum, $\chi_{i||}$, into one effective parameter and hence reduces the number of remaining spin components to four: the four spin components orthogonal to the orbital angular momentum. This is an important insight, which is directly related to the approximate decoupling of the inspiral and precession dynamics at leading order. If this was not the case, such a clean parameter split would not be possible and all six spin components would affect the inspiral as well as the precession rate of a given binary system.

Until now, these orthogonal spin components, which drive the precession of the orbital plane at leading order as can be seen from Eq.(3.16), have not been taken into account. In

Figure 6.1: The panel shows the evolution of the two spins projected onto the orbital angular momentum. The red graph shows the evolution of the parallel spin of the smaller black hole, $S_{1||}$, the blue curve that of the parallel spin of the larger black hole, $S_{2||}$ for the case described in the text. The two black lines indicate the mean value of each parallel spin with $\bar{S}_{1||} = 0.015$ and $\bar{S}_{2||} = -0.045$.

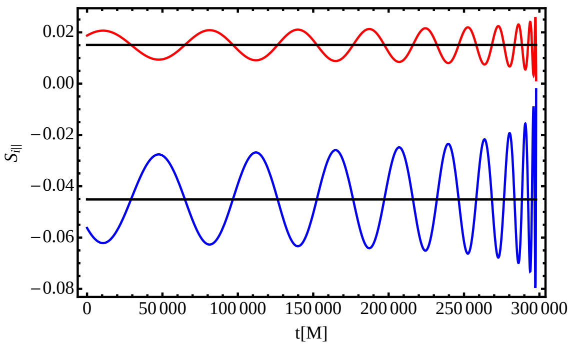

the following, we show that it is possible to faithfully approximate the precession in a generic binary system with only one additional spin parameter, a complementary *effective precession spin*, χ_p, instead of four additional spin components.

6.2.3 Effective precession spin χ_p

In order to construct a complete IMR model for precessing binaries from an underlying aligned-spin model, we are still left with modelling the precession dynamics as a function of the physical parameters. In order to do this efficiently, we aim to reduce the number of physical parameters to achieve a balance between physical information contained in the model and computational cost in the evaluation of the model. We are therefore interested in identifying the key directions and parameters that allow us to capture the main phenomenology of precessing binaries with as few parameters as possible. As mentioned before, we build our approach on the fact that the inspiral motion and the precession decouple approximately. This leaves us with the four remaining in-plane spin components, $\vec{S}_{1\perp}, \vec{S}_{2\perp} \in \mathbb{R}^2$ for $\hat{L} \equiv \hat{z}$, which are predominantly responsible for the precession of the orbital plane as can be seen from Eq.(3.16). We now aim to combine these four remaining parameters into only one meaningful quantity, which can then be used to accurately account for the induced orbital precession. The choice of this particular additional spin parameter, henceforth referred to as $\chi_{\rm p}$, to capture the main precessional behaviour of the orbital plane is motivated by the following observations.

In the previous chapters, we have seen that the inspiral rate of the binary is dominated by the components of the two spin angular momenta parallel to the orbital angular momentum, i.e., the contributions $\vec{S}_{i||}$ or, more precisely, $\vec{\chi}_{i||}$ (see Eq.(3.2) for example). In the case of spin-aligned binaries, these projected magnitudes are constant over time as they simply are the individually conserved spin magnitudes. In the case of double-spin precessing binaries, however, the projected magnitudes $S_{i||}$ are not exactly constant but slowly oscillate around some mean value over the course of the evolution. This behaviour is illustrated for the precessing binary $\vec{\chi}_1 = (0.4, -0.2, 0.3)$ and $\vec{\chi}_2 = (0.75, 0.4, -0.1)$[1] with mass ratio $q = 3$

[1] All illustrations in this section are for this particular spin configuration unless indicated otherwise.

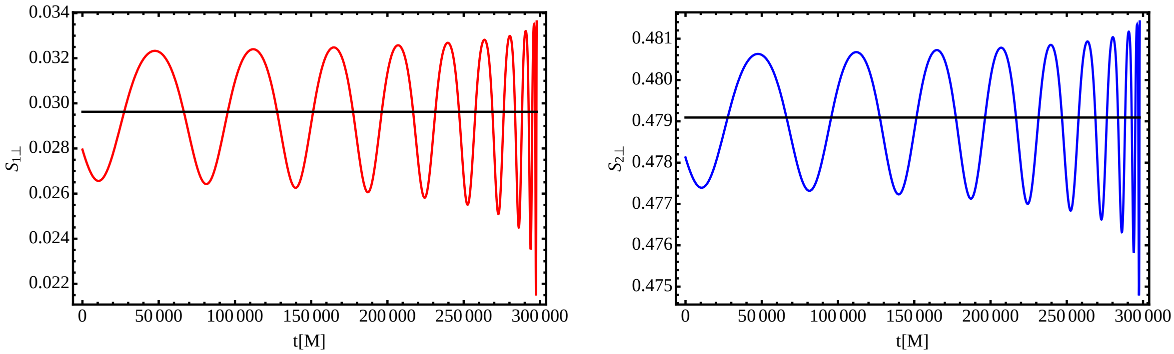

Figure 6.2: The left panels shows the evolution of the magnitude of $\vec{S}_{1\perp}$ as function of time, the right panel shows the evolution of the magnitude of $\vec{S}_{2\perp}$. Similar to the parallel spin magnitudes, the orthogonal spin magnitudes oscillate around some mean values, which are $\bar{S}_{1\perp} = 0.030$ and $\bar{S}_{2\perp} = 0.479$ respectively (solid black lines in the two panels).

in Fig. 6.1. We note that the individual total spin magnitudes S_i are still conserved. The observed oscillations in the parallel spin magnitudes must therefore be compensated by the orthogonal spin magnitudes at each moment in time.

Analogously, also the magnitudes of the spins orthogonal to the orbital angular momentum, $S_{i\perp}$, show a similar oscillatory behaviour over time. This is illustrated in Fig. 6.2 for the same configuration as in Fig. 6.1. We note that these oscillations occur on the precession and not the orbital timescale. These oscillations are a purely relativistic feature and occur due to the presence of spin-orbit and spin-spin couplings. By examining the evolution equation for the orbital angular momentum Eq.(3.16), we see that the driving force of the precession of $\hat{L}$ indeed are the spin components orthogonal to the instantaneous orbital angular momentum since $\vec{S}_i \times \hat{L} = \vec{S}_{i\perp} \times \hat{L}$. So far, we have seen that their magnitudes change periodically but additionally, the spin evolution equations suggest that these projections rotate within the orbital plane continuously changing their relative orientation in the plane. This in-plane motion is illustrated in Fig. 6.3, which shows the orthogonal spin unit vectors at three different times during the evolution but within one precession cycle. We note that the spins $\vec{S}_{i\perp}$ rotate at different rotational velocities, i.e., they have different precession rates around $\hat{L}$.

These two observations, 1) the oscillation of the magnitudes of the in-plane spins $S_{i\perp}$ around a *mean value* and 2) the continuous change of the relative position between the projected spin vectors in the plane, together with leading-order PN term in the precession equation for the orbital angular momentum Eq.(3.16), suggest the following effective precession spin parameter to capture the precession of the orbital plane in a fully generic binary

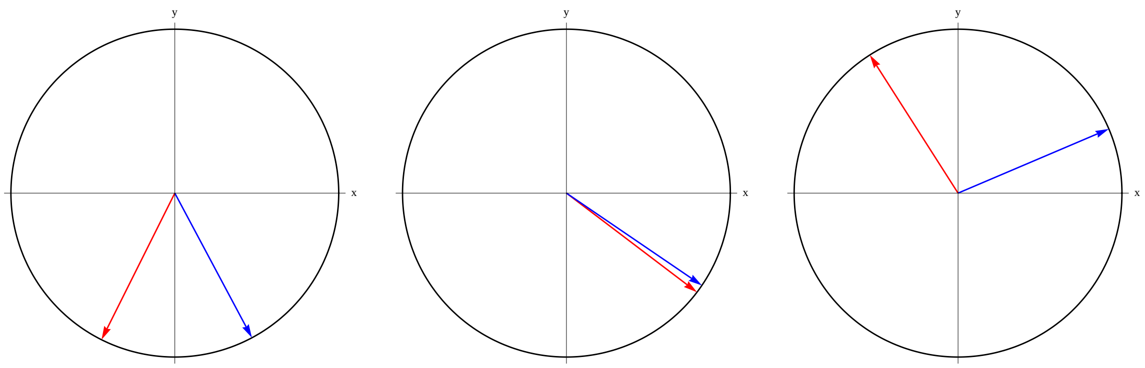

(a) $t = 0M$ **(b)** $t = 10000M$ **(c)** $t = 30000M$

Figure 6.3: The three panels show the unit vectors $\hat{S}_{1\perp}$ (red) and $\hat{S}_{2\perp}$ (blue) as contained in the orbital plane for three different times in the evolution as indicated. The orbital angular momentum $\hat{L}$ is perpendicular to the xy-plane. It is obvious that the spins in the plane continuously change their position in the plane as well as their relative orientation – the angle between them changes smoothly.

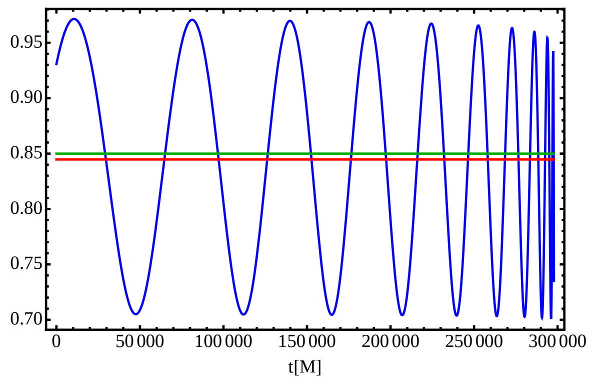

Figure 6.4: The panel shows the magnitude of the leading order precession term $||(A_1\vec{S} + A_2\vec{S}) \times \hat{L}||/(A_2 m_2^2)$ (blue), its true mean $\overline{||(A_1\vec{S} + A_2\vec{S}) \times \hat{L}||/(A_2 m_2^2)} = 0.845$ (red) and its approximation $\chi_p = 0.85$ (green).

configuration:

$$S_p := \frac{1}{2}\{A_1 S_{1\perp} + A_2 S_{2\perp} + |A_1 S_{1\perp} - A_2 S_{2\perp}|\}$$
$$\equiv \max(A_1 S_{1\perp}, A_2 S_{2\perp}), \tag{6.5}$$

where $A_1 = 2 + 3m_2/(2m_1)$ and $A_2 = 2 + 3m_1/(2m_2)$. This parameter is defined at the point where the binary configuration is specified, in our analysis at the initial time t_0, but it can be determined at any preferred point of definition like a specific GW frequency for example. We note, however, that the spin configuration at the initial point yields one specific value S_p, which necessarily changes due to the time-dependence of $S_{i\perp}$ when a different definition point is chosen. The change in χ_p, however, is small due the variation of $S_{i\perp}$ over the inspiral (see Fig. 6.2), unless the precession itself is very small. In those cases the relative change in χ_p can be very large and therefore strongly dependent on the chosen starting point.

By close inspection of Eq.(6.5) we understand the nature of its definition: it is the geometric mean of the relative orientation of the in-plane spins and their initial magnitudes, which are approximated as being constant over the evolution, weighted by the same mass weights that appear in Eq.(3.16). In other words, it is an approximation to the mean of the magnitude of the leading-order precession term, which can be interpreted as effective precession spin S_p:

$$S_p \approx \overline{||A_1\vec{S}_{1\perp} + A_2\vec{S}_{2\perp}||}. \tag{6.6}$$

We expect a binary with this precession spin S_p to exhibit a similar precession motion as a binary with initial in-plane spins $\vec{S}_{1\perp}$ and $\vec{S}_{2\perp}$.

In practice, we prefer to define spin configurations in terms of dimensionless spin parameters and therefore would like to use a dimensionless precession spin χ_p instead of S_p. In order to do so, we must make a choice regarding the distribution of the precession spin among the two black holes. Motivated by the fact that the in-plane spin of the smaller black hole becomes more and more negligible with increasing mass ratio, we assign the precession spin to the larger black hole, which, due to the mass weight in Eq.(6.5), yields:

$$\chi_p := \frac{S_p}{A_2 m_2^2}. \tag{6.7}$$

Eq.(6.5) does not exactly represent the mean value of the magnitude of the precession term over the inspiral phase but closely approximates this value. This is illustrated in Fig. 6.4. We also note here that for certain configurations, namely when $S_{1||}$ and $S_{2\perp}$ are both large, the Kerr limit $\chi_i \leq 1$ is not respected.

For most precessing configurations we find the deviation between the true mean value and χ_p to be of the order of a few percent at most. The choice of this particular precession spin is entirely based on the close examination of the PN evolution equation for the orbital angular momentum and the approximate decoupling of the inspiral and precession dynamics. By having chosen χ_p to be the approximate mean of the leading-order term in the PN precession equations, we do expect (by construction) to see a similar evolution of the orbital plane in a system where χ_p is used instead of $\vec{S}_{1\perp}$ and $\vec{S}_{2\perp}$. Whether this is true or not can best be seen from the evolution of the precession angles $(\iota(t), \alpha(t))$. A similar precession motion means that the two precession angles need to be sufficiently close to the angles in the generic system. This is illustrated for one generic case in Fig. 6.5. We see that the precession angles obtained from a configuration, where χ_p is used, indeed represent the average precession of the generic system with $\chi_{1\perp}$ and $\chi_{2\perp}$.

6.2.3.1 Limitations

Not all configurations, however, are precession dominated by the in-plane spin of the larger black hole. If the precession is dominated by the smaller black hole's spin, then S_p still represents the correct effective precession spin, but χ_p is then given by $\chi_p = (A_1 S_{1\perp})/(A_2 m_2^2)$. For each mass ratio one can define the minimal orthogonal spin on the larger black hole as

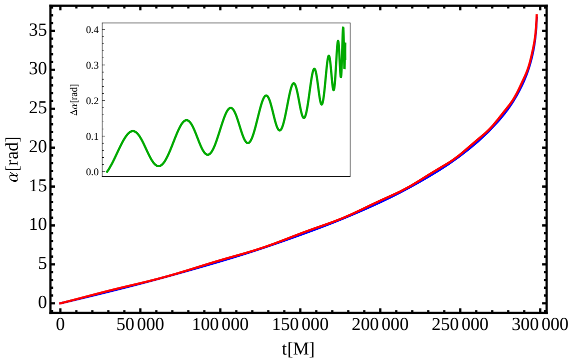

Figure 6.5: The left panel shows $\alpha(t)$ for the generic configuration $\{q = 3, \vec{\chi}_1 = (0.4, -0.2, 0.3), \vec{\chi}_2 = (0.75, 0.4, -0.1)\}$ (red) and the corresponding configuration utilising χ_p given by $\{q = 3, \vec{\chi}_1 = (0., 0., 0.3), \vec{\chi}_2 = (0.85, 0., -0.1)\}$ (blue). Since the two curves are not distinguishable over that time scale, the inset shows the difference $\Delta\alpha$ (green) as a function of time. The right panel compares the evolution of the opening angle of the precession cone $\iota(t)$. Both graphs reveal that the approximation discards the spin-spin couplings in the plane and therefore nutation effects (the visible oscillations).

a function of $\chi_{1\perp}$ such that the precession is predominantly driven by $\chi_{1\perp}$. The limit curves per mass ratio are illustrated in Fig. 6.6. For mass ratio $q = 3$ and a maximal in-plane spin of $\chi_{1\perp} = 1$, any in-plane spin $\chi_{2\perp}^{\max} \leq 0.289$ yields a system that is precession-dominated by the smaller black hole; for $q = 10$ this value drops to $\chi_{2\perp}^{\max} \leq 0.079$. For systems with very little precession, i.e., a very small precession cone $\iota \approx 0$, we find that χ_p does not capture the precession correctly (see Sec. 6.4.2.2 for further details) for certain binary orientations, which is reflected in a significantly different precession angle evolution as illustrated in Fig. 6.7.

Another interesting limit to test whether χ_p indeed encodes the average precession observed in a generic system is the equal-mass case. It is known analytically that for $q = 1$ the precession is dominated by the total spin S if spin-spin couplings are neglected [20]. χ_p, on the other hand, only represents a fraction of the total in-plane spin. Additionally, the two spins stay "interlocked", hardly changing their relative orientation and the in-plane spins precess at the same rate. Therefore averaging over the relative spin orientation in the plane is not applicable. This locking is illustrated in Fig. 6.8 for the same spin configuration as in Fig. 6.5 now evaluated for the mass $q = 1$. The precession term for this case is illustrated in the first panel of Fig. 6.9. We see that, as expected, χ_p underestimates the average precession of the system. We note, however, that χ_p is already a good estimator of the precession for mass ratios very close to the equal-mass limit. This is illustrated in the subsequent panels in the same Fig. 6.9, where we vary the mass ratio from equal-mass to mass ratio $q = 2$. We see that already at mass ratio $q = 1.2$, χ_p is a good estimator of the precession even for mass ratios close to equal-mass.

So far, we have explored the phenomenology of a single spin parameter χ_p to estimate the

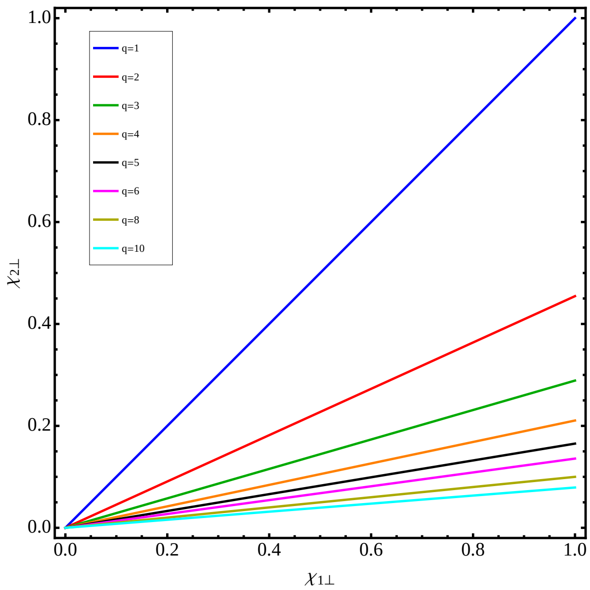

Figure 6.6: The panel shows the limit curves for the precession to be dominated by the smaller black hole for various mass ratios. The space below each graph represents the volume of possible in-plane spin combinations $(\chi_{1\perp}, \chi_{2\perp})$, which give a precession spin S_p dominated by the smaller black hole. Expectedly, the higher the mass ratio the less likely it is to have a configuration where the precession is dominated by $\chi_{1\perp}$.

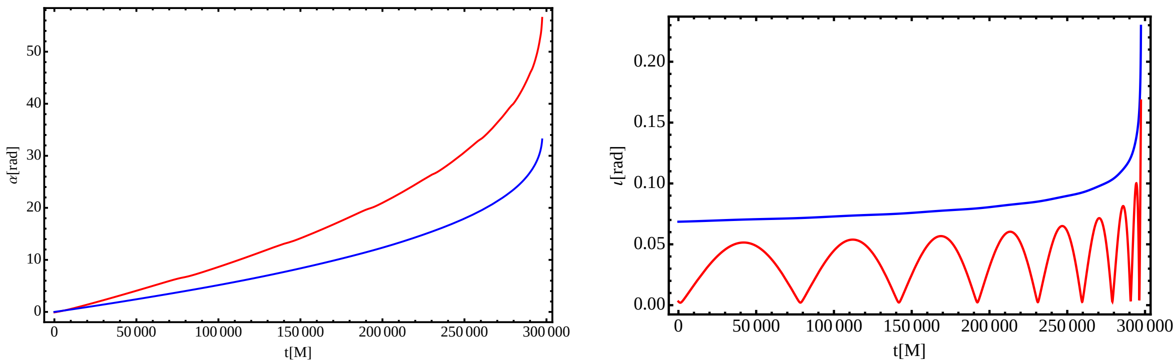

Figure 6.7: The left panel shows $\alpha(t)$ for the case $\{q = 3, \vec{\chi}_1 = (0.38, 0.319, -0.079), \vec{\chi}_2 = (-0.036, -0.036, -0.012)\}$ (red) and the corresponding configuration using χ_p given by $\{q = 3, \vec{\chi}_1 = (0., 0., -0.079), \vec{\chi}_2 = (0.143, 0., -0.012)\}$ (blue); the right panel compares the evolution of the opening angle of the precession cone $\iota(t)$. Both graphs highlight that in this case χ_p does not capture the precession of the system correctly.

average precession in a generic system and see good agreement when considering precession-related geometric quantities like the precession angles. However, keeping our goal of modelling precessing waveforms with a smaller set of physical parameters in mind, we need to investigate and quantify the agreement between fully generic waveforms and their parameter reduced counterparts. This will be the goal of the subsequent sections.

6.3 A post-Newtonian analysis

In the previous section we have introduced an effective precession spin χ_p Eq.(6.7), which encapsulates the average precession dynamics in a generic double-spin binary configuration.

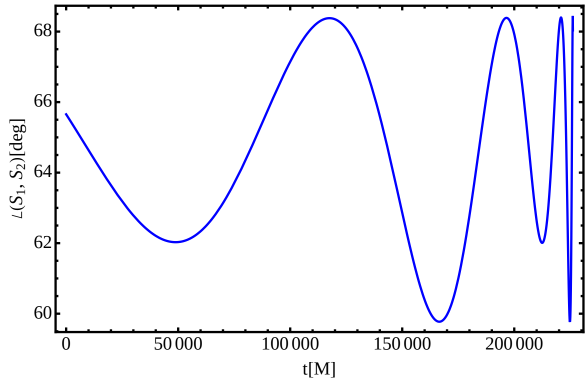

Figure 6.8: The left panel shows the angle between $\hat{S}_1$ and $\hat{S}_2$ for the same spin configuration as in Fig. 6.5 now evaluated for mass ratio $q = 1$. We see that they precess together, hardly changing their relative orientation.

Further, we have seen in Chapter 5, that the secular inspiral evolution of precessing binaries can be mapped onto the inspiral of aligned-spin binaries by either keeping the parallel spin components fixed or by combining them into one effective inspiral spin $\chi_{\rm eff}$. We have quantified the inspiral-spin mapping via match computation and will now present a similar analysis for the goodness of the precession spin.

In the subsequent analysis, a post-Newtonian framework is used to assess the quality of the choice of precession parameterisation during the inspiral. We aim to completely disentangle the effect of the effective parameterisation of the inspiral rate, and hence do not invoke the parameterisation with $\chi_{\rm eff}$ in this analysis, i.e., we will keep the parallel spin components $\chi_{i||}$ fixed in the comparison; the focus lies entirely on the mapping of four in-plane spin components $\vec{S}_{1\perp}$ and $\vec{S}_{2\perp}$ to χ_p. Schematically, the precession mapping we seek to investigate reads as follows:

$$\{q; \chi_{1||}, \chi_{2||}, \vec{\chi}_{1\perp}, \vec{\chi}_{2\perp}\}^{\rm FP} \mapsto \{q; \chi_{1||}, \chi_{2||}, \chi_p\}^{\rm RP}, \tag{6.8}$$

where FP stands for precessing configuration with a "full set of physical parameters" and RP stands for the corresponding precessing configuration with a "reduced set of physical parameters". We will later also combine $\chi_{1||}$ and $\chi_{2||}$ into $\chi_{\rm eff}$ (see Sec. 6.4.6), but for now we keep the parallel spin components fixed.

6.3.1 PN waveform generation

As opposed to the previous chapter, for efficiency reasons[2] the PN waveforms used in the analysis presented here are generated by integrating the 2.5PN orbit-averaged equations of motion under the assumption of quasi-spherical inspiral for $\vec{L}$ and $\vec{S}_i$ as given in Eq.(3.16)–Eq.(3.18). Further, we integrate the evolution equation for the orbital separation Eq.(3.22) as well as the evolution equation for the precession angle $\alpha(t)$ obtained by differentiating

[2]In order to perform a systematic analysis, we produce $\mathcal{O}(10^4)$ waveforms, which is more efficiently done by directly integrating the orbit-averaged PN equations than by using the Hamiltonian formulation.

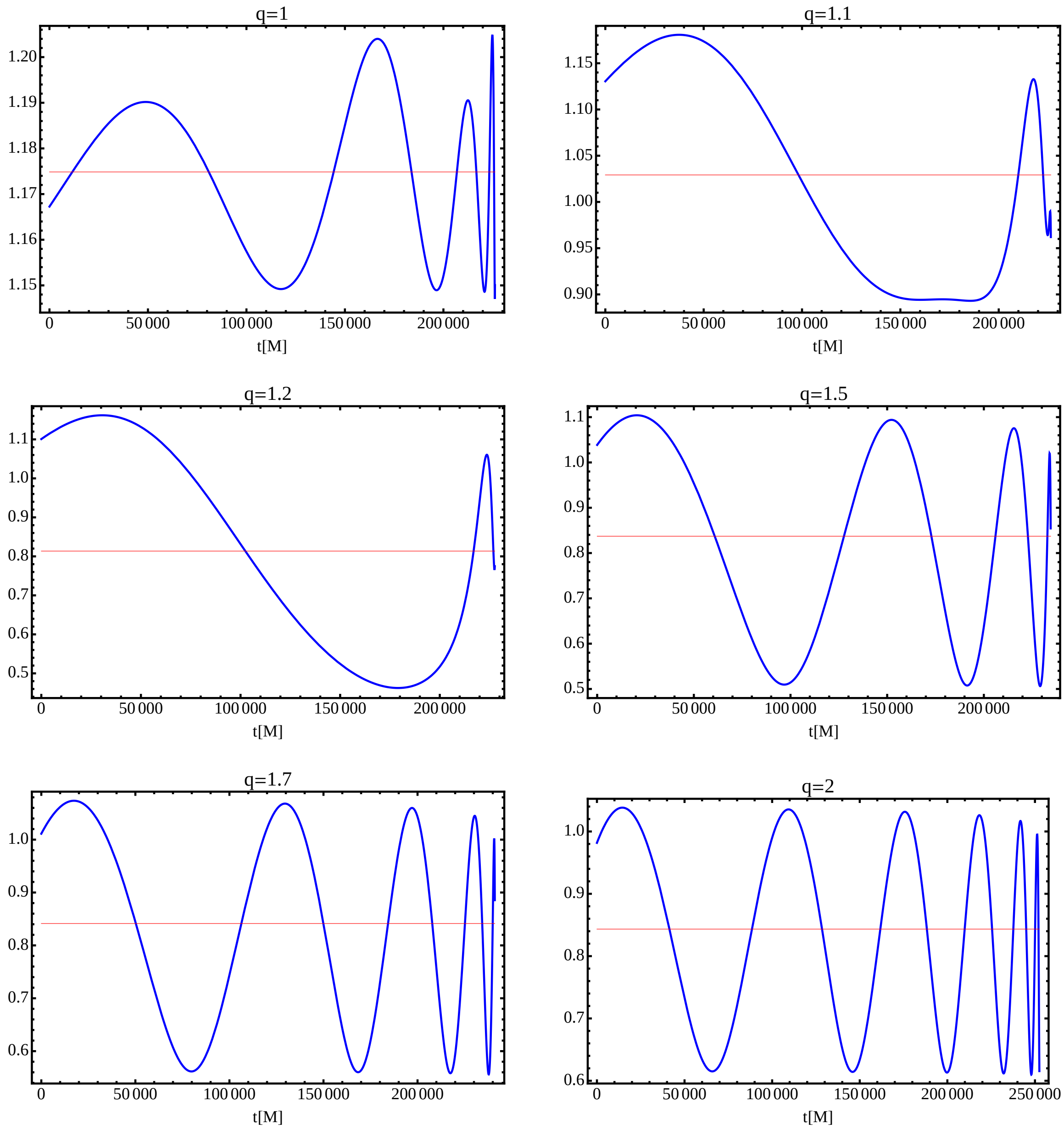

Figure 6.9: The panels show the precession term $||A_1\vec{S}_{1\perp} + A_2\vec{S}_{2\perp}||/(A_2 m_2^2)$ (blue) and its mean (red) as a function of time for different mass ratios q. The first panel shows the equal-mass case with a mean of 1.175. For this spin configuration, however, Eq.(6.7) yields $\chi_p = 0.85$. We see that at a small mass ratio of $q = 1.2$, χ_p is already a good estimator of the average precession.

Eq.(3.10) with respect to time,

$$\dot{\alpha}(t) = \frac{L_x \dot{L}_y - L_y \dot{L}_x}{L_x^2 + L_y^2 + \epsilon}, \tag{6.9}$$

where $\epsilon = 10^{-4}$ to ensure that the expression does not diverge in the numerical integration. We construct the orbital frequency from Eq.(3.23) and $\iota(t)$ from Eq.(3.9). We then integrate the equation for the orbital phase Eq.(3.21). The evolution is performed in the J_0-aligned frame and is aborted when a final separation of $r = 6M$, which corresponds to the Schwarzschild ISCO, is reached. As initial conditions we choose the spin components defined with respect to $\hat{L}_0 \equiv (0, 0, 1)$, the initial separation $r_0 = 40M$, the initial orbital phase $\Phi_0 = 0$ and the initial azimuth of $\hat{L}$ in the J_0-aligned frame. We also have to set the initial magnitude of the orbital angular momentum, which we choose to be the Newtonian value, $L_0 \equiv L_N = \mu\sqrt{M r_0}$. The transformation into the J_0-aligned frame is given by the following rotation matrix:

$$\mathbf{R} = \mathbf{R}_z(\epsilon_0 - \pi)\mathbf{R}_y(-\iota_0)\mathbf{R}_z(-\epsilon_0), \tag{6.10}$$

where ϵ_0 is the initial azimuth of the total angular momentum J_0.

Once we have solved for the dynamics of the binary, we use the mode expressions h_{lm} as given in [23] to construct the precessing waveforms. We only use the $(l = 2)$-modes and truncate the amplitudes at leading PN order (v^2), yielding the explicit following mode expressions:

$$h_{22} = -\frac{A}{2} e^{-2i(\iota - \alpha - \Phi)} \left[e^{4i\phi} \left(-1 + e^{i\iota}\right)^4 + \left(1 + e^{i\iota}\right)^4 \right] \tag{6.11}$$

$$h_{21} = -iAe^{-i(\alpha + 2\Phi + 2\iota)} \left[-e^{4i\Phi} \left(1 + e^{i\iota}\right) \left(-1 + e^{i\iota}\right)^3 - \left(1 + e^{i\iota}\right)^3 \left(-1 + e^{i\iota}\right) \right] \tag{6.12}$$

$$h_{20} = A\sqrt{\frac{3}{2}} e^{-2i(\iota + \Phi)} \left(-1 + e^{2i\iota}\right)^2 \left(1 + e^{4i\Phi}\right) \tag{6.13}$$

$$h_{2,-2} = -\frac{A}{2} e^{2i(\alpha + \Phi + \iota)} \left[e^{-4i(\Phi + \pi)} \left(-1 + e^{-i\iota}\right)^4 + \left(1 + e^{-i\iota}\right)^4 \right] \tag{6.14}$$

$$h_{2,-1} = iAe^{i(\alpha + 2\iota + 2\Phi + \pi)} \left[-e^{-4i(\Phi + \pi)} \left(-1 + e^{-i\iota}\right)^3 \left(1 + e^{-i\iota}\right) - \left(-1 + e^{-i\iota}\right) \left(1 + e^{-i\iota}\right)^3 \right] \tag{6.15}$$

with the amplitude factor

$$A = \frac{M\eta}{D_L} v^2 \sqrt{\frac{\pi}{5}}. \tag{6.16}$$

In the above equations D_L is the luminosity distance of the GW source which we set to $D_L = 1$.

6.3.2 Reduced-parameter waveforms: templates

As briefly mentioned in the motivation of this section, in order to test whether a reduced set of spin parameters indeed captures the main phenomenology of generic precessing compact binaries with a full set of spin parameters, we compare generic double-spin cases h^{FP} to parameter-reduced waveforms h^{RP}. The consequence of this reduced parameter choice is that any generic double-spin system with spins $\vec{S}_1$ and $\vec{S}_2$ is now approximated by one specific double-spin system. If this approximation holds, any generic configuration with arbitrary dimensionless spins $\vec{\chi}_1 = (\chi_{1x}, \chi_{1y}, \chi_{1z})$ and $\vec{\chi}_2 = (\chi_{2x}, \chi_{2y}, \chi_{2z})$ corresponds to a configuration with a reduced set up parameters such that:

$$\begin{aligned} \vec{\chi}_1 &\mapsto (0, 0, \chi_{1z}) \\ \vec{\chi}_2 &\mapsto (\chi_p, 0, \chi_{2z}), \end{aligned} \tag{6.17}$$

where we have defined the spin with respect to $\hat{L} \equiv \hat{z}$ in a Cartesian coordinate system. In words, the spin components parallel to the orbital angular momentum are fixed, but the in-plane spin components have been combined into the effective precession parameter χ_p, which is assigned to the larger black hole m_2. Without loss of generality, we have set $\chi_{2y} = 0$ in the template construction.

Alternatively, we could also combine the two parallel spin components into χ_{eff} as done in Chapter 5, but will not do so for the majority of the study as we predominantly want to test the validity of the χ_p-parameterisation independent of the χ_{eff}-parameterisation. Hence, the reduced model parameters are $q, \chi_{1||}, \chi_{2||}$ and χ_{p} unless otherwise indicated.

The choice of parameterisation as provided above is not unique: various combinations of different physical spins $\vec{S}_1, \vec{S}_2$ can yield the same set of model parameters $\{\chi_{1||}, \chi_{2||}, \chi_{\mathrm{p}}\}$ despite being physically completely different configurations. We see immediately that all configurations for one set of model parameters $(q, \chi_{1||}, \chi_{2||}, \chi_p)$ do not define a single configuration but an *approximate equivalence class* of precessing systems, i.e., various generic configurations map to the same point in the manifold of reduced-parameter configurations.

In order to assess whether this approximation indeed holds, matches between the waveform strains $h(\theta, \varphi)$ of the generic configuration and its corresponding RP-configuration for various binary orientations $\theta \in [0, \pi]$ and polarisation angles ψ are computed. Henceforth, we will refer to the full-parameter configuration as *signal* and to the reduced-parameter one as *template* T[3].

6.3.3 Precessing matches

We have seen in Sec. 2.4.2 that the agreement between two waveforms is commonly quantified by a single number, the *match* $\mathscr{M}$. It corresponds to the noise-weighted inner product

[3] Henceforth, sub- and superscripts S or T refer to signal or template respectively.

(overlap) between the two waveforms, whose agreement is investigated in Ref. [76]. For convenience, match calculations are performed in the frequency domain and hence the Fourier transform of the time-domain GW strain $h(t)$ has to be computed first. To do so, we utilise the *fast Fourier transform* routine in Mathematica.

As before, let the complex waveform strain be

$$h(t;\theta,\varphi) = h_+ - ih_\times \equiv \sum_{l,m} {}^{-2}Y_{lm}(\theta,\varphi)h_{lm}(t) \in \mathbb{C}. \tag{6.18}$$

The measured signal or *detector response*, however, is a real-valued function given by the parameterised superposition of the two fundamental polarisations

$$h^S_{\text{resp}}(t) = h_+(t)\cos 2\psi + h_\times(t)\sin 2\psi = \text{Re}\left(h(t)e^{2i\psi}\right) \in \mathbb{R}, \tag{6.19}$$

where ψ is the polarisation angle; it encodes the mixing of h_+ and $h_\times$. Analogously, the template is defined as

$$h^T_{\text{resp}} = \text{Re}\left(h^T(t)e^{2i\sigma}\right) \in \mathbb{R}, \tag{6.20}$$

where σ is the polarisation angle of the template.

The Fourier transform of the real-valued detector response strain is given by

$$\tilde{h}^S_{\text{resp}}(f) = \frac{1}{2}\left(\tilde{h}(f)e^{2i\psi} + \tilde{h}^*(-f)e^{-2i\psi}\right), \tag{6.21}$$

where we have used

$$\mathbb{C} \ni g(t) = f^*(t) \quad \Rightarrow \quad \tilde{g}(f) = \tilde{f}^*(-f). \tag{6.22}$$

We also know that given a real-valued function $a(t) \in \mathbb{R}$, its Fourier transform obeys $\tilde{a}(f) = \tilde{a}^*(-f)$. Thus, a symmetric inner product between two real functions $a, b \in \mathbb{R}$ can be defined by

$$\langle a|b\rangle = 2\int_{-\infty}^{\infty} \frac{\tilde{a}(f)\tilde{b}^*(f)}{S_n(|f|)}df \tag{6.23}$$

$$= \underbrace{2\int_{0}^{\infty} \frac{\tilde{a}(f)\tilde{b}^*(f)}{S_n(|f|)}df}_{I} + \underbrace{2\int_{-\infty}^{0} \frac{\tilde{a}(f)\tilde{b}^*(f)}{S_n(|f|)}df}_{I^*} \tag{6.24}$$

$$= 4\text{Re}\int_{0}^{\infty} \frac{\tilde{a}(f)\tilde{b}^*(f)}{S_n(|f|)}. \tag{6.25}$$

Combining Eq.(6.21) and Eq.(6.23), we find the polarisation-dependent match to be

$$\langle h^S_{\text{resp}}|h^T_{\text{resp}}\rangle = \text{Re}\int_{-\infty}^{\infty} \frac{\tilde{h}^S(f)\tilde{h}^{T*}(f)}{S_n(|f|)}e^{2i(\psi-\sigma)}df + \text{Re}\int_{-\infty}^{\infty} \frac{\tilde{h}^S(f)\tilde{h}^{T*}(-f)}{S_n(|f|)}e^{2i(\psi+\sigma)}df. \tag{6.26}$$

We explicitly give the expression as the phase optimisation in the match for precessing signals is directly related to the optimisation of the template polarisation. For nonprecessing signals, only one side of the frequency spectrum contributes, i.e., the second term in Eq.(6.26) vanishes. This is not true anymore in the case of precession – in particular for binary orientations close to edge-on, we find that the power in the negative frequency bins is non-negligible and must be taken into account. A match algorithm, which uses the double-sided frequency spectrum, was developed by Frank Ohme. Additionally, it optimises automatically over the template polarisation σ. All matches quoted in this section use this function and we also optimise over the azimuthal angle in the spin-weighted spherical harmonics of the template, φ_T.

The match is a very important figure of merit and in this analysis we are predominantly interested in whether the template faithfully (see Sec. 2.4.2 for details) represents the full-parameter signal waveforms. As a threshold we choose a minimum match of $\mathscr{M} = 0.965$. In the following, we will explore the match $\mathscr{M}$ as a function of the binary inclination θ and the signal polarisation ψ for a total binary mass of $M = 12M_\odot$ with a GW starting frequency of 20Hz and a cutoff frequency of 366Hz. For computational efficiency we use the early aLIGO noise curve.

6.4 Results

We have investigated the faithfulness of the reduced-parameter model by computing the match for selected cases of mass ratio $q = 3$ and mass ratio $q = 10$ before performing a large study with a set of 10,000 random binary configurations. For all investigated cases of mass ratio $q = 3$ we obtain matches above threshold for close-to-optimally oriented binaries with a sharp drop in the match towards the orientation $\theta = \pi/2$.

We emphasise that faithfulness is the lower bound for match calculations as no optimisations over physical parameters are performed; if we were to optimise over physical parameters as done in a GW search, the resulting fitting factor would by definition be larger (or the same). The results show very strong evidence in favour of the reduced parameterisation to capture the dominant precession effects.

6.4.1 Selected test cases

One of the most extreme cases to test the effectiveness of the reduced parameterisation is a double-spin case with two maximally spinning black holes. In order to maximise the precession effects, we choose both spins to be initially contained within the orbital plane, i.e., $\vec{\chi}_1 = (\pm 1, 0, 0)$ and $\vec{\chi}_2 = (\pm 1, 0, 0)$. By construction, the reduced-parameter configuration following the mapping Eq.(6.17) is given by $\vec{\chi}_1 = (0, 0, 0)$ and $\vec{\chi}_2 = (1, 0, 0)$. In the following we analyse various properties of this particular configuration and variations thereof for the moderate mass

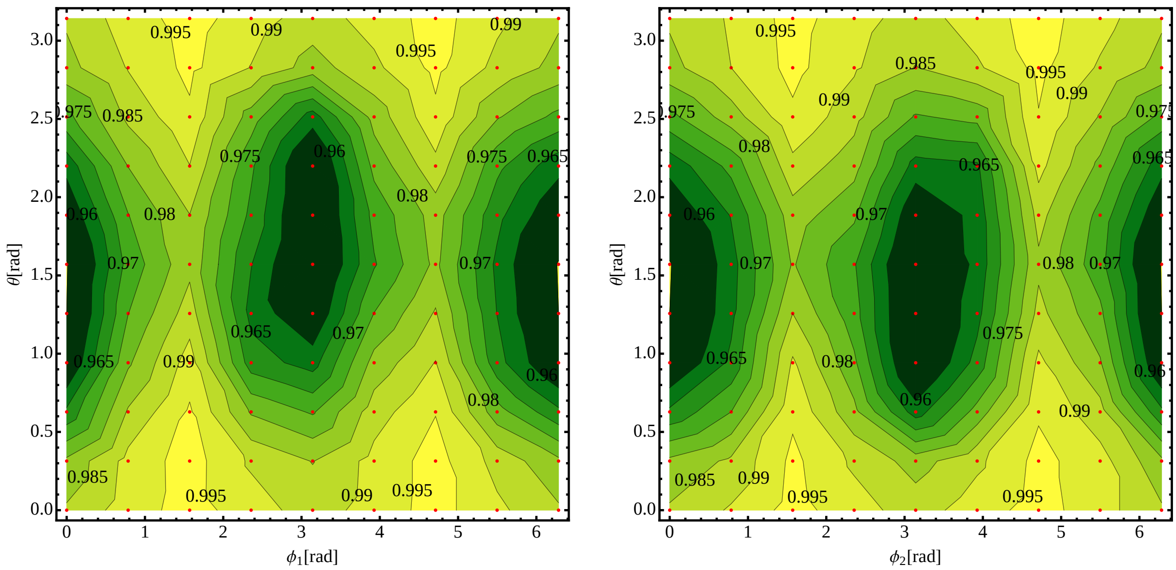

Figure 6.10: The left panel shows the match contours for the extremal case with varying in-plane orientation of $\vec{\chi}_1$, the right panel shows the contour for varying orientation of $\vec{\chi}_2$ as a function of the binary orientation θ. The red dots mark the actual points at which the matches are evaluated.

ratio $q = 3$.

6.4.1.1 Relative in-plane spin orientation

The first investigation concerns the influence of the *relative orientation of the spins in the plane*. Firstly, we fix $\vec{\chi}_2 \equiv (1, 0, 0)$ and vary the orientation of $\vec{\chi}_1 = (\cos\phi_1, \sin\phi_1, 0)$ with $\phi_1 \in [0, 2\pi]$ and $\Delta\phi_1 = 45°$. Secondly, we interchange the roles of $\vec{\chi}_1$ and $\vec{\chi}_2$ and now vary ϕ_2 in the same interval. To quantify the agreement between the rotated generic waveforms and the same template waveforms as constructed from Eq.(6.17), we compute the match for each in-plane orientation $\phi_{1,2}$ with the same template. We choose a set of different binary orientations $\theta \in [0, \pi]$ with $\Delta\theta = \pi/10$, but keep the signal polarisation fixed for a polarisation angle $\psi = 0$ and also set $\varphi_S = 0$. We only optimise over the template polarisation, a time shift and the angle φ in the spin-weighted spherical harmonics of the template strain.

The obtained results are illustrated in Fig. 6.10. In both cases we obtain very high matches but observe 1) a mild dependence on the relative orientation in the plane and 2) a strong dependence on the binary's orientation θ. The minimal match is $\mathscr{M}_{\min} = 0.95$ in both cases. We find that the lowest matches are clustered around $\theta \in [0.8, 2.1]$ and $\phi_{1,2} \in [0, 0.3] \cup [2.6, 3.6] \cup [5.8, 6.3]$. In Fig. 6.11 we show the explicit matches for three different initial relative angles $\phi_{1,2}$ as a function of the inclination of the binary. We find that the matches are relatively symmetric around $\theta = \pi/2$ as already suggested by the contour plots. However, depending on the initial in-plane angle enclosed by $\vec{S}_{1\perp}$ and $\vec{S}_{2\perp}$, we observe an overall shift towards lower matches. The lowest matches are obtained for $\phi_{1,2}$ close to

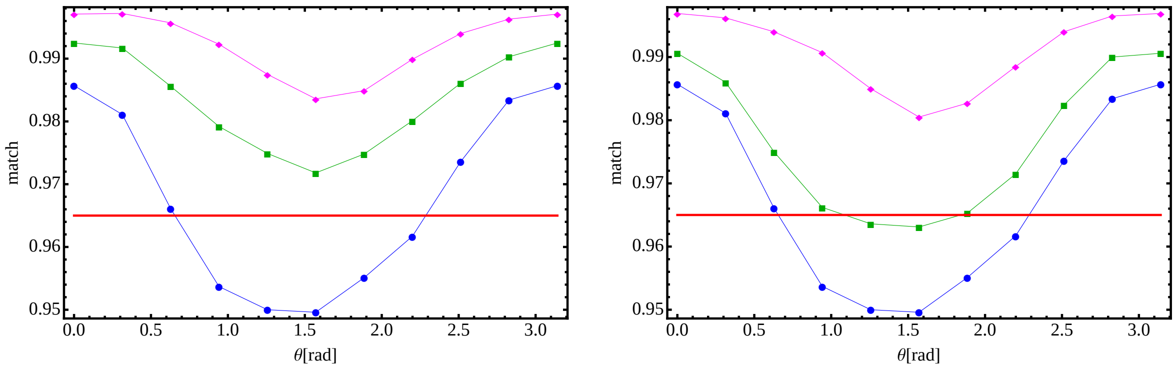

Figure 6.11: The left panel shows the match for the extremal case with varying in-plane orientation of $\vec{\chi}_1$, the right panel shows the contour for varying orientation of $\vec{\chi}_2$ as a function of the binary orientation θ for three different relative angles: $\phi_{1,2} = 0$ (blue), $\phi_{1,2} = 45°$ (green) and $\phi_{1,2} = 90°$ (magenta). The horizontal red line indicates a match of 0.965.

$0, \pi$ and 2π. For those orientations, the in-plane spin-spin contribution to the phase (i.e., $|\cos\phi_{1,2}| = 1$; see Eq.(3.23)) is maximised. This is the case at the initial time, when all orbital elements evolve more slowly and therefore we subsequently expect a significant difference in the GW phase evolution. We conclude that the main effect of the reduced parameterisation in this particular setup is the complete neglect of in-plane spin-spin coupling contribution. Although it varies with time, its magnitude is set by the initial value. Further, systems close to being edge-on are not faithfully recovered by the template waveforms, but as the match is only marginally below threshold, we expect that it can easily be enhanced by parameter optimisation. Also, waveforms from edge-on binaries will be the weakest signals observed in ground-based detectors.

6.4.1.2 Varying the in-plane spin magnitude

In this section we investigate the influence of the in-plane magnitude. We fix the relative spin orientation to $\phi_1 - \phi_2 = 0$ in this study as we have seen earlier that parallel in-plane spins yield the lowest matches for certain orientations. As before, the signal polarisation is fixed such that $\psi = 0$ and we also set $\varphi_S = 0$; we compute the match for various binary orientations. Firstly, we let $\vec{\chi}_2 = (1, 0, 0)$ and vary the magnitude of the spin on the smaller black hole such that $\vec{\chi}_1 = (\chi_{1x}, 0, 0)$. We then exchange the role of the two black holes and vary $\vec{\chi}_2 = (\chi_{2x}, 0, 0)$. The contours for the matches as a function of the in-plane spin magnitude of one of the holes and the binary orientation θ is shown in Fig. 6.12.

We find that the magnitude of the in-plane spin of the smaller BH is negligible up to $\chi_{1x} \simeq 0.8$ and up to $\chi_{2x} \simeq 0.7$ for the larger one. The lowest matches are recovered for maximal in-plane spins on both black holes, which is consistent with the results regarding the relative orientation. The contours once more indicate the influence of the spin-spin coupling

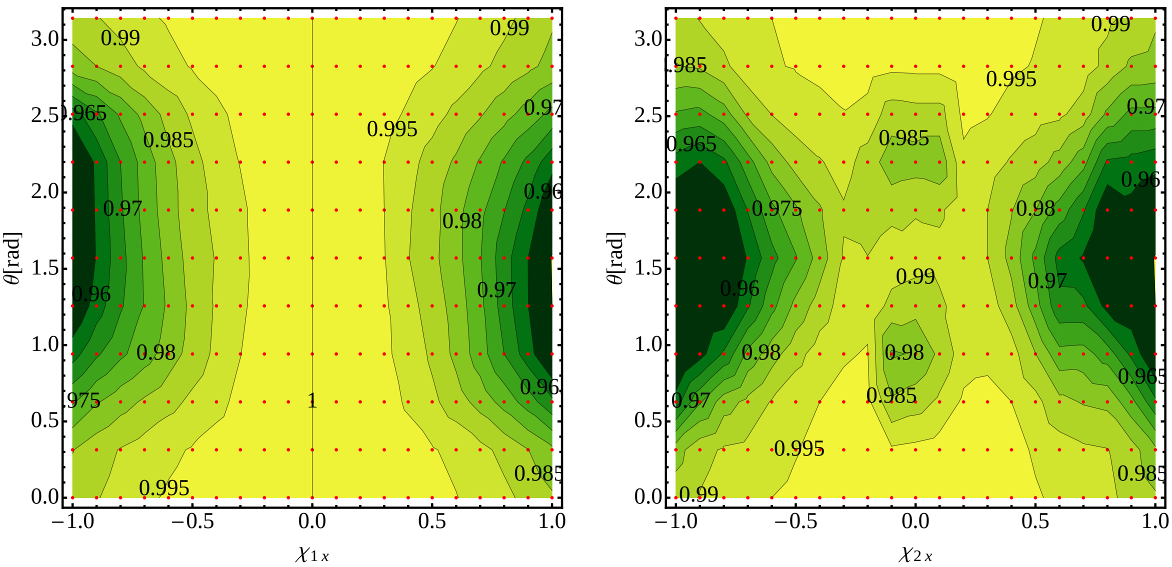

Figure 6.12: The left panel shows the match for $\vec{\chi}_1 = (\chi_{1x}, 0, 0)$ and $\vec{\chi}_2 = (1, 0, 0)$ against the appropriate reduced-parameter waveforms as a function of the binary orientation; the right panel shows the match for $\vec{\chi}_1 = (1, 0, 0)$ and $\vec{\chi}_2 = (\chi_{2x}, 0, 0)$ against the appropriate reduced-parameter template waveforms. The red dots mark the actual configurations used to obtain the contours.

term: from Eq.(3.23) we see that this term is proportional to $\left[\vec{S}_1 \cdot \vec{S}_2 - (\hat{L} \cdot \vec{S}_1)(\hat{L} \cdot \vec{S}_2)\right]$. The second term vanishes initially as we only consider spins in the plane and the first contribution determines the strength of the spin-spin contribution to the phasing. It follows immediately that the spin-spin term becomes more influential the larger the spin magnitudes (note that we have fixed $\hat{S}_1 \cdot \hat{S}_2 = 1$ initially). By applying the mapping to the reduced-parameter waveforms, we completely discard the spin-spin contribution in this example. We observe additional structures in the match contours when $\vec{\chi}_1$ is fixed and the in-plane spin magnitude of $\vec{\chi}_2$ is varied, in particular for $\chi_{2x} \simeq 0$.

6.4.1.3 The influence of parallel spins

The cases considered so far have allowed us to study the influence of the precession to some extent independently to the influence of the inspiral rate. In Chapter 5 we have seen that the precessional dynamics decouples approximately from the inspiral dynamics. The phasing of the in-plane spin cases is only modified by the spin-spin coupling term, which appears at higher PN order, as the otherwise dominant spin-orbit couplings vanish ($\chi_{i||} \equiv 0$). These cases are therefore an ideal testbed to investigate the spin-spin influences. These are, necessarily, very fine-tuned configurations and we wish to investigate more general systems. We now study the following configuration: the spin on the larger black hole is fixed and set to $\vec{\chi}_2 = (0.8, 0, -0.6)$ ($\chi_2 = 1$); we now vary the spin of the smaller black hole $\vec{\chi}_1 = (\chi_{1x}, 0, \chi_{1z})$. The results for three different binary inclinations are shown in Fig. 6.13. The lowest match we obtain is

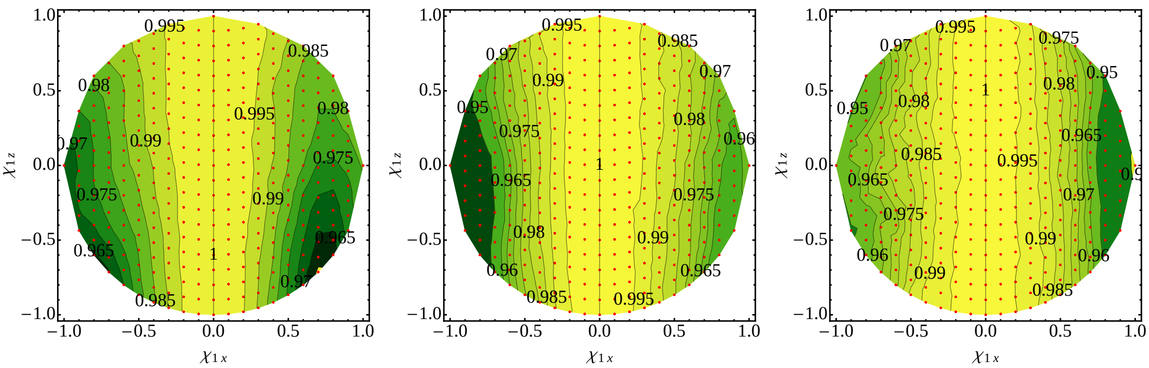

(a) $\theta = 0°$ **(b)** $\theta = 36°$ **(c)** $\theta = 90°$

Figure 6.13: The panel shows the match contours for three different binary inclinations for the configurations where $\vec{\chi}_2 = (0.8, 0, -0.6)$ and $\vec{\chi}_1 = (\chi_{1x}, 0, \chi_{1z})$. Each red dot represents one particular choice of $(\vec{\chi}_1, \vec{\chi}_2)$; all pairs were used to compute the contours. We find that the matches drop with increasing value of χ_{1x} and increasing inclination θ.

$\mathscr{M}_{\rm min} = 0.826$ for the configuration with $\vec{\chi}_1 = (1, 0, 0)$ for $\theta = 126°$. Following Eq.(6.17), the parallel components of the template waveform are the same as in the generic configuration (signal waveform). Keeping this in mind, Fig. 6.13 can be interpreted as follows: if $\chi_{1\perp} = 0$, then the reduced system exactly corresponds to the generic system and therefore obtain matches $\mathscr{M} = 1$. For $\chi_{1z} = 0$ we see a decreasing agreement with increasing $|\chi_{1\perp}|$ due to the neglect of the in-plane contribution to the spin-spin coupling. In between these extremes we see nearly vertical contours indicating that the mismatch is indeed dominated by the neglect of $(\hat{S}_1 \cdot \hat{S}_2)_\perp$ and rather independent of the parallel spin components as these are preserved in the particular mapping we use. Further, we note that the values of match contours decrease with increasing inclination.

6.4.2 Statistical analysis: a random sample of precessing configurations

Previously, we have analysed a handful of test cases, which allowed us to extract trends along several directions in the configuration space. Further, we were able to investigate the influence of the in-plane spin-spin coupling, which is completely neglected in our approximation. In order to quantify the goodness of the reduced-parameter configurations across the precessing binary parameter space, a statistically significant sample of all possible configurations needs to be analysed at various mass ratios. We construct 10,000 random binary spin configurations with uniform sampling in the dimensionless spin magnitudes $\chi_{1,2} \in [0, 1]$, the spin azimuth angles $\phi_{1,2} \in [0, 2\pi]$ as well as the cosine of the spin inclinations $\cos\theta_{1,2} \in [-1, 1]$.

This random set of spin pairs allows us to compute the distribution of the initial precession cone opening angles ι_0 for the sample at a given mass ratio and initial separation. The opening angles for the mass ratio $q = 3$ are shown in Fig. 6.14.

In the subsequent analysis of the sample, we quantify the agreement between the $(l = 2)$-

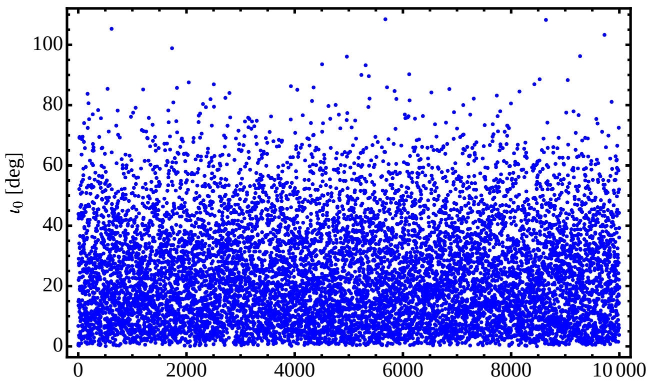

Figure 6.14: The panel shows the distribution of initial precession cone opening angles for the statistical sample computed from the initial spins $\vec{S}_i$ and the initial Newtonian orbital angular momentum L_N for an initial separation of $D_i = 40M$ and a mass ratio of $q = 3$.

waveform strain

$$h(t;\theta,\varphi) = \sum_{m=-2}^{2} h_{2m}(t) Y_{2m}^{-2}(\theta,\varphi)$$

for each configuration in the sample with its corresponding template waveform h^T given by Eq.(6.17) by computing the match $\mathscr{M}$. We optimise only over the following subset of extrinsic parameters: the polarisation σ of the template waveform, the azimuth φ in the spin-weighted spherical harmonics in the reduced-parameter GW strain as well as a time shift Δt. We repeat this match computation for each configuration for the signal polarisation angles $\psi \in \{0., \pi/8, \pi/4, 3\pi/8\}$ as well as for the binary orientations $\theta \in \{0, \pi/10, \pi/4, 2\pi/5, \pi/2, 3\pi/5, 4\pi/5, 11\pi/12\}$ with $\varphi_S = 0$. This yields 32 individual matches per configuration and a total of 320,000 matches. We repeat this calculation for various mass ratios but fix the following parameters in the analysis: the initial separation $D_i = 40M$ to obtain reasonably long inspiral waveforms in the time domain, which are sampled at $10M$. We set the total mass to $M = 12M_\odot$. This is an ad hoc choice, but was made to allow a wide frequency range in band, to minimise the effects of merger and ringdown and for reasons of computational cost efficiency. We fix the upper cutoff frequency to be $\mathrm{Mf}_{\mathrm{ISCO}} = (\pi 6^{3/2})^{-1}$ and use the anticipated early PSD noise curve for aLIGO [204].

6.4.2.1 Results for $q = 1$

As highlighted earlier, we expect our effective mapping to perform worse in the equal mass case. Apostolatos et al. [20] showed that for equal mass binaries the relative orientation between the two spin vectors, i.e. $\vec{S}_1 \cdot \vec{S}_2$, is constant in time if spin-spin term are neglected – the two spins are locked and therefore the binary follows the evolution of a single spin binary with a total spin magnitude $S = ||\vec{S}_1 + \vec{S}_2|| = \text{const}$. Since the in-plane spins rotate with the same precession frequency, the idea of averaging over the continuous change of the relative orientation is not applicable anymore as is illustrated in Fig. 6.8.

Therefore, we expect the equal-mass limit to provide a stringent test of the effectiveness

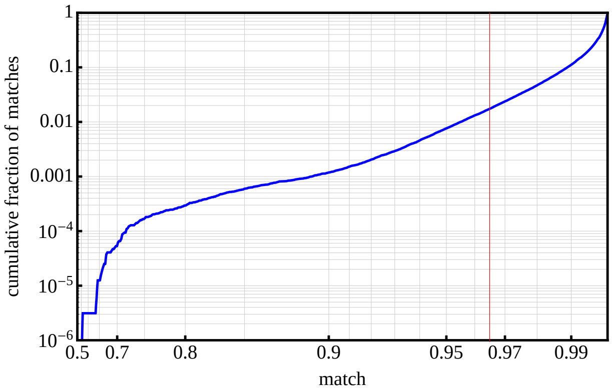

Figure 6.15: The panel shows the cumulative distribution function for all matches for the mass ratio $q = 1$ (blue). The red vertical line indicates a match of $\mathscr{M} = 0.965$. Only a fraction of 1.8% of all matches from the sample are below threshold.

of the χ_p-parameterisation. The cumulative distribution function (CDF) for the statistical sample is shown in Fig. 6.15. Surprisingly, we find that only 1.78% of all matches are below 0.965, showing that even in the equal-mass limit the precession in the system is faithfully represented by the effective precession parameter χ_p for most binary configurations and orientations. A total of 88.5% have a match $\mathscr{M} \geq 0.99$; the minimum match found is $\mathscr{M}_{\text{min}} = 0.558$ for the following spin configuration: $\{\chi_1, \theta_1, \phi_1\} = \{0.77, 0.25, 0.72\}$ and $\{\chi_2, \theta_2, \phi_2\} = \{0.49, 2.60, 1.06\}$[4], where the polar angles denote the orientation of $\vec{\chi}_i$ in the Cartesian source frame $\hat{L} \equiv \hat{z}$ with $\psi = \pi/4$ and $\theta = \pi/2$.

6.4.2.2 Results for $q = 3$

We expect the effective precession spin to work even better in the regime of comparable mass ratios as the averaging becomes more and more applicable due to mass weighting in Eq.(6.7) – the higher the mass ratio, the more negligible the spin on the smaller black hole for a wide range of $(\chi_{1\perp}, \chi_{2\perp})$-combinations (see Fig. 6.6). Mass ratio $q = 3$ provides us with the possibility to test the approximation in the lower mass-ratio end, where we do not yet have to be concerned about a wealth of cases that might undergo transitional precession [144]. The cumulative distribution function for $q = 3$ is shown in Fig. 6.16. Similar to the equal-mass study, we find that only a marginal fraction of 1.76% of all computed matches is below threshold. We have performed an additional analysis with randomly chosen azimuthal orientation φ_S of the binary. The results are illustrated in the right panel of Fig. 6.16: we find almost identical results and conclude that the restriction $\varphi_S = 0$ has no significant influence on the results.

The CDF for $q = 3$ and $q = 1$ look very similar, although the tail of the CDF towards low matches in Fig. 6.16 is much flatter than in Fig. 6.15, which is rather surprising at first glance. It can be explained by the pronounced error introduced for cases with very little precession, which are not well captured by χ_p. We find the lowest match to be $\mathscr{M}_{\text{min}} = 0.532$

[4]This is configuration number #3893 in the sample file.

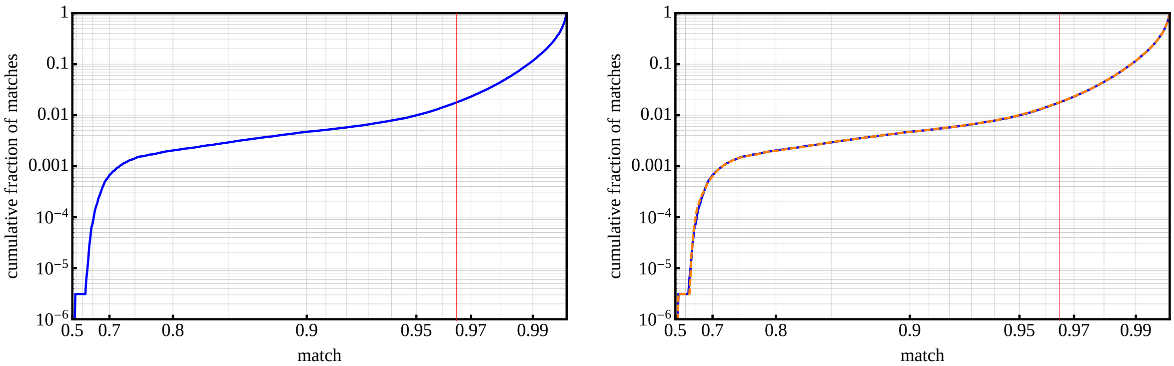

Figure 6.16: The left panel shows the cumulative distribution function for all matches computed from the complete set of 10,000 distinct spin configurations at mass ratio $q = 3$ (blue). The red vertical line indicates a match of $\mathscr{M} = 0.965$. Only a fraction of 1.76% of all matches are below threshold. The tail is flatter than for $q = 1$ as configurations where the spin of the smaller black hole dominates the precession are not faithfully represented by the choice of χ_p. The right panel shows the CDF for randomly chosen azimuthal orientations ($\varphi_S \neq 0$) of the signal (orange). We find no significant difference.

for the configuration $\{\chi_1, \theta_1, \phi_1\} = \{0.83, 2.44, 6.20\}$ and $\{\chi_2, \theta_2, \phi_2\} = \{0.80, 0.31, 2.31\}$[5], for $\psi = \pi/4$ and $\theta = \pi/2$.

Further, we find that a total of 1699 configurations are precession-dominated by the smaller black hole. However, only 4.7% of matches computed for those configurations result in a match below threshold. Further, we find that these sub-threshold matches are predominantly clustered around values for $\chi_{2\perp} \leq 0.08$, which is illustrated in the density plot in Fig. 6.17. We conclude that χ_p faithfully represents binaries that are precession-dominated by the smaller black hole – only systems with very little precession are not faithfully approximated.

6.4.2.3 Results for $q = 10$

In Fig. 6.6 we have seen that it is rather difficult to generically construct a precessing case, where the precession is dominated by the in-plane spin of the smaller black hole. We therefore expect the mapping onto the reduced-parameter waveforms to be even more faithful for higher mass ratios such as $q = 10$. On the other hand, we now expect transitional precession to occur more often within the sensitivity band of aLIGO. In order to identify the occurrence of transitional precession, we compute the angle between $\hat{J}(t_{\mathrm{end}})$ and $(0, 0, 1)$ at the end of the PN evolution. The angles $\theta_J(t_{\mathrm{end}})$ for the sample are shown in Fig. 6.18. The fraction of configurations undergoing either the full transitional phase or at least a part of this phase in band is 1.8% of all binary configurations in the sample[6].

We illustrate the results in the form of the cumulative distribution function (CDF) of the

[5] This is configuration number #1522 in the sample file.

[6] Following Apostolatos et al. [20], we impose the criterion that $\measuredangle(L, S) \geq 164°$ initially to determine the fraction of transitional cases.

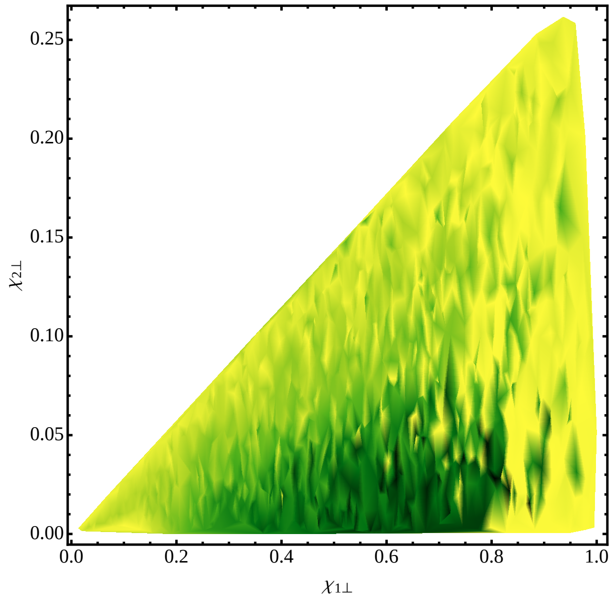

Figure 6.17: The plot shows the density of matches below threshold $\mathscr{M} < 0.965$ for all configurations in the sample that are precession-dominated by the smaller black hole. We see that the density of low matches is significantly higher for cases with $\chi_{2\perp} \leq 0.08$ (darker).

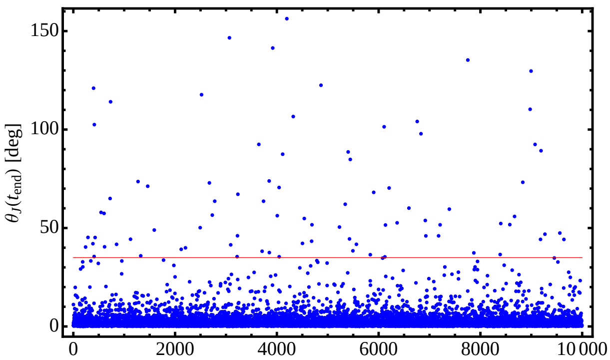

Figure 6.18: The panel shows the angle between $\hat{J}$ and the z-axis at the end of the PN evolution. We find several cases, which partially or fully undergo transitional precession within the frequency band of aLIGO. The red horizontal line indicates the maximal θ_J-angle found for $q = 3$.

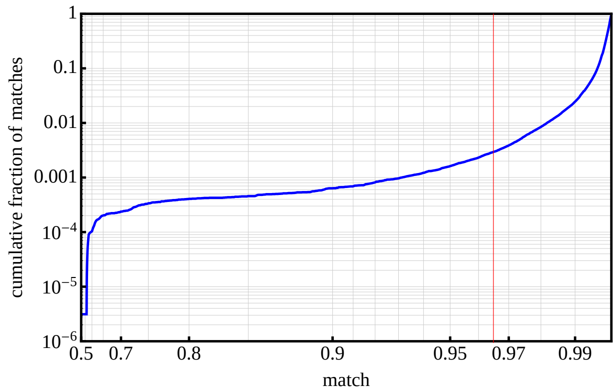

Figure 6.19: The panel shows the cumulative distribution function for all matches computed from the complete set of 10,000 distinct spin configurations at mass ratio $q = 10$ (blue). The red vertical line indicates a match of $\mathscr{M} = 0.965$. Only a fraction of 0.3% of all matches are below threshold.

match in Fig. 6.19. As expected, the tail is much flatter than for the low mass ratio end with a fraction of only 0.3% of all matches below threshold. The minimum match obtained is $\mathscr{M}_{\text{min}} = 0.484$ for the configuration $\{\chi_1, \theta_1, \phi_1\} = \{0.74, 1.65, 3.85\}$ and $\{\chi_2, \theta_2, \phi_2\} = \{0.60, 3.11, 1.23\}$[7], which undergoes the full transitional phase in band. The final angle between $\hat{J}$ and $(0, 0, 1)$ is $146.6°$. We illustrate the details of this particular case in the subsequent section.

6.4.3 Transitional precession

The analysis of the random spin configurations evaluated for the mass ratio $q = 10$ has revealed the occurrence of a very small number of initial spin configurations, which undergo partial or full transitional precession in band. As expected, these cases give, for certain orientations and polarisations, matches significantly below threshold, yielding matches as low as ~ 0.4.

Transitional precession occurs when the total spin $\vec{S}$ and the orbital angular momentum $\vec{L}$ have similar magnitude but are directed nearly opposite such that the magnitude of the total angular momentum J is small. For this to occur in the frequency band of ground-based GW detectors, the companions need to have very fine-tuned parameters when they enter the sensitivity band: the separation must not be too large as then $L \gg S$, and $\hat{S} \simeq -\hat{L}$ at the same time. A binary might start in a simply precessing phase, then undergoes the transitional phase if the appropriate conditions are fulfilled and then goes back into a state of simple precession, unless the binary has already merged. Fig. 6.20 shows the evolution of the precession angles $(\iota(t), \alpha(t))$ for the transitional configuration described previously. The corresponding reduced-parameter configuration is given by $\vec{\chi}_1 = (0, 0, -0.061)$ and $\vec{\chi}_2 = (0.058, 0, -0.596)$. The comparison of the two precession angles α and ι from the transitional configuration with its corresponding template configuration reveals a strong disagreement. This can be explained as follows: for transitional precession to also occur in the reduced-parameter configuration, it is crucial that parallel component of the total spin is close to $S_{||}$ in the generic configuration.

[7]This is configuration number #3068 in the sample file.

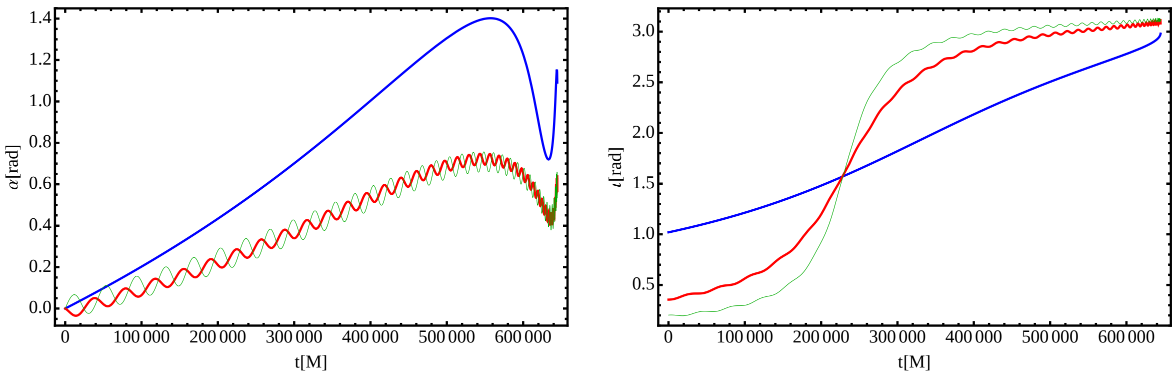

Figure 6.20: The left panel shows the PN evolution of the precession angle α for the transitional precession case described in the text (red) as well as $\alpha(t)$ for the corresponding reduced-parameter template (blue). The right panel compares the two precession cone opening angles. It is clear from those graphs that the mapping does not faithfully reproduce transitional precession. The green curves show the angles for a reduced-parameter system, where the precession is associated with the smaller black hole m_1, which appear to be closer to the angles in the generic system (red).

Since we fix the parallel spin components in the mapping, the fulfilment of this condition is guaranteed. At the same time, however, $S_\perp$ must also be similar to the full-parameter system. If it is too large, the transitional phase occurs at later times, if it is too small, the transition is shifted to earlier times. By construction, χ_p corresponds to an average in-plane spin, which does not necessarily correspond to $S_\perp$ of the generic system. We conclude that the faithful representation of transitional precession is highly sensitive to the initial value of $S_\perp$, but note that a different value of χ_p is in principle capable of capturing transitional precession (see the green graphs in Fig. 6.20), which can be exploited via parameter optimisation.

6.4.4 On the goodness of χ_p

The results obtained so far suggest that the single spin parameter χ_p faithfully represents the precession in a given generic double-spin system. What we have not yet investigated, however, is the goodness of this parameter, i.e., whether the theoretically predicted value of χ_p is the best value, or whether a different value yields better agreement. To do so, we determine the match of a generic case with a series of reduced-parameter configurations, where we vary the value of χ_p. Previously, we have seen that the match strongly depends on orientation θ of the binary as well as the polarisation angle ψ of the signal. We therefore repeat the analysis for several values of θ and ψ. The results are illustrated in Fig. 6.21 for the same configuration as depicted in Fig. 6.5. As expected, we find that for an optimally oriented binary (i.e., $\theta = 0$) the match depends only weakly on the explicit value of χ_p. This is consistent with the results obtained by Ajith [9] and confirms that a large fraction of optimally-oriented precessing binaries is well represented by aligned-spin binaries. For larger inclinations θ, however, the match becomes strongly dependent on χ_p, and the best match is indeed obtained for a χ_p-

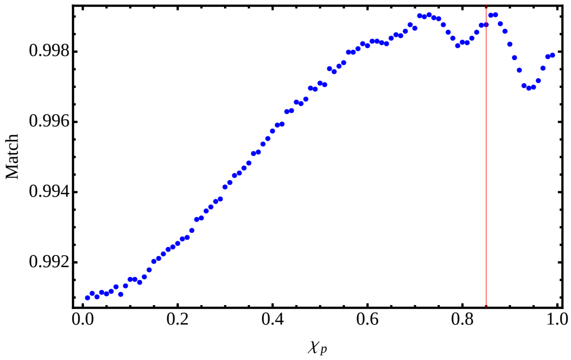

(a) $\theta = 0, \psi = \pi/8$

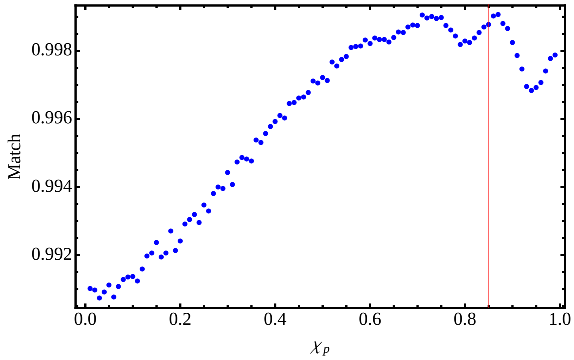

(b) $\theta = 0, \psi = \pi/4$

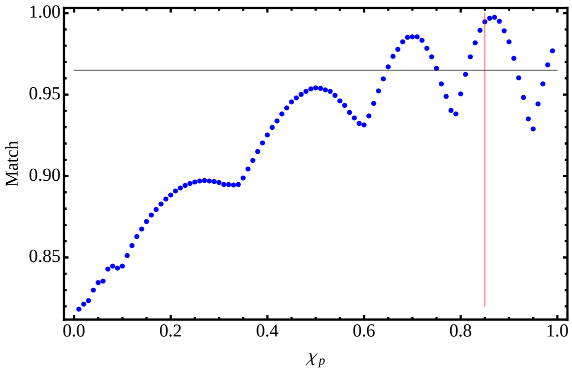

(c) $\theta = \pi/4, \psi = \pi/8$

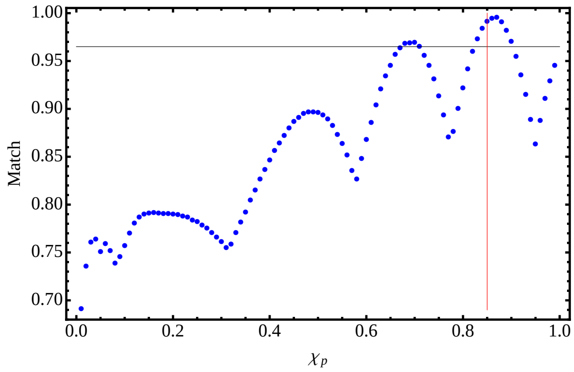

(d) $\theta = \pi/2, \psi = \pi/8$

Figure 6.21: The four panels show the matches for the case depicted in Fig. 6.5 with a series of reduced-parameter configurations with varying χ_p for four different pairs of binary orientation and signal polarisation (θ, ψ) as indicated in each panel. The red vertical line indicates the theoretical χ_p-value; the black horizontal line in the lower two panels indicates the threshold of $\mathscr{M} = 0.965$. We find a strong dependence of the match on the value of χ_p for growing inclinations, where waveform modulations become more pronounced. Moreover, the theoretical χ_p-value is very close to the value yielding the maximal match.

value close to the theoretically predicted one, indicating that χ_p does provide a meaningful parameterisation of the precession and allows for a faithful representation of a generic system in particular for large inclinations. Necessarily, this needs to be investigated in more detail for a larger number of precessing configurations, which is subject to future work.

6.4.5 Comparison with the *Physical Template Family*

It was first suggested by Buonanno et al. [60] in 2004 that a single-spin precessing waveform family is effectual in detecting generic double-spin precessing binaries. This quasi-physical template family (PTF) shows very high fitting factors. However, we are primarily interested in the faithful representation of the precession dynamics of generic binaries by a template family with a reduced set of physical parameters, and in particular how the mapping given in Eq.(6.17) compares to the pure single-spin approximation in PTF.

Let us first point out the differences between the two waveform families: based on the approximate decoupling between the inspiral and precession dynamics, we suggest that the inspiral is well described by the two parallel spin components, whereas the precession can be encapsulated in a complementary spin parameter. This yields a double-spin system with three spin parameters as given in Eq.(6.17). PTF, on the other hand, assigns the total spin S of the double-spin configuration to the larger black hole, resulting in a pure single-spin system, obtained by the following map:

$$\vec{\chi}_1 \mapsto (0, 0, 0), \tag{6.27}$$

$$\vec{\chi}_2 \mapsto \frac{\vec{\chi}_1 m_1^2 + \vec{\chi}_2 m_2^2}{m_2^2} \tag{6.28}$$

By comparing Eq.(6.17) with Eq.(6.27) we see immediately that they differ significantly. A direct comparison between those mappings allows us to establish which of them yields a more faithful representation of precessing inspiral waveforms.

We have investigated the faithfulness of both approximations for equal-mass and the comparable mass ratio $q = 3$ using the same sample of generic spin configurations as before. We apply our proposed mapping to each configuration as well as the PTF mapping and compute the matches with the double-spin configuration. Fig. 6.22 shows the cumulative distribution function for both mappings and the two mass ratios in direct comparison. For $q = 3$, we find that the mapping suggested by PTF results in 52.8% of all matches smaller than 0.965 compared to on $\sim 2\%$ for the mapping given in Eq.(6.17). We therefore conclude that the assignment of the total spin to the larger black hole does not yield a particularly faithful representation of the generic double-spin system, whereas the split into the parallel spin components $\chi_{i||}$ and χ_p yields matches above threshold for $\sim 98\%$ of all computed matches. At first glance, the results for the equal-mass case are rather surprising: we expect equal-mass precessing binaries to follow the evolution of single-spin binaries with the same total spin on one black hole [20]. However, this is only an exact statement if spin-spin couplings are neglected. Our proposed mapping also includes the coupling part $\left(\vec{S}_{1||} \cdot \vec{S}_{2||}\right)$, and performs similar to PTF in the equal-mass case.

6.4.6 χ_{eff}-parameterisation of the inspiral rate

In the analysis presented so far, we have kept the parallel spin components in the reduced-parameter system the same as in the full-parameter system. However, in Chapter 5 we have demonstrated that the secular evolution of the inspiral of precessing binaries is comparable to the inspiral rate of aligned-spin binaries parameterised by the effective inspiral spin χ_{eff} as given in Eq.(5.10). With the construction of a complete inspiral-merger-ringdown model of precessing binaries in mind, we now investigate the effect of the neglect of $\chi_{1||}$ and instead

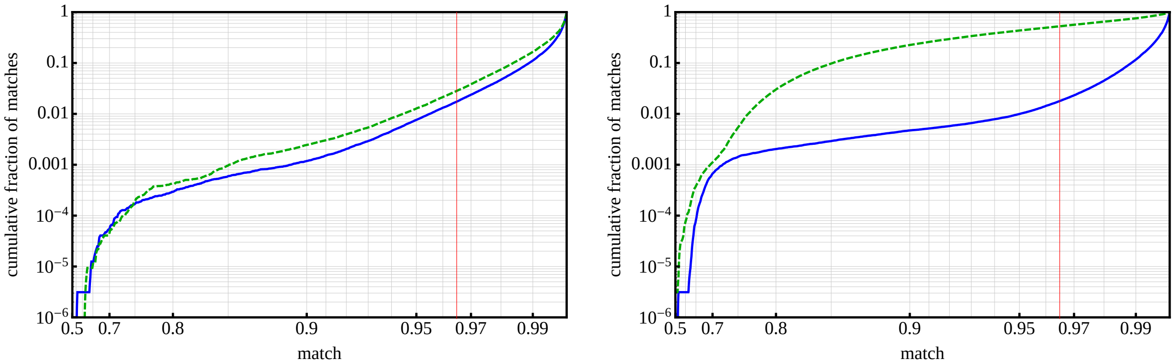

Figure 6.22: The two panels show the CDF for our proposed reduced-parameter mapping (blue) in comparison to the mapping provided by PTF (green). The left panel shows the results for the equal-mass case, the right panel for $q = 3$. Whereas only 1.76% of all matches are below threshold for our mapping, a significant fraction of 56% match below $\mathscr{M} \leq 0.965$ when the total spin is assigned to the larger black hole. For the equal-mass limit we find no significant difference between the PTF-parameterisation and χ_p.

use the effective inspiral spin. Schematically, the parameter-reduced template configuration as defined with respect to $\hat{L} \equiv \hat{z}$ is then given by:

$$\begin{aligned} \vec{\chi}_1 &\mapsto (0,0,0) \\ \vec{\chi}_2 &\mapsto\mapsto \left(\chi_p, 0, \frac{113\chi_{\rm eff}}{(113-76\eta)}\right). \end{aligned} \tag{6.29}$$

As an alternative effective parameterisation of the inspiral rate, without violating the physical range of the dimensionless spins, we will also choose the parallel spins to be equal and fulfilling

$$\chi_{i||} = 2\chi_{\rm eff}\left(1 - \frac{76\eta}{113} - \frac{\delta M}{M}\right)^{-1} \tag{6.30}$$

We investigate the faithfulness of these effective parameterisations using the same spin configurations as in the rest of this chapter and evaluate the matches for the comparable mass ratio $q = 3$. Fig. 6.23 illustrates the results in the form of the cumulative fraction of matches as a function of the match. We find that for the $\chi_{\rm eff}$-parameterisation as given in Eq.(6.29), $\sim 13.3\%$ of all matches are below the threshold, for the alternative effective parameterisation $\sim 15.5\%$ of all matches are ≤ 0.965. This is a rather large fraction compared to 1.8% we obtained by keeping the parallel spin components fixed. With the effective parameterisation of the inspiral, we have introduced an error in the secular phasing as well as the description of the precession dynamics, which leaves us with a significantly larger fraction of matches below threshold. However, we have not explored whether the matches would increase at the cost of parameter accuracy.

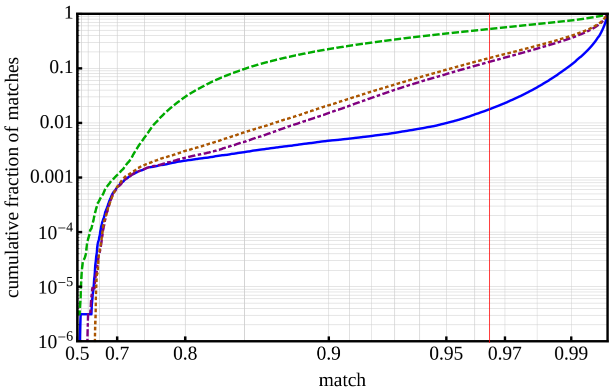

Figure 6.23: The panel shows the cumulative distribution function for $q = 3$ for the reduced parameterisation given by Eq.(6.17) (blue), the parameterisation suggested by PTF Eq.(6.27) (green), the χ_{eff}-parameterisation as given in Eq.(6.29) (purple) and the alternative χ_{eff}-parameterisation (orange) as given in Eq.(6.30). The match threshold of 0.965 is indicated by the red vertical line.

6.5 Discussion

In this chapter, we have explored the possibility of parameterising the precession in a generic double-spin system with only one precession spin. To obtain this parameter reduction, we have suggested a combination of a set of spin parameters, which are predominantly responsible for the leading-order precession effects in inspiral waveforms, into one effective precession spin χ_p. The definition of this parameter is motivated by the PN evolution equation for the orbital angular momentum L, which encodes the leading-order precession dynamics of the binary system. We have illustrated that the precession rate of the orbital angular momentum, i.e. $||\dot{\hat{L}}||$, is an oscillatory function over the course of the PN evolution. However, we postulated that the average precession exhibited by a generic system should be given by the mean of the precession rate. We have shown that the mean precession is well approximated by the precession spin χ_p, which is defined purely from the initial spins and the mass ratio.

In order to test whether the precession in generic systems is indeed well described by the average precession, we have computed matches between the waveforms from random binary configurations and their corresponding reduced-parameter configuration. Our results indicate that a reduced-parameter system built such that its initial precession rate corresponds to the average precession rate of the generic system indeed shows a very similar precession dynamics and the waveforms therefore have high overlaps (faithfulness). We have repeated the analysis for the mass ratios $1, 3$ and 10 using the same sample of $10,000$ arbitrary binary configurations. As expected, χ_p approximates the average precession rate better with increasing mass ratio: by definition, χ_p is the geometric mean of the in-plane spin orientation, under the assumption that the magnitudes $S_{i\perp}$ change only minimally. When the equal-mass limit is approached, the in-plane spins rotate at the same rate, therefore averaging over the spin orientation becomes invalid and χ_p approximates the true average precession rate less accurately. For moderate mass ratios ($q = 3$ to $q = 10$) we find that χ_p parameterises the precession very well. We will see in the next chapter how crucial the faithful representation of a precessing system defined intrinsically by seven physical parameters by a system with only four physical parameters is in order to construct simple analytic expressions for the precession angles $\alpha(t)$ and $\iota(t)$.

We have seen in Chapter 5 that the inspiral and precession dynamics decouple, and that the inspiral is well governed by the spin components parallel to L. In order to model the precession in the system, we have shown that only one extra spin parameter, χ_p, is needed to faithfully capture the precession of a given generic binary configuration. However, comparison with other possible parameterisations suggests that in order to accurately model the waveforms of precessing black hole binaries it is crucial to accurately describe the inspiral *and* the precession motion. Using the total spin of the generic binary or invoking different variations of the $\chi_{\rm eff}$-parameterisation has resulted in matches below 0.965 for more than $\sim 50\%$ respectively $\sim 15\%$ of all computed matches. In both cases (i.e., PTF and $\chi_{\rm eff}$), the inspiral rate as well as the precession description are altered. In particular, in the case of the effective parameterisation, the initial opening angle ι was modified and therefore χ_p not only needs to capture the bulk precession features, but also needs to compensate for the error in the inspiral phase, which results in biases of the physical parameters. However, our results also suggest that the effective parameterisation of the inspiral rate in combination with χ_p yields a significantly more faithful representation of a generic system than the PTF choice.

In previous efforts, either the inspiral or the modulations due to precession were described either inaccurately or in an ad hoc way with many degrees of freedom. Our results suggest that the effective parameterisation of the precession models the modulations accurately for most configurations and, in particular, binary orientations. Previous studies have already shown that the waveforms of optimally-oriented precessing binaries can be detected with aligned-spin binaries as the modulations in amplitude and phase strongly depend on the binary orientation (see e.g. [9]). Arbitrarily inclined systems, however, are not faithfully matched by aligned-spin waveforms and for a large volume of the binary parameter space, not even fitting factors above threshold can be obtained. Our results indicate that most binary inspirals are faithfully represented by precessing waveforms in the parameter manifold $\{q, \chi_{1||}, \chi_{2||}, \chi_p\}$ for arbitrary orientations and polarisations.

However, in this analysis we have focussed on inspiral waveforms only. It remains to be seen whether χ_p is a meaningful precession parameter during the late inspiral and merger. Further, we have not investigated the improvement of matches by optimising physical parameters. Therefore, the matches quoted here are lower bounds and are expected to improve at the cost of parameter accuracy. Some of these issues will be addressed in the next chapter.

CHAPTER 7

PhenomP

A first approximate phenomenological waveform model for precessing compact binaries

In this chapter, we present a prototype precessing IMR waveform model, henceforth referred to as "PhenomP", which captures the basic phenomenology of the full seven-dimensional parameter space of binary configurations with *only three physical parameters*. Its construction is entirely based on the ideas outlined in Chapter 5 and Chapter 6: firstly, we use an existing aligned-spin IMR waveform model parameterised by two physical parameters, the mass ratio and an effective spin $\chi_{\rm eff}$, to describe the secular motion and phasing of the binary as first suggested in [197]. Motivated by the results in Chapter 6, the aligned-spin waveform is then convolved with an approximate description of the precessional motion parameterised by only one additional physical parameter, the effective precession spin χ_p as introduced in Sec. 6.2.3. In other words, we simply "twist-up" an existing aligned-spin waveform model with an approximate model of the precessional motion as sketched in Eq.(5.19).

The fast and efficient generation of waveforms is essential for GW searches using the matched filtering algorithm as well as for source parameters measurements. For this purpose, we construct the precessing waveform model in the *frequency domain*. We have tested the model's fidelity for GW applications by comparison against PN-NR hybrid waveforms for a variety of configurations, but we emphasise that these numerical simulations were *not* used in the construction of the model. This prototype model is an ideal testbed to develop GW searches, to study the implications for astrophysical measurements, and, perhaps most importantly, as a simple conceptual framework to form the basis of generic-binary waveform modelling in the advanced-detector era. The work presented in this chapter has been adapted

from the following version of a paper submitted for publication:
[117] Mark Hannam, Patricia Schmidt, Alejandro Bohé, Leila Haegel, Sascha Husa, et al. "Twist and shout: A simple model of complete precessing black-hole-binary gravitational waveforms", submitted to Phys. Rev. Letters, 2013 (see arXiv:1308.3271v1 [gr-qc]).

7.1 Introduction

The inspiral and merger of black-hole binaries constitutes one of the most promising GW sources for ground-based interferometric GW detectors. As outlined in Chapter 2, the commonly used detection and interpretation strategies of these signals require analytic models that capture the phenomenology of all likely binary configurations; most of these will include complex precession effects due to the black-hole spins (see Chapter 3 for more details). However, most of the currently available waveform models of the two black holes' inspiral, merger and ringdown of the final black hole, only consider configurations where the black-hole spins are aligned with the binary's orbital angular momentum and therefore *do not* model precession.

While the binary's early inspiral can be modelled well with analytic PN calculations, the late inspiral and merger require 3D numerical solutions of the full nonlinear Einstein equations. In the case of generic binary configurations, these expensive NR calculations must span a binary parameter space that covers, for non-eccentric inspiral, seven dimensions: the mass ratio of the binary and the components of each black hole's spin vector. Previous work on phenomenological models of non-precessing binaries suggests that we require at least four simulations in each direction of parameter space that we intend to model [11, 12, 192]. This implies that we need $4^7 \approx 16,000$ numerical simulations to model the full parameter space, which is unfeasible in the near future. Therefore, it is necessary to identify approximations and degeneracies that make the task tractable and allow for reductions of the number of model parameters.

In Chapter 5 we identified an approximate mapping between inspiral waveforms from generic binaries and those from a *two-dimensional* parameter space $\{q, \chi_{\rm eff}\}$ of non-precessing binaries [197]. This approximation holds because precession has little effect on the inspiral rate and so precession effects approximately decouple from the overall inspiral. The inspiral can be described by an aligned-spin-binary model, neglecting the effect of breaking equatorial symmetry, which is responsible for large recoils [54]. We further proposed that, given a model for the precessional motion of a binary, we could construct an approximate waveform by "twisting up" the appropriate non-precessing-binary waveform with the precessional motion [197]. This technique was subsequently adopted to produce simple frequency-domain PN inspiral waveforms [148]. It was more recently suggested that this mapping also holds through merger and ringdown [176]. In this work we take this idea even further, in two crucial ways.

Based on the reduced-parameter mapping introduced in Chapter 6, firstly we use a high-order but single-spin PN description for the precession angles $(\iota(t), \alpha(t))$ to twist up a phenomenological inspiral-merger-ringdown model for aligned-spin binaries [192] known as "PhenomC". Secondly, we incorporate precession effects into the estimate of the final black-hole spin in the ringdown model [28]. These two additions allow us to provide the first frequency-domain inspiral-merger-ringdown model of generic binaries.

Additionally, we make use of the *single* complementary spin parameter introduced in Chapter 6 that captures the basic precession phenomenology of generic binary configurations [198]. Our final model has only *three* dimensionless physical parameters: the two parameters of previous aligned-spin models (the mass ratio $q = m_2/m_1 \geq 1$, an effective spin, χ_{eff}, which characterises the rate of inspiral), plus one additional parameter, the *effective precession spin*, χ_p.

The purpose of this model is to a) facilitate the development of computationally efficient generic-binary searches, b) provide a starting point to investigate the parameter-estimation possibilities (and limitations) of generic-binary observations in second-generation detectors and their astrophysical implications, and c) as a simple framework for the construction of more refined models calibrated to NR simulations. If the dominant parameter space of binary simulations can be reduced from seven to three dimensions (mass ratio, effective spin, precession spin), it may be feasible to produce a sufficient number of NR waveforms (∼100) to calibrate the model well before advanced detectors reach design sensitivity in 2018-20 [3]. The model can be further refined, based on the results of these studies. As such, this model provides a practical road map to model generic binaries to meet the needs of GW astronomy over the next decade. The model is provided in the LIGO Algorithm Library (LAL) data analysis software, to facilitate the development and testing of search and parameter estimation pipelines [2].

7.2 The waveform model

Following the idea of "twisting-up" a spin-aligned waveform model, our starting point is the frequency-domain IMR waveform model "PhenomC" by Santamaria et al. [192]. It is a phenomenological waveform model for aligned-spin black-hole-binaries, which includes the current state-of-the-art inspiral phase, TaylorF2 [22, 83, 85]. This particular waveform model describes the $(l = 2, m = |2|)$-modes of the waveform given as

$$\tilde{h}(f) = \tilde{A}(f) e^{i\tilde{\psi}(f)}, \tag{7.1}$$

where the GW amplitude $\tilde{A}(f)$ and phase $\tilde{\psi}(f)$ are given in [192].

Apart from the computational improvements, another advantage of constructing a waveform model in the frequency domain rather than in the time domain is the simple relation between the strain h and Ψ_4. In the time domain, they are related via two time integrations This is important since the construction of an IMR model requires the inclusion of numerical information. While integration amplifies numerical noise and also requires to fix the integration constants, in the frequency domain the integration is replaced by simple division:

$$\tilde{h}(f) = -\frac{\tilde{\Psi}_4(f)}{4\pi^2 f^2}. \tag{7.2}$$

Based on the approximate identification described in detail in Chapter 5, we map a given generic binary to the appropriate non-precessing waveform parameterised by $(M, \eta, \chi_{\rm eff})$, where $\eta = q/(1+q)^2$ is the symmetric mass ratio and $\chi_{\rm eff}$ differs slightly from the Eq.(5.10) (which is only appropriate for pure PN waveforms) and is given by:

$$\chi_{\rm eff} = \frac{m_1 \vec{\chi}_1 \cdot \hat{L}_N + m_2 \vec{\chi}_2 \cdot \hat{L}_N}{m_1 + m_2}. \tag{7.3}$$

In binary systems which undergo simple precession, the direction of $\hat{J}$ is approximately constant throughout the evolution, as the loss of angular momentum due to the emission of GWs is predominantly along $\hat{J}$. The emission orthogonal to $\hat{J}$ averages out due to the precession of $\hat{L}$ around $\hat{J}$ [20]. We therefore assume that the final spin is in the same direction as $\hat{J}$ through the inspiral. In order to account for precession affecting the final spin, we update the PhenomC final spin magnitude using the final spin formula in Barausse et al. [28] with only one black hole spinning.

We then approximate the $(l = 2)$-modes of a precessing binary waveform in the time domain by rotating the dominant modes of the corresponding non-precessing waveform [196, 197]. In the previous chapters, we have quadrupole-aligned the precessing waveform modes in order to obtain the evolution of the dominant emission direction. We have further seen that the identified direction denoted by the general Euler angles (β, γ) corresponds to the direction of the orbital angular momentum $\hat{L}$. At leading-order, however, the post-Newtonian orbital angular momentum *is* the Newtonian orbital angular momentum – the QA angles therefore approximately correspond to (ι, α). Making use of this approximation, we can write the precessing waveform modes in the time domain by inverting Eq.(5.8) and replacing the QA angles by

$$\beta(t) \mapsto -\iota(t), \tag{7.4}$$

$$\gamma(t) \mapsto -\alpha(t), \tag{7.5}$$

to obtain

$$h^P_{2m}(t) = e^{-im\alpha(t)} \sum_{|m'|=2} e^{im' \int \dot{\alpha}(t) \cos\iota(t)} d^2_{m'm}(-\iota(t)) h_{2m'}(t), \tag{7.6}$$

where $d^l_{m'm}$ denotes the Wigner d-matrices and $h_{2|m'|}$ are the aligned-spin modes from PhenomC. The angles α and ι that enter our model are defined as the polar angles parameterising the direction of the orbital angular momentum in the $\hat{J}_0$-aligned source frame as illustrated in Fig. 3.5.

During the inspiral phase, the angles and the waveform amplitude vary slowly on the precession timescale with respect to the orbital timescale (see Fig. 3.6), which allows us to make use of a stationary-phase-approximation (SPA) transformation from the time to the frequency domain. In the time domain we have assumed that the inspiral motion is well described by a series of quasi-circular orbits. The stationary-phase-approximation is the natural translation of the stationarity condition for the adiabatic inspiral regime in the time domain into the frequency domain. Its starting point is the Taylor expansion of the orbital phase of the binary $\Phi_{\text{orb}}(t)$ around a fixed point in time t_f such that

$$m\dot{\Phi}_{\text{orb}}(t_f) = 2\pi f, \tag{7.7}$$

yielding the GW phase in the frequency domain

$$\tilde{\psi}_{lm}(f) = 2\pi f t_f - m\Phi_{\text{orb}}(t_f) - \frac{\pi}{4}. \tag{7.8}$$

The above expressions can be rewritten in terms of the PN expansion parameter $v(t_f) = (M\dot{\Phi}_{\text{orb}}(t_f))^{1/3}$. The time $t(v)$ then corresponds to the time at which the binary is at the frequency corresponding to v and $\phi(v)$ is the phase of the binary at v. The PN expansions for each of these functions are known for aligned-spin systems. Precession, however, alters the frequency evolution of the binary and therefore $t(v)$. In the subsequent analysis we assume that the modification due to precession is small and therefore neglect the effect. Hence, the GW phase which enters Eq.(7.6) is the phase of the aligned-spin model PhenomC. The frequency-domain expressions are obtained in the following way.

Let the spin-aligned time-domain $(2,m)$-mode be given by

$$h_{2m}(t) = A(t)e^{-im\Phi_{\text{orb}}(t)}. \tag{7.9}$$

With the convention used in [192], the $(2,2)$-mode modelled in PhenomC transforms as

$$\tilde{h}_{22}(f)\Big|_{f\geq 0} = \tilde{A}(f)e^{i\tilde{\psi}_{22}(f)}. \tag{7.10}$$

The convention is chosen such that modes with $m \geq 0$ have positive support and modes with $m < 0$ have negative support in the frequency domain, i.e.

$$\tilde{h}_{2,-2}(f)\Big|_{f<0} = \tilde{A}(-f)e^{-i\tilde{\psi}_{22}(-f)}. \tag{7.11}$$

We note that $\left(\tilde{h}_{22}(-f)\right)^* = \tilde{h}_{2,-2}(f)$, where * denotes the complex conjugate. By making use of the SPA, we can absorb the angle-dependent functions in the slowly-varying amplitude yielding the final expressions for the precession waveform modes:

$$\tilde{h}^P_{2m}(f) = \begin{cases} e^{-i(m\alpha(-f)-2\epsilon(-f))} d^2_{-2m}(-\iota(-f))(\tilde{h}_{22}(-f))^* & f < 0 \\ e^{-i(m\alpha(f)-2\epsilon(f))} d^2_{2m}(-\iota(f))\tilde{h}_{22}(f) & f \geq 0, \end{cases} \tag{7.12}$$

where we have set $\epsilon := \int \dot{\alpha} \cos\iota$. The GW strain in the frequency domain is given by

$$\tilde{h}(f;\theta,\varphi) = \sum_{m=-2}^{2} Y^{-2}_{2m}((\theta,\varphi)\tilde{h}^P_{2m}(f) \equiv \tilde{h}_+(f) - i\tilde{h}_\times(f), \tag{7.13}$$

where we have used the linearity of the Fourier transform to obtain the equivalence. We emphasise at this point that modes with $l \neq 2$ are not modelled by the underlying spin-aligned model and can therefore not be constructed in the precessing model. The output of the model is not the waveform modes as given in Eq.(7.12), but the two fundamental polarisations $\tilde{h}^P_{+,\times}(Mf;\eta,\chi_{\rm eff},\chi_p;\theta,\phi)$, which can be obtained via the following relations:

$$\tilde{h}_+(f) = \mathcal{F}[\mathrm{Re}[h(t)]] = \frac{\tilde{h}(f) + \tilde{h}^*(-f)}{2}, \tag{7.14}$$

$$\tilde{h}_\times(f) = \mathcal{F}[-\mathrm{Im}[h(t)]] = \frac{\tilde{h}^*(-f) - \tilde{h}(f)}{2i}. \tag{7.15}$$

In order to finally compute the precessing waveforms, we need to obtain frequency domain expressions for the angles (ι, α). As we have seen in the previous chapters, these functions in general depend on all six spin components. As a first approximation, we approximate these angles by pure PN expressions for systems with only one spin in the orbital plane as motivated by the results in the previous chapter. However, the spin-aligned h_{lm}-modes model the complete signal including merger and ringdown. In our modelling scheme, we twist the *entire* non-precessing modes with those pure PN angles, and therefore formally continue the SPA treatment through merger and ringdown. Although we do not expect these expressions, or the approximation of slowly varying precession angles, to be valid through merger and ringdown, in practice we find that they mimic to reasonable accuracy the phenomenology of our complete PN-NR hybrids and only lead to small mismatches even for high masses, where the merger becomes important.

In PN theory, the inclination ι is simply the angle between $\hat{J}$ and $\hat{L}$ as given by Eq.(3.15). It depends on expressions for L, $S_{||}$ and $S_\perp$. For single-spin precessing binaries, the parallel and orthogonal spin components are approximately constant and will be assumed as such in the model. We therefore only need an expression for the magnitude of the orbital angular momentum $L(t)$. In practice we find that the accuracy in ι, which enters only in amplitude factors in Eq.(7.12), is not as critical as the accuracy of the precession angle α. Starting from

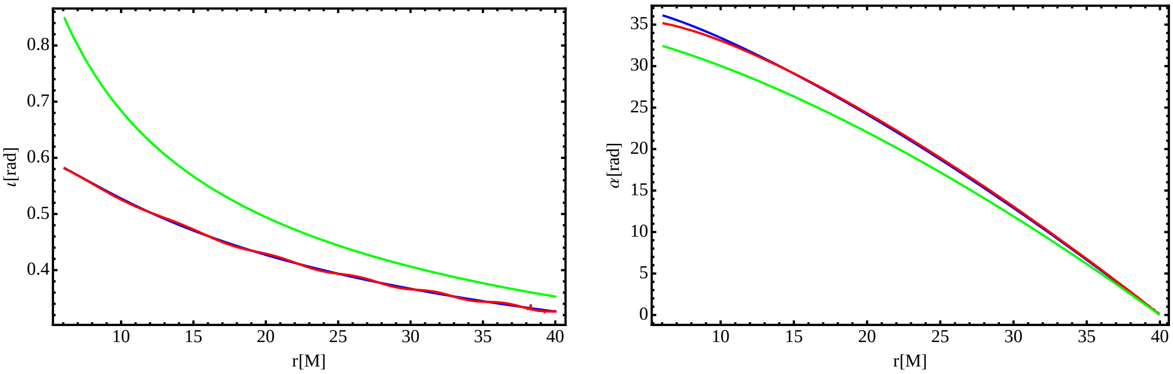

Figure 7.1: The left panel shows the PN evolution of the angle ι as constructed from Eq.(3.15) as a function of the separation r for the precessing $q = 3$ configuration described in Table 7.1. The blue graph shows ι as obtained from a full PN evolution of the precessing configuration, the red graph shows the approximation of ι for L as given in Eq.(7.16) and $S_\perp = 0.75$. The green graph shows ι computed from the same expression but now $L = L_{\rm N}$. We see that the neglect of SO-terms in the expression for L still captures the secular evolution of ι. The right panel shows the evolution of α according to Eq.(63a) in [20], which is applicable to this single-spin system, using $L_{\rm PN}$ (red) and $L_{\rm N}$ (green). The blue graph is α from the full PN evolution. We observe significant dephasing between the blue and the red graph.

Eq.(3.15), we find that it is sufficient to include only *nonspinning* PN corrections in L, i.e.,

$$L \approx L_{\rm N} + L_{\rm PN} + L_{\rm 2PN}, \tag{7.16}$$

as given in [133] to accurately approximate ι. The goodness of this approximation to ι is illustrated in the left panel Fig. 7.1.

The precession angle α, on the other hand, does not only affect the amplitude of the precessing waveform but more importantly strongly influences the phase evolution. It is related to the precession frequency by Eq.(3.11), which, for single-spin binaries at leading-order, is given by [20]

$$\omega_p := \frac{d\alpha}{dt} = \left(2 + \frac{3m_1}{2m_2}\right)\frac{J}{r^3}. \tag{7.17}$$

The right panel of Fig. 7.1 illustrates the effect of L on the evolution of α. We observe signifiant dephasing at smaller separations due to the approximation of L but also due to low PN order of the expression for α. Due to its influential contribution to the GW phasing, a higher-order expression for α is desired. This was derived by A. Bohé via the expression for $\dot\alpha$ in [44] (see Eqs (4.10a) and (4.8)) by inserting the highest-order (next-to-next-to-leading in spin-orbit) expressions available for the quantities entering the formula [47], PN re-expanding and averaging over the orientation of the spin in the orbital plane yielding

$$\begin{aligned}\alpha(\omega) =& \frac{5}{65028096q(1+q)^4\omega}\Big[(-338688(1+q)^4(3+4q) - 508032q(1+q)^4(3+4q)\chi_{\rm eff}\omega^{1/3}\\ &-3024(1+q)^2(2985+q(12890+q(15789+4988q+168(1+q)^2(3+4q)\chi_p^2)))\omega^{2/3}\\ &+(17660607+q(107348840-12192768\pi\chi_{\rm eff}+q(271003598+322056\chi_p^2\\ &+q(327403764+181442579q+39432548q^2+1512(2228+q(6726+q(8576\\ &+q(4821+956q))))\chi_p^2-127008q(1+q)^4(3+4q)\chi_p^4)-65028096\pi\chi_{\rm eff}\\ &-4064256\pi q(34+q(36+q(19+4q)))\chi_{\rm eff}\\ &+84672(1+q)^2(3+4q)(75+q(113+6q(1+q)^2\chi_p^2))\chi_{\rm eff}^2)))\omega^{4/3}\\ &-1008(1+q)^2(1344\pi(1+q)^2(3+4q)+q(-5253+q(-18854+q(-18197-2972q\\ &+168(1+q)^2(3+4q)\chi_p^2)))\chi_{\rm eff})\omega\log(\omega)\Big]\end{aligned} \tag{7.18}$$

7.2.1 Parameterisation

The only spin parameters in our model are $\chi_{\rm eff}$ and χ_p as defined in Eq.(7.3) and Eq.(6.7) respectively. The angle expressions (ι,α), require some choice for the distribution of χ across the two black holes and for our implementation we let $\chi_{1||}=0$ and $\chi_{2||}=(M/m_2)\chi_{\rm eff}$, i.e., all of the parallel spin is on the larger black hole. To ensure *physical* spins of $\chi_i\leq 1$ for each black hole, we could also choose $\chi_{1||}=\chi_{2||}=\chi_{\rm eff}$. We choose the in-plane spin χ_p to be associated with the larger black hole m_2, as precession effects are more strongly influenced by the spin on the larger black hole (see Sec. 6.2.3 for more details).

Despite the choice of the spin distribution, which effectively reduces the model to a single-spin model, we expect the model to capture the basic phenomenology of generic two-spin systems motivated by the analysis presented in Chapter 6. Briefly summarised, the argument was the following: for the effective precession spin, if $S_{1\perp}$ and $S_{2\perp}$ are the magnitudes of the projections of the two individual spins in the orbital plane, then, according to the PN precession equations Eq.(3.16)-Eq.(3.18), the precession rate at leading order is proportional to $(A_1S_{1\perp}+A_2S_{2\perp})$ when the vectors $\hat{S}_{1\perp}$ and $\hat{S}_{2\perp}$ are parallel, and proportional to $(A_1S_{1\perp}-A_2S_{2\perp})$ when they are antiparallel, where $A_i=2+(3m_{3-i})/(2m_i)$ for $i=1,2$. During the inspiral, to first approximation, the average precession rate is simply the maximum of these two spin contributions and we can define $S_p=\max(A_1S_{1\perp},A_2S_{2\perp})/A_2$. We expect that applying an in-plane spin of $\chi_p:=S_p/m_2^2$ to the larger black hole will mimic the main precession effects of the full two-spin system. The full system will exhibit additional oscillations (nutation) in the precession angles due to spin-spin coupling terms (see e.g., Fig. 4 of [60] and [198]), but we do not expect these effects to be detectable in most GW observations. We emphasise that these two effective parameters, $\chi_{\rm eff}$ and χ_p, can be mapped to a range of physically allowable individual black-hole spins $\vec{\chi}_1$ and $\vec{\chi}_2$:

$$\vec{\chi}_1 \mapsto (0, 0, 0), \tag{7.19}$$

$$\vec{\chi}_2 \mapsto \left(\chi_p, 0, \frac{M}{m_2}\chi_{\text{eff}}\right). \tag{7.20}$$

7.3 Results

The most reliable way to test any waveform model is to compare it against hybrid PN (inspiral) and NR (merger-ringdown) waveforms, which were not used for its calibration to NR simulation, if such a calibration was performed to construct the model. We emphasise, that no precessing NR simulations were used in the construction of PhenomP; NR data were only used to calibrate the underlying spin-aligned model PhenomC. A comparison with hybrid waveforms across the full parameter space of precessing binaries would require the same number of waveforms as needed to construct a seven-dimensional generic model, which is the computationally prohibitive task that we wished to circumvent in the first place. In practice, however, what we can do is identify what we expect to be challenging points in the binary parameter space. In this comparison we restrict ourselves to binaries with small mass ratios $q \leq 3$, because that is the mass ratio range to which the underlying aligned-spin model was calibrated to spinning-binary waveforms. To test the reliability of the model for GW detection, we construct three hybrids waveforms at mass ratios 2 and 3 for a variety of spin choices as listed in Tab. 7.1; the numerical simulations were produced with the BAM code [55] and hybrids were constructed by the method presented in Sec. 5.4 as well as in the inertial frame of the NR waveforms via backwards integration of the PN equations of motion as described in [164]. Among those precessing configurations is the $q = 3$ case where the larger black hole has a spin of $\chi_2 = 0.75$ in the orbital plane, which leads to strong precession effects, and two double-spin cases with mass ratio $q = 2$, which test our assumption that we can consider only a weighted average of the spins when constructing χ_p. The NR initial parameters are listed in Table 7.1.

As is standard in GW data analysis, we calculate the noise-weighted inner product as given in Eq.(2.75) between our source waveform (in this case the hybrid) and a model waveform family (either the original non-precessing PhenomC model or the new precessing PhenomP model). We use the current expectation for the design sensitivity of advanced LIGO [212], with a low-frequency cutoff of 20Hz. This inner product is maximised with respect to the parameters of the model, including the physical parameters $\{\eta, \chi_{\text{eff}}, \chi_p, M\}$, the binary orientation $\{\theta, \phi\}$ and the signal polarisation angle ψ. This optimised inner product is called the *fitting factor* (FF); its value indicates how well the signal can be found in detector data. Additionally, the bias between the best-fit model parameters and the true source parameters gives us an indication of the errors in a GW source parameter measurement.

q	2	2	3
$\vec{\chi}_1$	$\{0.5, 0, 0\}$	$\{-0.5, 0, 0\}$	$\{0, 0, 0\}$
$\vec{\chi}_2$	$\{0.75, 0, 0\}$	$\{0.75, 0, 0\}$	$\{0.75, 0, 0\}$
M_i	$\{0.285749, 0.453461\}$	$\{0.285556, 0.45335\}$	$\{0.47790, 1.02343\}$
$\vec{S}_1$	$\{-0.031, -0.045, 0.009\}$	$\{-0.032, -0.0196, 0.041\}$	$\{0, 0, 0\}$
$\vec{S}_2$	$\{-0.304, 0.057, 0.125\}$	$\{-0.322, 0.032, 0.079\}$	$\{-1.048, 1.197, 0.560\}$
$\vec{x}_1$	$\{0, 7.49238, 0\}$	$\{0, 7.3807, 0\}$	$\{0, 15.0478, 0\}$
$\vec{x}_2$	$\{0, -3.74619, 0\}$	$\{0, -3.69035, 0\}$	$\{0, -5.0159, 0\}$
D_i/M	11.2386	11.0711	10.05
p_x	∓ 0.073409	∓ 0.0735151	∓ 0.126292
p_y	∓ 0.000535843	∓ 0.000569491	∓ 0.00139578
p_z	± 0.0297503	± 0.0317812	± 0.0696932

Table 7.1: Parameters for the precessing configurations that were used to construct the PN-NR hybrid waveforms; $\vec{\chi}_1$ and $\vec{\chi}_2$ define the configuration at the initial separation $D_i/M = 40$ before the PN equations of motion are evolved.

We have computed fitting factors using PhenomC and PhenomP for total source masses M between $20\,M_\odot$ and $200\,M_\odot$ as functions of binary orientations. As an example, Fig. 7.2 shows results for the $q = 3$ high precession configuration at $M = 50M_\odot$, which proved to be the most challenging to our model yielding the lowest fitting factors. The obtained results are similar for lower masses, while the fitting factors improve for higher masses but at the expense of source parameter accuracy. The standard requirement for GW searches is that the fitting factor has to be above 0.965, which corresponds to a loss of no more than 10% of signals in a search (disregarding additional loss due to a discrete template bank). Comparing the two panels of Fig. 7.2 we see that while the fitting factors for PhenomC are above 0.97 only for near-optimal orientations (from which the precession has only a small effect on the signal), they are above 0.97 for almost all orientations with the PhenomP model. A complete study of the parameter biases has not been performed yet, but these results suggest that a measurement of χ_p reliably identifies precession.

7.4 Discussion and limitations

We have presented the first frequency-domain inspiral-merger-ringdown model for the GW signal from precessing black-hole-binaries. By incorporating a series of insights from our previous work (see Chapters 4-6), our model is constructed by a straightforward transformation of an aligned-spin waveform model, in this particular case PhenomC, into a precessing model. We would like to point out that in practice any workable non-precessing model could be used instead of PhenomC. In fact, our key idea of twisting up an aligned-spin model with expressions for the precessional dynamics has also been used to produce a precessing EOB model [174].

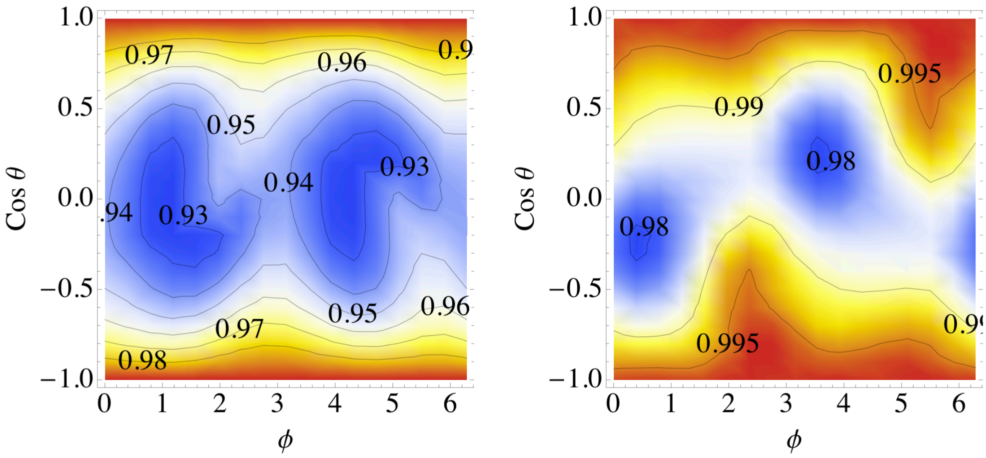

Figure 7.2: Fitting factors (as computed by A. Bohé) between the $q = 3$ highly-precessing binary and the non-precessing PhenomC (left panel) and precessing PhenomP (right panel) models, as a function of binary orientation angles (θ, ϕ) for a binary with a total mass of $50M_{\odot}$; at $\theta = 0$ an observer is oriented with the binary's total angular momentum. FF < 0.965 for many orientations with PhenomC, while for PhenomP it is well above 0.965 for all orientations.

As mentioned previously, the current model did not require any precessing-binary numerical simulations in its construction. The only calibration to NR data that is contained in the model is the original calibration of PhenomC. The expressions used to describe the precession dynamics are purely PN and therefore not valid for the late inspiral and merger regime. It is important to use extensive simulations to refine the model, in particular the expressions for ι and α, based on tests of the model's accuracy for GW searches and parameter estimation.

Finally, we are able to model the essential phenomenology of the seven-dimensional parameter space of binary configurations with a model that requires only three *physical* parameters. This will simplify the model's incorporation into search and parameter estimation pipelines, as well as making the problem of producing enough numerical simulations to produce a model of sufficient accuracy for GW astronomy with advanced detectors tractable.

Our ability to model generic waveforms with only two spin parameters implies strong degeneracies that will make it difficult to identify the individual black-hole spins. This may well be the reality of GW observations with second-generation detectors, for which 80% of signals will be at signal-to-noise ratios between 10 and 20, in which the subtle double-spin effects on the waveform may be difficult to identify. These are important issues that deserve further attention in future work.

The current model is valid only in the region of parameter space for which PhenomC was calibrated ($q \leq 3$, $|\chi_{\rm eff}| \leq 0.75$). More challenging precession cases are expected at higher mass ratios and spins (e.g., transitional precession), and the ability of our prescription to model those configurations will need to be tested when refined non-precessing-binary models become available.

CHAPTER 8

Conclusions

The gravitational-wave signatures from coalescing compact binaries, in particular binary black holes, are amongst the most promising candidates for the first detection with the advanced ground-based GW detectors aLIGO and VIRGO. Current detection strategies rely on theoretical knowledge of the gravitational waveforms emitted during the inspiral, merger and ringdown. However, the construction of waveform models seeks to combine information from analytic approximation methods as well as Numerical Relativity. Accurate descriptions of the complete GW signature from nonspinning or aligned-spin binaries have been presented previously [10, 12, 192], but modelling the signal from the most general class of black hole binaries, precessing black holes, has been an open task. In this thesis, we have presented geometric framework to construct precessing inspiral-merger-ringdown waveform models:

First, in Chapter 4 we introduced a co-precessing frame in the context of Numerical Relativity [196]. This has allowed us to accurately isolate the secular inspiral dynamics from the precession dynamics in a generic system. Based on this decoupling, we have shown in Chapter 5 that the secular inspiral phase of a given precessing binary can be accurately mapped onto the inspiral phase of a particular aligned-spin binary. Moreover, we have identified the corresponding aligned-spin binary to be defined by the spin components parallel to the orbital angular momentum of the precessing binary [197], which can be combined into one effective inspiral spin $\chi_{\rm eff}$. We have demonstrated the efficacy of this mapping for a large class of inspiral signals. Additionally, we have also tested at which point in the binary evolution this mapping breaks down and found that it is applicable even up to the late inspiral and merger. This investigation was later extended to a larger numerical study by Pekowsky et al. [176], confirming our results. Based on the fact that the decoupling of the inspiral and the precession holds well all the way up to merger, we proposed a systematic and general strategy to construct precessing waveform models, namely by "twisting up" existing aligned-spin waveform models with a physically meaningful rotation operator that encodes the precession dynamics.

In order to complete the task of constructing a precessing waveform model, however, the precession dynamics needs to be modelled as well, which was another integral part of this thesis (Chapter 6). Yet again we took inspiration from post-Newtonian theory and inspiral waveforms to find a simple way to describe the precession in a generic binary-black-hole system. Based on the PN evolution equations, which encode the precession, we proposed the construction of a simple effective precession spin χ_p to capture the precession dynamics on top of the inspiral [198]. We have shown that the defining geometric quantities, i.e., the inclination as well as the azimuthal rotation of the orbital plane, agree well between a system with two generic spin angular momenta and the corresponding system with χ_p as the orthogonal spin, which drives the precession. We have subsequently pursued this geometric approach to construct the first complete precessing inspiral-merger-ringdown waveform model in the frequency domain [117], which is presented in Chapter 7.

We emphasise that the geometric strategy of convolving an aligned-spin binary with a simple rotation operator, which encapsulates the precession motion, and the effective parameterisation are two separate things. The construction strategy we proposed is general and completely independent of the preferred parameterisation. However, given the dimensionality of the precessing parameter space, effective parameter reductions, which do not compromise the recovery of physical parameters to a high degree, are highly desirable, as they allow us to identify the principal directions in the binary parameter space and therefore admit a systematic exploration. This is of particular interest for NR simulations. The effective parameterisation we have suggested allows us to explore the binary parameter space numerically by mapping the seven-dimensional manifold onto a three-dimensional submanifold, allowing for a much better coverage.

However, the validity of the effective precession spin during the late inspiral and merger regime remains an open question. A careful numerical analysis is needed, as only a few numerical simulations of precessing binaries have been performed. It may well be that a single precession spin is not enough to capture effects like the recoil of the final black hole. Previous work has shown that the recoil velocity strongly depends on the direction of the spin in the orbital plane just before merger [54, 71] – χ_p does not encode any directional information. Whether or not this is relevant for GW astronomy, is another interesting question, which may be explored in the future.

Based on our strategy to turn an aligned-spin waveform into a precessing one, other precessing waveform models have been constructed following this successful approach [148, 174], meaning that there are now several precessing waveform models available to start working on a detection and parameter estimation infrastructure that also incorporates precession, which is of particular interest to the advanced GW detector era.

APPENDIX A

Transformation of $\Psi_{4,lm}$ under rotations

We aim to derive the transformation of the Weyl scalar Ψ_4 under a rotation $\mathbf{R} \in SO(3)$. A similar calculation is performed in [72]. It can be shown that the Weyl scalar is a field of spin-weight $s = -2$ and hence it can be expanded in a suitable basis is

$$\Psi_4 = \sum_{l,m} \Psi_{4,lm} Y_{lm}^{-2}, \tag{A.1}$$

where Y_{lm}^{-2} denote the spherical harmonics of spin-weight $s = -2$ [159]. For $s = 0$ we obtain the regular spherical harmonics Y_{lm}, which are the eigenfunctions of the angle-dependent part of the Laplace operator.

The transformation of the spin-weighted spherical harmonics is a simple composition of the transformation of the spin-basis-dependent part and of Y_{lm}. It is convenient to introduce standard polar coordinates (r, θ, φ) and to define Y_{lm} with respect to the polar angles (θ, φ). The spherical harmonics then have the form

$$Y_{lm}(\theta, \varphi) = \phi(\varphi)\Theta(\theta). \tag{A.2}$$

We will consider rotations $\mathbf{R}$, which transform angles $\Omega = (\theta, \varphi)$ to the new coordinates $\Omega' = (\theta', \varphi')$. The spin-weight-zero spherical harmonics Y_{lm} then transform according to $Y_{lm}(\theta, \varphi) \mapsto Y_{lm}(\theta', \varphi')$ by applying the operator $\mathbf{P}_R$, where R is a rotation about the z-axis by the angle γ such that $\varphi \mapsto \varphi' = \varphi + \gamma$ and $\theta = \theta'$, is given by

$$Y_{lm}(\theta', \varphi') \equiv \mathbf{P}_R Y_{lm}(\theta, \varphi) = e^{im\gamma} Y_{lm}(\theta, \varphi). \tag{A.3}$$

Now, let $\mathbf{R}(\gamma\beta\alpha)$ denote an arbitrary rotation by the Euler angles γ, β, α. Using the z-y-z convention, the spherical harmonics then obey the following transformation law [101, 225]:

$$Y_{lm}(\theta', \varphi') = \sum_{m'=-l}^{l} e^{im'\gamma} d^l_{m'm}(\beta) e^{im\alpha} Y_{lm}(\theta, \varphi), \tag{A.4}$$

where the $d^l_{m'm}$ denote the Wigner d-matrices given by [191]

$$\begin{aligned} d^l_{m'm} =& \sqrt{(l+m)!(l-m)!(l+m')!(l-m')!} \\ &\times \sum_k \frac{(-1)^{k+m'-m}}{k!(l+m-k)!(l-m'-k)!(m'-m+k)!} \\ &\times (\sin\frac{\beta}{2})^{2k+m'-m} (\cos\frac{\beta}{2})^{2l-2k-m'+m}. \end{aligned} \tag{A.5}$$

Due to the properties of the group $SO(3)$, the inverse transformation is then given by

$$Y_{lm}(\theta, \varphi) = \sum_{m'=-l}^{l} e^{-im'\gamma} d^l_{m'm}(-\beta) e^{-im\alpha} Y_{lm'}(\theta', \varphi'). \tag{A.6}$$

The next step is to include the change of spin-basis under a rotation. According to [14] a quantity η of spin-weight s obeys the following law under a change of the spin basis:

$$\eta' = \eta e^{is\chi}. \tag{A.7}$$

Combining Eqs.(A.6) and (A.7) yields the transformation law for the spin-weighted spherical harmonics:

$$Y^s_{lm}(\theta, \varphi) = e^{-is\chi} \sum_{m'=-l}^{l} e^{-im'\gamma} d^l_{m'm}(-\beta) e^{-im\alpha} Y^s_{lm'}(\theta', \varphi'). \tag{A.8}$$

We invert Eq.(A.1) to determine the transformation law for the $\Psi_{4,lm}$-modes,

$$\begin{aligned} \Psi_{4,lm} &= \int \Psi_4 \overline{Y^s_{lm}(\theta, \varphi)} d\Omega \\ &= \int e^{-is\chi} \Psi'_4 e^{is\chi} \sum_{m'} e^{im'\gamma} d^l_{m'm}(-\beta) \\ &\qquad \times e^{im\alpha} \overline{Y^s_{lm'}(\theta', \varphi')} d\Omega' \\ &= \sum_{m'=-l}^{l} e^{im'\gamma} d^l_{m'm}(-\beta) e^{im\alpha} \Psi'_{4,lm'}, \end{aligned} \tag{A.9}$$

where the overline denotes complex conjugation. We see that explicit knowledge of χ as a function of θ and φ is not necessary to determine the coefficients $\Psi_{4,\ell m}$. This transformation law can now be applied to any given $\Psi'_{4,lm}$, e.g., our numerical data, in order to change the frame of reference. The remaining free parameters are the three angles that determine the general rotation. In practice, to determine the dominant emission direction one does not need to perform the third rotation about α [72, 225]. In Chapter 4 we therefore restrict ourselves to a rotation about two the Euler angles, β and γ, only. Since we aim to align the orbital angular momentum with the z-axis at every instant of time, i.e., $\hat{L} \mapsto \hat{z}$, a simple calculation shows that in order to fulfill this $\beta = -\theta$ and $\gamma = -\varphi$ are required, where (θ, φ) are the polar coordinates determining the direction of $\hat{L}$.

APPENDIX B

Numerical Relativity simulations

Here we list the main configuration parameters of the Numerical Relativity simulations conducted during my PhD research. These were carried out on various superclusters in Europe: Vienna Scientific Cluster (Austria), Curie (France), Hermit (HLRS, Germany) and SuperMUC (LRZ, Germany).
The variables $\{q, \vec{a}_1, \vec{a}_2\}$ denote the initial PN spin parameters; all other entries denote the initial parameters of the NR simulation.

config	q	$\vec{a}_1$	$\vec{a}_2$	M_i	$\vec{S}_1$	$\vec{S}_2$	$\vec{x}_1$	$\vec{x}_2$	D_i/M	$\vec{p}$
q1_a0_a0.25_64	1	(0,0,0)	(0.25,0,0)	$\{0.489, 0.476\}$	(0,0,0)	(-0.062,0.002,0.004)	(0,6.367,0)	(0,-6.367,0)	12.733	$(\mp 0.082, \mp 0.0004, \pm 0.005)$
q1_a0_a0.5_64 q1_a0_a0.5_80	1	(0,0,0)	(0.5,0,0)	$\{0.489, 0.434\}$	(0,0,0)	(0.124,-0.003,0.014)	(0,6.273,0	(0,-0.673,0)	12.546	$(\mp 0.082, \mp 0.0005, \mp 0.0098)$
q1_a0_a0.75_64	1	(0,0,0)	(0.75,0,0)	$\{0.489, 0.338\}$	(0,0,0)	(0.185,-0.005,0.032)	(0,6.309,0)	(0,-6.309,0)	12.618	$(\mp 0.081, \mp 0.0005, \mp 0.015)$
q2_a0_a0.25_64	2	(0,0,0)	(0.25,0,0)	$\{0.484, 0.9597\}$	(0,0,0)	(0.248,-0.007,0.029)	(0,12.056,0)	(0,-6.028,0)	12.056	$(\mp 0.112, \mp 0.0006, \mp 0.014)$
q2_a0_a0.5_64	2	(0,0,0)	(0.5,0,0)	$\{0.323, 0.583\}$	(0,0,0)	(0.216,-0.006,0.051)	(0,8.092,0)	(0,-4.046,0)	12.138	$(\mp 0.073, \mp 0.0004, \mp 0.018)$
q2_a0_a0.75_64	2	(0,0,0)	(0.75,0,0)	$\{0.484, 0.681\}$	(0,0,0)	(0.707,-0.0240.250)	(0,11.836,0)	(0,-5.918,0)	11.386	$(\mp 0.108, \mp 0.0007, \mp 0.039)$
q2_a-0.5_a0.75_64	2	(-0.5,0,0)	(0.75,0,0)	$\{0.286, 0.453\}$	(-0.032,-0.0196,0.041)	(-0.322,0.032,0.079)	(0,7.381,0)	(0,-3.690,0)	11.0711	$(\mp 0.074, \mp 0.0006, 0.032)$
q2_a0.5_a0.75_64 q2_a0.5_a0.75_80	2	(0.5,0,0)	(0.75,0,0)	$\{0.286, 0.453\}$	(-0.031,-0.045,0.009)	(-0.304,0.057,0.125)	(0,7.492,0)	(0,-3.746,0)	11.239	$(\mp 0.0734, \mp 0.0005, \pm 0.0298)$
q3_a0_a0.25_64	3	(0,0,0)	(0.25,0,0)	$\{0.240, 0.722\}$	(0,0,0)	(-0.138,0.005,0.025)	(0,8.698,0)	(0,-2.899,0)	11.958	$(\mp 0.064, \mp 0.0003, 0.012)$
q3_a0_a0.5_64	3	(0,0,0)	(0.5,0,0)	$\{0.241, 0.658\}$	(0,0,0)	(0.264,0.009,0.096)	(0,8.782,0)	(0,-2.927,0)	11.709	$(\mp 0.061, \mp 0.0003, \pm 0.023)$
q3_a0_a0.75_64	3	(0,0,0)	(0.75,0,0)	$\{0.240, 0.512\}$	(0,0,0)	(0.371,-0.011,0.201)	(0,8.475,0)	(0,-2.825,0)	11.300	$(\mp 0.058, \mp 0.0004, \pm 0.033)$
q3_a0_a0.75_64	3	(0,0,0)	(0.53,0.53,0)	$\{0.240, 0.512\}$	(0,0,0)	(-0.371,0.011,0.201)	(0,8.512,0)	(0,-2.837,0)	11.350	$(\mp 0.058, \mp 0.0004, 0.032)$
q3_a0_a0.75_64	3	(0,0,0)	(0,0.75,0)	$\{0.240, 0.513\}$	(0,0,0)	(-0.373,0.009,0.197)	(0,9.514,0)	(0,-3.171,0)	12.686	$(\mp 0.054, \mp 0.0003, \pm 0.029)$
q3_a0_a0.75_64	3	(0,0,0)	(-0.53,0.53,0)	$\{0.240, 0.512\}$	(0,0,0)	(-0.370,0.011,0.202)	(0,8.435,0)	(0,-2.812,0)	11.247	$(\mp 0.058, \mp 0.0004, \pm 0.033)$
q3_a0_a0.75_64	3	(0,0,0)	(-0.75,0,0)	$\{0.240, 0.512\}$	(0,0,0)	(-0.371,0.011,0.201)	(0,8.475,0)	(0,-2.825,0)	11.300	$(\mp 0.058, \mp 0.0003, \pm 0.033)$
q3_a0_a0.75_64	3	(0,0,0)	(-0.53,-0.53,0)	$\{0.240, 0.512\}$	(0,0,0)	(0.371,-0.011,0.201)	(0,8.512,0)	(0,-2.837,0)	11.3497	$(\mp 0.058, \mp 0.0004, 0.032)$
q3_a0_a0.75_64	3	(0,0,0)	(0,-0.75,0)	$\{0.240, 0.513\}$	(0,0,0)	(-0.371,0.010,0.1999)	(0,8.844,0)	(0,-2.948,0)	11.792	$(\mp 0.057, \mp 0.0003, \pm 0.031)$
q3_a0_a0.75_64	3	(0,0,0)	(-0.53,0.53,0)	$\{0.240, 0.512\}$	(0,0,0)	(-0.370,0.011,0.202)	(0,8.435,0)	(0,-2.812,0)	11.247	$(\mp 0.058, \mp 0.0004, \pm 0.033)$
q3_a0.5_a0.75_64	3	(0,0,-0.5)	(0.559,0,-0.5)	$\{0.213, 0.512\}$	(-0.022,-0.003,-0.022)	(-0.417,0.022,-0.062)	(0,8.399,0)	(0,-2.7998,0)	11.199	$(\mp 0.057, \mp 0.0004, \pm 0.039)$
q3_a0.5_a0.75_64	3	(0,0,-0.5)	(0.73,0,0.17)	$\{0.213, 0.513\}$	(-0.018,-0.0002,-0.025)	(-0.324,0.013,0.269)	(0,8.075,0)	(0,-2.692,0)	10.767	$(\mp 0.061, \mp 0.0004, \pm 0.032)$
q3_a0.5_a0.75_64	3	(0,0,-0.5)	(0.75,0,0)	$\{0.213, 0.512\}$	(0.023,0.004,-0.020)	(0.367,-0.017,0.208)	(0,8.144,0)	(0,-2.715,0)	10.858	$(\mp 0.059, \mp 0.0005, \mp 0.036)$

Bibliography

[1] Advanced Virgo Baseline Design. URL https://pub3.ego-gw.it/codifier/includes/showTmpFile.php?doc=2219&calledFile=VIR-027A-09.pdf.

[2] LSC algorithm library (LAL). URL http://www.lsc-group.phys.uwm.edu/lal.

[3] J. Aasi et al. Prospects for Localization of Gravitational Wave Transients by the Advanced LIGO and Advanced Virgo Observatories. 2013.

[4] J. Aasi et al. Gravitational waves from known pulsars: results from the initial detector era. *Astrophys.J.*, 785:119, 2014. doi:10.1088/0004-637X/785/2/119.

[5] J. Abadie et al. Predictions for the Rates of Compact Binary Coalescences Observable by Ground-based Gravitational-wave Detectors. *Class.Quant.Grav.*, 27:173001, 2010. doi:10.1088/0264-9381/27/17/173001.

[6] J. Abadie et al. Beating the spin-down limit on gravitational wave emission from the Vela pulsar. *Astrophys.J.*, 737:93, 2011. doi:10.1088/0004-637X/737/2/93.

[7] P. Ade et al. Detection of B-Mode Polarization at Degree Angular Scales by BICEP2. *Phys.Rev.Lett.*, 112:241101, 2014. doi:10.1103/PhysRevLett.112.241101.

[8] P. Ajith. Gravitational-wave data analysis using binary black-hole waveforms. *Class.Quant.Grav.*, 25:114033, 2008. doi:10.1088/0264-9381/25/11/114033.

[9] P. Ajith. Addressing the spin question in gravitational-wave searches: Waveform templates for inspiralling compact binaries with nonprecessing spins. *Phys.Rev.*, D84:084037, 2011. doi:10.1103/PhysRevD.84.084037.

[10] P. Ajith, S. Babak, Y. Chen, M. Hewitson, B. Krishnan, et al. Phenomenological template family for black-hole coalescence waveforms. *Class.Quant.Grav.*, 24:S689–S700, 2007. doi:10.1088/0264-9381/24/19/S31.

[11] P. Ajith, S. Babak, Y. Chen, M. Hewitson, B. Krishnan, et al. A Template bank for gravitational waveforms from coalescing binary black holes. I. Non-spinning binaries. *Phys.Rev.*, D77:104017, 2008. doi:10.1103/PhysRevD.79.129901, 10.1103/PhysRevD.77.104017.

[12] P. Ajith, M. Hannam, S. Husa, Y. Chen, B. Brügmann, et al. Inspiral-merger-ringdown waveforms for black-hole binaries with non-precessing spins. *Phys.Rev.Lett.*, 106:241101, 2011. doi:10.1103/PhysRevLett.106.241101.

[13] P. Ajith, M. Boyle, D. A. Brown, B. Brgmann, L. T. Buchman, et al. The NINJA-2 catalog of hybrid post-Newtonian/numerical-relativity waveforms for non-precessing black-hole binaries. *Class.Quant.Grav.*, 29:124001, 2012. doi:10.1088/0264-9381/30/19/199401, 10.1088/0264-9381/29/12/124001.

[14] M. Alcubierre. *Introduction to 3+1 Numerical Relativity*. Oxford University Press, 2008. ISBN 978-0-19-920567-7.

[15] B. Allen. The Stochastic gravity wave background: Sources and detection. 1996. URL `http://arxiv.org/abs/gr-qc/9604033`.

[16] K. Alvi. Energy and angular momentum flow into a black hole in a binary. *Phys.Rev.*, D64:104020, 2001. doi:10.1103/PhysRevD.64.104020.

[17] M. Ansorg, B. Brügmann, and W. Tichy. A single-domain spectral method for black hole puncture data. *Phys.Rev.*, D70:064011, 2004. doi:10.1103/PhysRevD.70.064011.

[18] T. A. Apostolatos. Search templates for gravitational waves from precessing, inspiraling binaries. *Phys.Rev.*, D52:605–620, 1995. doi:10.1103/PhysRevD.52.605.

[19] T. A. Apostolatos. Construction of a template family for the detection of gravitational waves from coalescing binaries. *Phys.Rev.*, D54:2421–2437, 1996. doi:10.1103/PhysRevD.54.2421.

[20] T. A. Apostolatos, C. Cutler, G. J. Sussman, and K. S. Thorne. Spin induced orbital precession and its modulation of the gravitational wave forms from merging binaries. *Phys.Rev.*, D49:6274–6297, 1994. doi:10.1103/PhysRevD.49.6274.

[21] R. L. Arnowitt, S. Deser, and C. W. Misner. The dynamics of general relativity. *Gen.Rel.Grav.*, 40:1997–2027, 2008. doi:10.1007/s10714-008-0661-1.

[22] K. G. Arun, B. R. Iyer, B. S. Sathyaprakash, and P. A. Sundararajan. Parameter estimation of inspiralling compact binaries using 3.5 post-Newtonian gravitational wave phasing: The Non-spinning case. *Phys.Rev.*, D71:084008, 2005. doi:10.1103/PhysRevD.71.084008, 10.1103/PhysRevD.72.069903.

[23] K. G. Arun, A. Buonanno, G. Faye, and E. Ochsner. Higher-order spin effects in the amplitude and phase of gravitational waveforms emitted by inspiraling compact binaries: Ready-to-use gravitational waveforms. *Phys.Rev.*, D79:104023, 2009. doi:10.1103/PhysRevD.79.104023, 10.1103/PhysRevD.84.049901.

[24] J. G. Baker, J. Centrella, D.-I. Choi, M. Koppitz, and J. van Meter. Gravitational wave extraction from an inspiraling configuration of merging black holes. *Phys.Rev.Lett.*, 96:111102, 2006. doi:10.1103/PhysRevLett.96.111102.

[25] J. G. Baker, M. Campanelli, F. Pretorius, and Y. Zlochower. Comparisons of binary black hole merger waveforms. *Class.Quant.Grav.*, 24:S25–S31, 2007. doi:10.1088/0264-9381/24/12/S03.

[26] J. G. Baker et al. Mergers of non-spinning black-hole binaries: Gravitational radiation characteristics. *Phys.Rev.*, D78:044046, 2008. doi:10.1103/PhysRevD.78.044046.

[27] R. Balasubramanian, B. Sathyaprakash, and S. Dhurandhar. Gravitational waves from coalescing binaries: Detection strategies and Monte Carlo estimation of parameters. *Phys.Rev.*, D53:3033–3055, 1996. doi:10.1103/PhysRevD.54.1860.2, 10.1103/PhysRevD.53.3033.

[28] E. Barausse and L. Rezzolla. Predicting the direction of the final spin from the coalescence of two black holes. *Astrophys.J.*, 704:L40–L44, 2009. doi:10.1088/0004-637X/704/1/L40.

[29] B. Barker and R. O'Connell. Derivation of the equations of motion of a gyroscope from the quantum theory of gravitation. *Phys.Rev.D*, 2:1428, 1970.

[30] B. Barker and R. O'Connell. Nongeodesic motion in General Relativity. *Gen.Relativ. and Gravit.*, 5:539, 1974.

[31] B. Barker and R. O'Connell. The gravitational interaction: spin, rotation and quantum effects – a review. *Gen.Relativ. and Gravit.*, 11:149, 1979.

[32] T. W. Baumgarte and S. L. Shapiro. On the numerical integration of Einstein's field equations. *Phys.Rev.*, D59:024007, 1999. doi:10.1103/PhysRevD.59.024007.

[33] T. W. Baumgarte and S. L. Shapiro. *Numerical Relativity*. Cambridge University Press, 2010. ISBN 978-0-521-51407-1.

[34] M. J. Berger and J. Oliger. Adaptive Mesh Refinement for Hyperbolic Partial Differential Equations. *J.Comput.Phys.*, 53:484, 1984. doi:10.1016/0021-9991(84)90073-1.

[35] L. Blanchet. Gravitational-wave tails of tails. *Class.Quant.Grav.*, 15:113–141, 1998. doi:10.1088/0264-9381/15/1/009.

[36] L. Blanchet. Gravitational radiation from post-newtonian sources and inspiralling compact binaries. *Living Reviews in Relativity*, 17(2), 2014. doi:10.12942/lrr-2014-2. URL `http://www.livingreviews.org/lrr-2014-2`.

[37] L. Blanchet and G. Faye. General relativistic dynamics of compact binaries at the third post-Newtonian order. *Phys.Rev.*, D63:062005, 2001. doi:10.1103/PhysRevD.63.062005.

[38] L. Blanchet and B. R. Iyer. Third post-Newtonian dynamics of compact binaries: Equations of motion in the center-of-mass frame. *Class.Quant.Grav.*, 20:755, 2003. doi:10.1088/0264-9381/20/4/309.

[39] L. Blanchet, G. Faye, B. R. Iyer, and B. Joguet. Gravitational wave inspiral of compact binary systems to 7/2 post-Newtonian order. *Phys.Rev.*, D65:061501, 2002. doi:10.1103/PhysRevD.71.129902, 10.1103/PhysRevD.65.061501.

[40] L. Blanchet, B. R. Iyer, and B. Joguet. Gravitational waves from inspiralling compact binaries: Energy flux to third post-Newtonian order. *Phys.Rev.*, D65:064005, 2002. doi:10.1103/PhysRevD.65.064005, 10.1103/PhysRevD.71.129903.

[41] L. Blanchet, T. Damour, G. Esposito-Farese, and B. R. Iyer. Gravitational radiation from inspiralling compact binaries completed at the third post-Newtonian order. *Phys.Rev.Lett.*, 93: 091101, 2004. doi:10.1103/PhysRevLett.93.091101.

[42] L. Blanchet, A. Buonanno, and G. Faye. Higher-order spin effects in the dynamics of compact binaries. II. Radiation field. *Phys.Rev.*, D74:104034, 2006. doi:10.1103/PhysRevD.81.089901, 10.1103/PhysRevD.75.049903, 10.1103/PhysRevD.74.104034.

[43] L. Blanchet, G. Faye, B. R. Iyer, and S. Sinha. The Third post-Newtonian gravitational wave polarisations and associated spherical harmonic modes for inspiralling compact binaries in quasi-circular orbits. *Class.Quant.Grav.*, 25:165003, 2008. doi:10.1088/0264-9381/25/16/165003, 10.1088/0264-9381/29/23/239501.

[44] L. Blanchet, A. Buonanno, and G. Faye. Tail-induced spin-orbit effect in the gravitational radiation of compact binaries. *Phys.Rev.*, D84:064041, 2011. doi:10.1103/PhysRevD.84.064041.

[45] L. Blanchet, A. Buonanno, and G. Faye. Tail-induced spin-orbit effect in the gravitational radiation of compact binaries. *Phys.Rev.*, D84:064041, 2011. doi:10.1103/PhysRevD.84.064041.

[46] A. Bohé, S. Marsat, and L. Blanchet. Next-to-next-to-leading order spinorbit effects in the gravitational wave flux and orbital phasing of compact binaries. *Class.Quant.Grav.*, 30:135009, 2013. doi:10.1088/0264-9381/30/13/135009.

[47] A. Bohé, S. Marsat, G. Faye, and L. Blanchet. Next-to-next-to-leading order spin-orbit effects in the near-zone metric and precession equations of compact binaries. *Class.Quant.Grav.*, 30: 075017, 2013. doi:10.1088/0264-9381/30/7/075017.

[48] J. M. Bowen and J. W. York, Jr. Time asymmetric initial data for black holes and black hole collisions. *Phys.Rev.*, D21:2047–2056, 1980. doi:10.1103/PhysRevD.21.2047.

[49] M. Boyle, D. A. Brown, and L. Pekowsky. Comparison of high-accuracy numerical simulations of black-hole binaries with stationary phase post-Newtonian template waveforms for Initial and Advanced LIGO. *Class.Quant.Grav.*, 26:114006, 2009. doi:10.1088/0264-9381/26/11/114006.

[50] M. Boyle, R. Owen, and H. P. Pfeiffer. A geometric approach to the precession of compact binaries. *Phys.Rev.*, D84:124011, 2011. doi:10.1103/PhysRevD.84.124011.

[51] S. Brandt and B. Brügmann. A Simple construction of initial data for multiple black holes. *Phys.Rev.Lett.*, 78:3606–3609, 1997. doi:10.1103/PhysRevLett.78.3606.

[52] R. J. M. P. Breuer, R. A. and S. Waller. Some properties of spin-weighted spheroidal harmonics. *Proc. R. Soc. Lond. A.*, 358:71–86, 1977.

[53] B. Brügmann, W. Tichy, and N. Jansen. Numerical simulation of orbiting black holes. *Phys.Rev.Lett.*, 92:211101, 2004. doi:10.1103/PhysRevLett.92.211101.

[54] B. Brügmann, J. A. González, M. Hannam, S. Husa, and U. Sperhake. Exploring black hole superkicks. *Phys.Rev.*, D77:124047, 2008. doi:10.1103/PhysRevD.77.124047.

[55] B. Brügmann et al. Calibration of Moving Puncture Simulations. *Phys.Rev.*, D77:024027, 2008. doi:10.1103/PhysRevD.77.024027.

[56] Y. Bruhat. Théoème d'existence pour certains systèmes d'équations aux dérivées partielles non linéaires. *Acta Mathematica*, 88(1):141–225, 1952. doi:10.1007/BF02392131.

[57] A. Buonanno and T. Damour. Effective one-body approach to general relativistic two-body dynamics. *Phys.Rev.*, D59:084006, 1999. doi:10.1103/PhysRevD.59.084006.

[58] A. Buonanno and T. Damour. Transition from inspiral to plunge in binary black hole coalescences. *Phys.Rev.*, D62:064015, 2000. doi:10.1103/PhysRevD.62.064015.

[59] A. Buonanno, Y. Chen, and M. Vallisneri. Detecting gravitational waves from precessing binaries of spinning compact objects: Adiabatic limit. *Phys.Rev.*, D67:104025, 2003. doi:10.1103/PhysRevD.67.104025, 10.1103/PhysRevD.74.029904.

[60] A. Buonanno, Y. Chen, Y. Pan, and M. Vallisneri. A Quasi-physical family of gravity-wave templates for precessing binaries of spinning compact objects. 2. Application to double-spin precessing binaries. *Phys.Rev.*, D70:104003, 2004. doi:10.1103/PhysRevD.74.029902, 10.1103/PhysRevD.70.104003.

[61] A. Buonanno, Y. Chen, and T. Damour. Transition from inspiral to plunge in precessing binaries of spinning black holes. *Phys.Rev.*, D74:104005, 2006. doi:10.1103/PhysRevD.74.104005.

[62] A. Buonanno, Y. Pan, J. G. Baker, J. Centrella, B. J. Kelly, et al. Toward faithful templates for non-spinning binary black holes using the effective-one-body approach. *Phys.Rev.*, D76:104049, 2007. doi:10.1103/PhysRevD.76.104049.

[63] A. Buonanno, L. E. Kidder, and L. Lehner. Estimating the final spin of a binary black hole coalescence. *Phys.Rev.*, D77:026004, 2008. doi:10.1103/PhysRevD.77.026004.

[64] A. Buonanno, B. Iyer, E. Ochsner, Y. Pan, and B. S. Sathyaprakash. Comparison of post-Newtonian templates for compact binary inspiral signals in gravitational-wave detectors. *Phys. Rev.*, D80:084043, 2009. doi:10.1103/PhysRevD.80.084043.

[65] A. Buonanno, Y. Pan, H. P. Pfeiffer, M. A. Scheel, L. T. Buchman, et al. Effective-one-body waveforms calibrated to numerical relativity simulations: Coalescence of non-spinning, equal-mass black holes. *Phys.Rev.*, D79:124028, 2009. doi:10.1103/PhysRevD.79.124028.

[66] A. Buonanno, L. E. Kidder, A. H. Mroue, H. P. Pfeiffer, and A. Taracchini. Reducing orbital eccentricity of precessing black-hole binaries. *Phys.Rev.*, D83:104034, 2011. doi:10.1103/PhysRevD.83.104034.

[67] A. Buonanno, G. Faye, and T. Hinderer. Spin effects on gravitational waves from inspiraling compact binaries at second post-Newtonian order. *Phys.Rev.*, D87(4):044009, 2013. doi:10.1103/PhysRevD.87.044009.

[68] M. Campanelli, C. Lousto, P. Marronetti, and Y. Zlochower. Accurate evolutions of orbiting black-hole binaries without excision. *Phys.Rev.Lett.*, 96:111101, 2006. doi:10.1103/PhysRevLett.96.111101.

[69] M. Campanelli, C. O. Lousto, and Y. Zlochower. Gravitational radiation from spinning-black-hole binaries: The orbital hang up. *Phys. Rev.*, D74:041501, 2006. doi:10.1103/PhysRevD.74.041501.

[70] M. Campanelli, C. O. Lousto, Y. Zlochower, B. Krishnan, and D. Merritt. Spin Flips and Precession in Black-Hole-Binary Mergers. *Phys.Rev.*, D75:064030, 2007. doi:10.1103/PhysRevD.75.064030.

[71] M. Campanelli, C. O. Lousto, Y. Zlochower, and D. Merritt. Maximum gravitational recoil. *Phys. Rev. Lett.*, 98:231102, 2007. doi:10.1103/PhysRevLett.98.231102.

[72] M. Campanelli, C. O. Lousto, H. Nakano, and Y. Zlochower. Comparison of Numerical and Post-Newtonian Waveforms for Generic Precessing Black-Hole Binaries. *Phys.Rev.*, D79:084010, 2009. doi:10.1103/PhysRevD.79.084010.

[73] S. M. Carroll. *Spacetime and Geometry*. Addison Wesley, 2004. ISBN 0-8053-8732-3.

[74] G. M. Clemence. The relativity effect in planetary motions. *Rev.Mod.Phys.*, 19:361–364, 1947. doi:10.1103/RevModPhys.19.361.

[75] G. B. Cook. Initial data for numerical relativity. *Living Reviews in Relativity*, 3(5), 2000. doi:10.12942/lrr-2000-5. URL `http://www.livingreviews.org/lrr-2000-5`.

[76] C. Cutler and E. E. Flanagan. An overview of gravitational-wave sources. *Phys.Rev.*, D49:2658, 1994.

[77] T. Damour. Coalescence of two spinning black holes: An effective one- body approach. *Phys. Rev.*, D64:124013, 2001. doi:10.1103/PhysRevD.64.124013.

[78] T. Damour. Introductory lectures on the Effective One Body formalism. *Int.J.Mod.Phys.*, A23: 1130–1148, 2008. doi:10.1142/S0217751X08039992.

[79] T. Damour and A. Nagar. Comparing Effective-One-Body gravitational waveforms to accurate numerical data. *Phys.Rev.*, D77:024043, 2008. doi:10.1103/PhysRevD.77.024043.

[80] T. Damour and A. Nagar. An improved analytical description of inspiralling and coalescing black-hole binaries. *Phys.Rev.*, D79:081503, 2009. doi:10.1103/PhysRevD.79.081503.

[81] T. Damour, B. R. Iyer, and B. S. Sathyaprakash. Improved filters for gravitational waves from inspiralling compact binaries. *Phys.Rev.*, D57:885–907, 1998. doi:10.1103/PhysRevD.57.885.

[82] T. Damour, P. Jaranowski, and G. Schäfer. Poincaré invariance in the ADM Hamiltonian approach to the general relativistic two-body problem. *Phys.Rev.*, D62:021501, 2000. doi:10.1103/PhysRevD.62.021501.

[83] T. Damour, B. R. Iyer, and B. S. Sathyaprakash. A Comparison of search templates for gravitational waves from binary inspiral. *Phys.Rev.*, D63:044023, 2001. doi:10.1103/PhysRevD.63.044023, 10.1103/PhysRevD.72.029902.

[84] T. Damour, P. Jaranowski, and G. Schäfer. Dimensional regularization of the gravitational interaction of point masses. *Phys.Lett.*, B513:147–155, 2001. doi:10.1016/S0370-2693(01)00642-6.

[85] T. Damour, B. R. Iyer, and B. S. Sathyaprakash. A Comparison of search templates for gravitational waves from binary inspiral - 3.5PN update. *Phys.Rev.*, D66:027502, 2002. doi:10.1103/PhysRevD.66.027502.

[86] T. Damour, P. Jaranowski, and G. Schäfer. Hamiltonian of two spinning compact bodies with next-to- leading order gravitational spin-orbit coupling. *Phys.Rev.*, D77:064032, 2008. doi:10.1103/PhysRevD.77.064032.

[87] T. Damour, A. Nagar, E. N. Dorband, D. Pollney, and L. Rezzolla. Faithful Effective-One-Body waveforms of equal-mass coalescing black-hole binaries. *Phys.Rev.*, D77:084017, 2008. doi:10.1103/PhysRevD.77.084017.

[88] T. Damour, A. Nagar, M. Hannam, S. Husa, and B. Brügmann. Accurate Effective-One-Body waveforms of inspiralling and coalescing black-hole binaries. *Phys.Rev.*, D78:044039, 2008. doi:10.1103/PhysRevD.78.044039.

[89] V. C. de Andrade, L. Blanchet, and G. Faye. Third post-Newtonian dynamics of compact binaries: Noetherian conserved quantities and equivalence between the harmonic coordinate and ADM-Hamiltonian formalisms. *Class.Quant.Grav.*, 18:753–778, 2001. doi:10.1088/0264-9381/18/5/301.

[90] S. Dhurandhar and B. Sathyaprakash. Choice of filters for the detection of gravitational waves from coalescing binaries. 2. Detection in colored noise. *Phys.Rev.*, D49:1707–1722, 1994. doi:10.1103/PhysRevD.49.1707.

[91] F. W. Dyson, A. S. Eddington, and C. R. Davidson. A determination of the deflection of light by the sun's gravitational field, from observations made at the solar eclipse of May 29, 1919. *Phil.Trans.Roy.Soc.*, A220:(571–581): 291–333, 1920. doi:10.1098/rsta.1920.0009.

[92] A. Einstein. Die Grundlage der allgemeinen Relativitätstheorie. *Ann. Phys.*, 354(7):769–822, 1916.

[93] A. Einstein. Über Gravitationswellen. *Sitzber. König.-Preuss. Akad. Wiss.*, pages 154–167, 1918.

[94] S. Fairhurst and P. Brady. Interpreting the results of searches for gravitational waves from coalescing binaries. *Class.Quant.Grav.*, 25:105002, 2008. doi:10.1088/0264-9381/25/10/105002.

[95] M. Favata. Nonlinear gravitational-wave memory from binary black hole mergers. *Astrophys.J.*, 696:L159–L162, 2009. doi:10.1088/0004-637X/696/2/L159.

[96] G. Faye, L. Blanchet, and A. Buonanno. Higher-order spin effects in the dynamics of compact binaries. I: Equations of motion. *Phys.Rev.*, D74:104033, 2006. doi:10.1103/PhysRevD.74.104033.

[97] E. E. Flanagan and S. A. Hughes. The Basics of gravitational wave theory. *New J.Phys.*, 7:204, 2005. doi:10.1088/1367-2630/7/1/204.

[98] A. Friedman. Über die Krümmung des Raumes. *Z. Physik*, 10:377–386, 1922.

[99] A. Friedman. Über die Möglichkeit einer Welt mit konstanter negativer Krümmung des Raumes. *Z. Physik*, 21:326–332, 1924.

[100] L. A. Gergely. Spin spin effects in radiating compact binaries. *Phys.Rev.*, D61:024035, 2000. doi:10.1103/PhysRevD.61.024035.

[101] J. N. Goldberg, A. J. MacFarlane, E. T. Newman, F. Rohrlich, and E. C. G. Sudarshan. Spin s spherical harmonics and edth. *J.Math.Phys.*, 8:2155, 1967. doi:10.1063/1.1705135.

[102] A. Gopakumar, M. Hannam, S. Husa, and B. Brügmann. Comparison between numerical relativity and a new class of post-Newtonian gravitational-wave phase evolutions: the non-spinning equal-mass case. *Phys.Rev.*, D78:064026, 2008. doi:10.1103/PhysRevD.78.064026.

[103] L. Grishchuk. Amplification of gravitational waves in an istropic universe. *Sov.Phys.JETP*, 40: 409–415, 1975.

[104] H. Grote. The status of GEO 600. *Class.Quant.Grav.*, 25:114043, 2008. doi:10.1088/0264-9381/25/11/114043.

[105] A. H. Guth. The Inflationary Universe: A Possible Solution to the Horizon and Flatness Problems. *Phys.Rev.*, D23:347–356, 1981. doi:10.1103/PhysRevD.23.347.

[106] A. H. Guth and S. Pi. Fluctuations in the New Inflationary Universe. *Phys.Rev.Lett.*, 49: 1110–1113, 1982. doi:10.1103/PhysRevLett.49.1110.

[107] S. G. Hahn and R. W. Lindquist. The two body problem in geometrodynamics. *Ann. Phys.*, 29: 304–331, 1964. doi:10.1016/0003-4916(64)90223-4.

[108] M. Hannam. Modelling gravitational waves from precessing black-hole binaries: Progress, challenges and prospects. *Gen.Rel.Grav.*, 46:1767, 2014. doi:10.1007/s10714-014-1767-2.

[109] M. Hannam, S. Husa, B. Brügmann, J. A. González, and U. Sperhake. Beyond the Bowen-York extrinsic curvature for spinning black holes. *Class.Quant.Grav.*, 24:S15–S24, 2007. doi:10.1088/0264-9381/24/12/S02.

[110] M. Hannam, S. Husa, D. Pollney, B. Brügmann, and N. Ó Murchadha. Geometry and Regularity of Moving Punctures. *Phys.Rev.Lett.*, 99:241102, 2007. doi:10.1103/PhysRevLett.99.241102.

[111] M. Hannam, S. Husa, B. Brügmann, and A. Gopakumar. Comparison between numerical-relativity and post-Newtonian waveforms from spinning binaries: the orbital hang-up case. *Phys. Rev.*, D78:104007, 2008. doi:10.1103/PhysRevD.78.104007.

[112] M. Hannam, S. Husa, F. Ohme, B. Brügmann, and N. Ó Murchadha. Wormholes and trumpets: the Schwarzschild spacetime for the moving-puncture generation. *Phys.Rev.*, D78:064020, 2008. doi:10.1103/PhysRevD.78.064020.

[113] M. Hannam, S. Husa, U. Sperhake, B. Brügmann, and J. A. González. Where post-Newtonian and numerical-relativity waveforms meet. *Phys.Rev.*, D77:044020, 2008. doi:10.1103/PhysRevD.77.044020.

[114] M. Hannam, S. Husa, and N. Ó Murchadha. Bowen-York trumpet data and black-hole simulations. *Phys.Rev.*, D80:124007, 2009. doi:10.1103/PhysRevD.80.124007.

[115] M. Hannam, S. Husa, F. Ohme, and P. Ajith. Length requirements for numerical-relativity waveforms. *Phys.Rev.*, D82:124052, 2010. doi:10.1103/PhysRevD.82.124052.

[116] M. Hannam, S. Husa, F. Ohme, D. Müller, and B. Brügmann. Simulations of black-hole binaries with unequal masses or non-precessing spins: accuracy, physical properties, and comparison with post-Newtonian results. *Phys.Rev.*, D82:124008, 2010. doi:10.1103/PhysRevD.82.124008.

[117] M. Hannam, P. Schmidt, A. Bohé, L. Haegel, S. Husa, et al. Twist and shout: A simple model of complete precessing black-hole-binary gravitational waveforms. *submitted to Phys.Rev.Letters*, 2013. URL `http://arxiv.org/abs/1308.3271`.

[118] M. Hannam et al. The Samurai Project: verifying the consistency of black-hole-binary waveforms for gravitational-wave detection. *Phys.Rev.*, D79:084025, 2009. doi:10.1103/PhysRevD.79.084025.

[119] G. M. Harry. Advanced LIGO: The next generation of gravitational wave detectors. *Class.Quant.Grav.*, 27:084006, 2010. doi:10.1088/0264-9381/27/8/084006.

[120] J. B. Hartle. *Gravity*. Addison Wesley, 2003. ISBN 0-8053-8662-9.

[121] J. Hartung and J. Steinhoff. Next-to-leading order spin-orbit and spin(a)-spin(b) Hamiltonians for n gravitating spinning compact objects. *Phys.Rev.*, D83:044008, 2011. doi:10.1103/PhysRevD.83.044008.

[122] J. Hartung and J. Steinhoff. Next-to-next-to-leading order post-Newtonian spin(1)-spin(2) Hamiltonian for self-gravitating binaries. *Annalen Phys.*, 523:919–924, 2011. doi:10.1002/andp.201100163.

[123] S. W. Hawking and G. F. R. Ellis. *The large scale structure of space-time*. Cambridge University Press, 1973. ISBN 0-521-09906-4. Reprint 1999.

[124] I. Hinder, A. Buonanno, M. Boyle, Z. B. Etienne, J. Healy, et al. Error-analysis and comparison to analytical models of numerical waveforms produced by the NRAR Collaboration. *Class.Quant.Grav.*, 31:025012, 2014. doi:10.1088/0264-9381/31/2/025012.

[125] R. Hulse and J. Taylor. Discovery of a pulsar in a binary system. *Astrophys.J.*, 195:L51–L53, 1975. doi:10.1086/181708.

[126] S. Husa, J. A. González, M. Hannam, B. Brügmann, and U. Sperhake. Reducing phase error in long numerical binary black hole evolutions with sixth order finite differencing. *Class.Quant.Grav.*, 25:105006, 2008. doi:10.1088/0264-9381/25/10/105006.

[127] S. Husa, M. Hannam, J. A. González, U. Sperhake, and B. Brügmann. Reducing eccentricity in black-hole binary evolutions with initial parameters from post-Newtonian inspiral. *Phys.Rev.*, D77:044037, 2008. doi:10.1103/PhysRevD.77.044037.

[128] P. Jaranowski and G. Schäfer. 3rd post-Newtonian higher order Hamilton dynamics for two-body point-mass systems. *Phys.Rev.*, D57:7274–7291, 1998. doi:10.1103/PhysRevD.57.7274.

[129] P. Jaranowski and G. Schäfer. The Binary black hole problem at the third post-Newtonian approximation in the orbital motion: Static part. *Phys.Rev.*, D60:124003, 1999. doi:10.1103/PhysRevD.60.124003.

[130] P. Jaranowski and G. Schäfer. Dimensional regularization of local singularities in the 4th post-Newtonian two-point-mass Hamiltonian. *Phys.Rev.*, D87:081503, 2013. doi:10.1103/PhysRevD.87.081503.

[131] M. Kamionkowski, A. Kosowsky, and A. Stebbins. A Probe of primordial gravity waves and vorticity. *Phys.Rev.Lett.*, 78:2058–2061, 1997. doi:10.1103/PhysRevLett.78.2058.

[132] R. P. Kerr. Gravitational field of a spinning mass as an example of algebraically special metrics. *Phys.Rev.Lett.*, 11:237–238, 1963. doi:10.1103/PhysRevLett.11.237.

[133] L. E. Kidder. Coalescing binary systems of compact objects to post-Newtonian 5/2 order. 5. Spin effects. *Phys.Rev.*, D52:821–847, 1995. doi:10.1103/PhysRevD.52.821.

[134] L. E. Kidder. Using full information when computing modes of post-Newtonian waveforms from inspiralling compact binaries in circular orbit. *Phys.Rev.*, D77:044016, 2008. doi:10.1103/PhysRevD.77.044016.

[135] K. D. Kokkotas and B. Schmidt. Quasi-normal modes of stars and black holes. *Living Reviews in Relativity*, 2(2), 1999. doi:10.12942/lrr-1999-2. URL `http://www.livingreviews.org/lrr-1999-2`.

[136] B. Krishnan, C. O. Lousto, and Y. Zlochower. Quasi-Local Linear Momentum in Black-Hole Binaries. *Phys.Rev.*, D76:081501, 2007. doi:10.1103/PhysRevD.76.081501.

[137] J. Lattimer and M. Prakash. The physics of neutron stars. *Science*, 304:536–542, 2004. doi:10.1126/science.1090720.

[138] G. Lemaître. Un Univers Homogène de Masse Constante et de Rayon Croissant Rendant Compte de la Vitesse Radiale des Nébuleuses Extragalactiques. *Ann. Soc. Sci. Bruxelles I*, A 47:49–, 1927.

[139] G. Lemaître. L'Univers en Expansion. *Ann. Soc. Sci. Bruxelles I*, A 53:51–, 1933.

[140] J. Lense and H. Thirring. Über den Einfluss der Eigenrotation der Zentralkörper auf die Bewegung der Planeten und Monde nach der Einsteinschen Gravitationstheorie. *Physikalische Zeitschrift*, 19:156163, 1918.

[141] M. Levi. Binary dynamics from spin1-spin2 coupling at fourth post-Newtonian order. *Phys.Rev.*, D85:064043, 2012. doi:10.1103/PhysRevD.85.064043.

[142] A. Lichnerowicz. L'intégration des équations de la gravitation relativiste et la problème des n corps. *J. Math. Pures et Appl.*, 23(37), 1944.

[143] A. D. Linde. A New Inflationary Universe Scenario: A Possible Solution of the Horizon, Flatness, Homogeneity, Isotropy and Primordial Monopole Problems. *Phys.Lett.*, B108:389–393, 1982. doi:10.1016/0370-2693(82)91219-9.

[144] C. O. Lousto and Y. Zlochower. Where angular momentum goes in a precessing black hole binary. *Phys.Rev.*, D89:021501, 2014. doi:10.1103/PhysRevD.89.021501.

[145] C. O. Lousto, M. Campanelli, and Y. Zlochower. Remnant Masses, Spins and Recoils from the Merger of Generic Black-Hole Binaries. *Class.Quant.Grav.*, 27:114006, 2010. doi:10.1088/0264-9381/27/11/114006.

[146] G. Lovelace. Reducing spurious gravitational radiation in binary-black-hole simulations by using conformally curved initial data. *Class.Quant.Grav.*, 26:114002, 2009. doi:10.1088/0264-9381/26/11/114002.

[147] G. Lovelace, M. Boyle, M. A. Scheel, and B. Szilagyi. Accurate gravitational waveforms for binary-black-hole mergers with nearly extremal spins. *Class.Quant.Grav.*, 29:045003, 2012. doi:10.1088/0264-9381/29/4/045003.

[148] A. Lundgren and R. O'Shaughnessy. A single-spin precessing gravitational wave in closed form. *Phys.Rev.*, D89:044021, 2014. doi:10.1103/PhysRevD.89.044021.

[149] M. Maggiore. *Gravitational Waves Volume 1: Theory and Experiments*. Oxford University Press, 2008. ISBN 978-0-19-857074-5. Reprint 2013.

[150] A. A. Michelson and E. Morley. On the Relative Motion of the Earth and the Luminiferous Ether. *American Journal of Science*, 34(203):333–345, 1887.

[151] C. W. Misner, K. S. Thorne, and J. A. Wheeler. *Gravitation*. W. H. Freeman and Company, 1970. ISBN 0-7167-0344-0.

[152] V. Moncrief. Gravitational perturbations of spherically symmetric systems. I. The exterior problem. *Annals Phys.*, 88:323–342, 1974. doi:10.1016/0003-4916(74)90173-0.

[153] A. H. Mroue, L. E. Kidder, and S. A. Teukolsky. Ineffectiveness of Padé resummation techniques in post-Newtonian approximations. *Phys.Rev.*, D78:044004, 2008. doi:10.1103/PhysRevD.78.044004.

[154] A. H. Mroue, H. P. Pfeiffer, L. E. Kidder, and S. A. Teukolsky. Measuring orbital eccentricity and periastron advance in quasi-circular black hole simulations. *Phys.Rev.*, D82:124016, 2010. doi:10.1103/PhysRevD.82.124016.

[155] A. H. Mroue, M. A. Scheel, B. Szilagyi, H. P. Pfeiffer, M. Boyle, et al. A catalog of 174 binary black-hole simulations for gravitational-wave astronomy. *Phys.Rev.Lett.*, 111:241104, 2013. doi:10.1103/PhysRevLett.111.241104.

[156] A. Nagar and L. Rezzolla. Gauge-invariant non-spherical metric perturbations of Schwarzschild black-hole spacetimes. *Class.Quant.Grav.*, 22:R167, 2005. doi:10.1088/0264-9381/23/12/C01, 10.1088/0264-9381/22/16/R01.

[157] E. Newman and R. Penrose. An Approach to gravitational radiation by a method of spin coefficients. *J.Math.Phys.*, 3:566–578, 1962. doi:10.1063/1.1724257.

[158] E. T. Newman and A. I. Janis. Note on the Kerr spinning particle metric. *J.Math.Phys.*, 6: 915–917, 1965. doi:10.1063/1.1704350.

[159] E. T. Newman and R. Penrose. Note on the Bondi-Metzner-Sachs group. *J.Math.Phys.*, 7: 863–870, 1966. doi:10.1063/1.1931221.

[160] E. T. Newman, R. Couch, K. Chinnapared, A. Exton, A. Prakash, et al. Metric of a Rotating, Charged Mass. *J.Math.Phys.*, 6:918–919, 1965. doi:10.1063/1.1704351.

[161] G. Nordström. On the Energy of the Gravitational Field in Einstein's Theory. *Verhandl. Koninkl. Ned. Akad. Wetenschap., Afdel. Natuurk., Amsterdam*, 26:1201–1208, 1918.

[162] NRAR. NRAR. URL `https://www.ninja-project.org/doku.php?id=nrar:home`.

[163] E. Ochsner and R. O'Shaughnessy. Asymptotic frame selection for binary black hole spacetimes II: Post-Newtonian limit. *Phys.Rev.*, D86:104037, 2012. doi:10.1103/PhysRevD.86.104037.

[164] F. Ohme. *Bridging the gap between post-Newtonian theory and Numerical Relativity in gravitational-wave data analysis*. PhD Thesis, Universität Potsdam, 2012. URL `http://opus.kobv.de/ubp/volltexte/2012/6034/`.

[165] F. Ohme. Analytical meets numerical relativity - status of complete gravitational waveform models for binary black holes. *Class.Quant.Grav.*, 29:124002, 2012. doi:10.1088/0264-9381/29/12/124002.

[166] N. O'Murchadha and J. W. York. Initial - value problem of general relativity. 1. General formulation and physical interpretation. *Phys.Rev.*, D10:428–436, 1974. doi:10.1103/PhysRevD.10.428.

[167] B. O'Neill. *Semi-Riemannian Geometry With Applications to Relativity*. Academic Press, 1983. ISBN 978-0123994615.

[168] R. O'Shaughnessy, B. Vaishnav, J. Healy, Z. Meeks, and D. Shoemaker. Efficient asymptotic frame selection for binary black hole spacetimes using asymptotic radiation. *Phys.Rev.*, D84: 124002, 2011.

[169] R. O'Shaughnessy, J. Healy, L. London, Z. Meeks, and D. Shoemaker. Is J enough? Comparison of gravitational waves emitted along the total angular momentum direction with other preferred orientations. *Phys.Rev.*, D85(6):084003, 2012. doi:10.1103/PhysRevD.85.084003, 10.1103/PhysRevD.87.069901.

[170] R. O'Shaughnessy, L. London, J. Healy, and D. Shoemaker. Precession during merger: Strong polarization changes are observationally accessible features of strong-field gravity during binary black hole merger. *Phys.Rev.*, D87(4):044038, 2013. doi:10.1103/PhysRevD.87.044038.

[171] B. J. Owen. Search templates for gravitational waves from inspiraling binaries: Choice of template spacing. *Phys.Rev.*, D53:6749–6761, 1996. doi:10.1103/PhysRevD.53.6749.

[172] Y. Pan, A. Buonanno, L. T. Buchman, T. Chu, L. E. Kidder, et al. Effective-one-body waveforms calibrated to numerical relativity simulations: coalescence of non-precessing, spinning, equal-mass black holes. *Phys.Rev.*, D81:084041, 2010. doi:10.1103/PhysRevD.81.084041.

[173] Y. Pan, A. Buonanno, M. Boyle, L. T. Buchman, L. E. Kidder, et al. Inspiral-merger-ringdown multipolar waveforms of nonspinning black-hole binaries using the effective-one-body formalism. *Phys.Rev.*, D84:124052, 2011. doi:10.1103/PhysRevD.84.124052.

[174] Y. Pan, A. Buonanno, A. Taracchini, L. E. Kidder, A. H. Mroue, et al. Inspiral-merger-ringdown waveforms of spinning, precessing black-hole binaries in the effective-one-body formalism. *Phys.Rev.*, D89:084006, 2014. doi:10.1103/PhysRevD.89.084006.

[175] Y. Pan et al. A data-analysis driven comparison of analytic and numerical coalescing binary waveforms: Nonspinning case. *Phys.Rev.*, D77:024014, 2008. doi:10.1103/PhysRevD.77.024014.

[176] L. Pekowsky, R. OShaughnessy, J. Healy, and D. Shoemaker. Comparing gravitational waves from nonprecessing and precessing black hole binaries in the corotating frame. *Phys.Rev.*, D88 (2):024040, 2013. doi:10.1103/PhysRevD.88.024040.

[177] P. Peters. Gravitational Radiation and the Motion of Two Point Masses. *Phys.Rev.*, 136:B1224–B1232, 1964. doi:10.1103/PhysRev.136.B1224.

[178] P. Peters and J. Mathews. Gravitational radiation from point masses in a Keplerian orbit. *Phys.Rev.*, 131:435–439, 1963. doi:10.1103/PhysRev.131.435.

[179] E. Poisson. Gravitational waves from inspiraling compact binaries: The quadrupole-moment term. *Phys.Rev.*, D57:5287–5290, 1998. doi:10.1103/PhysRevD.57.5287.

[180] D. Pollney and C. Reisswig. Gravitational memory in binary black hole mergers. *Astrophys.J.*, 732:L13, 2011. doi:10.1088/2041-8205/732/1/L13.

[181] R. A. Porto, A. Ross, and I. Z. Rothstein. Spin induced multipole moments for the gravitational wave flux from binary inspirals to third Post-Newtonian order. *JCAP*, 1103:009, 2011. doi:10.1088/1475-7516/2011/03/009.

[182] F. Pretorius. Numerical relativity using a generalized harmonic decomposition. *Class.Quant.Grav.*, 22:425–452, 2005. doi:10.1088/0264-9381/22/2/014.

[183] F. Pretorius. Evolution of binary black hole spacetimes. *Phys.Rev.Lett.*, 95:121101, 2005. doi:10.1103/PhysRevLett.95.121101.

[184] M. Pürrer, S. Husa, and M. Hannam. An efficient iterative method to reduce eccentricity in numerical-relativity simulations of compact binary inspiral. *Phys.Rev.*, D85:124051, 2012. doi:10.1103/PhysRevD.85.124051.

[185] E. Racine, A. Buonanno, and L. E. Kidder. Recoil velocity at 2PN order for spinning black hole binaries. *Phys.Rev.*, D80:044010, 2009. doi:10.1103/PhysRevD.80.044010.

[186] T. Regge and J. A. Wheeler. Stability of a Schwarzschild singularity. *Phys.Rev.*, 108:1063–1069, 1957. doi:10.1103/PhysRev.108.1063.

[187] H. Reissner. Über die Eigengravitation des elektrischen Feldes nach der Einsteinschen Theorie. *Ann. Phys.*, 355(9):106–120, 1916.

[188] L. Rezzolla, P. Diener, E. N. Dorband, D. Pollney, C. Reisswig, et al. The Final spin from the coalescence of aligned-spin black-hole binaries. *Astrophys.J.*, 674:L29–L32, 2008. doi:10.1086/528935.

[189] H. P. Robertson. Relativistic cosmology. *Rev.Mod.Phys.*, 5:62–90, 1933.

[190] H. P. Robertson. Kinematics and World Structure. *Astrophys.J.*, 82:248, 1935.

[191] J. J. Sakurai. *Modern Quantum Mechanics*. Addison-Wesley Publishing Company, revised edition, 1994. ISBN 0-201-53929-2.

[192] L. Santamaria, F. Ohme, P. Ajith, B. Brügmann, N. Dorband, et al. Matching post-Newtonian and numerical relativity waveforms: systematic errors and a new phenomenological model for non-precessing black hole binaries. *Phys.Rev.*, D82:064016, 2010. doi:10.1103/PhysRevD.82.064016.

[193] B. Sathyaprakash. Filtering post-Newtonian gravitational waves from coalescing binaries. *Phys.Rev.*, D50:7111–7115, 1994. doi:10.1103/PhysRevD.50.R7111.

[194] B. Sathyaprakash and S. Dhurandhar. Choice of filters for the detection of gravitational waves from coalescing binaries. *Phys.Rev.*, D44:3819–3834, 1991. doi:10.1103/PhysRevD.44.3819.

[195] B. S. Sathyaprakash and B. F. Schutz. Physics, astrophysics and cosmology with gravitational waves. *Living Reviews in Relativity*, 12(2), 2009. doi:10.12942/lrr-2009-2. URL `http://www.livingreviews.org/lrr-2009-2`.

[196] P. Schmidt, M. Hannam, S. Husa, and P. Ajith. Tracking the precession of compact binaries from their gravitational-wave signal. *Phys.Rev.*, D84:024046, 2011. doi:10.1103/PhysRevD.84.024046.

[197] P. Schmidt, M. Hannam, and S. Husa. Towards models of gravitational waveforms from generic binaries: A simple approximate mapping between precessing and non-precessing inspiral signals. *Phys.Rev.*, D86:104063, 2012. doi:10.1103/PhysRevD.86.104063.

[198] P. Schmidt, F. Ohme, and M. Hannam. Towards models of gravitational waveforms from generic binaries II: Modeling precession effects with a single effective precession parameter. 2014. URL `http://arxiv.org/abs/1408.1810`.

[199] B. Schutz. *A first course in general relativity*. Cambridge University Press, second edition, 2009. ISBN 978-0-521-88705-2.

[200] K. Schwarzschild. Über das Gravitationsfeld eines Massenpunktes nach der Einsteinschen Theorie. *Sitzber. König.-Preuss. Akad. Wiss.*, pages 189–196, 1916.

[201] U. Seljak and M. Zaldarriaga. Signature of gravity waves in polarization of the microwave background. *Phys.Rev.Lett.*, 78:2054–2057, 1997. doi:10.1103/PhysRevLett.78.2054.

[202] M. Shibata and T. Nakamura. Evolution of three-dimensional gravitational waves: Harmonic slicing case. *Phys.Rev.*, D52:5428–5444, 1995. doi:10.1103/PhysRevD.52.5428.

[203] Shoemaker, David and Losurdo, Giovanni. Possible scenarios for commissioning and early observing with the second generation detectors. Technical Report LIGO-G10001760-v7, LIGO Project, 2010. URL `https://dcc.ligo.org/DocDB/0009/G1000176/007/Advanced%20Virgo%20and%20LIGO%20post-project%20progression.pdf`.

[204] D. Shoemaker (LIGO Scientific Collaboration). Advanced LIGO anticipated sensitivity curves. 2010. URL `https://dcc.ligo.org/LIGO-T0900288/public`.

[205] K. Somiya. Detector configuration of KAGRA - the Japanese cryogenic gravitational-wave detector. *Class.Quant.Grav.*, 29:124007, 2012. doi:10.1088/0264-9381/29/12/124007.

[206] A. A. Starobinsky. Spectrum of relict gravitational radiation and the early state of the universe. *JETP Lett.*, 30:682–685, 1979.

[207] A. A. Starobinsky. Dynamics of Phase Transition in the New Inflationary Universe Scenario and Generation of Perturbations. *Phys.Lett.*, B117:175–178, 1982. doi:10.1016/0370-2693(82)90541-X.

[208] J. Stewart and M. Walker. Perturbations of spacetimes in general relativity. *Proc.Roy.Soc.Lond.*, A341:49–74, 1974. doi:10.1098/rspa.1974.0172.

[209] R. Sturani, S. Fischetti, L. Cadonati, G. Guidi, J. Healy, et al. Complete phenomenological gravitational waveforms from spinning coalescing binaries. *J.Phys.Conf.Ser.*, 243:012007, 2010. doi:10.1088/1742-6596/243/1/012007.

[210] A. Taracchini, Y. Pan, A. Buonanno, E. Barausse, M. Boyle, et al. Prototype effective-one-body model for nonprecessing spinning inspiral-merger-ringdown waveforms. *Phys.Rev.*, D86:024011, 2012. doi:10.1103/PhysRevD.86.024011.

[211] S. A. Teukolsky. Perturbations of a rotating black hole. 1. Fundamental equations for gravitational electromagnetic and neutrino field perturbations. *Astrophys.J.*, 185:635–647, 1973. doi:10.1086/152444. Ph.D. Thesis (Advisor: Kip S. Thorne).

[212] The LIGO Scientific Collaboration. Advanced ligo anticipated sensitivity curves. Technical Report LIGO-T0900288-v3, LIGO Project, 2009. URL `https://dcc.ligo.org/DocDB/0002/T0900288/003/AdvLIGO%20noise%20curves.pdf`.

[213] J. Thornburg. Coordinates and boundary conditions for the general relativistic initial data problem. *Class.Quant.Grav.*, 4(5):1119, 1987. URL `http://stacks.iop.org/0264-9381/4/i=5/a=013`.

[214] K. Thorne. Multipole Expansions of Gravitational Radiation. *Rev.Mod.Phys.*, 52:299–339, 1980. doi:10.1103/RevModPhys.52.299.

[215] K. S. Thorne. Gravitational radiation. In S. W. Hawking and W. Israel, editors, *Three hundred years of gravitation*, pages 330–458. Cambridge University Press, Cambridge, UK, 1987.

[216] W. Tichy and P. Marronetti. The Final mass and spin of black hole mergers. *Phys.Rev.*, D78:081501, 2008. doi:10.1103/PhysRevD.78.081501.

[217] C. Van Den Broeck, D. A. Brown, T. Cokelaer, I. Harry, G. Jones, et al. Template banks to search for compact binaries with spinning components in gravitational wave data. *Phys.Rev.*, D80:024009, 2009. doi:10.1103/PhysRevD.80.024009.

[218] R. M. Wald. *General Relativity*. The University of Chicago Press, 1984. ISBN 0-226-87033-2.

[219] S. Waldman. The Advanced LIGO Gravitational Wave Detector. 2011.

[220] A. G. Walker. On Milne's Theory of World-Structure. *Proc. London Math. Soc*, 42:90–127, 1937.

[221] J. Weber. Observation of the thermal fluctuations of a gravitational-wave detector. *Phys.Rev.Lett.*, 17:1228–1230, Dec 1966. doi:10.1103/PhysRevLett.17.1228. URL `http://link.aps.org/doi/10.1103/PhysRevLett.17.1228`.

[222] J. Weber. Evidence for discovery of gravitational radiation. *Phys.Rev.Lett.*, 22:1320–1324, Jun 1969. doi:10.1103/PhysRevLett.22.1320. URL `http://link.aps.org/doi/10.1103/PhysRevLett.22.1320`.

[223] S. Weinberg. *Gravitation and Cosmology: Principles and Applications of the General Theory of Relativity*. John Wiley & Sons, 1972. ISBN 978-0471925675.

[224] J. M. Weisberg and J. H. Taylor. Relativistic binary pulsar B1913+16: Thirty years of observations and analysis. *ASP Conf.Ser.*, 328:25, 2005.

[225] E. P. Wigner. *Group Theory and its Application to the Quantum Mechanics of Atomic Spectra*. Academic Press Inc., New York, 1959. ISBN 978-0127505503.

[226] C. M. Will and A. G. Wiseman. Gravitational radiation from compact binary systems: Gravitational wave forms and energy loss to second post-Newtonian order. *Phys.Rev.*, D54:4813–4848, 1996. doi:10.1103/PhysRevD.54.4813.

[227] J. W. York. Mapping onto solutions of the gravitational initial value problem. *J.Math.Phys.*, 13:125–130, 1972. doi:10.1063/1.1665945.

[228] J. W. York. Conformally invariant orthogonal decomposition of symmetric tensors on Riemannian manifolds and the initial value problem of general relativity. *J.Math.Phys.*, 14:456–464, 1973. doi:10.1063/1.1666338.

[229] J. W. York. Covariant decompositions of symmetric tensors in the theory of gravitation. *Ann. Inst. Henri Poincaré*, 21(4):319–322, 1974.

[230] J. W. York. Kinematics and dynamics of general relativity. In L. L. Smarr, editor, *Sources of gravitational radiation*, pages 83–126. Cambridge University Press, Cambridge, UK, 1979. ISBN 0-521-22778-X.

[231] J. Zendri, L. Baggio, M. Bignotto, M. Bonaldi, M. Cerdonio, et al. Status report and near future prospects for the gravitational wave detector AURIGA. *Class.Quant.Grav.*, 19:1925–1933, 2002. doi:10.1088/0264-9381/19/7/394.

[232] F. Zerilli. Gravitational field of a particle falling in a schwarzschild geometry analyzed in tensor harmonics. *Phys.Rev.*, D2:2141–2160, 1970. doi:10.1103/PhysRevD.2.2141.